University of Windsor
Scholarship at UWindsor

Electronic Theses and Dissertations Theses, Dissertations, and Major Papers

7-29-2020

Supportless Fabrication, Experimental, and Numerical Analysis of the Physical Properties for a Thin-Walled Hemisphere

Hamed Kalami
University of Windsor

Follow this and additional works at: https://scholar.uwindsor.ca/etd

Recommended Citation
Kalami, Hamed, "Supportless Fabrication, Experimental, and Numerical Analysis of the Physical Properties for a Thin-Walled Hemisphere" (2020). *Electronic Theses and Dissertations*. 8416.
https://scholar.uwindsor.ca/etd/8416

This online database contains the full-text of PhD dissertations and Masters' theses of University of Windsor students from 1954 forward. These documents are made available for personal study and research purposes only, in accordance with the Canadian Copyright Act and the Creative Commons license—CC BY-NC-ND (Attribution, Non-Commercial, No Derivative Works). Under this license, works must always be attributed to the copyright holder (original author), cannot be used for any commercial purposes, and may not be altered. Any other use would require the permission of the copyright holder. Students may inquire about withdrawing their dissertation and/or thesis from this database. For additional inquiries, please contact the repository administrator via email (scholarship@uwindsor.ca) or by telephone at 519-253-3000ext. 3208.

Supportless Fabrication, Experimental, and Numerical Analysis of the Physical Properties for a Thin-Walled Hemisphere

By

Hamed Kalami

A Dissertation
Submitted to the Faculty of Graduate Studies
through the Department of Mechanical, Automotive & Materials Engineering
in Partial Fulfillment of the Requirements for
the Degree Doctor of Philosophy
at the University of Windsor

Windsor, Ontario, Canada

2020

© 2020 Hamed Kalami

Supportless Fabrication, Experimental, and Numerical Analysis of the Physical Properties for a Thin-Walled Hemisphere

by

Hamed Kalami

APPROVED BY:

E. Toyserkani, External Examiner
University of Waterloo

M. Wang
Department of Mechanical, Automotive & Materials Engineering

J. Johrendt
Department of Mechanical, Automotive & Materials Engineering

D. Green
Department of Mechanical, Automotive & Materials Engineering

J. Urbanic, Advisor
Department of Mechanical, Automotive & Materials Engineering

May 12, 2020

DECLARATION OF CO-AUTHORSHIP / PREVIOUS PUBLICATION

I. Co-Authorship

I hereby declare that this thesis incorporates material that is result of joint research, as follows:

All chapters of the thesis were done under the supervision of Professor Jill Urbanic. In all cases, the key ideas, primary contributions, experimental designs, data analysis, interpretation, and writing were performed by the author, and the contribution of co-author was primarily through the provision of supervision, comments, suggestions, and recommendations.

I am aware of the University of Windsor Senate Policy on Authorship and I certify that I have properly acknowledged the contribution of other researchers to my thesis, and have obtained written permission from each of the co-author(s) to include the above material(s) in my thesis.

I certify that, with the above qualification, this thesis, and the research to which it refers, is the product of my own work.

II. Previous Publication

This thesis includes one original paper that has been previously published/submitted for publication in a peer reviewed journal, as follows:

Dissertation Chapter	Publication title/full citation	Publication status*
Chapter [4]	*Process Planning of Creating a Surface Dome with Bead Deposition Additive Manufacturing. Hamed Kalami and Jill Urbanic. 2019, IFAC-PapersOnLine* [1]	*published*
Chapter [4]	*Process Planning Solution Strategies for Fabrication Thin-Wall Domes using DirectEnergy Deposition. Hamed Kalami and Jill Urbanic, 2020, International Journal of Computer Integrated Manufacturing*	*Submitted*

I certify that I have obtained a written permission from the copyright owner(s) to include the above published material(s) in my thesis. I certify that the above material describes work completed during my registration as a graduate student at the University of Windsor.

III. General

I declare that, to the best of my knowledge, my thesis does not infringe upon anyone’s copyright nor violate any proprietary rights and that any ideas, techniques, quotations, or any other material from the work of other people included in my thesis, published or otherwise, are fully acknowledged in accordance with the standard referencing practices. Furthermore, to the extent that I have included copyrighted material that surpasses the bounds of fair dealing within the meaning of the Canada Copyright Act, I certify that I have obtained a written permission from the copyright owner(s) to include such material(s) in my thesis.

I declare that this is a true copy of my thesis, including any final revisions, as approved by my thesis committee and the Graduate Studies office, and that this thesis has not been submitted for a higher degree to any other University or Institution.

ABSTRACT

Although multi-axis bead deposition-based additive manufacturing processes have been investigated in many aspects in the literature, a general process planning approach to address collision detection and prevention still needs to be developed to fabricate complex thin-wall geometries in a supportless fashion. In this research, an algorithm is presented that partitions the surfaces of the part and finds the appropriate tool orientation for each partition to avoid collisions. This algorithm is applied to segment the surface of a thin-wall hemisphere dome and fabricate it without the need of support structures. Two main fabrication strategies are developed: wedge-shaped partitioning, and a rotary toolpath. A five-axis toolpath and a 2+1+1-axis toolpath is introduced to fabricate the partitioned build scenarios. A rotary (1+3-axis) toolpath is also developed. It is concluded that planar slicing brings limitations to reduce the number of partitions that can be modified by a constant step over toolpath.

On one hand, the partitioning strategy provides an opportunity to fabricate geometries in a supportless fashion by direct energy deposition additive manufacturing, on the other hand, it introduces physical properties challenges such as surface roughness and hardness variations. Process planning, data collection, and experimental/numerical procedures are implemented to investigate the surface roughness variations (Ra measurement) of fabricated domes. Hence, two solutions are developed using Matlab programming. A mount solution uses the magnified pictures of the exposed surface edges of mount samples as input data. The other solution uses a 3D point cloud of the surface. The innovation of the 3D point cloud solution is the distance factor that is applied in the calculations. The results of this solution are compared to the mount solution. Since the input data of the mount solution is more accurate, the results are more reliable than the 3D point cloud method. The Ra variation diagrams show lower Ra values for the 5-axis sample and the highest values for the rotary sample. Large surface irregularities are noticed at the transition points between partitions, which escalates the roughness values drastically in the region. The sudden alteration of the tool orientation between partitions causes these surface irregularities.

Additionally, process planning, data collection, and experimental/numerical analyses are developed to explore hardness variations of the fabricated domes along the

slicing direction. The hardness diagram of the 2+1+1-axis sample shows a recognizable pattern for partitions 2-4. The hardness is around 200 (HV) within the partitions but drops to 150 (HV) at the transition points between partitions. Partitions 5-8 show a less recognizable pattern. Although the rotary sample is fabricated in 3 intermittent fabrication sections, it does not show any significant pattern related to the sectioning. The statistical analysis of the hardness shows the highest standard deviation for the 5-axis sample and the least for the rotary one.

Finite element analysis of the hardness and residual stress are performed by the ESI Sysweld software for 144 beads of the 2+1+1-axis sample. To reduce the calculation time (a factor of 15 times), a variable mesh size of the beads and substrate are introduced. This means that the element size of the beads grows for the regions farther from the measurement region. The resultant hardness diagram predicts the peak and valley of the experimental diagram for the partitions 1-4, but it misses some patterns for partitions 5-8. Fast Fourier transformation analyses of the surface roughness and experimental/numerical hardness data show a repetitive pattern by the wavelength of the partition length. The preparation time and accuracy of the finite element analysis results reveal that an experimental fabrication and measurement test is preferred at this time, or a new method of numerical analysis is required.

This research clearly illustrates the challenges associated with building a complex component and understanding its characteristics. On one hand, splitting the part geometry by different partitioning shapes facilitates the fabrication of the geometries in a supportless fashion. However, this fabrication strategy introduces inconsistency in the mechanical properties. Hardness variations generated by a partitioning strategy needs to be dealt with (possibly by a post-heat treatment). Surface quality at the transient points needs to be investigated more. This foundational research highlights the process planning challenges associated with metal bead based deposition processes, and highlights relevant challenges for similar process families.

DEDICATION

I dedicate this dissertation to my family especially my parents for their support and love.

ACKNOWLEDGEMENTS

I would like to appreciate my advisor Professor Jill Urbanic for her support, guidance, and persistence all the way through this research. Her wisdom and knowledge have been the major help during this exploration journey.

I would like to thank CAMufacturing Solutions, Inc. especially the president, Bob Hedrick, for sharing knowledge and facility as well as his financial support.

I would like to thank my committee members, Dr. Jennifer Johrendt, Dr. Daniel Green, Professor Michael Wang and external examiner Professor Ehsan Toyserkani for their time, consideration and comments that improved the quality of the dissertation.

I would like to thank Mitacs Accelerate for financial support.

I would like to thank Lincoln Laser Solutions and Whitfield Welding Inc. for sharing their facilities.

I would like to thank Inspect X. Metrology Services for sharing their facilities.

I would like to thank Dr. Ahmad Barari for sharing the facilities of his Lab.

I would like to thank my friends (especially Shahab, Keyhan and Alireza), colleagues and everyone who helped me in any way during the completion of this research.

TABLE OF CONTENTS

DECLARATION OF CO-AUTHORSHIP / PREVIOUS PUBLICATION III

ABSTRACT V

DEDICATION VII

ACKNOWLEDGEMENTS VIII

LIST OF TABLES XIII

LIST OF FIGURES XV

LIST OF APPENDICES XXIII

LIST OF ABBREVIATIONS/SYMBOLS XXIV

NOMENCLATURE XXVI

1 CHAPTER 1 INTRODUCTION 1

1.1 Metal Additive Manufacturing Background 5

1.1.1 Powder Bed Fusion AM 5

1.1.2 Powder Fed AM 7

1.2 Process Planning of DED AM 8

1.3 Multi Axis Configurations 14

1.3.1 Tilt and Lead/Lag Angles 15

1.3.2 Support Structure Elimination by Multi Axis System 16

1.4 Toolpath Verification 19

1.5 Pre-build Setup, Fabrication and Post Processing 20

1.6 Surface roughness measurement 21

1.7 Research Motivation and Objectives 22

1.8 Research Constraints 24

1.9 Dissertation Outline..25

2 CHAPTER 2 LITERATURE REVIEW...27

2.1 Process Planning for Collision Detection and Avoidance 27

2.2 Supportless Fabrication of Complex Geometries Leveraging Geometrical Partitioning 30

2.3 Surface Roughness of DED Built Components 33

2.4 Experimental and Numerical Studies of the Hardness of DED Built Parts 36

3 CHAPTER 3 METHODOLOGY 41

3.1 Process Planning of Collision Detection and Prevention.........................41

3.2 Partitioning the Case Study Sample 49

3.2.1 Wedge-Shaped Partitioning 51

3.2.2 Dome Fabricated by a Rotary 1+3-Axis Toolpath..............................56

3.3 Experimental Procedure 58

3.4 Microhardness Measurements..61

3.4.1 Sample Preparation 63

3.4.2 Proper Load Determination...66

3.5 Surface Roughness Measurement 69

3.5.1 Standard Measurement Techniques 70

3.5.2 Roughness Calculation from Points on Mounted Sample 70

3.5.3 Surface Roughness Measurement from 3D Point Cloud 77

3.6 FEA Simulation for the Hardness for 2+1+1-Axis Sample 84

3.6.1 Calculation Theories 85

3.6.2 Applied FEA Algorithm 87

4 CHAPTER 4 PROCESS PLANNING FOR COLLISION AVOIDANCE RESULTS 93

4.1 Dome Fabricated by Wedge Shape Partitioning 93

4.1.1 Dome Fabricated by 5-Axis Toolpath..93

4.1.2 Dome Fabricated by 2+1+1-Axis Toolpath.......................................96

4.2 Dome Fabricated by Rotary 1+3-Axis Toolpath.....................................98

5 CHAPTER 5 SURFACE ROUGHNESS TESTS RESULTS.......................101

5.1 Surface Roughness Measurement from Mount Samples 101

5.1.1 Verification Test of the Mount Program..101

5.1.2 Sensitivity Study of the Mount Program 103

5.1.3 Roughness Variations for the 5-Axis Sample..................................108

5.1.4 Roughness Variation for 2+1+1-Sample 111

5.1.5 Roughness Variation for Rotary Sample 116

5.1.6 Statistical Analysis of the Mount Solution 119

5.2 Surface Roughness Measurements from the 3D Point Cloud Data 122

5.2.1 Roughness Variations for the 5-Axis Sample from the 3D Point Cloud Data 123

5.2.2 Roughness Variations for the 2+1+1-Axis Sample from the 3D Point Cloud Data 125

5.2.3 Roughness Variations for the Rotary Toolpath Sample 129

5.2.4 Sensitivity Study for the 3D Point Cloud Program...........................130

5.2.5 Statistical analysis of the 3D point cloud solution............................132

6 CHAPTER 6 MICROHARDNESS RESULTS 136

6.1 Microhardness Results for the 5-Axis Toolpath Sample 136

6.1.1 Hardness variation test across surface of the 5-axis sample.............137

6.1.2 Hardness variation for 5-axis sample...138

6.2 Microhardness Results for the 2+1+1-Axis Toolpath Sample...............139

6.2.1 Hardness variation test across the surface of the 2+1+1-sample 141
6.2.2 Hardness Variations for the 2+1+1-Axis Sample 143
6.3 Microhardness Results for the Rotary Toolpath Sample 145
6.4 Statistical Analysis for the Microhardness Results 146

7 CHAPTER 7 SIMULATION OF MECHANICAL PROPERTIES 150
7.1 Hardness Simulation 150
7.1.1 Mesh Dependency Test (Convergence Test) 151
7.1.2 Analysis Based on Constant Laser Efficiency 156
7.1.3 Analysis Based on Constant Melt Pool Size....................................163
7.1.4 Discussion 165
7.2 Residual Stress Variation 169

8 CHAPTER 8 SUMMARY, CONCLUSION AND FUTURE WORK 171
8.1 Summary 171
8.2 Conclusion...173
8.3 Future Work 174

REFERENCES/BIBLIOGRAPHY..176

APPENDICES 189
A. Appendix A Surface Roughness Data 189
B. Appendix B Hardness data...193

VITA AUCTORIS 199

LIST OF TABLES

Table 1-1. Additive Manufacturing Processes [4] [5] 2

Table 1-2. Some advanced support structures 4

Table 2-1. Literature review of process planning for collision detection and avoidance . 30

Table 2-2. Literature review of collision detection and prevention................................. 32

Table 2-3. . Literature review summery of surface roughness measurement 35

Table 2-4. Literature review summary of hardness measurement and FEA simulation... 39

Table 3-1. Mechanical properties of stainless steel-grade 410 [124] 59

Table 3-2. Process parameters of direct energy deposition additive manufacturing (*) for 0.3 mm slice height (**) for 0.5 mm slice height 59

Table 3-3. Average of mean diagonal of 3 indentations for each load 67

Table 5-1. Point coordinate sample made by a contact-based surface roughness facility102

Table 5-2. Verification of results made by prepared Matlab program with results of contact-based measurement 103

Table 5-3. Table of primary statistical analysis of Ra for the mount solution............... 119

Table 5-4. P-values of different distributions 120

Table 5-5. Data extracted from Burr distribution 121

Table 5-6. Input parameters of sensitivity experiments... 131

Table 5-7. P-values of different distributions of 3D-point cloud solution..................... 132

Table 6-1. Partitions and their indentation test numbers 140

Table 6-2. Comparison of P-values of four distributions 147

Table 7-1. Mesh dependency check (convergence test) 153

Table 7-2. Setup parameters 154

Table 7-3. Achieved simulation parameters 158

Table 7-4. Some of the studied parameters for sensitivity analysis for simulation 1 (partitions 1, 2). The value in parentheses is applied for the rest of the beads of each partition 161

Table 7-5. Some of the studied parameters for sensitivity analysis simulation 2 (partitions 3, 4). The value in parentheses is applied for the rest of the beads of each partition 161

Table 7-6. Studied parameters for sensitivity analysis in partition 8. (*) substrate temperature 100 °C. The value in parentheses is applied for the rest of the beads of each partition 162
Table 7-7. Comparison of the simulation and experimental FFT results 169
Table A-1. Surface roughness values........ 189
Table B-1. All Hardness data........ 193

LIST OF FIGURES

Figure 1-1. Processes of building a part by RP 1

Figure 1-2. The printed part (a) With support structure (b) Support structure removed (Image courtesy of PADT, Inc.) [18] 4

Figure 1-3. Powder bed additive manufacturing process [27] 6

Figure 1-4. Powder feed additive manufacturing process [40] 8

Figure 1-5. Hierarchical process planning steps of DED AM [43] 10

Figure 1-6. Modifying the geometry of cooling channel to make it buildable by DED AM. a) Before modification. b) Modified cooling holes 11

Figure 1-7. Planar slicing (a) 2+1-Axis slicing (b) adaptive slicing (c) 2+multi-axis slicing 12

Figure 1-8. (a) Planar slicing. (b) Cylindrical slicing 12

Figure 1-9. Curvilinear surface slicing 13

Figure 1-10. Comparison of planar slicing and constant step over for slicing a thin wall geometry 13

Figure 1-11. Translational and rotary movements of a sample 5-axis machine 14

Figure 1-12. Material sublimation at the corner (made by DED AM) [45] 15

Figure 1-13. Mostly common axis configurations for DED AM 15

Figure 1-14. Lead/ lag angle 16

Figure 1-15. Tilt angle 16

Figure 1-16. Schematic explanation of a) Overhang angle b) Support structure 17

Figure 1-17. Material collapse for the regions that have high overhang angle [48] 18

Figure 1-18. Simple support structure for AM processes 18

Figure 1-19. a) Applying tilt angle to reduce overhang angle b) When nozzle is tangent to surface real overhang angle is zero 19

Figure 1-20. Collision (a) Between nozzle and previously deposited layers. (b) Nozzle and the table 20

Figure 1-21. Avoiding the (a) collision by (b) Tilting the nozzle 20

Figure 1-22. Illustration of surface roughness terminology 21

Figure 1-23. Surface roughness comparison of different manufacturing processes (LPBF: Laser powder bed fusion) [54] 22

Figure 1-24. A simple half tube that results in collision with previous deposited layers . 23
Figure 3-1. The process flow illustrating the research methodology............................... 42
Figure 3-2 (a) A thin-wall surface sample with inclined surfaces (b) Collision of the nozzle to previously deposited layers.. 42
Figure 3-3. Collision detection and prevention algorithm 45
Figure 3-4. Three main slicing directions X, Y, Z 45
Figure 3-5. Three-axis and 5-axis determination 46
Figure 3-6. (a) Surfaces that need 3 axis toolpath in purple and 5 axis ones in blue. (b) Driving curve that are needed to make 5 axis toolpath... 47
Figure 3-7. (a) Merged toolpath. (b) Collision between nozzle and deposited layers 47
Figure 3-8. Collided surfaces in red, colliding surfaces in yellow and other ones in grey48
Figure 3-9. (a) Partitioned surfaces in yellow and green. (b) Toolpath and tool orientation of split surfaces 48
Figure 3-10. Tool orientation of product surfaces from 2 views 49
Figure 3-11. Regions of a dome that violate maximum allowed overhang angle and relevant support structure based on (a), (b), (c) 3 main slicing directions 50
Figure 3-12. (a), (b) Bead deposition for lower layers. (c) Crash occurred at top layers (d) Crash even when nozzle tilted upward 51
Figure 3-13. Collision of the nozzle to trunnion table (slice direction from (Figure 3-11 (b)) 52
Figure 3-14. Partitioned geometry of the dome on the substrate 52
Figure 3-15. (a) Real layer height change when overhang angle changes drastically. (b) Layer height at zero overhang angle (c) Layer height increase (d) the relation between slice height and layer height.. 53
Figure 3-16. Slicing direction and nozzle tangency in 5-axis solution............................. 54
Figure 3-17. Schematic of the fabrication of 4 partitions using a 5-axis system.............. 54
Figure 3-18. Partitioning strategy of 2+1+1 axis 56
Figure 3-19. Collision made from initial rotary axis strategy... 56
Figure 3-20. (a) Rotary toolpath to build the dome at the end of a round bar. (b) Base layers at the end of the bar. (c) Rotary toolpath to build dome on top of the base...................... 57

Figure 3-21. Three segments of rotary toolpath dome. First and last layers are magnified to illustrate the changes of real layer height. 57
Figure 3-22. Experimental flow to build the case study samples 58
Figure 3-23. Utilized DED machine to manufacture samples (1) nozzle (2) chuck (3) installed substrate 60
Figure 3-24. Round substrate (all dimensions in mm) 60
Figure 3-25. Vickers hardness indentation and minimum allowed distance between two indentations 61
Figure 3-26. Process flow of micro hardness measurement 62
Figure 3-27. Wire EDM cut line and indentation direction for 5-axis sample 63
Figure 3-28. Mounted specimen of partitions 3 and 4 64
Figure 3-29. Cut line for 2+1+1 axis sample 64
Figure 3-30. Two mounts of 2+1+1 axis specimen 65
Figure 3-31. (a) Cut line (b) The specimen is cut into three smaller specimens 65
Figure 3-32. Hardness indentations on of rotary sample mount 66
Figure 3-33. Three indentations of all available load options (The same load indentations are encased with the same color circle). 67
Figure 3-34. Calculated graphs showing relationship between diagonal and load [127]. The test values are also showed by vertical lines 68
Figure 3-35. Comparison of indentations made by (a) 25 gf at 1500 magnification (b) 25 gf at 750 magnification (c)500 gf at 750 magnification 69
Figure 3-36. Roughness measurement edges in mount 71
Figure 3-37. Merged pictures of the edge of the sample 71
Figure 3-38. Scale of the edge pictures plus the sketch points. 72
Figure 3-39. Flow chart used in Matlab program which measures surface roughness from a set of points at the edge of mount sample 73
Figure 3-40. (a) Initial points and the center of constructed arc. (b) Translated points. (c) Rotation 74
Figure 3-41. Polar projection lines and mean points 75
Figure 3-42. Best-fitting a new arc through points of measurement region 76
Figure 3-43. Flattening of points for further roughness calculations 76

Figure 3-44. Illustration of area between mean line and surface profile 77
Figure 3-45. Removing points that are far from measurement line. Reference points on reference plane 79
Figure 3-46. Flow chart used in Matlab program which measures surface roughness from 3D point cloud. (*) same operations with mount solution... 80
Figure 3-47. Rotation of point cloud to XY plane 81
Figure 3-48. Rotated point cloud and its projection on XY plane 81
Figure 3-49. The intersection curve and nearby 3D points.. 82
Figure 3-50. Illustration of finding the mean point based on the weight of the points..... 83
Figure 3-51. Projection of points to projection lines and finding the mean point on each line. 84
Figure 3-52. 3D Gaussian conical heat source model.. 86
Figure 3-53. Initial boundary conditions for the FEA simulation 87
Figure 3-54. Flow chart of numerical analysis applied in this research 90
Figure 3-55. Variable mesh size for beads.. 91
Figure 4-1. All 5 axes involvement in making the hemisphere dome 93
Figure 4-2. Building the dome in two sections by 180 degree rotation 94
Figure 4-3. (a) Substrate at its horizontal position. (b) Building the first half of the dome (c) Rotation of A-axis 180° (d) Building the second half 95
Figure 4-4. Production stages of the dome in 5-axis. (a) to (d) Produced partitions 1 to 4 respectively 95
Figure 4-5. Completed 4 sections of 5-axis dome 95
Figure 4-6. 2+1+1-Axis deposition of dome (a) First partition (b) 5th-partition............... 96
Figure 4-7. 2+1+1-Axis manufacturing of dome (a) to (d) Partitions 1 to 4 97
Figure 4-8. Completed 2+1+1 axis dome. Partitions 1-8.. 97
Figure 4-9. Diameter measurement from point cloud... 98
Figure 4-10. (a) Rotary deposition toolpath (b) Initial layers (c) Half fabricated dome .. 98
Figure 4-11. Sample made by rotary toolpath strategy... 99
Figure 4-12. Comparison of inner and outer diameters 99
Figure 4-13. Thickness comparison... 100
Figure 5-1. A sample surface texture profile is used to verify the Matlab program....... 102

Figure 5-2. Dependency of surface roughness result made by Matlab program to number of projection lines 104
Figure 5-3. Regions of mount samples with different surface quality 105
Figure 5-4. Sensitivity analysis for determination of measurement length 106
Figure 5-5. Comparison of measurements of transition points with layers inside partitions 107
Figure 5-6. Measurement regions for sequential regions 107
Figure 5-7. Layer height increase 108
Figure 5-8. Direction of surface roughness measurement in 5-axis sample. 109
Figure 5-9. Inner edge of 5 axis sample 110
Figure 5-10. FFT diagram and frequency study of the 3rd partition for 5-axis dome 111
Figure 5-11. 2+1+1 axis specimen that contains partitions 1-4 112
Figure 5-12. Surface roughness variation of 2+1+1-axis sample for partitions 1-4 113
Figure 5-13. Material collapse because of sudden nozzle orientation change in 2+1+1 axis sample 114
Figure 5-14. 2+1+1 axis specimen that contains partitions 5-8 114
Figure 5-15.Surface roughness variation of 2+1+1 sample for partitions 5-8 115
Figure 5-16. FFT diagram and frequency study of the 2+1+1-axis dome 116
Figure 5-17. Rotary toolpath mount sample 117
Figure 5-18. Ra variation of rotary toolpath sample- inner surface 118
Figure 5-19. FFT diagram and frequency study of the rotary sample 119
Figure 5-20. Burr distribution of the mount solution results. 121
Figure 5-21. Mode and standard deviation (mount solution) 122
Figure 5-22. Skewness and Kurtosis- mount solution 122
Figure 5-23. Example of point cloud filtration of partitions 5-8 of 2+1+1 sample 123
Figure 5-24. Comparison of R_a between 3D point cloud and mount solutions for 5 axis-partition 3 (a) Inner surface (b) Outer surface 124
Figure 5-25. FFT diagram and frequency study of the 5-axis by 3D point cloud (a) Inner surface (b) Outer surface 125
Figure 5-26.Point cloud of partitions 1-4 of 2+1+1 sample 126
Figure 5-27. Point cloud of partitions 5-8 of 2+1+1 sample 126

Figure 5-28. Comparison of R_a between 3D point cloud and mount solutions for 2+1+1 axis- partitions 1-4 (a) Inner surface (b) Outer surface 127

Figure 5-29. Comparison of R_a between 3D point cloud and mount solutions for 2+1+1 axis- partitions 5-8 (a) Inner surface (b) Outer surface 128

Figure 5-30. FFT diagram and frequency study of the 2+1+1-axis by 3D point cloud (a) Inner surface (b) Outer surface 129

Figure 5-31. Roughness variation of rotary toolpath sample 130

Figure 5-32. Sensitivity test of distance between boundary planes and distance coefficient 131

Figure 5-33. Initial statistical analysis of 3D point cloud solution 132

Figure 5-34. Histograms and Burr distributions of 2+1+1-Axis partitions 1-4 by 3D point cloud 133

Figure 5-35. Comparison of statistical analysis between mount solution and 3D point cloud 134

Figure 6-1. Microhardness indentations on partition 3. Four indentations for each test point are made. 136

Figure 6-2. Hardness test across the surface 137

Figure 6-3. Hardness variation across the surface of 5 axis specimen (a) For 300 gf indentation (b) For 1000 gf indentation 138

Figure 6-4. Standard deviation of hardness across the surface of 5-axis sample. 138

Figure 6-5. Hardness variation along 5-Axis sample by 1000 gf indentation 139

Figure 6-6. FFT analysis for 5-Axis sample 139

Figure 6-7. Hardness indentations on 2 mounts of 2+1+1 axis samples 140

Figure 6-8. Hardness test across the surface and test rows 141

Figure 6-9. Hardness variation across the surface of 2+1+1 axis sample- mount 1 142

Figure 6-10. Standard deviation of hardness across the surface of 2+1+1-sample 143

Figure 6-11. Micro hardness chart for 2+1+1 axis sample divided based on the partitions 144

Figure 6-12. FFT diagram of microhardness for 2+1+1-axis sample 145

Figure 6-13. Micro indentations on rotary specimen 145

Figure 6-14. Hardness variation for rotary sample 146

Figure 6-15. FFT diagram of micro-hardness for rotary sample 146
Figure 6-16. Average, Average-Median, and Max-Min for hardness results................ 147
Figure 6-17. Histograms and Burr distributions of hardness results 148
Figure 6-18. Modes and standard deviations of hardness results 149
Figure 6-19. Skewness and Kurtosis of hardness results... 149
Figure 7-1. Modeling the partitions and beads for FEA analysis 150
Figure 7-2. Variable mesh structure of beads and substrate 151
Figure 7-3. Three beads are simulated for mesh dependency check 152
Figure 7-4. Models with finer mesh to do the dependency check. 153
Figure 7-5. Yield strength variation of mesh types... 154
Figure 7-6. Partitions used for parameters-finding simulations..................................... 155
Figure 7-7. The simulation of the dome is divided into 4 sections................................ 156
Figure 7-8. (a) Temperature history points are investigated. (b) Temperature history of point 1.. 157
Figure 7-9. (a) Temperature history of points 2, 3 (b) A closer look at temperature histories of points 2, 3 at deposition time... 158
Figure 7-10. Comparison of experimental to simulation results of the hardness 160
Figure 7-11. Hardness variation results of the simulation 160
Figure 7-12. Effect of FEA parameters on hardness variation in simulation 1 (partitions 1, 2) 161
Figure 7-13. Effect of FEA parameters on hardness variation simulation 2 (partitions 3, 4) 162
Figure 7-14. Effect of FEA parameters on hardness variation in partition 8................. 163
Figure 7-15. Magnified charts of Figure B-5.. 163
Figure 7-16. Laser efficiency of the beads within partitions 164
Figure 7-17. Melt pool sizes of some beads 164
Figure 7-18. Hardness variation of the constant melt pool approach 165
Figure 7-19. (a) Constant temperature along the partition 8 during cooling (b) The temperature history of some points along partition 8 166
Figure 7-20. (a) Heat dissipation from the thin wall (b) Austenite percentage of the partition 8 (c) Martensite percentage of the partition 8.. 167

Figure 7-21. Hardness variation of partition 2 167
Figure 7-22. Comparison between the results of two applied simulation methods with the experimental result 168
Figure 7-23. FFT diagram of simulation data of the hardness for 2+1+1-axis sample .. 169
Figure 7-24. Residual stresses of partitions 1-4 170
Figure 0-1. Hardness Diagrams of 5-axis sample 190
Figure 0-2. Hardness Diagrams of 2+1+1-axis sample 191

LIST OF APPENDICES

Appendix A. Surface Roughness Data...189

Appendix B. Hardness data...193

LIST OF ABBREVIATIONS/SYMBOLS

2D	2 Dimensional
3D	3 Dimensional
AM	Additive Manufacturing
ASTM	American Society For Testing And Materials
BAAM	Big Area Additive Manufacturing
CAD	Computer Aided Design
CMM	Coordinate Measurement Machine
DED	Direct Energy Deposition
DFAM	Design For Additive Manufacturing
DLMD	Direct Laser Metal Deposition
DLP	Digital Light Processing
DMD	Direct Metal Deposition
DMLS	Direct Metal Laser Sintering
EBM	Electron Beam Melting
EDM	Electro Discharge Machining
FDM	Fused Deposition Modeling
FEA	Finite Element Analysis
FFT	Fast Fourier Transformation
HAZ	Heat Affected Zone
HLB-IPF	Hollow-Laser Beam With Internal Powder Feeding
HRB	Hardness Rockwell B
HV	Hardness Vickers
IFM	Infinite Focus Measurement Machine
K-S	Kolmogorov-Smirnov
LBDMD	Laser-Based Direct Metal Deposition
LMD	Laser Metal Deposition
LOM	Laminated Object Manufacturing

LSAM	Large Scale AM
MJF	Multi-Jet Fusion
PFLAM	Powder Feed Laser Additive Manufacturing
RM	Rapid Manufacturing
RMS	Root Mean Square
RSM	Response Surface Methodology
RP	Rapid Prototyping
SHS	Selective Heat Sintering
SLA	Stereolithography
SLS	Selective Laser Sintering
STL	Stereolithography
TAS	Topography Analysis And Simulation
TLS	Terrestrial Laser Scanner
UC	Ultrasonic Consolidation

NOMENCLATURE

α	Angle Between Projection Lines
θ	Angle of a Wedge-Shaped Partition
λ	Conductivity Coefficient
ρ	Mass Density
a	Thermal Diffusivity Coefficient
A_{uv}	Proportion of Transformed Phase from I to J In a Time Unit
C	Specific Heat
d	Distance of the Point to the Reference Plane
d_1, d_2	Diagonal Lengths of the Hardness Indentations
d_{ave}	Mean of Diagonal Length
d_i	Distance of 3D Points to Reference Plane
F	Indentation Load
gf	Gram Force
H	Distance from Mean Point to the Origin
h_i	Distance of Projected Points on Lines from the Origin
(i , j, k)	Unit Vectors of X, Y, Z Axes Respectively
L	Length of the Measurement Region
L_1	Length of Best-Fitted Arc Between Two Adjacent Projection Lines
L_p	Arc Length of the Partitions from the Bottom Layer
$L_{uv}(T)$	Latent Heat of U to V Transformation
m	Height of the Mean Line From Reference Line
M_i	Point Weight
n	Distance Coefficient
N	Cross Product of V1 and V2
n_n	Number of Projection Lines
n_p	Number of Points on a Projection Line
P	Phase Proportion
P_x, P_y, P_z	Components of Point Coordinates
P_x', P_y', P_z'	Rotated Point Coordinates
Q	Heat Source
q_0	Heat Flux Density

R	Distances from Origin to Mean Point
Ra	Surface Roughness
r_e	Beam Radius at Exposure Surface
r_i	Beam Radius at Penetration Depth
R_m	Radius of the Arc
R_p	Distances from Origin to Projected Points
T	Temperature in Kelvin
u, v	Phase Indexes
V1	Vector from the Rotation Reference Point to Second Reference Point
V2	Vector from the Rotation Reference Point to Third Reference Point
(Xr,Yr,Zr)	Coordinate System Components on Reference Plane
z_e	Height of Exposure Surface
z_i	Height of the Penetration Depth

CHAPTER 1

INTRODUCTION

During the 1980s a new manufacturing method was developed which enabled the fabrication of patterns, or prototypes of parts and assemblies from plastics directly from a computer aided design (CAD) file. It was called rapid prototyping (RP) as the product was suitable just for visually investigating the shape and assembly feasibility of the real part. This technology builds 3D objects by adding material layer-upon-layer [2][3]. Figure 1-1 shows schematic processes for producing a prototype by RP. The process respectively includes computer aided design (CAD) preparation (Figure 1-1 (a)), slicing the geometry (Figure 1-1(b)), and building the layers (Figure 1-1 (c), (d)). The benefits of RP were appropriate for low volume production as there is no need to fabricate a mold or any other tool. Moreover, the time between the product design to the first actual product was much shorter than when using traditional manufacturing techniques such as casting and injection molding. On the other hand, it was not cost-efficient for higher production rates. Also, the product did not have the strength of one made by injection molding using the same material.

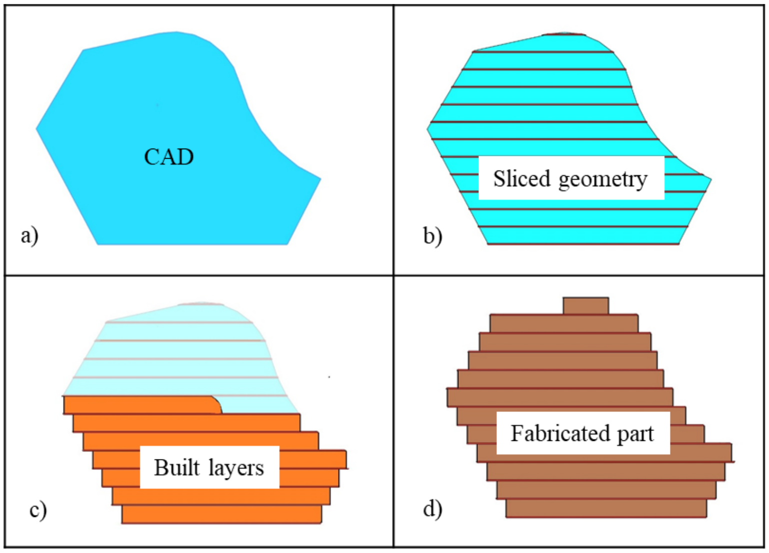

Figure 1-1. Processes of building a part by RP

Later, the name of the process changed from rapid prototyping to rapid manufacturing (RM) because its technology advanced from just making plastic prototypes to metal functional products. Recently, the RM name has been modified to be called additive manufacturing (AM). ASTM defines AM as “a process of joining materials to make objects from 3D model data, usually layer upon layer, as opposed to subtractive manufacturing methodologies. Synonyms for this process are: additive fabrication, additive processes, additive techniques, additive layer manufacturing, layer manufacturing, and free form fabrication” [4].

Nowadays there are many different AM technologies used in industry. Various physical phenomena, materials, and mechanisms are utilized to make a product. Table 1-1 categorizes some of the most common AM processes. Based on the physical state of the used material, there are 3 types of AM processes: (i) liquid based, (ii) solid based and (iii) powder based. Metal additive manufacturing technologies mainly use metal powder to build a part. This research focuses on direct energy deposition (DED), which is a powder fed AM system.

Table 1-1. Additive Manufacturing Processes [4] [5]

AM Type	Technology		Process Name
Liquid Based	Vat photo polymerization		Stereolithography (SLA) [5]
			Digital Light Processing (DLP) [6]
	Material Jetting		Multi-jet fusion (MJF) [7]
Solid Based	Sheet Lamination		Laminated Object Manufacturing (LOM) [8]
			Ultrasonic Consolidation (UC) [9]
	Material Extrusion		Fused Deposition Modeling (FDM) [10]
Powder Based	Powder bed fusion	Laser heat	Electron Beam Melting (EBM) [11]
			Selective Laser Sintering (SLS) [12]
			Direct Metal Laser Sintering (DMLS) [13]
		Binder Jetting	3D Inkjet printing [14]
	Powder feed		**Direct Energy Deposition (DED)** [15]

Additive manufacturing processes allow the fabrication of parts directly from a computer-aided design (CAD) file. The CAD-file describes the geometry and size of the parts to be built. For the first step, the geometry should be saved in the needed build format. Most of the AM processes require a stereolithography (STL) file format as the input file. An STL file tessellates the surface of the part into triangles and saves facets of all triangles. The information of all these triangles forms the surface of the designed 3D structure. Then the *.stl file is opened in the appropriate software to be sliced into layers with the user selected thickness and component build orientation. For solid parts, each layer can be filled by a peripheral contour and filled with beads deposited in a raster pattern. A single or parallel fill travel path is used for each layer of a thin-walled part. Finally, the toolpath file is uploaded to the AM machine in order to fabricate the product.

As shown in Table 1.1, there are two main powder-based AM processes: (i) powder bed fusion and (ii) powder fed systems. The number of required axes and mechanisms for providing the powder to the printing zone are the main differences between these technologies. For many technologies, the build chamber is encased. For the DLMS and SLS processes, the chamber is filled with a neutral gas; whereas, powder fed AM has the option to provide shielding gas from the nozzle locally just above the melt pool. Polymer, ceramics and metal powders can be used in these processes [16].

In most of the AM processes, there is a necessity to create two different structures, the main structure for the component, and support structures. Support structures provide a ‘platform’ for overhang features. The main CAD geometry represents the desired object, and a support structure is an auxiliary that needs to be removed. Because of the inherent nature of AM processes, support structures are required to support overhanging features while building a part in most of the AM techniques such as SLM, DMLS, and FDM.

Material extrusion additive manufacturing is a technology that melts plastic filaments to make the parts. Most of these machines are provided with at least 2 nozzles, one for making the model and the other for making the support structure. Two methods are available to remove support structures, and are material dependent; solving it in a solution and mechanically removing. If the support structure material is compatible with a provided solution, the fabricated part is left in a solution to dissolve the support structure. If not, the support structure should be removed manually [17]. Figure 1-2 (a) shows a part fabricated with black material that has a support structure fabricated with a white material. The top part of the black part has a horizontal platform that would collapse without a support structure. After the part is fabricated, the white support structure needs to be removed.

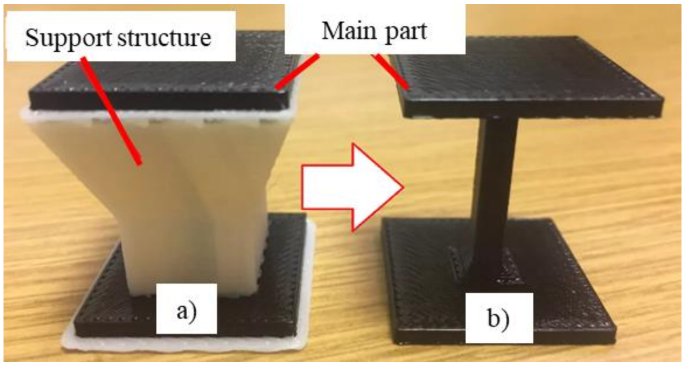

Figure 1-2. The printed part (a) With support structure (b) Support structure removed (Image courtesy of PADT, Inc.) [18]

Table 1-2 introduces some advanced support structure solutions found in the literature. In this table, applicable AM processes for each support structure type are mentioned. These support structures have differences that are appropriate for their mentioned application. Some like “Gyroid and Diamond lattice structures” contain overhang features that cannot be produced by the FDM or DED process. These structures are applicable for powder bed processes. Although the tree shape structures are mentioned to be applicable for 3 axis material extrusion, it seems it can be developed for powder fed AM processes as well.

Table 1-2. Some advanced support structures

Name of the support structure	Applicable process
Gyroid and diamond lattice structures [19]	Powder bed
Solid truncated octahedron support [20]	Powder bed
Cellular support structures [21]	Powder bed
Tree-like structure support [22]	Material extrusion
Branching support [23]	Material extrusion
Y shape support [24]	Powder bed
Grain support structure [25]	Material extrusion

All research solutions represented in Table 1-2 are trying to minimize the material usage for support structures, as building support structures are costly and time-consuming. Support structure removal adds extra costs and time to the total build process. Therefore, removing the necessity for support structures is very beneficial.

A technical explanation of the key AM terms for this research, such as slicing and overhang angles, will be explained in more detail. Surface roughness and hardness are mechanical properties that are explored and are introduced.

1.1 *Metal Additive Manufacturing Background*

In the background section, a brief explanation of the differences between the powder bed and powder fed AM technologies is covered. Since direct energy deposition (DED) is specifically used in this research to build metal AM products, it will be explained in more detail. The capability of a DED machine in building complex parts is highly dependent on the number of axes. Hence, later in this chapter, a brief explanation of multi-axis controllers is covered.

1.1.1 Powder Bed Fusion AM

For powder bed fusion AM processes, the powder is provided on the platform layer after layer. Figure 1-3 shows a schematic of a powder bed system. In this system, a powder roller carries powder evenly from the powder feed tank to the build tank. After each layer is built the powder feed tank lifts a little and the substrate of the build tank goes down as high as one slice height to make space for powder for the next layer. After the roller distributes the powder on the build tank by the height of one layer, powder particles should be bound together in the needed areas within the layer.

For a binder jetting based process, an inkjet print head deposits droplets of a liquid binding agent selectively onto the powder layer and make a solid layer. Then the build tank lowers and the roller spreads powder again. When the powder is spread evenly onto the build platform, the inkjet print head deposits binder droplets on the needed areas to solidify the layer [26]. Polymer, ceramic, plaster and metal powder can be used here.

For powder bed techniques that are specialized for producing metal parts, a concentrated heating source is used to sinter or melt the particles and bind them together. Electron Beam Melting (EBM), Selective Laser Sintering (SLS), Selective Heat Sintering (SHS) and Direct Metal Laser Sintering (DMLS) have similar powder spreading systems but instead of using an inkjet printhead, a laser or electron beam scans the powder and fuses or melts it to form the needed shape in each layer. The powder distribution technology is the same as the binder jet’s system. This process repeats for the next layers until the object is formed. The main difference between EBM and other laser-based powder bed methods is that the EBM happens in a vacuum chamber instead of neutral gas chamber.

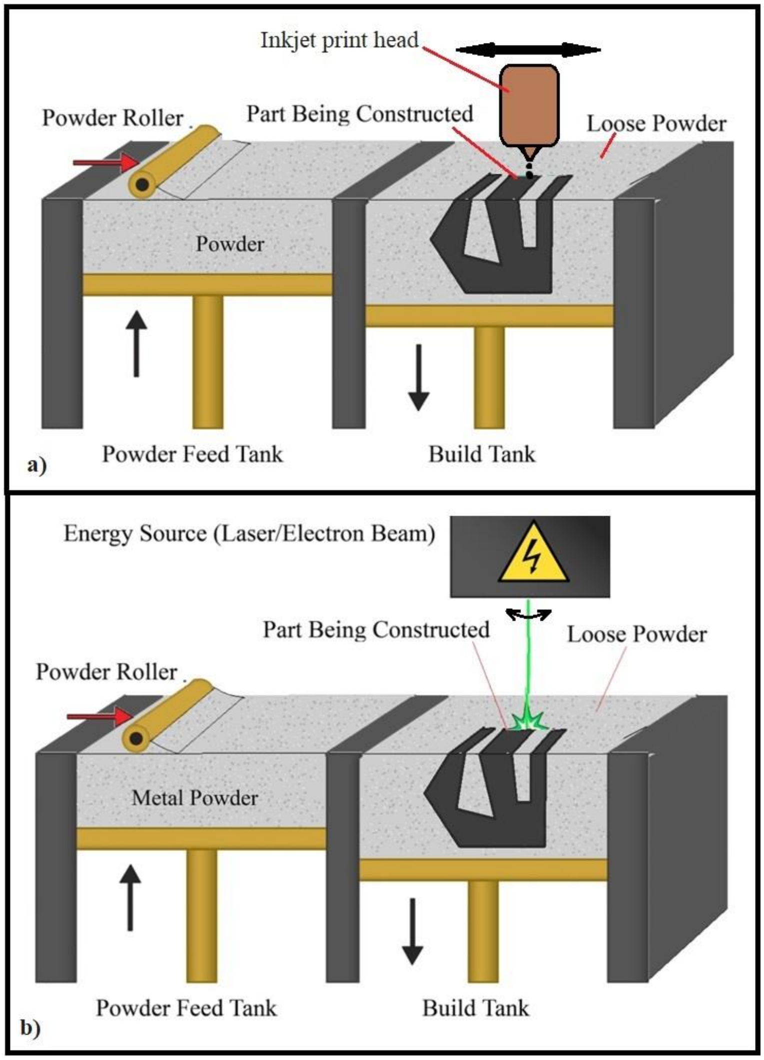
Inkjet print head
Powder Roller
Part Being Constructed
Loose Powder
Powder
Powder Feed Tank
Build Tank
a)
Energy Source (Laser/Electron Beam)
Part Being Constructed
Loose Powder
Powder Roller
Metal Powder
Powder Feed Tank
Build Tank
b)

Figure 1-3. Powder bed additive manufacturing process [27]

Support structures are necessary for laser-based powder-bed AM to fix the part to the substrate and to conduct heat away from the part. This reduces the thermal distortion and the residual stresses [28]. However, the removing process of the support structure introduces safety concerns. The product needs to be removed from the build tank and cleaned as it is covered with metal powder. Since most support structure designs are hollow, they can trap the powder. And the powder particles are small enough to be absorbed by inhalation. Therefore, during support structure removing operations, the health of the operator is at risk [29].

1.1.2 Powder Fed AM

For a powder fed system, the powder is distributed from a nozzle where required. ASTM defines direct energy deposition (DED) as “an additive manufacturing process in which focused thermal energy is used to fuse materials by melting as they are being deposited. Focused thermal energy means that an energy source (e.g., laser, electron beam, or plasma, etc) is focused to melt the materials being deposited” [30].

Powder-fed AM system uses DED technology to deliver energy to melt pool. It is also known as laser cladding, direct metal deposition (DMD), laser metal deposition (LMD) [31], direct laser metal deposition (DLMD) [32][33] and powder feed laser additive manufacturing (PFLAM) [34]. This process has a nozzle that delivers the powder and inert gas from the ducts around the laser nozzle (Figure 1-4). The laser beam heats the melt pool on the substrate, and at the same time, the powder is delivered into the melt pool. The nozzle follows the toolpath on the substrate to deposit the first layer. Then it follows the toolpath of the second layer to deposit the material onto the first layer. This process continues until the product is built [35][36].

DED can be used for various applications such as fabricating a new part, repairing a damaged part, and surface coating a part with another material to modify the surface characteristics. This research focuses on fabricating new parts. It is common to utilize this system to repair mold tool surfaces, turbine blades or coating the surface of oil and gas drilling components. Shaft repair using laser cladding technology is also very common in the industry. The softer substrate metal can be coated by a hard one, or coating metal part with the materials which resist high temperatures or chemicals. [37] [38][39].

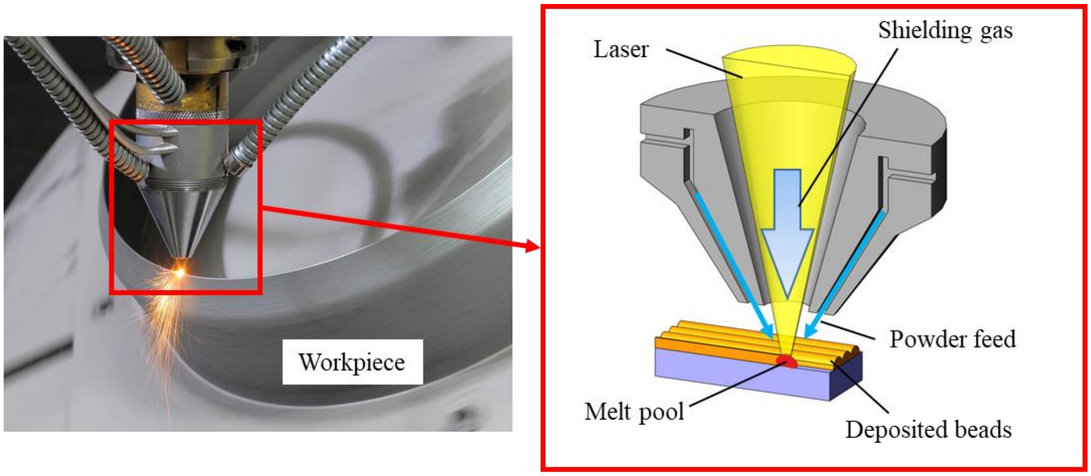

Figure 1-4. Powder feed additive manufacturing process [40]

DED components can be mounted on a multi-axis CNC system to increase its capability to produce more complex products. The AM processes mentioned in Table 1-1 have integrated pre-set operating parameters and limited user interactions. In contrast, DED AM does not have a standard interface or process parameter set to minimize the user's interactions for process planning. Much research is needed to automate this process.

1.2 *Process Planning of DED AM*

A manufacturing process plan is a set of sequential processes in order to achieve some targets and to meet the required domain constraints [41]. Figure 1-5 shows a hierarchical process planning steps that need to be followed to produce an object by the DED AM process.

As with any manufacturing process, process planning starts with the new product and its application. Being manufacturable is an essential factor to consider when a product is being designed. Design for manufacturability (DFM) is the methodology to guarantee at the concept stage that the fabrication of a product is reproducible, consistent, reliable and cost-effective [42]. By implementing DFM in AM products, with a minor change in geometry of the product, AM fabrication can be easier and less costly. A 'design for AM (DFAM)' example is shown in Fig. 1-6. Producing circular conformal cooling channels by DED AM is a challenge because, at the top segment of the cooling channel, the overhang angle exceeds the maximum allowed (Figure 1-6 (a)). By changing the top section form of the cooling hole into a triangular shape, the part can be built by either DED AM or powder bed AM process without the need for support structures (Figure 1-6 (b)).

After finalizing the CAD file, it should be converted into an *.stl file or any format that is compatible with the available toolpath generation software. In this research, Solidworks and Mastercam programs are used to create and modify the CAD files.

Since additive manufacturing is based on layer-upon-layer production, the CAD geometry needs to be sliced to be usable for this fabrication process. The three main parameters for slicing a component are: (i) the slice type, (ii) the component build orientation and (iii) the slice height. Slicing has a significant role in AM processes, as it affects the surface quality, the support structure volume, the mechanical quality, and the build time. Slicing methods can be categorized into planar slicing, radial slicing, curvilinear slicing, and constant step over.

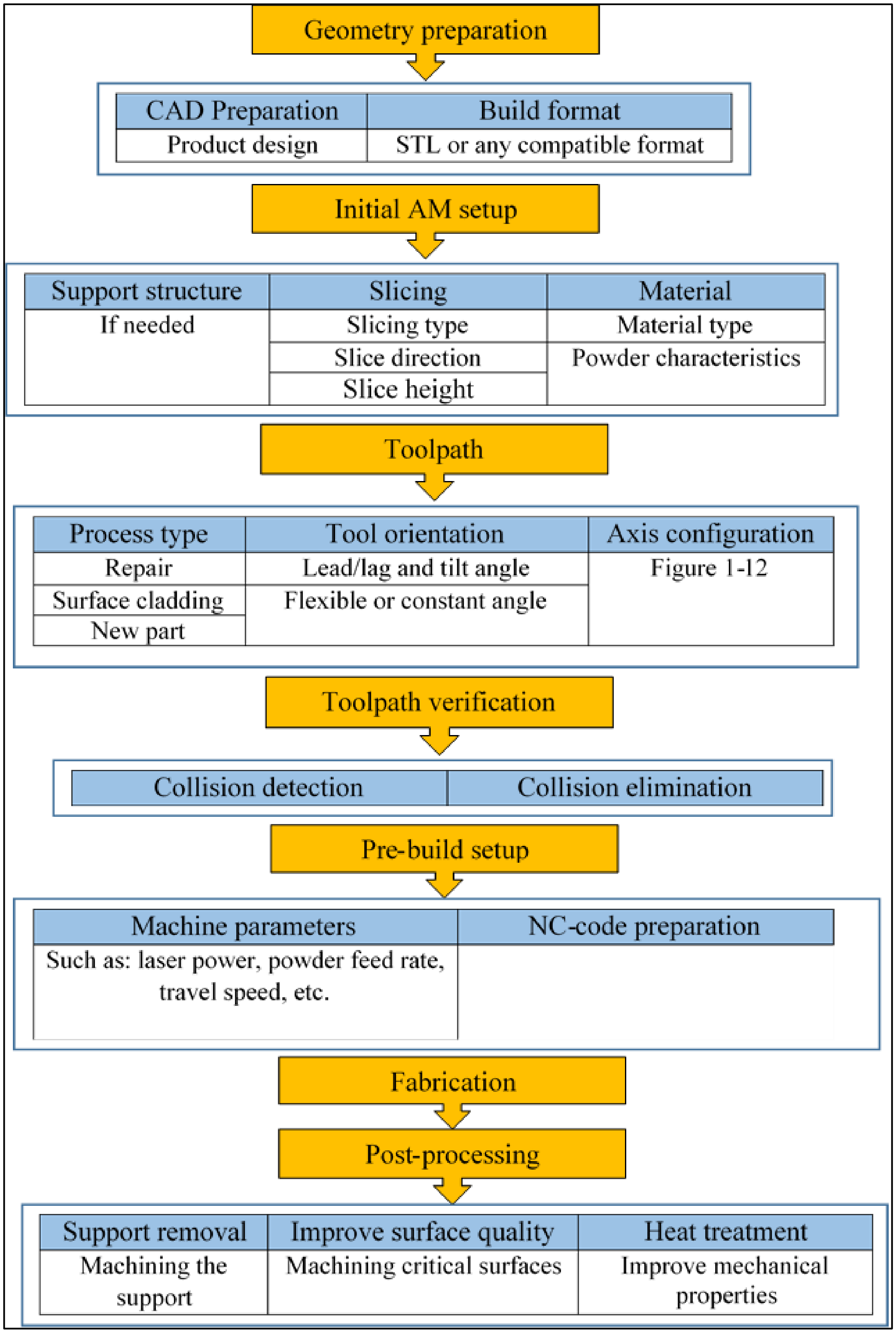
Geometry preparation
CAD Preparation
Build format
Product design
STL or any compatible format
Initial AM setup
Support structure
Slicing
Material
If needed
Slicing type
Material type
Slice direction
Powder characteristics
Slice height
Toolpath
Process type
Tool orientation
Axis configuration
Repair
Lead/lag and tilt angle
Figure 1-12
Surface cladding
Flexible or constant angle
New part
Toolpath verification
Collision detection
Collision elimination
Pre-build setup
Machine parameters
NC-code preparation
Such as: laser power, powder feed rate, travel speed, etc.
Fabrication
Post-processing
Support removal
Improve surface quality
Heat treatment
Machining the support
Machining critical surfaces
Improve mechanical properties

Figure 1-5. Hierarchical process planning steps of DED AM [43]

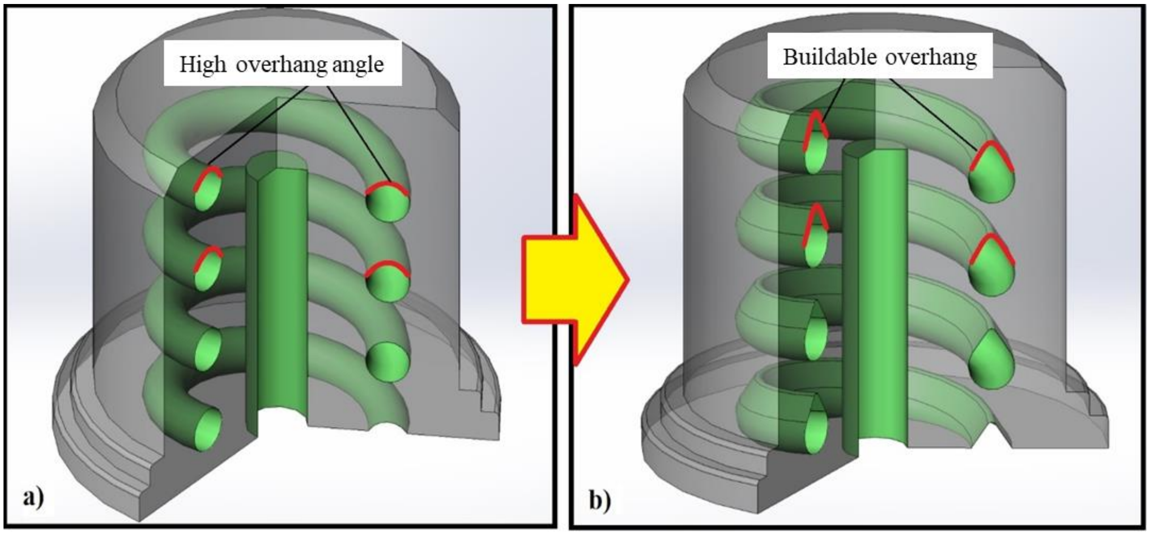

Figure 1-6. Modifying the geometry of cooling channel to make it buildable by DED AM. a) Before modification. b) Modified cooling holes

Planar slicing- Planar slicing is the most common method of slicing to prepare the geometry for an AM process. Figure 1-7 shows how the geometry is sliced by this method. The planar slicing can be categorized into 3 methods:

(i) In 2+1-Axis planar slicing (also called 2.5-Axis), there is just one slicing direction which is perpendicular to the build platform in conventional AM processes like FDM and SLA. This build strategy is simple and does not introduce collision issues. However, support structures are required for overhanging features. This type of slicing is used in all AM systems such as powder-bed AM, traditional FDM, and SLA machines (Figure 1-7 (a)).

(ii) (ii) In adaptive slicing, slice height is variable (Figure 1-7 (b)). It can be used to build overhang features by introducing smaller slice height [44].

(iii) (iii) As 2+multi-axis planar slicing is shown in Figure 1-7 (c), each section of the part can be made by 2+1-axis planar slicing then the table rotates to build the next section by changing the slice direction. In this case, a surface of the first section works as the substrate to build the next section. Although by this method, overhang features may be fabricated without the need for support structure, it can cause collisions.

Radial slicing- In some cases, a feature is needed to be added onto a round workpiece. In this case, planar slicing is not suitable because it creates intermittent tool paths at both sides of the substrate (Figure 1-8 (a)). It is better to slice the part by radial surfaces that are co-axial with the substrate. (Figure 1-8 (b)).

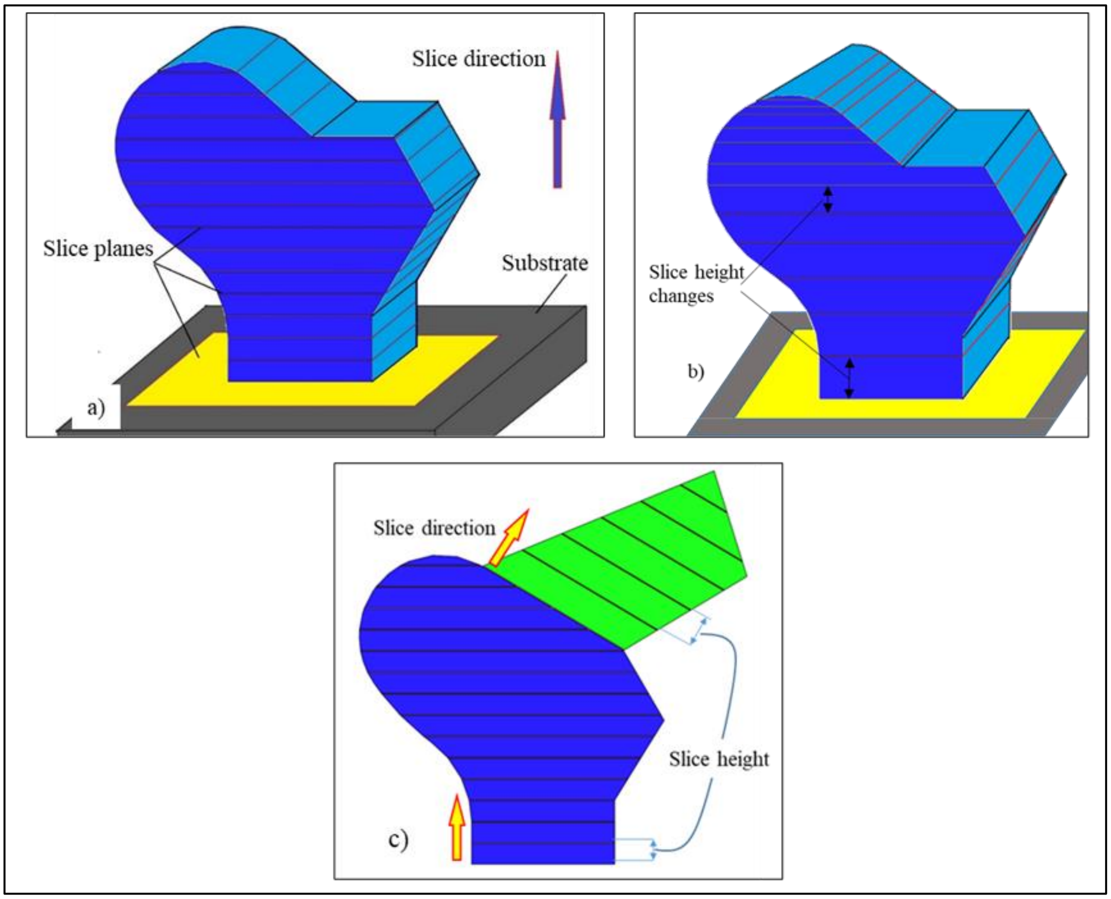
Slice direction
Slice planes
Substrate
a)
Slice height changes
b)
Slice direction
Slice height
c)

Figure 1-7. Planar slicing (a) 2+1-Axis slicing (b) adaptive slicing (c) 2+multi-axis slicing

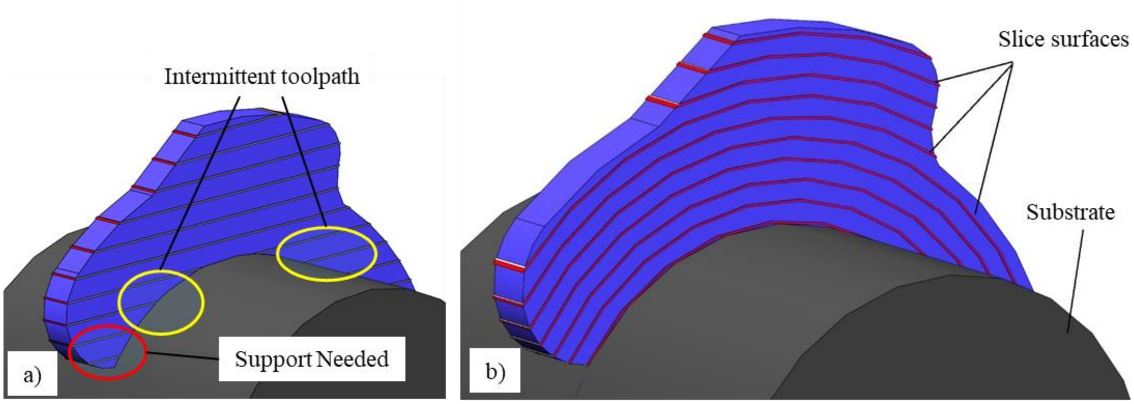
Intermittent toolpath
Support Needed
a)
Slice surfaces
Substrate
b)

Figure 1-8. (a) Planar slicing. (b) Cylindrical slicing

Curvilinear surface slicing- Similar to radial slicing, if the substrate has a curvilinear surface, slices with the same shape of the substrate can help build a part with better quality (Figure 1-9). Radial or curvilinear are not just limited to similar substrate shape. Even for some part geometries, applying radial or curvilinear surface slicing on a flat substrate can be beneficial in reducing the support structure.

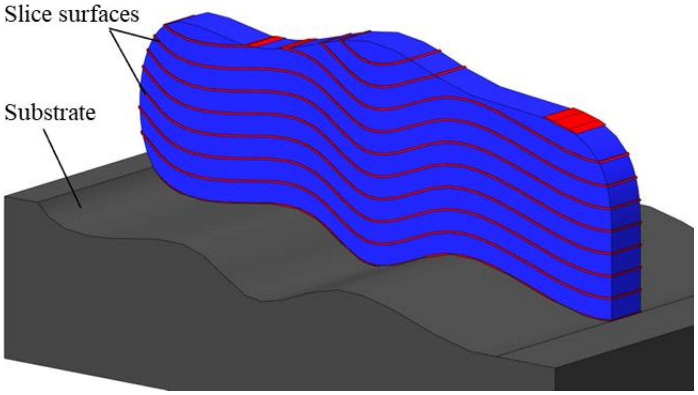

Figure 1-9. Curvilinear surface slicing

Constant Step Over- Figure 1-10 illustrates an example geometry for a thin wall surface that needs to be built by DED AM. The surface bends in the middle and it causes the overhang angle to increase drastically. Figure 1-10 (a) indicates how the real layer height varies when the geometry is sliced by a planar slicing method. The layer height is larger for the areas that have a larger overhang angle. On the other hand, Figure 1-10 (b) demonstrates another slicing method called constant step over. In this method, a driving curve needs to be created at the lower edge of the surface. This curve will be offset along the surface such that the distances between curves stay constant. As a result, the real heights of the layers stay constant.

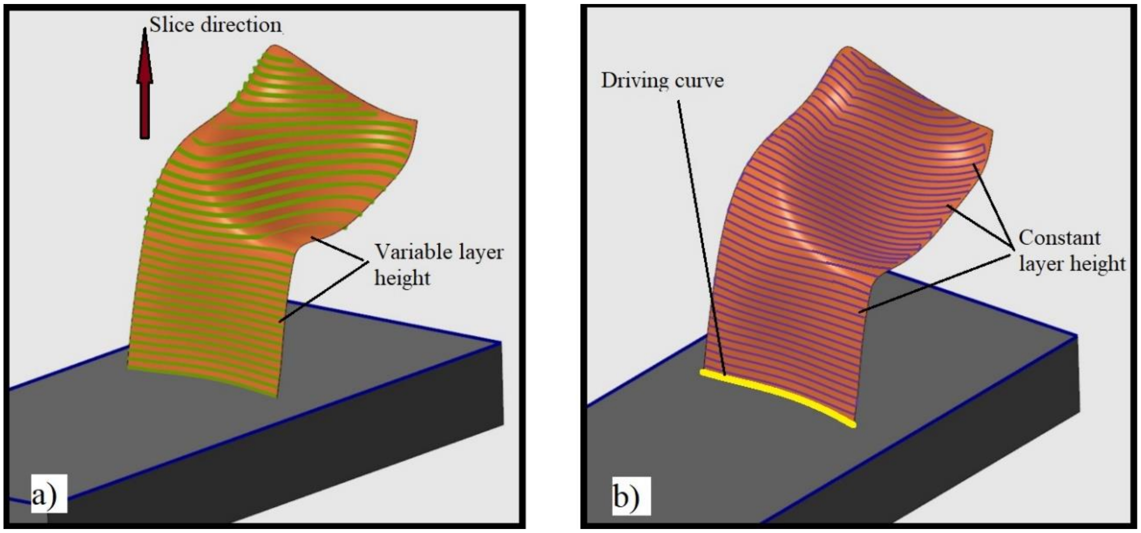

Figure 1-10. Comparison of planar slicing and constant step over for slicing a thin wall geometry

As shown in Figure 1-5 for the process planning for the DED AM process, when the slicing type is determined, the slice direction and the height needs to be decided. These two parameters should be selected based on the machine parameters and machine capabilities. Also, choosing a proper slice direction can minimize overhanging features and consequently decreases the complexity of the production.

1.3 *Multi Axis Configurations*

For parts that have overhang features, a four or more axis machine is needed to fabricate the product in a supportless manner. Here in this research, a 5-axis machine is applied to build samples. Figure 1-11 illustrates a schematic of the 5-axis machine and its available movements. Using all 5 axes to build a part introduces some DED specific challenges as shown in Figure 1-12. In this figure, a sharp corner of a part that is built by DED AM is shown. The machine response time to traverse the interior corner caused material sublimation. The solution for this issue is to introduce a fanning movement for the nozzle to gradually change the orientation when it traverses from the first edge to the second. Linking the machine kinematics, dynamics, and motion controls is an on-going area of research for machine tool companies and researchers and is outside the scope of this work; however, if a process can be developed to apply less simultaneous axis motion, it decreases the process complexity. As Figure 1-13 indicates, axis configurations can be optimized to use less axes working simultaneously. This will be explored in this research to study the feasibility of making a complex part by less than 5 axes being active simultaneously.

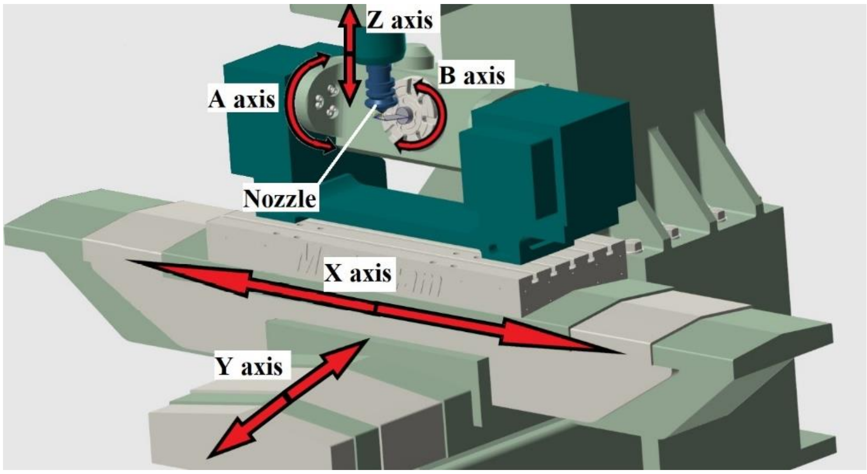

Figure 1-11. Translational and rotary movements of a sample 5-axis machine

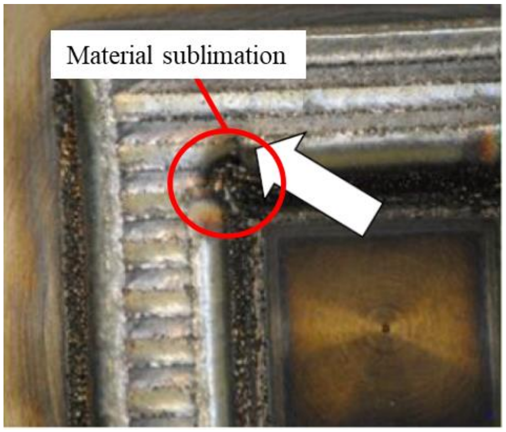

Figure 1-12. Material sublimation at the corner (made by DED AM) [45]

2+1 Axis	•2 axes make the travel path in the layer and 1 axis is between-layer movement
2+1+1 Axis	•2 axes make the travel path in the layer and 1 axis is between-layer movement. 1 axis alters between features
3 Axis	•All 3 axes are involved at the same time
2+2 Axis	•2 axes make the travel path in the layer and 2 axes between-layer movement.
4 Axis	•All 4 axes are involved at the same time
4+1 Axis	•4 axes for deposition toolpath and 1 axis for altering between layers
5 Axis	•All 5 axies are needed to work at the same time

Figure 1-13. Mostly common axis configurations for DED AM

In order to make the part in a 5-axis mode, the tilt and lead/lag angle play an important role.

1.3.1 Tilt and Lead/Lag Angles

As Figure 1-14 shows, the lead and lag angles refer to the angle that the nozzle inclines either forward or backward as it travels. When it leans forward it is called a lead angle and when it leans backward it is a lag angle [46]. Here, F is the direction that the nozzle travels to deposit the material, N is the slice direction and C is the cross product of F and N. Lead and lag angles are formed when the nozzle rotates around the melt pool point while the nozzle axis lies on the F-N plane [1].

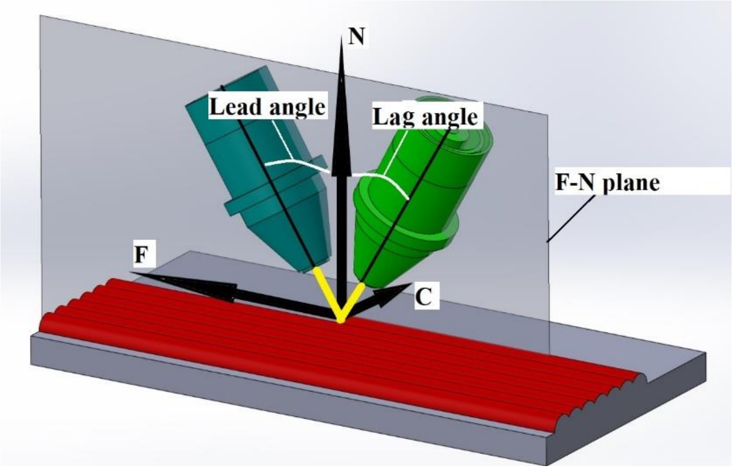

Figure 1-14. Lead/ lag angle

The other angle that is widely used in 5-axis DED is the tilt angle. As Figure 1-15 illustrates, this angle is formed when the nozzle tilts to the side. In this case, the nozzle rotates in the C-N plane. In this picture, N can be either the slicing direction used in traditional slicing or the surface tangency vector when using a constant step over when the product has thin-wall geometry. The tilt angle cannot be larger than a certain value due to process instability issues.

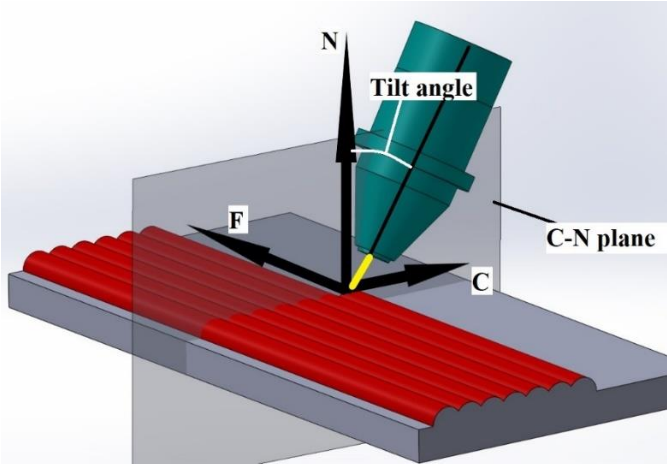

Figure 1-15. Tilt angle

1.3.2 Support Structure Elimination by Multi Axis System

Support structures are needed for areas where an overhang angle exceeds the maximum allowed value. Figure 1-16 indicates that the overhang angle is the angle between the slicing direction and the tangent line of the surface. Based on the DED machine type, material, and process parameters, there is a maximum allowable overhang angle. If the overhang angle exceeds this value, the material collapses as shown in Figure 1-17. In this picture, a thin-walled part is shown where the overhang angle increases as the height increases. The area highlighted as region 1 has a buildable overhang angle but the angle in region 2 exceeds the process limits. The collapsed material is apparent in region 2 for the experimental part.

There are 2 possible solutions to eliminate the material collapsing problem, adding a material stock below the regions that have a high overhang angle or using an appropriate tilt angle to reduce the real overhang angle. The former solution is not practical as it adds post-processing costs to machine the stock away, and furthermore, may cause chatter and part deflection (for thin walled parts) which complicates the process [47]. However, for other AM processes a simple support structure can be helpful (Figure 1-18) In this picture, there is a gap between the bottom of the part and the substrate, so the green surface in Figure 1-18 (b) can be added to act as a support structure. This surface can be removed after fabrication by a simple machining process.

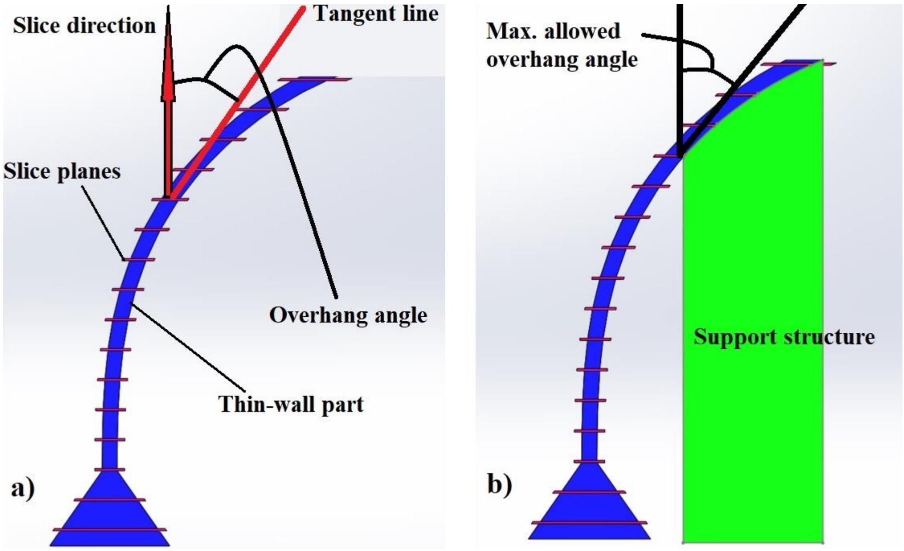

Figure 1-16. Schematic explanation of a) Overhang angle b) Support structure

As shown in Figure 1-16, the overhang angle is the angle between the slice direction and the surface tangent line. If the overhang angle is more than a maximum allowable value, support structures are needed. But, as Figure 1-19 shows, by utilizing a 5 axis machine and an appropriate tilt angle, the real overhang angle can be reduced (In order to simplify the pictures, it is assumed that the part is fixed while the nozzle is moving and rotating but in reality, the nozzle is in vertical orientation and the part rotates to provide the required orientations between the part and the nozzle). By rotating the table, the angle between the nozzle axis and its tangent line (α in Figure 1-19 (a)) will be zero (ideal situation). Here, α is the angle between the tangent line and the nozzle axis and it is called the "tilted overhang angle"; β is the angle between the slice direction and the nozzle axis and it is called the "tilt angle"; and α+β is the angle between the slice direction and the tangent line so it is the "overhang angle" (Figure 1-19 (a)). In a 3-axis system, the nozzle axis is the same as the slice direction (β=0), so there is the angle α between the tangent line and the slice direction. In a 5-axis system, if the tilt angle increases to the point of reaching the overhang angle (Figure 1-19 (b)), the tilted overhang angle will be zero. In this condition, material will not collapse, since the next layer will be supported by the previous one.

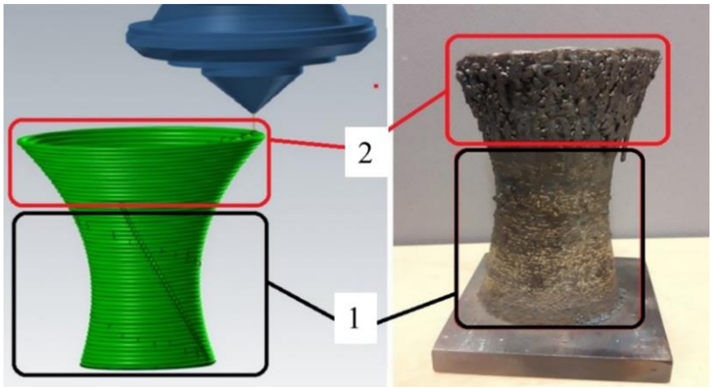

Figure 1-17. Material collapse for the regions that have high overhang angle [48]

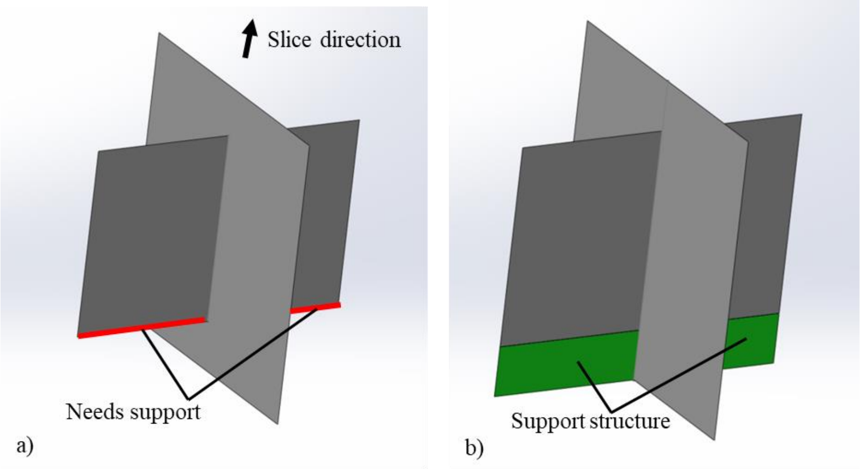

Figure 1-18. Simple support structure for AM processes

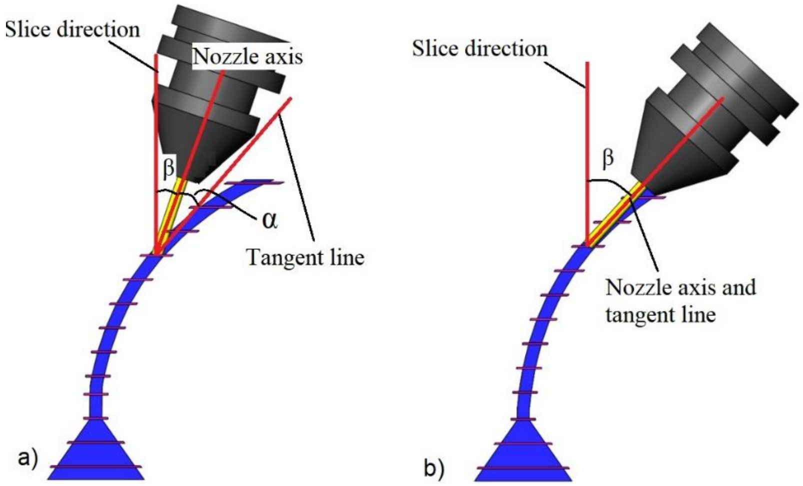

Figure 1-19. a) Applying tilt angle to reduce overhang angle b) When nozzle is tangent to surface real overhang angle is zero

After all these parameters are defined, the toolpaths are created. The toolpath defines both the path that the nozzle needs to travel to deposit the material and its orientation at every point. In this research, the APLUS software is used to generate toolpaths. This software can create 5-axis toolpaths based on planar slicing, radial slicing and constant step over slicing for surfaces. Also, APLUS has parameters for the variable tilt angle capability that allows the nozzle to stay tangent to the surface.

1.4 *Toolpath Verification*

When the toolpath is created, it is important to verify the travel paths for any possible collisions. As Figure 1-20 shows, collisions can occur between the nozzle and previously deposited layers (Figure 1-20 (a)) or between the nozzle and the substrate (Figure 1-20 (b)). A solution to avoid a collision is to tilt the nozzle to the appropriate side to prevent interference (Figure 1-21). Another solution is partitioning the surfaces into buildable segments and introducing an appropriate nozzle orientation to avoid collisions. The latter approach to resolve the collision problem will be explored in more detail in the methodology chapter.

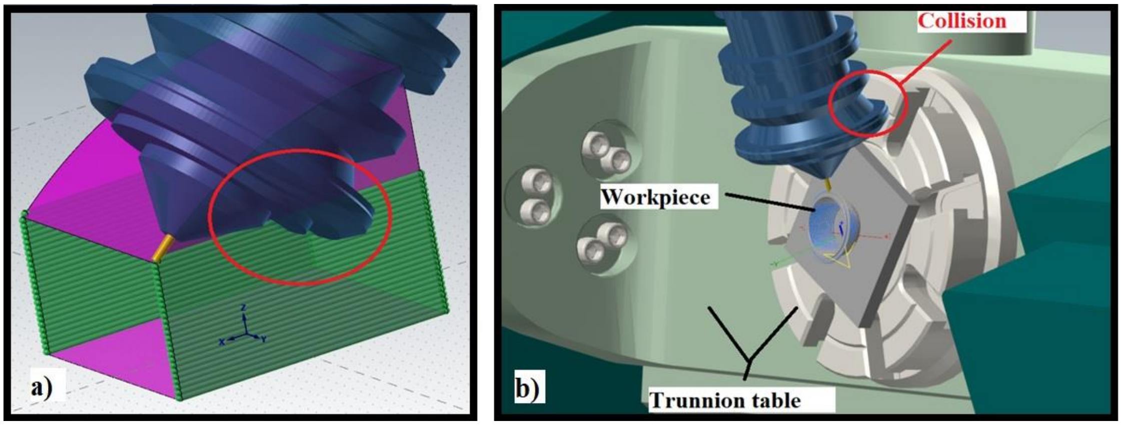
a)
Collision
Workpiece
b)
Trunnion table

Figure 1-20. Collision (a) Between nozzle and previously deposited layers. (b) Nozzle and the table

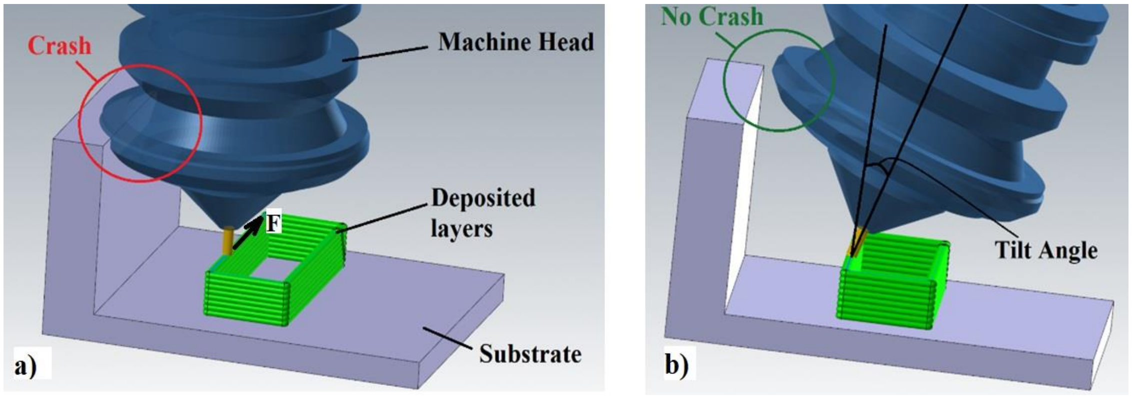
Crash
Machine Head
Deposited layers
F
Substrate
a)
No Crash
Tilt Angle
b)

Figure 1-21. Avoiding the (a) collision by (b) Tilting the nozzle

1.5 *Pre-build Setup, Fabrication and Post Processing*

After a toolpath is finalized, machine parameters such as laser power, laser diameter, powder feed rate, etc., need to be set. Finding the appropriate values of these parameters is based on experience, and available literature from previous studies [49][50][51]. Studying the process parameters to bead geometry relationships is beyond the scope of this research.

The last AM process planning step is creating the NC-code and importing it to the DED machine. The NC-code contains all the machine parameters, the toolpath, and the tool orientation. Then the machine fabricates the part. After the part is built, post-processing is required. Some post-processing operations include sandblasting to remove residual stresses, and/or finishing machining of the product to achieve the tolerances.

1.6 *Surface roughness measurement*

The surface texture consists of two main irregularities: surface roughness and waviness. These irregularities usually have a pattern and have a dominant direction (Figure 1-22). To measure the surface roughness other larger-scale noises like waviness and nominal geometry profile should be eliminated.

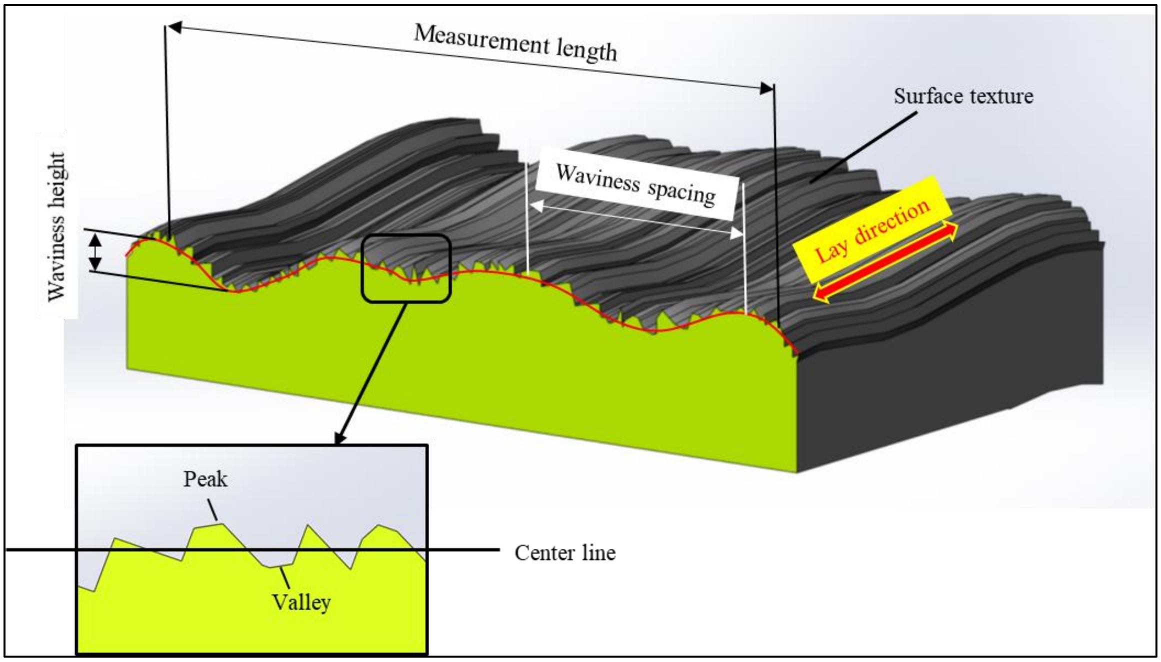

Figure 1-22. Illustration of surface roughness terminology

Here some of surface roughness terminologies are explained [52]:

Roughness- finer irregularities of the surface that are resulted from the production process. The tool chatter or traverse feed marks are the main reasons for roughness in machining whereas being layer-based and material collapse are the main reasons in AM.

Waviness- the form error of the surface originated from inaccurate geometry of the production tool. The roughness is superimposed in the waviness of the surface.

Lay- the direction of the predominant surface pattern, mainly caused by the production process. The direction of the staircase effect in AM is the lay of the surface.

Surface texture- the deviations of the surface from the nominal shape.

Surface roughness measurements for AM built parts have been a challenge since the AM technology was introduced. AM built parts have rough surfaces as the fabrication process is layer-based. Some developing material extrusion AM technologies such as big area AM (BAAM) and large scale AM (LSAM) have very large beads (i.e., 20 mm wide and 5 mm thick). Therefore, surface roughness measurement for these products can be more challenging [53].Figure 1-23 compares the approximate surface roughness (Ra) of DED AM with other AM processes and some traditional manufacturing processes. The Ra values of the DED processes are between 15 to more than 100 µm; whereas, milling and electro discharge machining (EDM) processes have surfaces that are less than 10 µm. Therefore, many of surface roughness measurement systems that are designed for traditional manufacturing techniques are not applicable for DED products.

DED AM built products usually contain curved surfaces. This also makes it difficult to measure their surface roughness by conventional measuring techniques such as contact based systems (i.e., profilometer). Contact based systems are mostly specified for flat surface measurements.

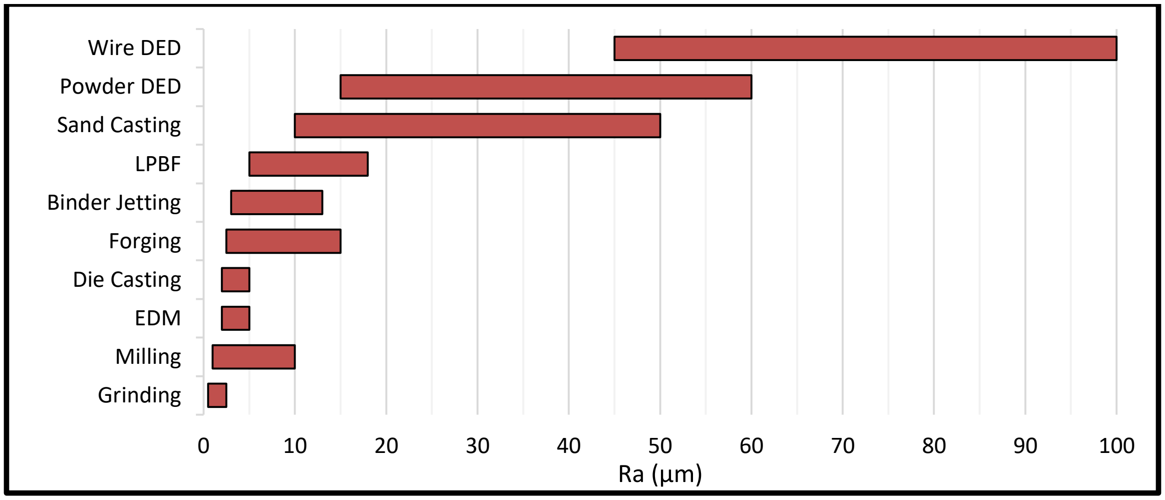

Figure 1-23. Surface roughness comparison of different manufacturing processes (LPBF: Laser powder bed fusion) [54]

1.7 *Research Motivation and Objectives*

Since the DED process is a relatively new manufacturing technology, there are many research opportunities with this technology. As explained in greater detail in Chapter 2, many researchers have explored DED AM from different aspects. Previous process planning studies for multi-axis DED AM of complex parts focused more on dividing the geometries into recognized design features (simple extrusions and sweeps). They divided the part geometry into the available recognized features to avoid collisions. However, a general algorithm to split the geometry into segments that are not dependent on individual features is needed. Experimental studies and simulations for single bead or simple multiple bead scenarios have been investigated. However, experimental and numerical analysis investigations for a more complex component have not been considered.

To build a complex part by a DED process, there can be geometrical boundaries of the product that makes it hard or even impossible to build in a supportless fashion. Complex geometries that include high overhang angles can cause collisions of machine/head components such as the nozzle to either the machine table or previously deposited layers. The first part of this research investigates the collisions caused by the product geometry (Figure 1-24). This leads to the machine head interference with previously deposited layers. Regardless of the slicing direction, for some parts collision can occur if it is required to be built without support structures. The proposed solution is based on partitioning the surfaces that cause collisions and applying different slicing directions and tool orientations for each partition to eliminate the interference problem. This solution will be explained in more detail in Section 3.1 of the methodology chapter.

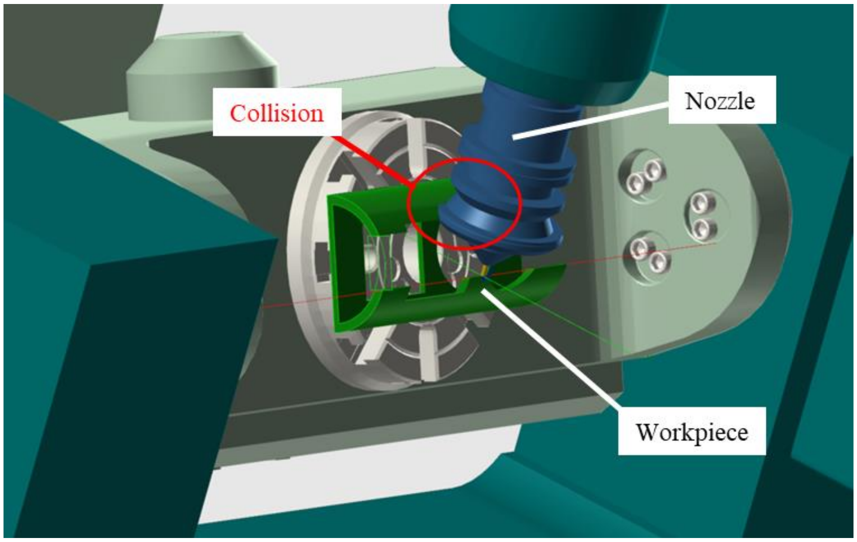

Figure 1-24. A simple half tube that results in collision with previous deposited layers

The second part of this research realizes solutions to measure the surface roughness for DED AM built parts. Two solutions are proposed and developed, including roughness measurements from a mounted sample and from a 3D scanned point cloud. Variations of roughness (Ra) along the slice direction of a circular surface are investigated. More explanations for the Ra calculation as well as the Matlab code that evaluates Ra of the case study samples are explained in more detail in Section 3.5 of the methodology chapter.

Since AM parts are built in layers and the heat distribution is not uniform during fabrication, mechanical properties such as hardness vary. Knowing the distribution of mechanical properties such as the hardness and the residual stress distribution helps to ensure that the product has the proper quality characteristics for its application. In this research, the Vickers microhardness of a thin wall sample is measured experimentally. The general hardness pattern for the thin-walled parts is evaluated. The experimental hardness results are used to verify the implemented finite element analysis (FEA) model.

Predicting the mechanical properties of a product prior to fabrication is a crucial requirement to design and build functional components. Traditional manufacturing technologies such as casting, machining, and injection molding have specialized software programs that have been developed to predict the quality for those products built by these processes. On the other hand, there are many parameters involved in AM processes which makes the prediction challenging. FEA analysis is a useful tool to simulate the coupled thermal-metallurgical-mechanical analysis for DED AM. The focus of the analysis here is to measure the hardness and residual stresses within the sample part at specific points. The main drawback of FEA analysis is it is very time-consuming. As analyzing the deposition of a single bead may take hours, it is anticipated to take days to analyze a simple multi-layer part. The analysis time for a 144-layer thin wall part is reduced in this research. The results are compared with experimental hardness results.

The objective of this research is to develop a process planning solution for supportless fabrication of complex thin-wall geometries using a multi-axis material deposition system. The proposed solution is based on partitioning the geometry surfaces in such a way that collisions are avoided. This research also explores surface roughness variations for round surfaces, and experimental and FEA prediction of hardness and other mechanical properties. In the FEA prediction model, a solution is provided to decrease the simulation time for a relatively large model.

1.8 *Research Constraints*

In this research 410 stainless steel is used for the experimental fabrication. The geometry is limited to thin-wall parts. It means the surface geometries have a constant thickness and the thickness value is negligible compared to geometry size. Explorations about metallurgical properties of the product, post heat treatment, distortion and microscale investigations such as the microstructure are outside the scope of this research. This research investigates the properties of the whole product rather than the properties at the bead-scale. Other DED challenges such as process planning for thin-wall junctions, thin-wall thick-wall junctions are not investigated here and is considered for future work.

Machine kinematics of the multi-axis machines to solve the nozzle travel inconsistencies (in addition to the dwell time that cause the material to sublimate at the corners) are not investigated here. A fabrication constraint that relates to the utilized DED machine is that the B-axis rotation is limited to 0 °-90°. The fabrication process of the case study samples is planned appropriately to overcome this (explained more in detail in Chapter 4).

Developing a surface roughness measurement technique that is applicable for any geometry is considered as future work. Also, it needs to be mentioned that the product properties (surface roughness and hardness) are measured and interpreted here whereas modifying them can be implemented in another research project.

The FEA simulation is a time-consuming process and it may take days or even weeks to implement a simulation for a realistic product. Although a method is used here to reduce the simulation drastically, analyzing a geometry that includes many beads takes a long time. Therefore, there is a limitation in the number of beads utilized in this analysis.

1.9 *Dissertation Outline*

This dissertation is divided into eight chapters, which are summarized as follows. In Chapter 2, the previous literature that is related to the research objectives is reviewed. There are two motivations for this review: (i) to get theoretical and methodological insights from previous similar research to help this current research, and (ii) to find gaps in the available research. This chapter covers literature related to process planning of multi-axis DED AM, collision detection and avoidance, supportless production of complex geometries, surface roughness for curvilinear surfaces, and finally experimental and numerical studies related to hardness for the DED process.

In Chapter 3, the methodology and theories for this study are explained. The collision detection and prevention algorithm is explained in detail, as well as the hardness test and surface roughness measurement strategies. The applied theories and procedures for the FEA analysis are in the last section of this chapter.

The results are presented in four chapters. In Chapter 4, the results for the partitioning case studies are presented. In Chapter 5, the results of surface roughness measurement by two methods of mount-based 2D and 3D point cloud are covered. In Chapter 6, the experimental results for microhardness for the three case study samples are presented.

In Chapter 7, the results of the FEA analysis of the case study sample are presented. The hardness and residual stresses for the case studies are presented and discussed. In Chapter 8, a summary and conclusion for the research, as well as future work, is covered.

CHAPTER 2

LITERATURE REVIEW

2.1 *Process Planning for Collision Detection and Avoidance*

Process planning for additive manufacturing generally consists of CAD model design, CAD-to-STL conversion, slicing, toolpath planning for each slice, fabrication, and final finishing [55][56]. If each of these steps is considered in more detail, they may differ slightly for different AM technologies. Likewise, bead deposition AM processes follow a specific process plan from product design to manufacturing. Although many papers focus on different perspectives of process planning of bead deposition based AM such as reducing material consumption, managing and reducing voids, etc. [57][58], other issues such as process planning for collision detection and avoidance need more investigation.

Since AM processes have appeared, product designers felt less restrained, because buildable geometries are not bound by traditional manufacturing constraints. What distinguishes AM from conventional manufacturing technologies is that complex parts can be produced without the need for fixtures, tooling, or other facilities. Although it is mostly believed that AM can fabricate any arbitrary complex geometry, it still has limits [59]. Consequently, an AM designer should consider manufacturability and geometry constraints of the particular AM process being used. DED as an AM technology has its constraints which need to be considered in the product design. Vayre et al. identified two main constraints for DED AM, the collision between the nozzle and the part and the effect of the nozzle acceleration and deceleration on the bead height [60]. This paper applied a design for additive manufacturing (DFAM) approach. Also, topology optimization solutions were applied to optimize the geometry of a loaded bracket.

In topology optimization, the shape of the product is optimized to use the least material without affecting the strength of the product significantly whereas manufacturability needs to be considered as well. Optimized geometry is usually too complex to be built by conventional manufacturing techniques such as die casting and machining. Many researchers have considered fabricating topology optimized parts using an AM process [61]. Usually, topology optimized geometries have complex shapes that cause an inherent geometrical collision if it is being built by the DED process. Therefore, more research is needed in this field.

Five-axis manufacturing, regardless of being additive or subtractive (machining), may cause a collision of the tool to the workpiece or machine table. There have been many studies to predict the collision during toolpath generation. Since multi-axis machining is relatively older than multi-axis AM, there have been more studies on process planning to avoid the collision in subtractive manufacturing. Also, there is a main difference between the types of collisions in these two technologies. In the subtractive process, the main collision probability is between the tool and machined geometries, whereas it is between the nozzle and continuously creating beads in AM. And contrary to machining, more potential collision areas (previous toolpaths) are being created in DED AM, as more layers are deposited. Also, there are differences between machining and additive process planning: for instance in AM the toolpath cannot cross itself, material piles up at a constant start-stop point, environment temperature and atmosphere influence the product quality, bead geometry varies by overlapping conditions [43].

Regardless of focusing on subtractive or additive processes, the literature that considered process planning for collision detection and prevention is reviewed. Schumann [62] offered a hull-concept based collision prevention mechanism for all axes without using any sensors on the machine. Hull-concept considers a safe stopping distance for the moving axes. This system detects potential collision possibilities throughout the working process and can prevent operator faults. Likewise, Yau et al. [63] proposed an online collision detection function that foresees the toolpath in real-time and stops the process before a collision occurs at a safety distance. The safety distance is defined by minimum distance that the machine can stop at the maximum feed rate. However, the type of collision that they studied is different from what is being explored in this research. What they explored is applicable to avoid collision caused by operator fault or machine error. These types of interferences occur during the fabrication process whereas, the inherent collision that results from the geometrical complexity of the product should be considered before the fabrication starts. To solve the former issue, the machine dynamics should be considered, but for the latter, process planning and part geometry need to be optimized.

Zhiwei et al. [64] presented a tool orientation collision-free area for free-form surface machining. It is claimed that this solution considers both efficiency and precision for finding a collision in 5-axis finishing machining. However, the research focus is adapting tool orientation to avoid collision, whereas geometry segmentation is needed in most of the AM collision cases.

Tang and Bohez [65] proposed a collision detection and prevention algorithm which is based on a bonding volume and a sweep plane approach. Initially, the bounding sphere algorithm investigates the possibility of collision, and if a collision is anticipated, it will be explored more by the sweep plane algorithm. Sweep planes are bodies of machine and workpiece geometries that are sliced by parallel planes. For collision avoidance, if it occurs in G00 mode (rapid movement) the proper axis moves toward predicted direction to avoid it. For G01 (machining travel speed), an appropriate lead/lag or tilt angle is applied. This paper brings a suitable method that can prevent collision by machine movements but did not investigate interferences that can be prevented by segmentation.

Wang et al. [66] presented a collision detection solution besides the tool orientation adjustment method to avoid collision in the multi-axis milling system. Three main types of collisions are defined here based on the colliding section of the tool: the bottom of the cutting tool (rear interference), cutter flutes (local interference) and cutter shank (global interference).

Chen et al. [67] proposed a collision detection methodology for filleted-end milling tools. They categorized the surfaces into convex and non-convex regions. There is no interference for convex regions but for non-convex regions, they detected and prevented local gouging. Likewise, Xu et al. [68] proposed an algorithm to create a collision-free toolpath for direct ball-end milling tools. This method creates a surface from a point cloud.

Plakhotnik et al. considered altering the tool orientation (tilt and lead/lag) to avoid collisions in DED. They prefer a lead/lag solution rather than a tilting orientation as it does not change the width of the spot size on the bead [69]. This finding can be transferred to the collision avoidance algorithm by giving a priority to the lead/lag angle rather than tilt angle.

Table 2-1 lists available literature regarding collision detection for both additive and subtractive manufacturing processes. There are limited multi-axis DED collision detection strategies. The needed methodology for the DED process is different from the machining process because the material is being removed in subtractive processes but it is continuously added in the DED process. Also, the tool can stop at a position to change the orientation in machining but it creates material sublimation in AM (Section 1.3). Furthermore, the DED nozzle is usually bigger and more complex than the geometry of the milling tools.

Table 2-1. Literature review of process planning for collision detection and avoidance

	Additive (A) Subtractive (S)	AM Process Planning	Collision Detection	Collision Prevention strategy			Shape of the tool	
				Machine stop	Tool orientation	Partitioning	AM nozzle	Milling tool
Schumann [62]	S		√	√				
Yau [63]	S		√	√				√
Zhiwei [64]	S		√					√
Tang [65]	S		√		√			√
Wang [66]	S		√		√			√
Chen [67]	S		√		√			√
Xu [68]	S		√		√			√
Lauwers [70]	S		√		√			√
Chen [71]	S		√		√			√
Plakhotnik [69]	A	√	√		√		√	
This research	A	√	√		√	√	√	

2.2 *Supportless Fabrication of Complex Geometries Leveraging Geometrical Partitioning*

On one hand, introducing multi-axis DED machines improved its potentiality to fabricate complex geometries, on the other hand, this brought complexity to the process planning especially when the geometry intricacy increases. The challenge is in toolpath, tool orientation, and appropriate process parameters to fabricate the part without the need for a support structure. This section reviews the papers that focus on fabricating complex 3D objects utilizing the DED process. The main solution to build points with complex geometries that cause a collision is to split them into their constitutive features and build them sequentially. Some papers that developed this technique will be discussed here.

Boisselier et al. [72] investigated methods in the optimization of material deposition toolpaths to build freeform metal parts. They studied the challenge of keeping deposition velocity as constant as possible. Panchagnula et al. [73] investigated rotary thin-wall geometries by keeping the tool tangent to the surface. None of them investigated the collision elimination strategy. Both pieces of research fabricated a geometry that needed simple partitioning. The product is made up of a main rotary body with some extruded features attached to the side.

Shi et al. [74] applied a hollow-laser beam with internal powder feeding (HLB-IPF) head to make overhang angle structures. They applied the 6-axis robot to keep tangent to the surface when making a rotary vase-shaped part. This paper explores how to apply multi-axis DED to keep tangent to the surface but does not provide a sectioning algorithm for complex parts. Ding et al. [75] used an 8-axis robotized laser-based direct metal deposition system. They coupled a 6-axis robot arm with a table-table rotary system. They built a 4-blade propeller by sectioning it into 5 parts, the rotary core and 4 extruded blades. This approach works for components where some features are added to a revolved base part. It is not a general solution but illustrates the potential of a partitioning solution. Dwivedi et al. [76] worked on an approach to fabricate slender structures using laser-based direct metal deposition (LBDMD). The nozzle starts from a point and rises as it is continuously depositing material like continuous casting. The nozzle tilts to make slender overhang features, and two slender parts were built in this research. However, this paper is more about controlling machine parameters than a process plan for making complex parts.

Sundaram and Choi [77] developed a direct slicing procedure for process planning of the 5-axis laser aided direct metal deposition. They developed a 5-axis algorithm to slice the part. But the studied parts are solid geometries consisting of some basic extruded features. Also, they did not make any product experimentally. The mentioned solutions split the geometry to discrete features that are easy to be separated. Kapil et al. [44] proposed different slicing methods to eliminate support structures. Planar adaptive planar slicing and non-planar slicing (radial slicing) are used to build on overhang impeller. Non-planar slicing resulted in the best quality. This paper did not consider a collision avoidance strategy.

Murtezaoghlu et al. [78] explored a strategy to split the geometry into discrete sections using infinite planes. They considered decomposition of the solid model, build direction, sequencing build order, and slicing. A decomposition algorithm is applied to segment free-form features. This paper does not consider the collision detection but it finds the best sectioning plane to make the geometry buildable with less sections. The applied decomposition algorithm can be used for this research.

Table 2-2. Literature review of collision detection and prevention

	Additive (A) Subtractive (S)	Thin Wall Deposition	AM Process Planning	Collision Detection	Partitioning for Collision Prevention			Overhang structure
					Sectioning surfaces	Available features	Tool orientation	
Boisselier [72]	A	√				√		√
Panchagnula [73]	A	√						√
Shi [74]	A	√						√
Ding [75]	A	√	√			√		√
Kapil [44]	A	√	√					√
Dwivedi [76]	A					√		√
Sundaram [77]	A		√					√
Murtezaoghlu [78]	A	√	√		√			√
Ren [79]	A	√	√			√	√	√
Newman [80]	S & A		√			√		
Lee [81]	A	√	√			√	√	√
Ruan [82]	A		√	√		√	√	√
Current research	A	√	√	√	√		√	√

The overhang features can be fabricated supportless by adaptive slicing if their violation angle is not significant. For the geometries that consist of a base and attached features, the feature based partitioning works, but the connection geometries between features may be problematic (Fig. 1 in [78]). More complex geometries require surface partitioning. Table 2-2 summarizes the reviewed literature to compare the problems of DED AM they are solving. Although few of them focus on detecting collisions or partitioning the geometry, their approach is different from the current research or generality of their solution is not comparable. The current research focuses on the process planning of complex-geometry, thin-wall parts to find any collision and proposes an algorithm to partition the surfaces of the geometry to solve this problem.

2.3 *Surface Roughness of DED Built Components*

Surface roughness is one of the drawbacks of AM products if it is compared to machined products. This motivated researchers to investigate how to improve surface roughness quality. In much of the available literature, the surface quality is improved by changing process parameters or adaptive slicing.

As AM products may contain curved and rough surfaces, measuring their surface roughness is a challenge [83]. In this case, the nominal curved profile must be removed before the roughness equation is applied [84]. Furthermore, other macro irregularities like waviness need to be removed as well. A skidded tactile roughness tester filters most of the macro surface textures mechanically but the remained noise that affects roughness values needs to be filtered mathematically.

Collecting the needed primary data of the surface textures is another crucial task that affects the calculated result. There are different methods to convert the surface texture into numerical data such as contact-based, focus variation, and confocal laser scanning microscope systems [85]. Many of these technologies like 3D scanning can provide point coordinates of the surface [86]. The point cloud has all the position data of the surface that can be used to measure surface properties. Using these point coordinates for measuring surface roughness has been explored by many researchers. Fadzil et al. [83] measured human skin surface roughness to study the skin scaliness for psoriasis. They measured the 3D surface roughness with standard clustering techniques. A digital image analysis method was developed to measure the surface roughness. Drbul et al. [84] developed a strategy to filter the surface profile from roughness measurements. They filtered the nominal profile and waviness by Fast Fourier Transformation (FFT).

Wu et al. [87] developed a machine learning algorithm to calculate the surface roughness of FDM products. A sensor collects the surface roughness in real time while producing the part. They optimized these parameters and verified by experimental results. Prasad et al. [88] used speckle metrology system by means of special optical fibers to measure surface roughness of AM products. They calibrated their measured values by a contact based surface tester machine. Here, they used a flat surface as specimen. They did not mention the mathematical model they used to extract the roughness value from created images.

Urbanic and DiCecco [53] investigated and compared the impact of different bead shapes on surface roughness by virtual simulation for material extrusion processes. They measured the roughness for different boundary models such as rectangular, obround, and elliptical bead shapes. Lalehpour and Barari [89] found a theoretical formula for surface roughness of additive manufactured products. They considered that the mean centerline assumed in prior research had been wrong; instead they proposed that the centerline passes through the midpoint of cusp edges. These two papers focused on mathematically formulating the roughness and bead shape whereas this research explores the solutions to measure the fabricated products. The roughness of produced parts may be different from what is mathematically derived because other parameters such as material collapse, overheated beads, and bead deformation can affect the surface roughness.

Surface roughness measurement is applicable to explore the irregularities of the terrain. In this case, a point cloud is generated by other techniques like terrestrial laser scanner (TLS). Mills and Fotopoulos [90] used a terrestrial light detection and TLS to scan ground surfaces and extract surface roughness value for geological purposes. They verified their results by comparing the surface roughness values of a known test sample that is measured by TLS system with the numerical simulation results. Their measurement was applicable for a 2D flat surface. Tonietto et al. [91] calculated a best fit plane through the point cloud to represent the nominal surface, which signifies that this process is only specified for flat surfaces. They split the surface into squares and used a gray-scale color code to show the roughness value. Vijayarangan [92] presented a technique that uses 3D laser scanning to measure the surface roughness of metal castings. This technique uses a method that changes a point cloud into an orthogonal coordinate system. They measured RMS (root mean square) of the cast surfaces. This test shows that the measurement error is reduced for rougher surfaces.

Prezestacki et al. [93] investigated the surface quality of laser cladded parts and used an infinite focus measurement (IFM) machine to extract surface texture. They measured the surface roughness for round surface of a laser cladded cylinder. They prepared a Matlab based program called Topography analysis and simulation (TAS) to analyze the topography of the surface texture [94]. Sachdeva et al. [95] studied the effect of SLS process parameters such as laser power, scan spacing, substrate temperature, and hatch length on the surface roughness.

Table 2-3. . Literature review summery of surface roughness measurement

	Application		Curved surface	3D point cloud	Mount method
	AM	Geographical			
Fadzil [83]			√	√	
Drbul [84]			√		
Wu [87]	√				
Urbanic [53]	√				
Lalehpour [89]	√			√	
Mills [90]		√		√	
Tonietto [91]		√		√	
Vijayarangan [92]				√	
Prezestacki. [93]	√		√	√	
Bliss [94]			√	√	
Sachdeva [95]	√				
Current research	√	√	√	√	√

Based on the reviewed literature, prior to calculating the roughness, the noise of the waviness and surface profile should be eliminated. A beneficial mathematical tool for this is FFT analysis. Also, the accuracy of the 3D scanner should be appropriate based on the roughness of the surface. Table 2-3 presents a summary of reviewed literature that considered surface roughness measurement by different methods. As the surface texture size of the ground is much larger than the accuracy of the applied scanners, 3D point cloud data is suitable in the geology field to measure the roughness of the ground. Also, in the literature, mostly the roughness of flat surfaces is measured. Therefore, a solution that measures surface roughness of produced AM built parts which are mostly rough and curved shape is missing. Furthermore, the 3D point cloud has limited accuracy for fine surfaces which introduces error into the calculations. The mounted samples exhibit a polished and sharp cross-sections of the surfaces. These edges contain detailed surface textures which can be seen under magnification. A major benefit of this method over the other methods is that the textures that either stylus or the light cannot reach is included in the roughness measurement value.

2.4 *Experimental and Numerical Studies of the Hardness of DED Built Parts*

There are many parameters affecting the quality, microstructure and mechanical properties of DED-built products. The laser power, powder feed rate, substrate temperature, and many other process parameters influence the quality of the product. Many researchers explored the impact of these parameters on hardness, residual stress, and deflection experimentally and/or numerically [96]. Numerical results are mostly verified by experimental or previous research.

During bead deposition in DED, parts are built by depositing each layer on top of the previous one. Since the introduced heat of the depositing layer transfers into previous layers, the material in each layer experiences thermal cycles. These repetitive thermal cycles lead to changes in microstructure and mechanical properties of the deposited layers [97]. This makes the mechanical properties vary from point to point. In order to control the deposition process and predict the quality of products, research has been conducted to implement FEA analysis of the DED process. In this section literatures that are focused on the simulation of single bead deposition, overlapping cladding, and multi-bead thin-wall deposition of the DED process are reviewed.

Baek et al. [98] studied the effect of preheating temperature of an AISI D2 substrate in DED deposition of tool steel M4 deposition. This showed that hardness increases slightly for higher preheating temperatures. Since the size of carbides increases for lower cooling rates. Chew et al. [99] developed a 3D FEA model to analyze the residual stresses of AISI 4340 steel. They simulated substrate heating without powder being fed, single bead deposition, and deposition of two overlapping beads. The hardness results for a single bead showed a higher value in the clad and heat affected zone (HAZ) region than the unaffected region. Then, these models were used to simulate 10 overlapping beads. Caiazzo et al. [100] experimentally found the geometry of the bead to simulate the temperature history of the multi-track and multi-layer deposition. Gao et al. [101] applied FEA using a birth and death element technique to implement a thermal simulation of the single bead deposition. Zhang et al. [97] and Long et al. [102] developed a numerical simulation model to investigate the effect of substrate preheating on temperature history, stress and thermal behavior. Also, they experimentally studied the effect of substrate preheating on surface quality, hardness and some other characteristics of thin wall parts. Their case study sample was a 4 bead thick, 3 bead high sample on a plate. A 10-layer thin-wall part was fabricated to experimentally investigate the effect of preheating on hardness. It showed that hardness increases as the preheating temperature rises.

Li et al. [103] explored the temperature history of thin-wall parts by an analytical computation model. Heigel et al. [104] developed a thermo-mechanical model of DED considering the gas flow during the deposition. The heat convection from the surface that is generated from the deposition process is measured and applied in the model.

Javidani et al. [105] made a 30-layer thin wall part by DED process to study how microhardness and microstructure change along the deposition direction. They used AlSi10Mg powder material to build the part. Their results showed that at the bottom layers hardness decreases to some point, then it is stable along the wall and then decreases again.

Wang et al. [106] showed mechanical anisotropy properties of the parts that are produced by DED process. This includes constituent phases, microhardness, and microstructure in addition to strength and elongation characteristics. Their sample was a block made up of 3 different alloys of steel deposited on top of each other. It is mentioned that for the same samples, microhardness increases as the measurement point is farther from the substrate.

Shim et al. [107] investigated microhardness, location of the melting pool, and microstructures in addition to geometric accuracy of the DED built part. The dependency of single-layer height to two machine parameters, specific energy density and powder feed density was investigated. Hardness results show the highest values at top layers. Microhardness fluctuates in the horizontal direction when the part is made by feedback real-time control method.

Huang et al. [108] developed a model to predict bead dimensions, wetting angle, heating and cooling rate for single-bead and multi-bead deposition as well as multi-layer walls. They considered powder feeding in their simulation model. Their results show that the most sensitive factor to change the bead height is powder feed rate and specific heat has the least effect. It means by a minor change of powder feed rate, bead height varies a lot. In another paper, Huang et al. [109] established a relation between process parameters of powder fed AM and temperature, cooling rate and solidification rate which are called transient thermal characteristics. They studied a one-bead deposition case.

Ansari et al. [110] studied DED bead deposition of water-atomized iron powder. They experimentally studied the effect of different parameters on the microstructure and geometry of single bead deposition such as bead height. A surface response methodology (RSM) was performed to optimize the parameters. Nazemi et al. [111] used Sysweld software as FEA tool to simulate the temperature history, microhardness and residual stresses for laser cladding of P420 stainless steel on AISI 1018 low/medium carbon steel plate. They implemented the FEA analysis and verification experiments on both single bead and 3 side-by-side beads. Alam et al. [112] accomplished the same experiment for the single bead mostly focusing on residual stress, microhardness, and microstructure.

Urbanic et al. [56] developed a process planning for hybrid manufacturing. As a case study, they built the upper section of a T-section by DED process and machined to size finishing. They simulated the longitudinal and transverse laser cladding bead to cover the whole surface of a plate by FEA analysis. Hardness, transverse residual stress, and distortion were measured.

Table 2-4 summarizes the mentioned papers as well as some other related literature that focus on the experimental and numerical exploration for multi-bead deposition of DED AM. These papers are categorized into the papers that investigate one bead, overlapping multi-track beads, and thin wall deposition. Some papers focus on simulation of the single bead to predict its geometry or mechanical properties such as hardness, residual stress, microstructure, etc. Some other researchers studied the deposition for several beads. This includes a couple of side-by-side beads or thin walls made up of up to 10 to 20 beads. The

Table 2-4. Literature review summary of hardness measurement and FEA simulation

	Bead Simulation	Bead Geometry	Hardness	Wall Deposition	Wall Simulation	Simulation of Partitioned whole part
Chew [99],	√		√			
Caiazzo [100]	√	√				
Gao [101]	√					
Li [103]	√			√	√	
Javidani [105]			√	√		
Baek [98]			√			
Wang [106]			√			
Shim [107]			√	√		
Huang [108]	√	√	√	√	√	
Huang [109]	√	√				
Ansari [110]		√				
Nazemi [111]	√		√			
Zhang [97]	√		√	√	√	
Long [102]	√		√	√	√	
Zhang [113]			√	√	√	
Kumar [114]	√	√		√	√	
Bontha [115]					√	
Wang [116]		√		√		
Wu [117]				√		
He [118]		√		√		
Lu [119]				√		
Lee [81]				√		
Nazemi [120]	√	√				
Peng [121]				√		
Current Research	√		√	√	√	√

main barrier to simulate more beads is that the simulation run time rises radically for more beads. Therefore, FEA simulation is almost an impractical solution to predict the properties and problems of AM built part. Also, these studies did not experimentally investigate the mechanical properties of a real geometrically complex part. FEA analysis can be applicable for industrial usage if it can analyze the bead-deposition based products with reasonable run time.

Here, the mechanical properties of a fully built product will be investigated both by FEA analysis and experimentally. The hardness variation of a complex thin-wall part that is produced in several intermittent partitions will be explored. The focus is to find a variation pattern of hardness in the built case study sample. Furthermore, it includes a FEA simulation of the whole complex thin-wall part. An innovative solution is applied here to decrease the simulation run time of actual complex parts.

Since powder fed AM is a relatively new process, researchers are investigating many different aspect, but a major not addressed is addressing process planning fabrication for complex geometries using 5 axis tool paths without introducing collisions when multi-axis tool paths are being used. A solution that has been explored is dividing the geometry into sections, and building them sequentially. Most researchers do not introduce a general solution for surface geometries. They split the geometry to a main body and available attached design features (typically extrusions). A general process planning algorithm to partition the geometry surfaces and determine nozzle orientation is needed for DED systems. This partitioning needs to be independent of the constituent features.

Additionally, a solution for surface roughness measurements for large bead AM processes is missing in the literature. Processes such as BAAM and LSAM are made of very large beads. Conventional measurement systems are not applicable. Furthermore, an algorithm to measure the surface finish curved surfaces is required since AM built parts usually have curved surfaces. The surface roughness of a sample flat surface cannot represent the curved surfaces because of the staircase effect and material collapse problems.

Furthermore, FEA analysis of mechanical properties of a whole thin-wall geometry component that has more than 100 beads in a reasonable run time is missing in the papers. The methodology to achieve these results will be covered in the next chapter.

CHAPTER 3

METHODOLOGY

This chapter discusses the methodology, techniques, and theories that were applied to achieve the objectives of research. The first section explores the process planning algorithm that proposes how to detect the collisions and also how to partition the geometry appropriately to avoid collisions to create a supportless fabrication solution. Following the proposed 2D and 3D solution approaches for the surface roughness measurement, techniques, and standards regarding the microhardness measurement are explained. Lastly, the theories and the algorithm for an FEA model of the mechanical properties and thermal history are investigated for the multi-bead thin-wall component case studies. The process flow illustrating the research methodology is shown in Figure 3-1.

3.1 *Process Planning of Collision Detection and Prevention*

In bead deposition based AM processes, the material is provided from the machine head, along with relative movement between the nozzle and the substrate to deposit beads at determined paths and form the geometry of the product. Movement varies from a simple 2+1 axes in Fortus 400mc FDM processes to more than 6 axes in robotized DED machines [122]. Although multi-axis bead deposition is capable of making more complex parts, it introduces some issues such as complicated controllers, cost, and the possibility of collision. Collisions between the machine head and previously deposited layers are as problematic as collisions between the machine head and the machine table.

Fabricating thin-wall parts that contain more overhang features increases the possibility of collision. An algorithm is developed that finds and eliminates possible collisions as well as supports. Here, a partitioning strategy segments the surfaces of the thin-wall geometry to eliminate the interferences. As an example, Figure 3-2 (a) shows a thin wall geometry containing an overhanging surface, a set of junctions, and curved surfaces. If the goal is to keep the nozzle tangent to the surface (tilted overhang angle to be zero (Section 1.3)), previously deposited layers will cause an interference condition. Figure 3-2 (b) shows how a tilted workpiece collides with the nozzle.

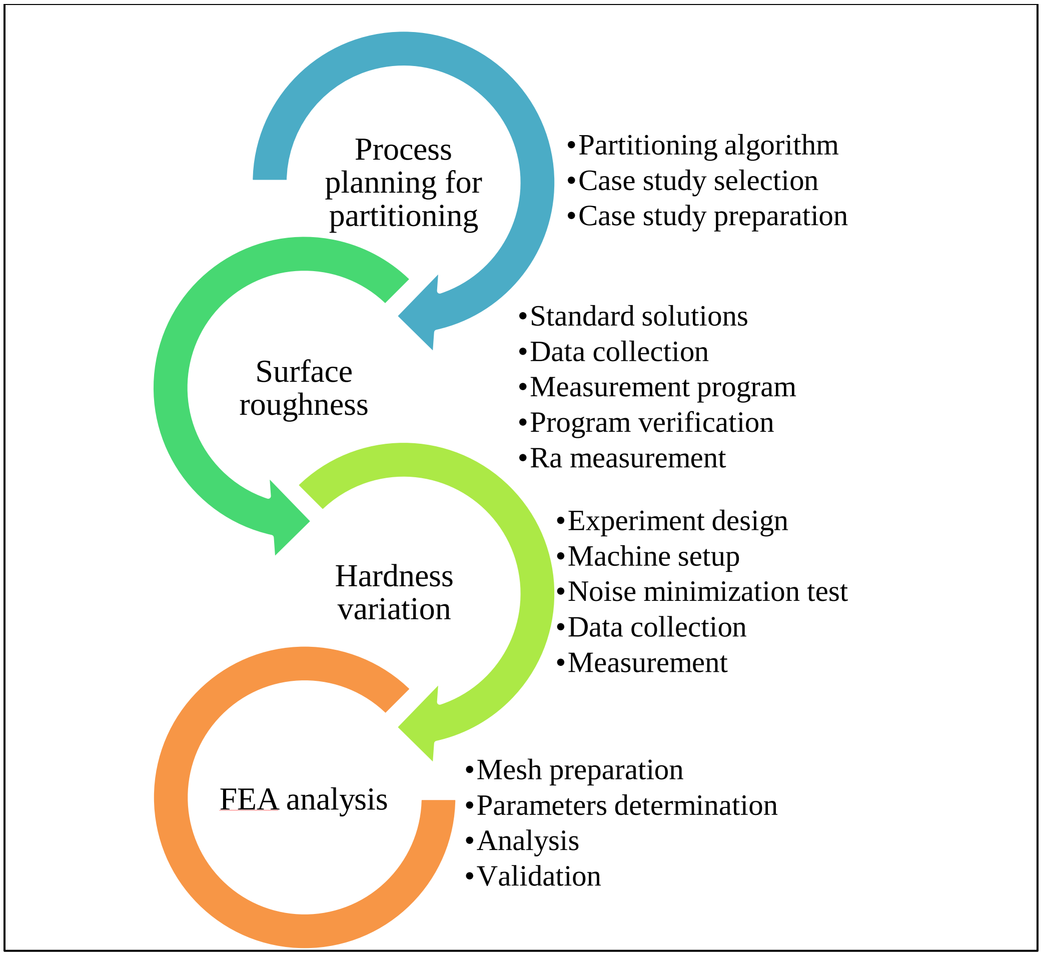
Process planning for partitioning
•Partitioning algorithm
•Case study selection
•Case study preparation
Surface roughness
•Standard solutions
•Data collection
•Measurement program
•Program verification
•Ra measurement
Hardness variation
•Experiment design
•Machine setup
•Noise minimization test
•Data collection
•Measurement
FEA analysis
•Mesh preparation
•Parameters determination
•Analysis
•Validation

Figure 3-1. The process flow illustrating the research methodology

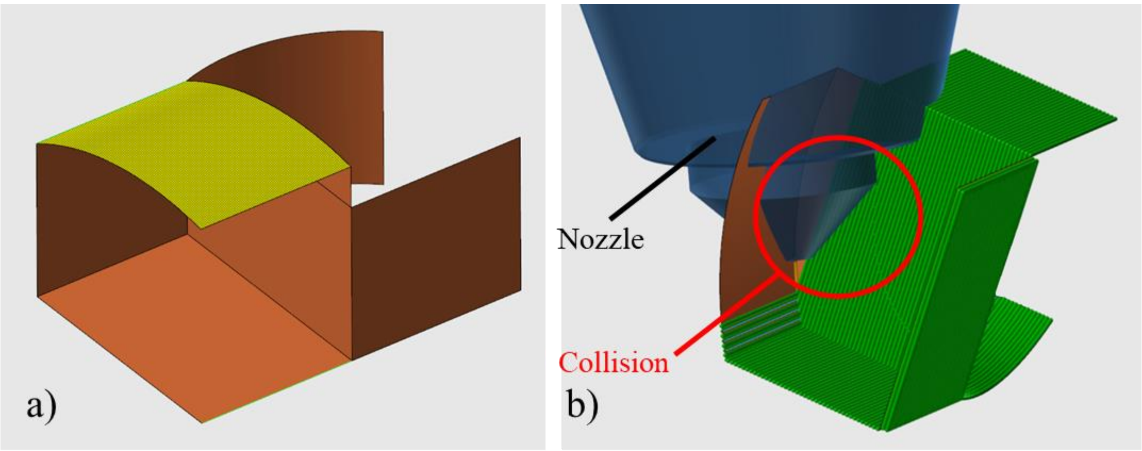
a)
Nozzle
Collision
b)

Figure 3-2 (a) A thin-wall surface sample with inclined surfaces (b) Collision of the nozzle to previously deposited layers

Figure 3-3 illustrates the algorithm for partitioning the part. This tool will partition the thin wall surface geometries appropriately in order to detect and prevent collisions. The algorithm boxes that are filled with grey requires the user to manually enter data. In this research, an algorithm has been developed. Further research and development to program the tools are considered for future study.

Freeform surface geometries are utilized here because this partitioning method is applicable for thin-wall models. The maximum allowed overhang angle needs to be inserted as input data as this varies based on the material, system, and operating parameters [44] [73]. There are two reasons that the maximum overhang angle needs to be inserted. The first reason is to find out whether the part can be built by 3 axis toolpaths without exceeding the maximum overhang angle or if 5-axis toolpaths are needed. The second reason is to limit the maximum tilt angle during the tool orientation calculations. The maximum allowed tilted overhang angle determines the maximum angle that the nozzle axis and surface tangent line can have without material collapsing.

To make the geometry buildable through the thin-wall production process, the geometry needs to be cleaned up such as removing small fillets. These features are hard to achieve in the thin-wall DED AM process. Also, the surface geometry of the part needs to be extracted. The user selects three initial orientations. As Figure 3-4 shows, the 3 standard *X*, *Y*, and *Z* Cartesian plane orientations are selected for this example.

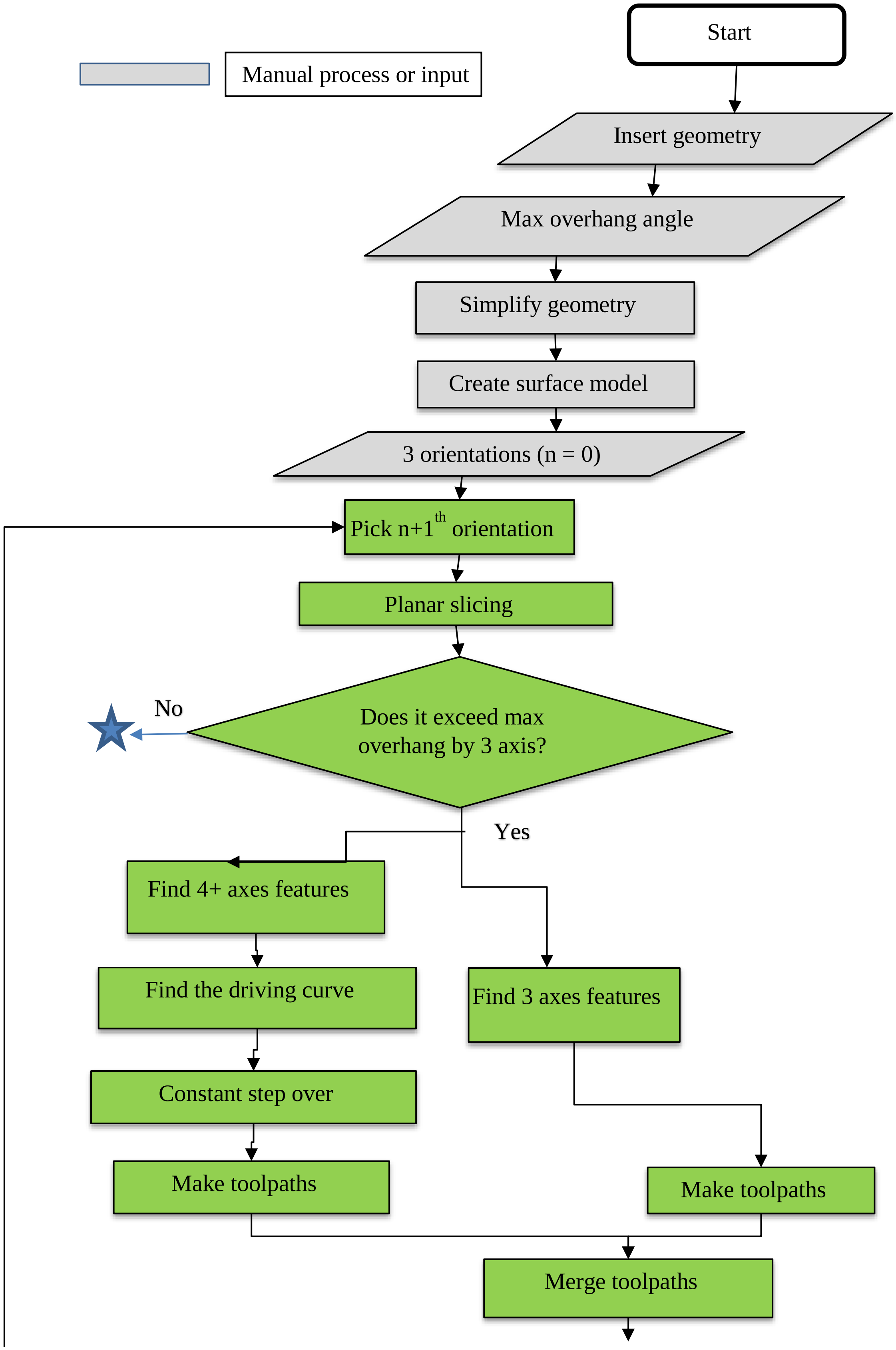
Manual process or input
Start
Insert geometry
Max overhang angle
Simplify geometry
Create surface model
3 orientations (n = 0)
Pick n+1th orientation
Planar slicing
Does it exceed max overhang by 3 axis?
No
Yes
Find 4+ axes features
Find the driving curve
Constant step over
Make toolpaths
Find 3 axes features
Make toolpaths
Merge toolpaths

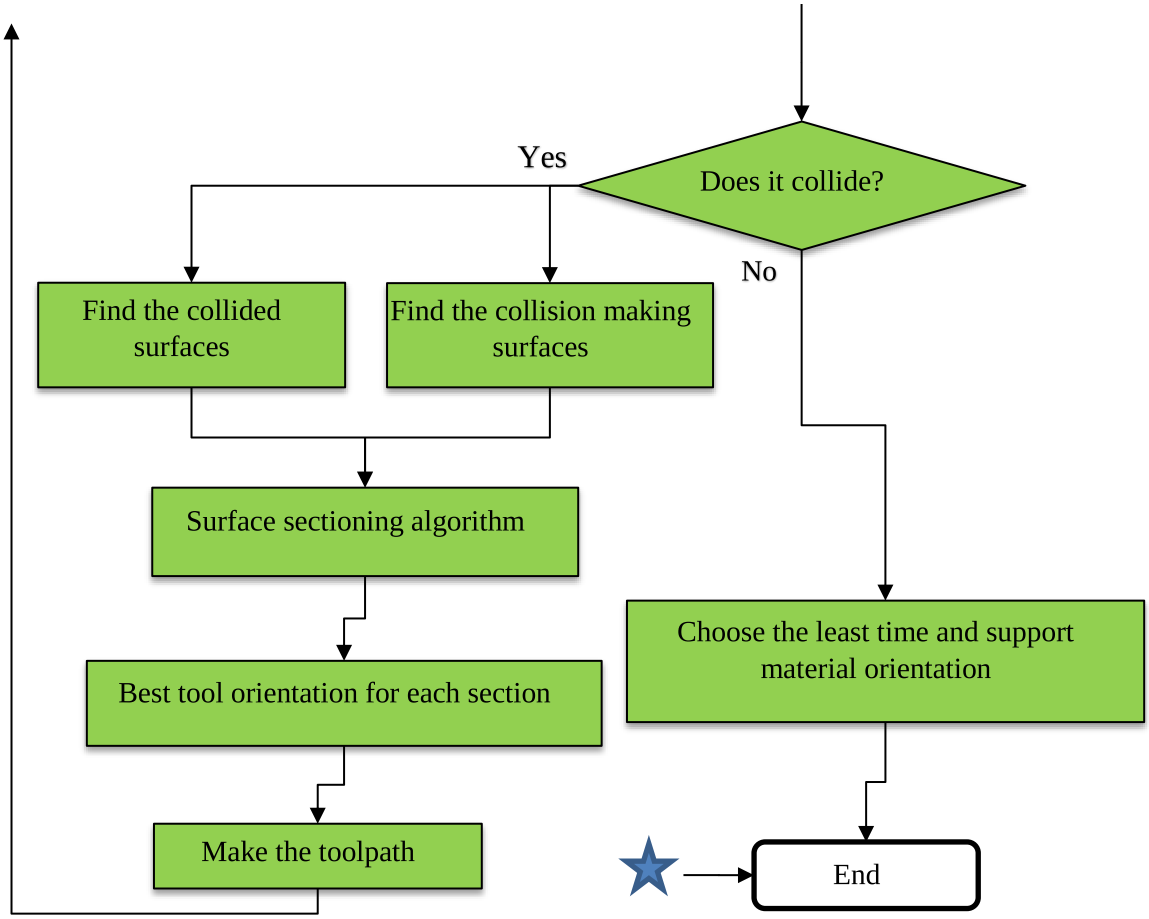
Yes
Does it collide?
No
Find the collided surfaces
Find the collision making surfaces
Surface sectioning algorithm
Best tool orientation for each section
Make the toolpath
Choose the least time and support material orientation
End

Figure 3-3. Collision detection and prevention algorithm

The software picks the first selected orientation to investigate in more detail for any collision and evaluates how to solve it. Based on the first selected orientation, all surfaces of the geometry are planar sliced.

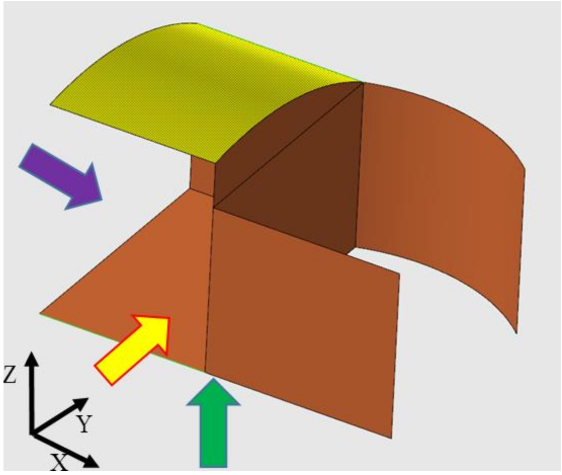

Figure 3-4. Three main slicing directions X, Y, Z

After the geometry is sliced in a planar style for the first slicing orientation, all surfaces are checked whether their overhang angle exceeds the maximum allowed value. If not, the whole part can be built by 2+1-axis toolpaths at this slicing direction. In other words, applying a 3-axis toolpath simplifies the process effectively so that the nozzle does not need to rotate to build inclined surfaces. This process eliminates the necessity of later collision detection and partitioning steps, but if the geometry includes surfaces that overhang more than allowed, the algorithm proceeds to the next steps.

The surfaces that need 3-axis and 5-axis to be built need to be distinguished. In order to determine this, a plane is created perpendicular to the toolpath. The normal vector and a reference vector on the plane are also generated. As Figure 3-5 (a) shows, if the angle between the nozzle axis and these two vectors remains constant, the surface is 2+1-axis. If just the angle between the nozzle axis and reference vector changes, 4 axes are needed (Figure 3-5 (b)) and if both angles between the nozzle axis and reference vector/ normal vector change, the surface needs all 5 axes (Figure 3-5 (c)).

Figure 3-6 (a) illustrates 3-axis and 5-axis surfaces in purple and blue, respectively. Planar slicing is not applicable for 5-axis toolpaths because the real distance between layers will not be the same as the planar slicing height. So the driving curves (yellow) need to be found to make toolpaths on 5-axis surfaces.

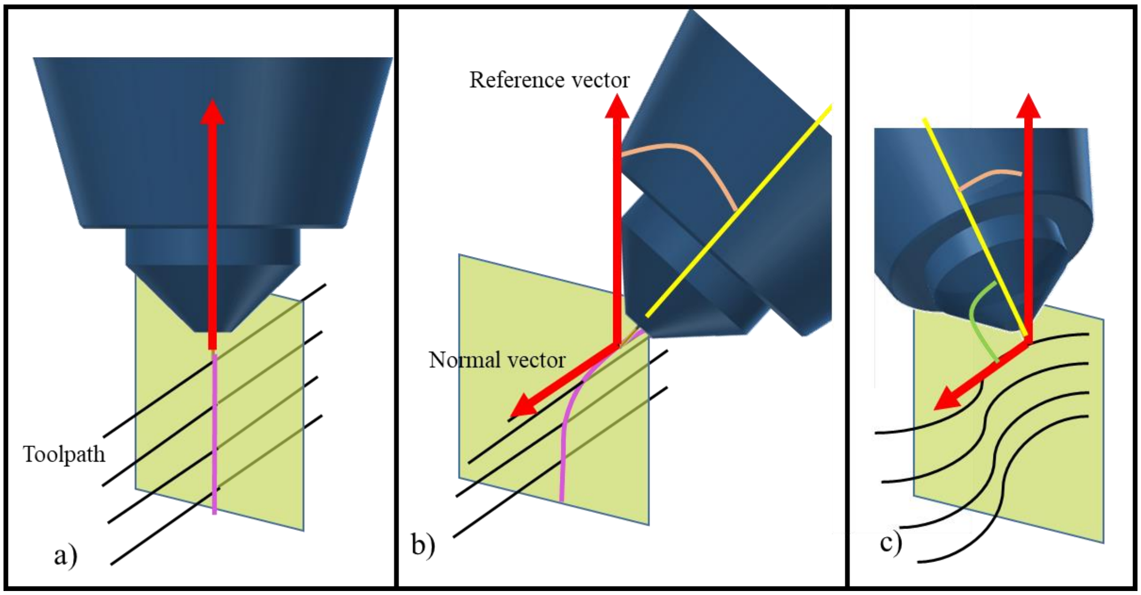

Figure 3-5. Three-axis and 5-axis determination

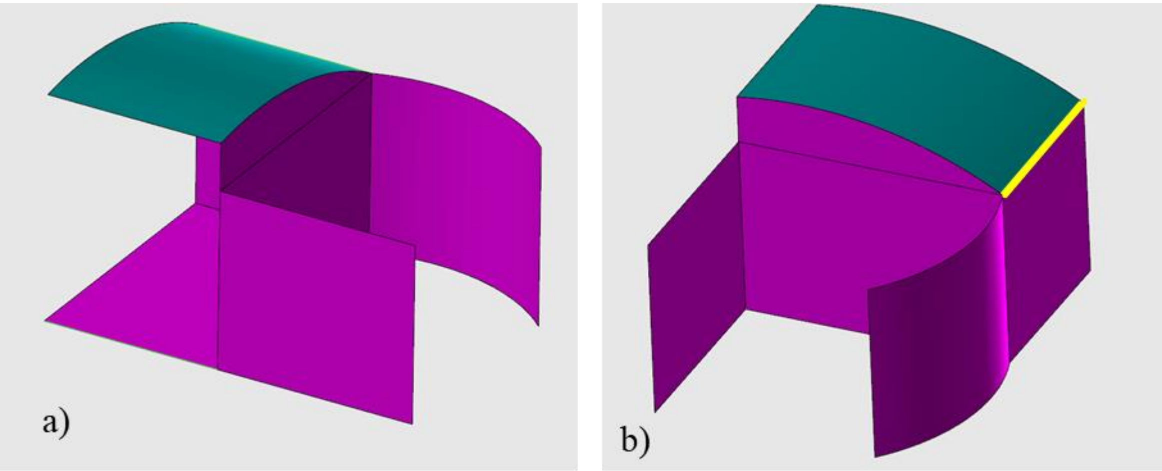

Figure 3-6. (a) Surfaces that need 3 axis toolpath in purple and 5 axis ones in blue. (b) Driving curve that are needed to make 5 axis toolpath

After the toolpaths of all surfaces are merged (Figure 3-7 (a)), simulations are performed to verify the results (Mastercam backplot tool). For this research, the geometry of the nozzle is modeled and simplified. If the distance between any point on the toolpath and the machine head geometry is less than a preset value, a collision is detected. As shown in Figure 3-7 (b), a collision occurs when virtually fabricating the top 5-axis surface. In this example, the nozzle hits the layers that are already deposited for the 3-axis vertical wall.

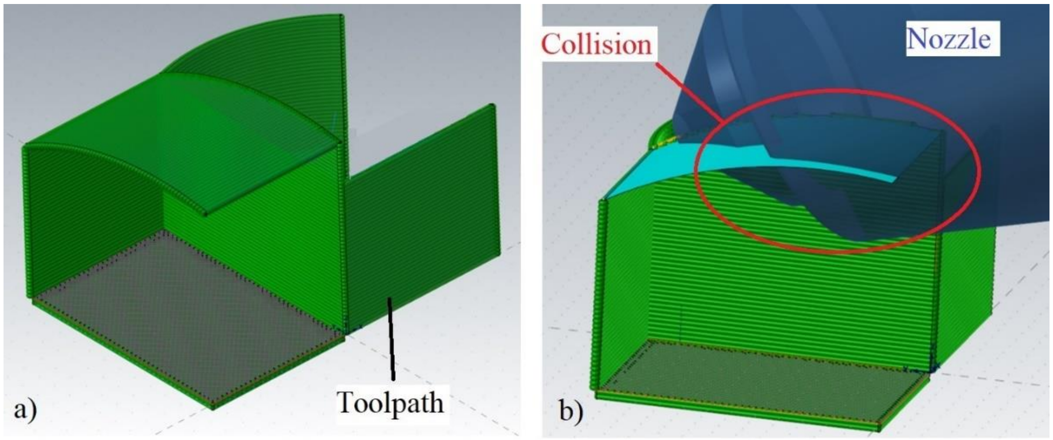

Figure 3-7. (a) Merged toolpath. (b) Collision between nozzle and deposited layers

When a collision is detected, the surfaces with which the nozzle collides, and the surfaces that cause the collision should be determined. In this example, as shown in Figure 3-8, the surfaces that cause a collision when they are being built are shown in yellow. On the other hand, surfaces with which the nozzle collides are shown in red. Partitioning should be applied to these surfaces.

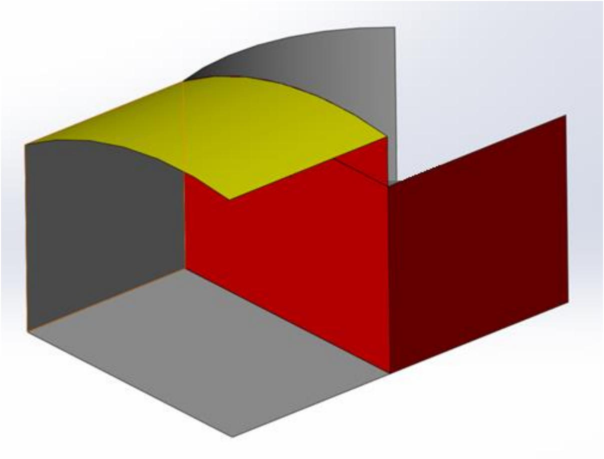

Figure 3-8. Collided surfaces in red, colliding surfaces in yellow and other ones in grey

The surface partitioning algorithm splits surfaces and finds the best tool orientation to eliminate interference conditions. The partitioned surfaces are shown in yellow and green colors in Figure 3-9 (a). The proper tool orientation for each surface is shown in Figure 3-10. The toolpaths of two partitions are shown in green and brown. Further study and explorations in detail about the partitioning technique will be considered as future work as heat cycling issues also need to be considered for a complete solution.

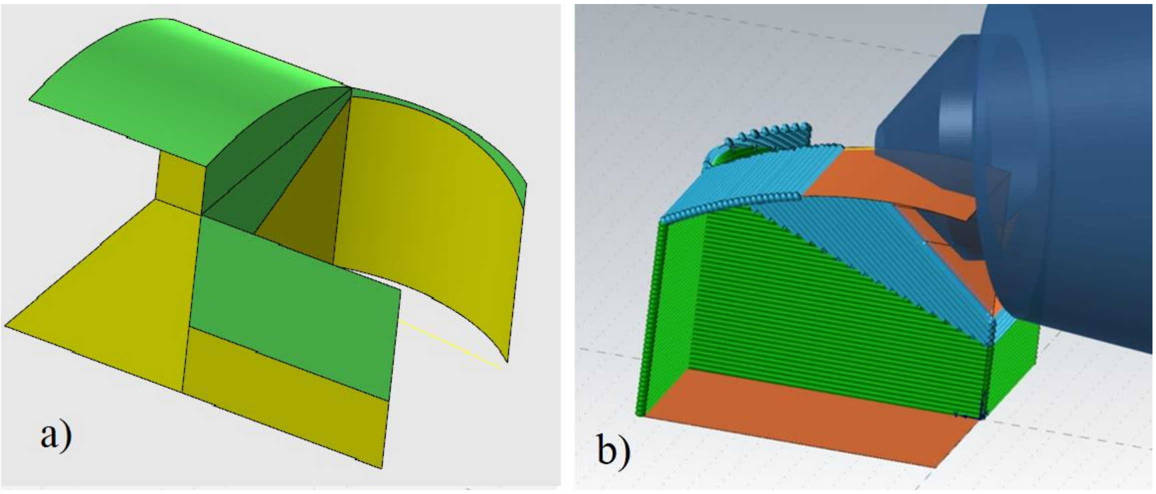

Figure 3-9. (a) Partitioned surfaces in yellow and green. (b) Toolpath and tool orientation of split surfaces

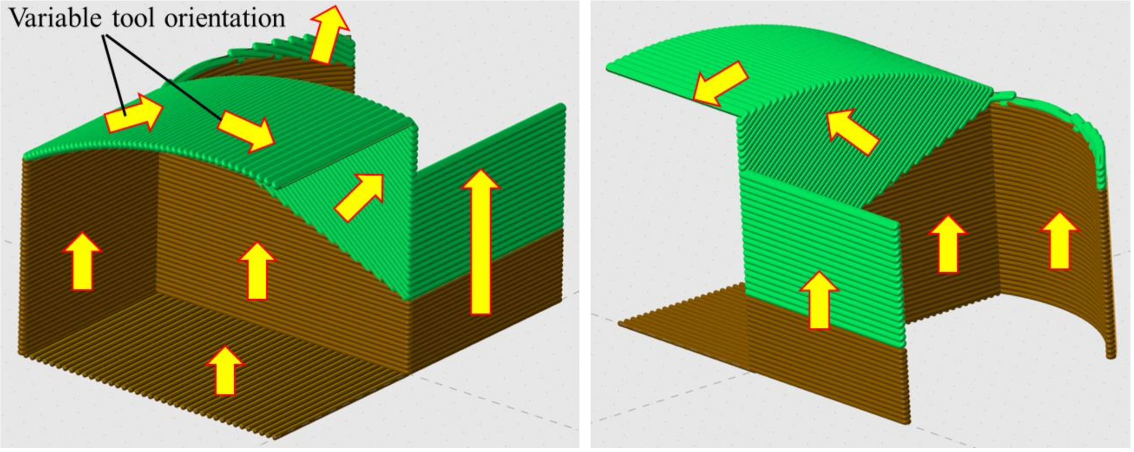

Figure 3-10. Tool orientation of product surfaces from 2 views

3.2 *Partitioning the Case Study Sample*

The case study is a thin-wall hemisphere dome with a nominal diameter of 45 mm and a wall thickness of 2 mm. This geometry is chosen because it includes a continuously variable overhang angle in two directions. Also, fabricating a part that contains surface dome by a bead deposition based AM process brings manufacturability challenges. If a process planning for building a surface dome without supports is developed, this geometry can be used in actual product designs and even topology optimized geometries. Multi-axis DED introduces collisions when the support structure is eliminated. Here, the partitioning algorithm is manually being applied to split the surface of this case study part. Developing a program to perform this automatically is future work.

If the surface dome needs to be made by a 3-axis bead deposition system, regardless of slicing direction, it needs support structure in some regions. Considering a maximum allowed overhang angle of 20°, Figure 3-11 shows the regions where support structures are needed (pictures are prepared using Insight® software version 12.2). For all 3 slicing directions, much support material is needed. Therefore, a 3-axis toolpath is not capable of building a thin wall dome in a supportless mode.

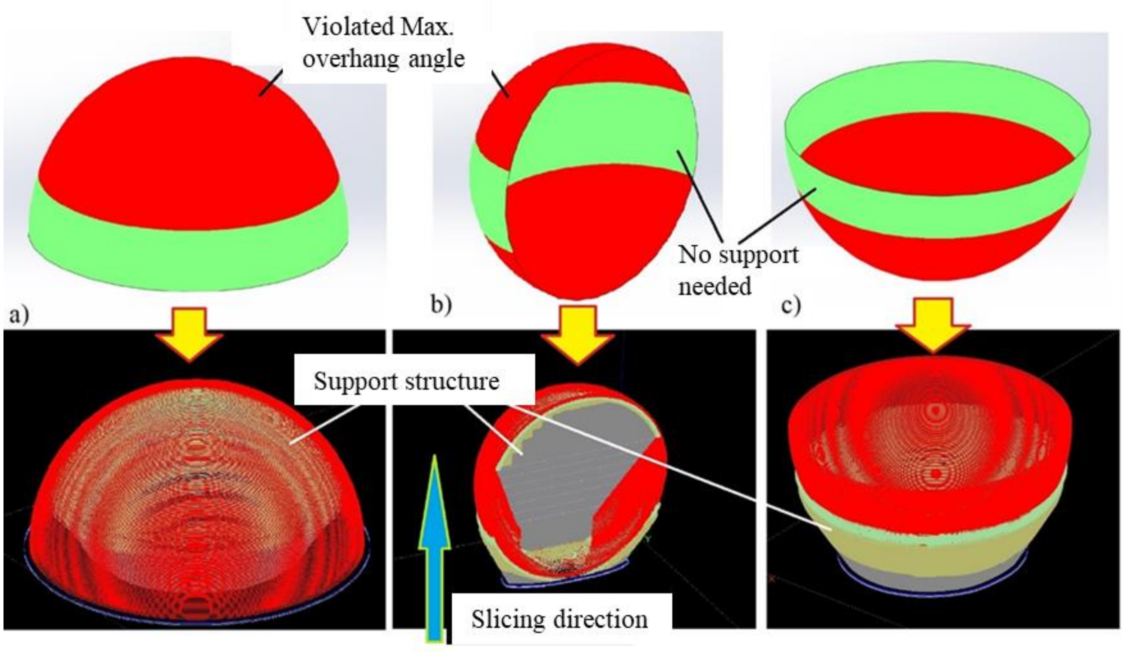

Figure 3-11. Regions of a dome that violate maximum allowed overhang angle and relevant support structure based on (a), (b), (c) 3 main slicing directions

All 3 orientations shown in Figure 3-11 cause a collision at some point during layer deposition when using 5-axis motion. For instance, based on the slice direction shown in Figure 3-11 (a), at higher layers, the nozzle collides with the previously deposited layers. This is shown in Figure 3-12. As Figure 3-12 (a), (b) illustrate, the nozzle deposits material in the lower layers without any collisions. But in higher layers, the nozzle axis is almost perpendicular to the slice direction. The first possible solution is to tilt the nozzle (Figure 1-21). However, for this case study, although the nozzle is tilted upward (Figure 3-12 (d)) it still causes a collision with the higher layers. Based on the collision prevention partitioning strategy presented in this research, the collision caused by this slicing orientation cannot be solved by partitioning the part geometry. So, this orientation is not explored further.

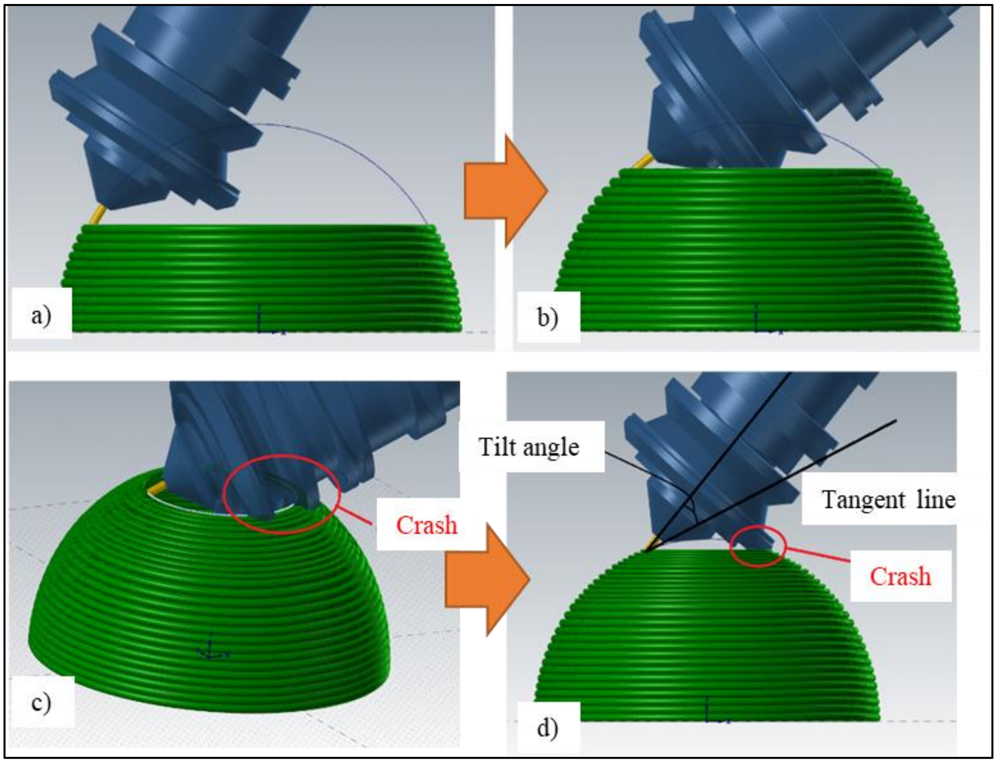

Figure 3-12. (a), (b) Bead deposition for lower layers. (c) Crash occurred at top layers (d) Crash even when nozzle tilted upward

However, the orientations shown in Figure 3-11 (b), (c) can be sectioned properly to become DED manufacturable. These partitioning solutions can be applied to fabricate products that contain a dome in their geometries. The first partitioning solution that is developed based on Figure 3-11 (b) is called wedge shape partitioning. The toolpath developed from the slicing orientation of Figure 3-11 (c) is called a rotary toolpath.

3.2.1 Wedge-Shaped Partitioning

The build direction that is shown in Figure 3-11 (b) leads to a collision between the nozzle and trunnion table when the nozzle is depositing the bottom layers (Figure 3-13). In this case, if the deposition starts at a distance away from the trunnion table, collisions can be avoided. Hence, a substrate is machined from a round bar to make a distance between the table and where the dome is being built. As Figure 3-14 displays the shape and dimensions of the substrate, its one end is rounded to install into the chuck and the other end is flat to perform as the deposition substrate.

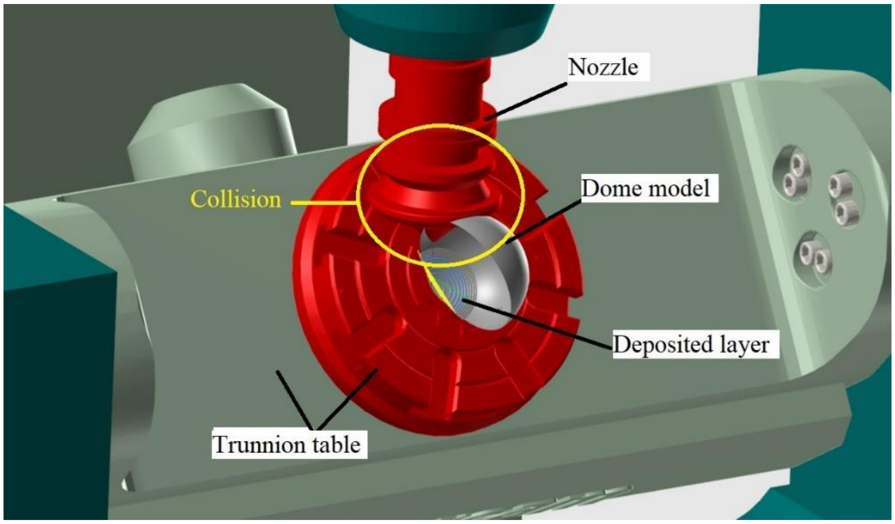

Figure 3-13. Collision of the nozzle to trunnion table (slice direction from (Figure 3-11 (b))

Collisions and the maximum allowed overhang angle are considered for partitioning the geometry. The solution for the former one is to partition the geometry into wedge-shaped surfaces as half of its edge is protruded from the substrate (Figure 3-14). In this way, the collision probability is eliminated. The number of wedge shape partitions depends on two parameters: the planar slicing limitation for major variation of overhang angle, and the maximum allowed overhang angle.

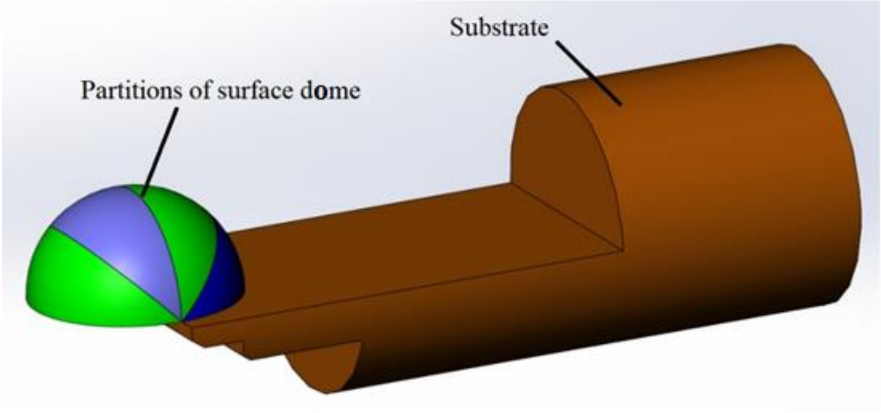

Figure 3-14. Partitioned geometry of the dome on the substrate

The limitation for planar slicing is that the distances between layers (i.e., the stair case effect) vary when the overhang angle changes. As Figure 3-15 (a) shows for slicing of the half dome, the real layer height changes from bottom layers to top ones. Figure 3-15 (b), (c) show that the layer height is equal to the slice height when the overhang angle is zero but it increases as the overhang angle increases. The effect of a small change in slice height is negligible in the quality of the product but if the slice height change is extreme, the final quality can be affected [123]. It is very important to mention that this is an issue for thin-wall parts, not for solid parts. The departed layer is supported by the previous solid layer in solid parts, but it makes a real gap between layers in thin wall parts.

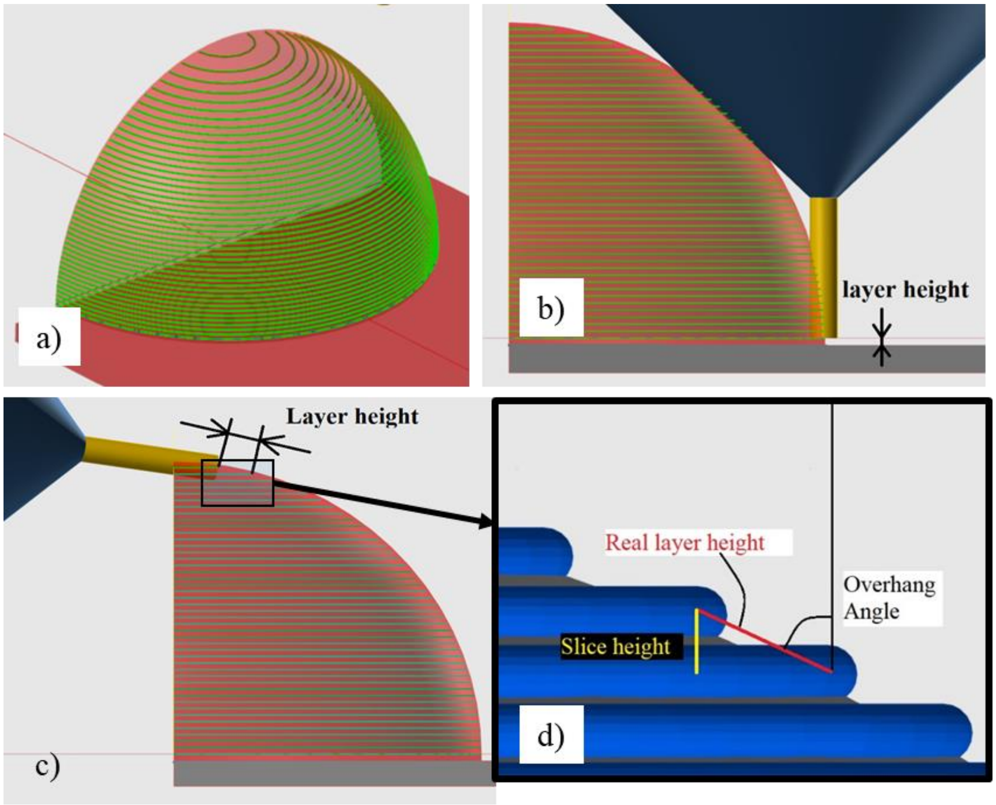

Figure 3-15. (a) Real layer height change when overhang angle changes drastically. (b) Layer height at zero overhang angle (c) Layer height increase (d) the relation between slice height and layer height

The relation between the actual layer height, slice height, and overhang angle is shown in Figure 3-15 (d). As Equation (1) calculates, increasing overhang angle causes a greater difference between the slice height and the real layer height.

$$Real\ layer\ height = \frac{Slice\ height}{\sin(90° - overhang\ angle)} \tag{1}$$

The number of wedge shape segments depends on the number of machine axes, the maximum allowed overhang angle, and the slicing method. The number of required segmentations is less if a 5-axis machine is employed than if a 3-axis machine is utilized because the component can rotate and keep tangent to the nozzle (**Error! Reference source ot found.**). Additionally, if the machine provides a higher maximum allowed overhang angle, the dome can be fabricated with fewer partitions. If a modified slicing method like constant stepover is applied, it modifies the number of partitions. Considering the mentioned parameters, three toolpath methods are explored for the wedge-shape partitioning method, 5-axis, 2+1+1-axis, and constant step over.

Dome fabricated by a 5-axis toolpath- If a dome is split into two partitions, the issue explained in Figure 3-15 occurs. Thus, the number of partitions is increased to 4 to keep the difference between the real layer height and the slice height lower. As a result, the partition angle and overhang angle at the highest layer of each partition is 45°. The slice height for the wedge-shaped partition samples is 0.5 mm. Thus, based on Equation (1) and the highest overhang angle in each partition, the real layer height at the top layer of each partition is 40 percent larger than the slice height (Figure 3-16). This means that the layer height varies from 0.5 mm to 0.7 mm within each partition in the 5-axis sample.

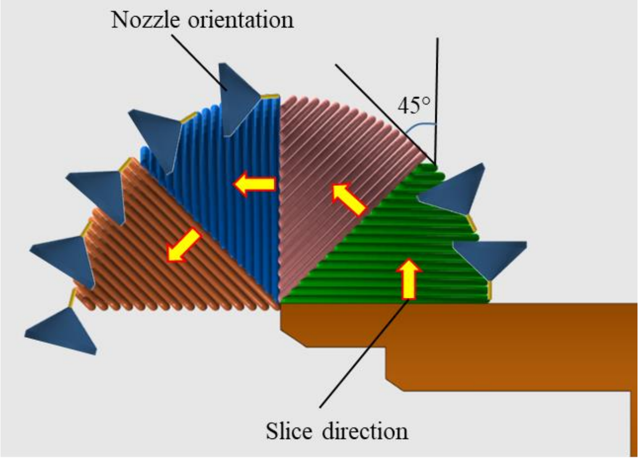

Figure 3-16. Slicing direction and nozzle tangency in 5-axis solution

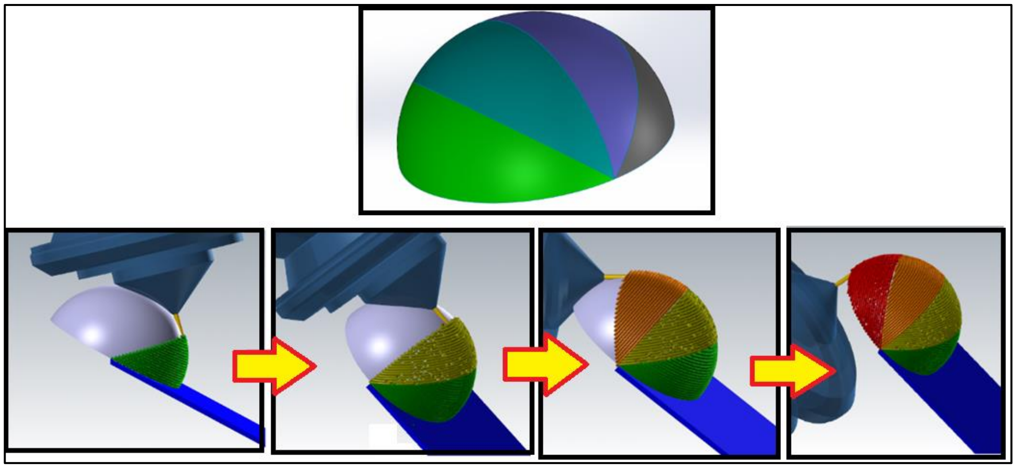

Figure 3-17. Schematic of the fabrication of 4 partitions using a 5-axis system

Dome fabricated by a 2+1+1-axis toolpath- Using a toolpath that requires fewer machine axes brings many benefits to the process. A less expensive machine is needed for the process, the complexity of the process, and the possibilities of a collision are lower. The wedge-shaped partitioning method is modified to fabricate the hemisphere dome in 2+1+1-axis. The main difference between the new approach and the 5-axis method is that the surface of the workpiece should keep the same orientation during each partition fabrication and cannot maintain the tangency to the nozzle. Hence, not violating the maximum overhang angle is the main issue here. It was advised by the DED machine manufacturer that the maximum allowed overhang angle is 20° but it is better it does not exceed 10°. Therefore, 10° is the target maximum overhang angle. If the overhang angle exceeds 10°, there is a possibility of collisions, but if it is higher than 20° the quality of product is affected since there will be significant material collapse.

As Figure 3-18 shows, the slicing direction is kept perpendicular to the bisector plane of each partition. Thus, in each partition, the beads below the angle bisector plane have a negative overhang and the beads above that have a positive one. By maintaining the maximum overhang angle below 10° both below and above the bisector plane, partitions of 20° can be achieved (Equation (2)). As a result, the number of partitions is 9 (Equations (2), (3)). Although the overhang angle becomes 11.25°, the number of partitions is kept at 8. The reason is that if the dome is divided into 9 partitions, the angle range of the 5th partition is 80-100°. Fabrication of this last partition would be problematic based on the machine controller.

$$\frac{\theta}{2} = 10° \rightarrow \theta = 20° \tag{2}$$

$$Number\ of\ partitions = \frac{180°}{20°} = 9 \tag{3}$$

$$Number\ of\ partitions\ kept\ at\ 8 \rightarrow Max.overhang\ angle = \frac{180°}{8 \times 2} = 11.25°$$

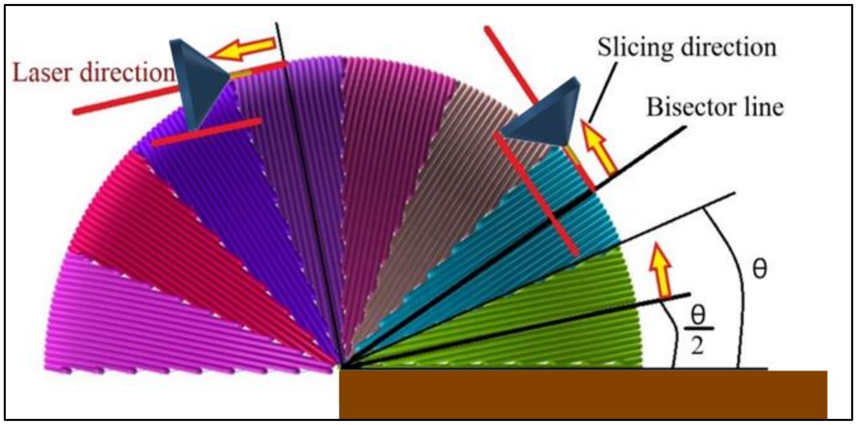

Figure 3-18. Partitioning strategy of 2+1+1 axis

Here, two translational X, Y axes are needed to build each layer. Then, Z-axis increases one slice thickness to start depositing the next layer. After a partition is built, the B-axis rotates 22.5° to reorient the nozzle appropriately for the next partition. Therefore, this process can be called 2+1+1-axis because just 2 axes (X, Y) are involved in depositing each bead and Z-axis is used to shift into the next bead. The B-axis relocates the nozzle from one partition to the next.

3.2.2 *Dome Fabricated by a Rotary 1+3-Axis Toolpath*

This solution is based on the slicing orientation that is depicted in Figure 3-11 (c). This method introduces collisions if it is being built the way it is shown in Figure 3-19.

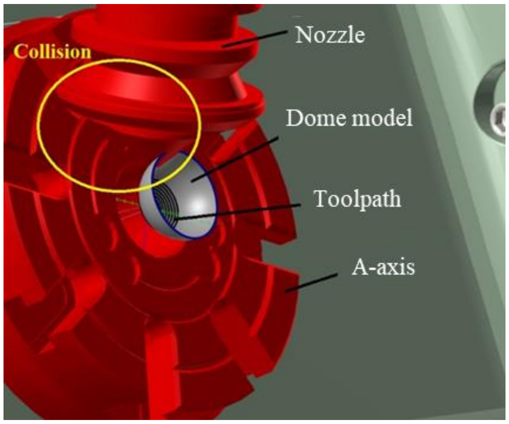

Figure 3-19. Collision made from initial rotary axis strategy

The solution is building the dome at the end of a round bar (Figure 3-20 (a)). First, some beads are needed to be deposited at the end of the bar (3-axis planar slicing) as illustrated in Figure 3-19 (b). This creates the base for building the dome (Figure 3-19 (c)).

When the part is built at the end of the bar, collisions between the nozzle and the substrate are eliminated.

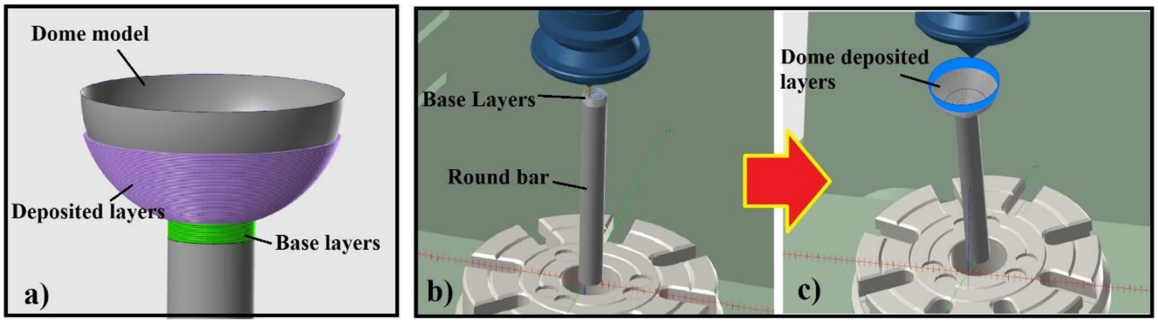

Figure 3-20. (a) Rotary toolpath to build the dome at the end of a round bar. (b) Base layers at the end of the bar. (c) Rotary toolpath to build dome on top of the base

Rotary toolpath with planar slicing- Here, the nominal diameter of the dome is 60 mm with a thickness of 2 mm. The bottom of the dome starts from the end of the round bar which is 20 mm in diameter. The applied slice height is 0.3 mm. The dome is built in three segments from the bottom to the top. The first section is 4 mm high, and the second and third segments are 15 mm and 10 mm, respectively. This sectioning was implemented to investigate the part visually during manufacturing and to investigate the effect of intermittent deposition heat on the hardness of the part.

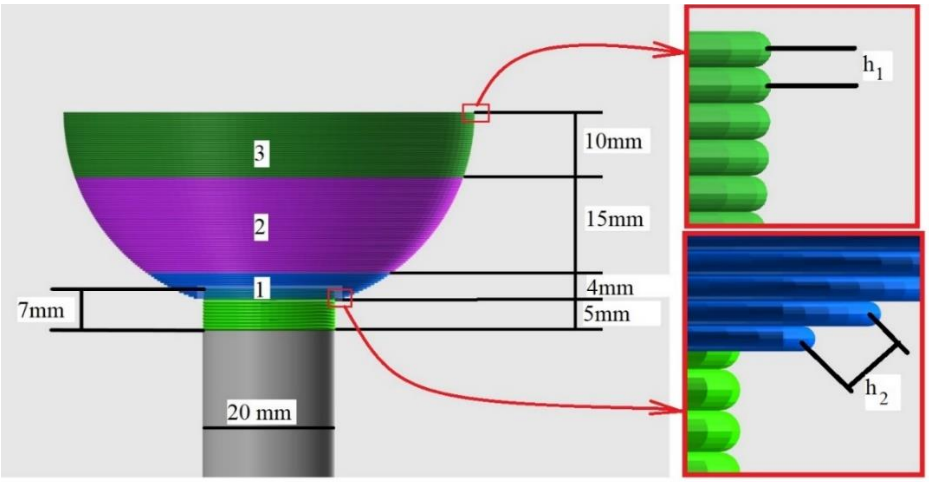

Figure 3-21. Three segments of rotary toolpath dome. First and last layers are magnified to illustrate the changes of real layer height.

Figure 3-21 shows a magnified view of the first and last layers. The real height of the highest layer is h_1=0.3 mm (the same as slice height) because surface tangency is the same as slice direction. Since the first layer has an overhang angle of about 70°, the real layer height is about h_2=0.85 mm for the first layer. The impact of layer height variation on surface roughness and hardness is presented in Chapter 5.

3.3 *Experimental Procedure*

The experimental process flow to build the dome from the partitioned geometry to the fabricated product is shown in Figure 3-22. When the model is split into several sections and the tool orientations are found, AM toolpaths are generated using APLUS. This software is specialized for creating AM toolpaths and is an add-on to the Mastercam software.

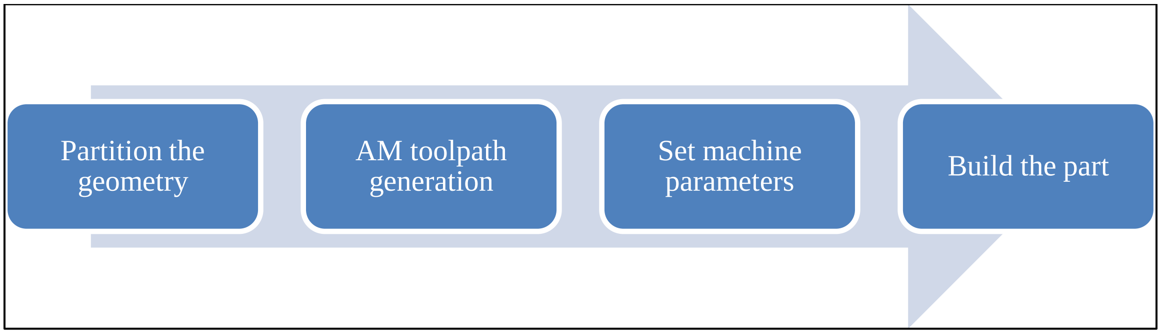

Figure 3-22. Experimental flow to build the case study samples

The fabrication material is stainless steel-grade 410 (UNS S41000). Its mechanical properties are presented in Table 3-1. The material of the substrate is AISI 1018.

There are many process parameters in DED AM that affect the quality of the final product (Table 3-2). These parameters should be set appropriately to produce a product with acceptable quality. Based on experience, the laser power starts with 900 Watts for the first layer and decreases to 700 Watts for the rest when building the different case study samples. The high power of the first layer ensures a better bond of the first layer to the substrate. Since the substrate is at room temperature (20°C) at the beginning of the process, its large volume dissipates the laser power. Consequently, higher laser power is needed at the beginning to melt the surface of the substrate. Then, power can be decreased for subsequent layers because the deposition area is heated enough. Developing control strategies for AM processes is an ongoing area of research, and new rules are being developed continuously.

Table 3-1. Mechanical properties of stainless steel-grade 410 [124]

	Chemical composition (weight %)	Density (kg. m^{-3})	Yield strength (MPa)	Ultimate strength (MPa)	Hardness		Powder specification	
					Rockwell (HRB)	Vickers (HV)	Powder size (μm)	Density (kg. m^{-3})
410 SS	Fe- Cr (12.5)- Mn (1)- Si (1)- C (0.15)- Ni (0.75)-P (0.04)-S (0.03)	7800	275-825	450-825	95	217	53-150	4260
Low carbon 1018	Fe- Mn (0.6)- P (0.04)- C (0.15)- S (0.05)	7870	370	440	71	131	N/A	N/A

Table 3-2. Process parameters of direct energy deposition additive manufacturing (*) for 0.3 mm slice height (**) for 0.5 mm slice height

Input Parameter	Value	Explanation
Power (W)	900-700	The material, size and shape of the powder
Travel speed (mm/min)	500	The relative speed between nozzle and table
Powder feed rate (g/min)	15 *-20 **	The volumetric feed rate of the powder
Contact tip to work piece distance	12mm	The distance between powder converge point and the substrate surface
Surface normal to laser angle	90 degrees	The angle between laser beam and substrate
Shielding gas type	Argon	The shielding gas is an inert gas
Shielding gas flow (liter/min)	19	The volumetric feed rate of inert gas
Laser spot shape, heat profile	Circle, Gaussian	
Laser spot size (mm)	2	This determines the energy concentration in mel pool
Focal length (mm)	400	The length form nozzle tip that laser converges

The samples were manufactured by the Lincoln Laser Solutions Company, utilizing a 5-axis direct energy deposition machine. The mentioned machine has one translational movement (Z-axis) provided from the head in addition to 2 translational (X, Y axes) and 2 rotational movements (A, B axes) provided by the table (Figure 3-23). In this machine, the substrate is installed on a chuck mounted on the A-axis. For this reason, a substrate is designed and machined that has a round bar at one end and a flat surface at the other (Figure 3-24). The round side will be clamped in the chuck while the domes are fabricated onto the flat section.

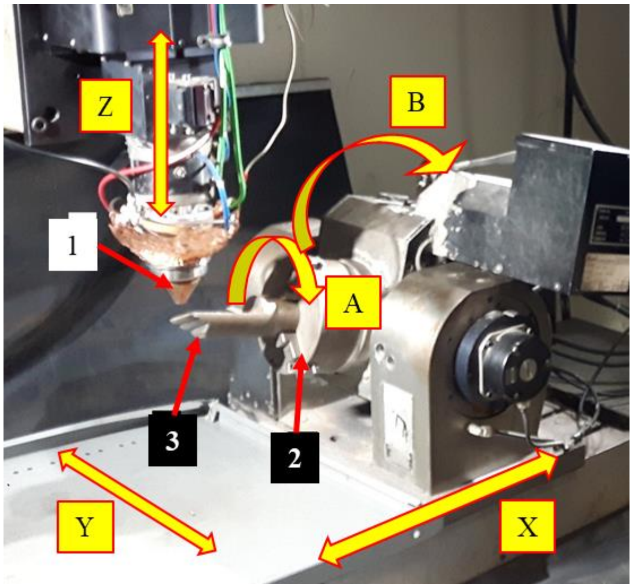

Figure 3-23. Utilized DED machine to manufacture samples (1) nozzle (2) chuck (3) installed substrate

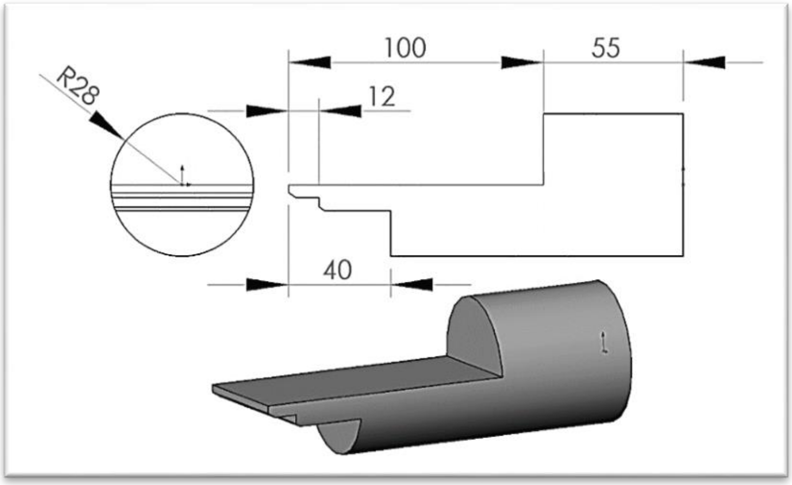

Figure 3-24. Round substrate (all dimensions in mm)

3.4 *Microhardness Measurements*

In order to investigate the mechanical properties of the samples, their microhardness is measured experimentally. Other mechanical properties such as ultimate strength can be calculated from the hardness values [125], [126] and this data is used to verify the outcome of the numerical analysis.

In this research, the Vickers hardness (HV) technique is used to measure the hardness. The HV is obtained by applying a force on a Vickers indenter onto the surface of the specimen. The HV indenter is a square-based pyramidal-shaped diamond with face angles of 136°. After the indenter is loaded onto the workpiece surface, it produces a diamond shape track on the surface (Figure 3-25). The load range that machines usually provide is from 1 to 1000 gram force (gf). The load should be exerted on the surface for a specific time which is set to 12 seconds here. The indentation diagonals are measured with a light microscope after the load is removed. All measurements of the current research are performed based on the ASTM E384-17 standard. The HV number is calculated by dividing the load by the surface area of the permanent impression made by the indenter.

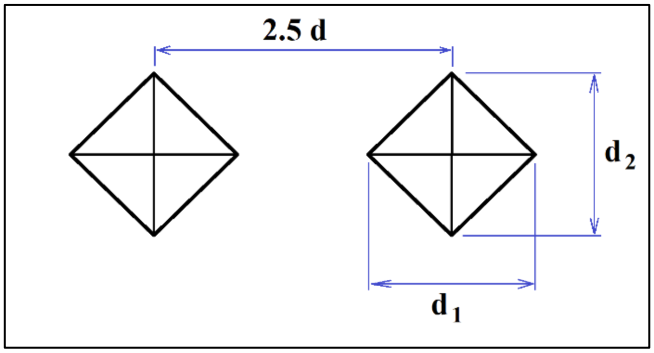

Figure 3-25. Vickers hardness indentation and minimum allowed distance between two indentations

The surface area can be calculated based on the mean of two diagonals. The resultant formula is:

$$HK = 1854.4 \times \left(\frac{F}{{d_{ave}}^{2}}\right) \tag{4}$$

$$d_{ave} = \frac{d_1 + d_2}{2} \tag{5}$$

F = load in gram force (gf)

d_{ave} = mean of two diagonals d_1, d_2

Some notes are from the ASTM E384-17 standard test for micro indentation hardness [127]:

- The distance between two indentations should be at least 2.5 times the mean diagonal of indentation. If the distance is smaller, the second indentation changes the dimensions of the first one.
- For forces larger than 25 gf, the Vickers micro-hardness numbers statistically match the Vickers macro-hardness numbers.
- Since etching changes the mechanical properties of the surface, the specimen surface should not be etched before making the indentation.

The required sequence of operations to measure the microhardness is shown in Figure 3-26. It starts with the sample preparation. In this regard, if the inside body of the sample is required to be measured, the sample should be cut.

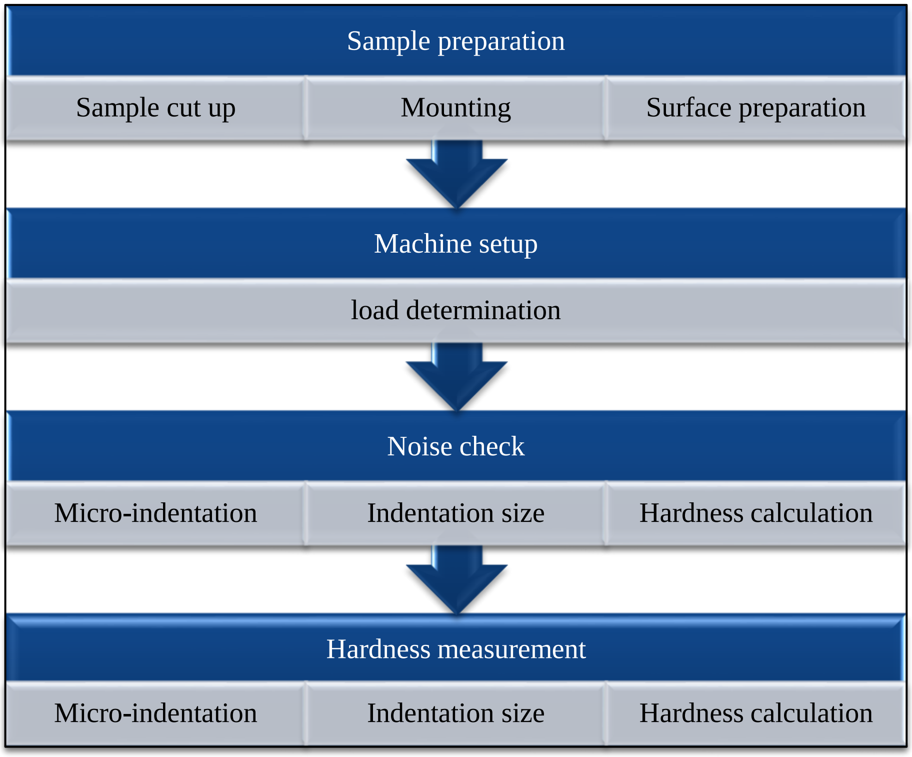
Sample preparation
Sample cut up
Mounting
Surface preparation
Machine setup
load determination
Noise check
Micro-indentation
Indentation size
Hardness calculation
Hardness measurement
Micro-indentation
Indentation size
Hardness calculation

Figure 3-26. Process flow of micro hardness measurement

3.4.1 Sample Preparation

The cut line should be near the inspection location. Any technique that can cut the metal is applicable such as electro-discharge machining (EDM) wire cut, band saw, cutting wheel, etc. The cutting heat needs to be minimized because the generated heat affects the hardness and mechanical properties. The heat-affected zone is trivial in EDM wire cut, it can be removed by a fine grinding operation.

Mounting the cut part makes it easier to hold it during grinding and hardness measurement. Sufficient grinding and polishing removes the cutting HAZ as well as it makes a mirror surface finish and consequently more accurate indentation measurement. Grinding papers MetLab P400, P800, P1200, P1500, P4000 as well as an alumina polishing suspension (size 3 and 1 μm) are used to achieve a mirror-like surface finish.

Figure 3-27 shows the cut line of the 5-axis sample on the model (Figure 3-27 (a)) and on the fabricated sample (Figure 3-27 (b)). The cut line is perpendicular to all slicing planes and passes through the middle of the dome. The partitions 1 and 2 are dismissed but partitions 3 and 4 are mounted for further surface roughness and hardness investigations (Figure 3-28).

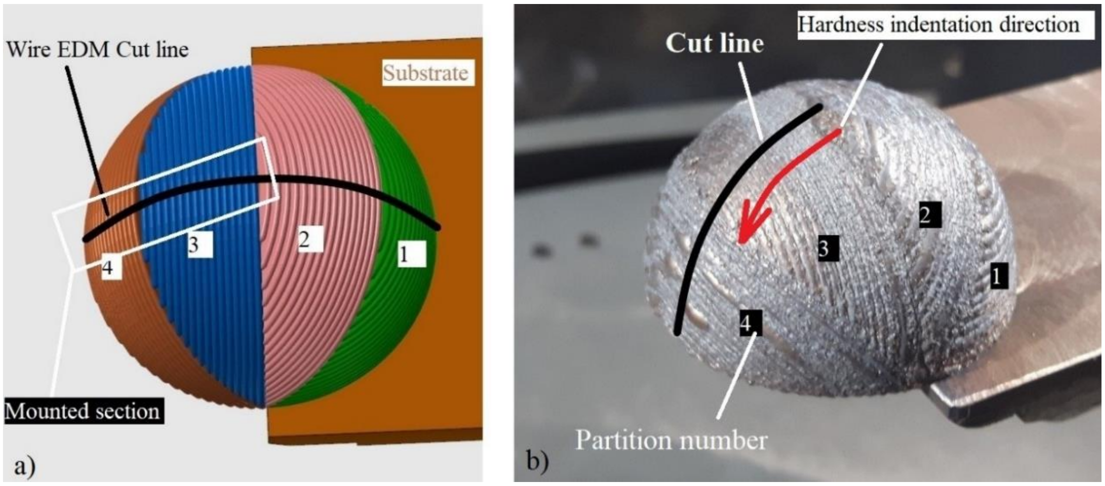

Figure 3-27. Wire EDM cut line and indentation direction for 5-axis sample

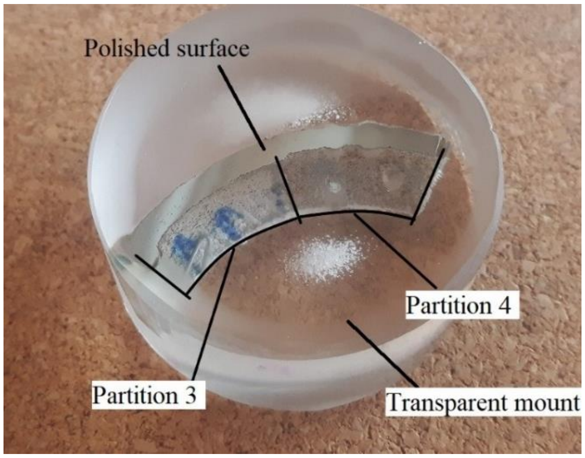
Polished surface
Partition 4
Partition 3
Transparent mount

Figure 3-28. Mounted specimen of partitions 3 and 4

Figure 3-29 shows the cut line of 2+1+1-axis sample. The cut line is perpendicular to all slicing planes and passes through the middle of the dome.

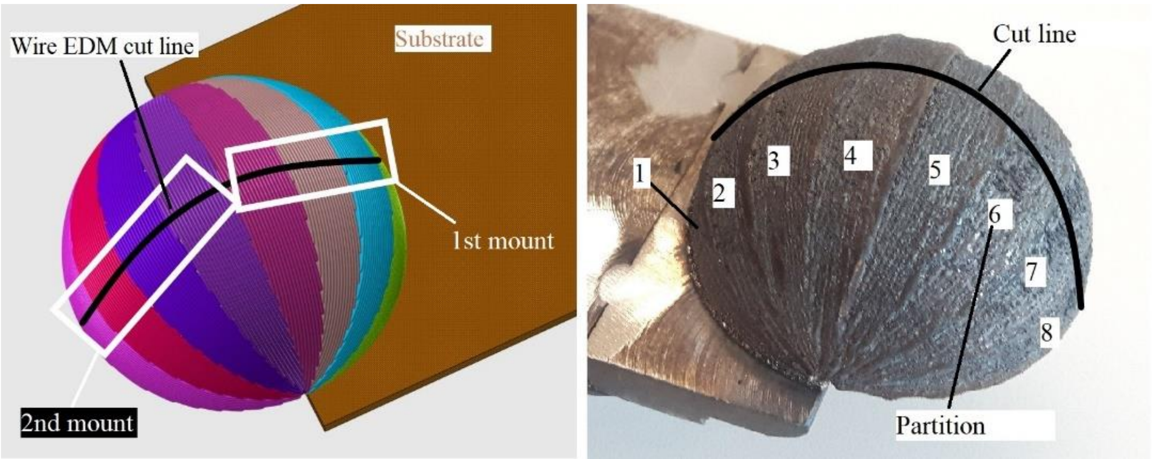
Wire EDM cut line
Substrate
1st mount
2nd mount
Cut line
1
2
3
4
5
6
7
8
Partition

Figure 3-29. Cut line for 2+1+1 axis sample

Since the diameter of mount is limited to 37 mm and cannot encase all partitions into one, two mounted samples are prepared for this case.

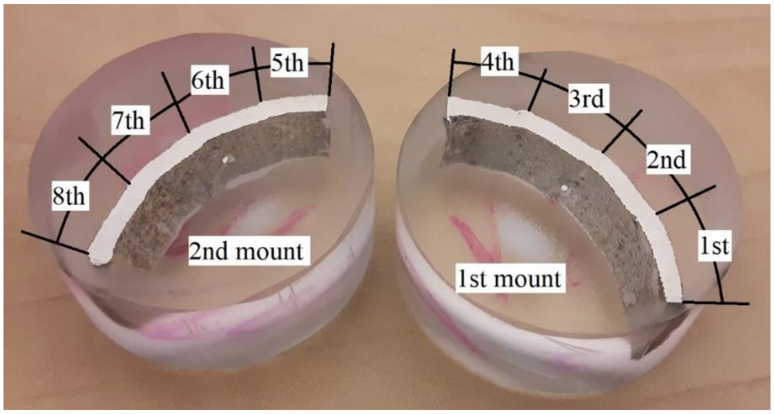
5th
6th
7th
8th
4th
3rd
2nd
1st
2nd mount
1st mount

Figure 3-30. Two mounts of 2+1+1 axis specimen

To measure hardness of the rotary sample, the part is cut through the cut-line as shown in Figure 3-31. Hardness measurements are not performed on the round bar section. Since the whole cut part cannot be mounted as a single specimen, it was cut into three smaller sections (Figure 3-31 (b)). Specimen 1 is mounted for further hardness measurements (Figure 3-32)

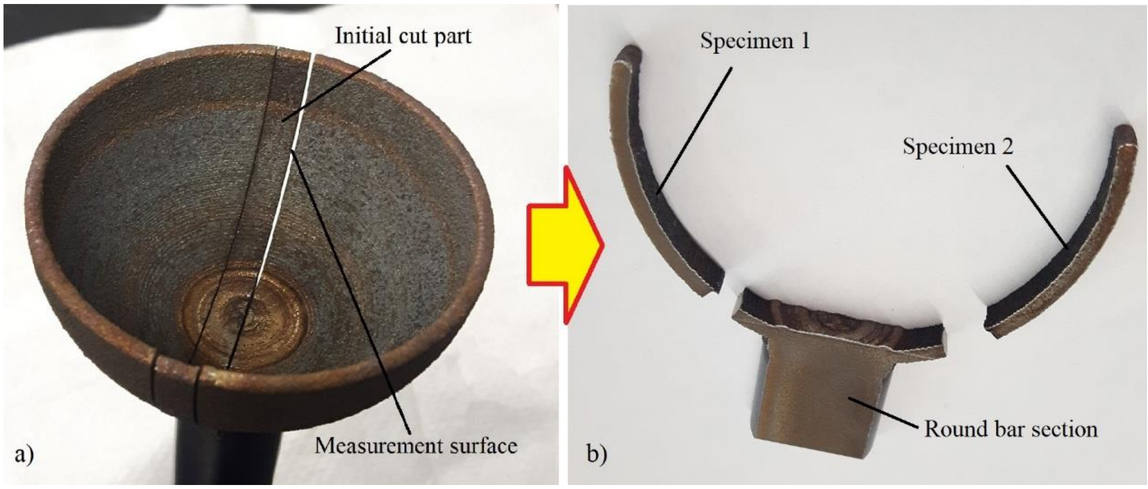
Initial cut part
Measurement surface
a)
Specimen 1
Specimen 2
Round bar section
b)

Figure 3-31. (a) Cut line (b) The specimen is cut into three smaller specimens

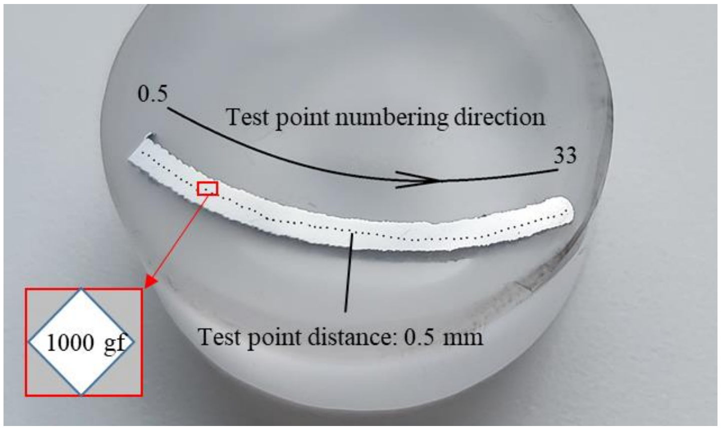

Figure 3-32. Hardness indentations on of rotary sample mount

3.4.2 *Proper Load Determination*

Micro-hardness measurement machines provide a variety of loads: 10, 25, 50, 100, 200, 300, 500, and 1000 gf. The proper load needs to be selected to have the most accurate HV results. Two methods are applied in this research to find the proper load:

- Hardness sensitivity to diagonal variation of the indentations.
- Image quality and the maximum magnification of the microscope.

Hardness sensitivity test can be performed by making a set of indentations by using all loads that are provided with a micro-hardness test machine. Figure 3-33 shows an experiment in which 3 sets of indentations are made by all the provided loads. This experiment is implemented for partition 5 of the 2+1+1-sample. Three indentations for every available load was made on a small region of the sample. This is assumed that the material hardness in this region is uniform. The mean diagonals of these indentations are measured. As there are 3 indentations for each load, the average of these mean diagonals was measured (Table 3-3). For example, the average mean diagonal of three indentations of 10 gf is 7.6 μm.

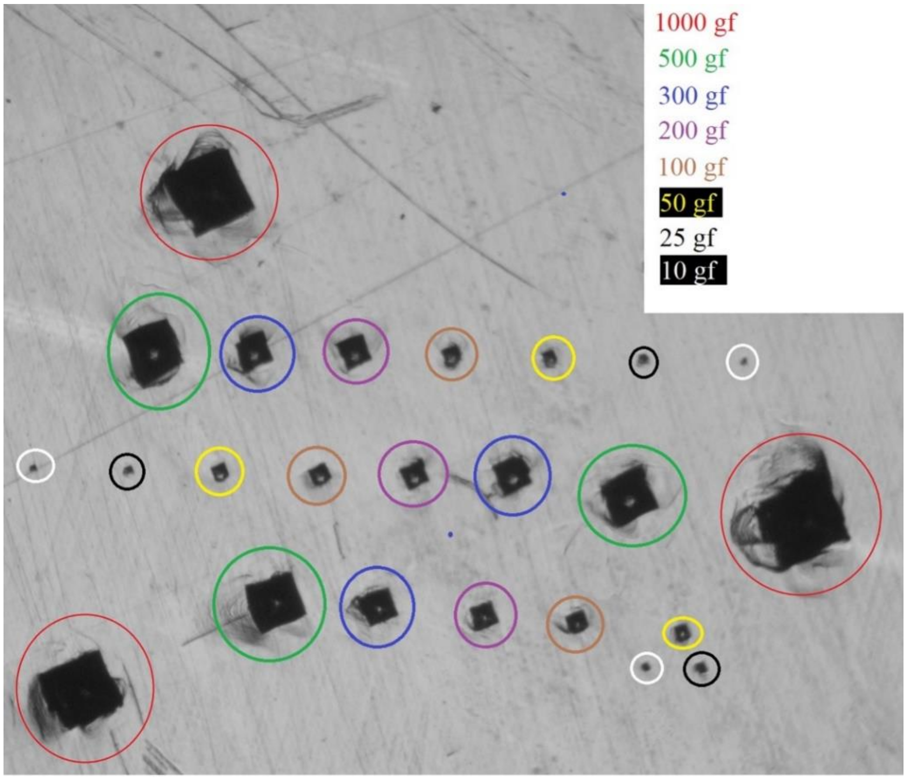

Figure 3-33. Three indentations of all available load options (The same load indentations are encased with the same color circle).

Table 3-3. Average of mean diagonal of 3 indentations for each load

Load (gf)	Mean diagonal values (µm)	Mean diagonal average (µm)
10	7.3, 8.8, 6.5	7.6
25	10, 9.7, 10	9.9
50	21, 21.5, 18.3	20.3
100	27.5, 26, 25	26.2
200	34.5, 36.3, 40	37.3
300	45.3, 46.5, 47.3	46.3
500	71.3, 68.5, 72.2	70.7
1000	99, 95.5, 94	96.2

Based on measured mean diagonal and applied load, there is a standard set of graphs to help find the proper load [127]. These graphs are drawn from Equation (4). Each curve represents the equation for a load. These graphs (Figure 3-34) demonstrate the relationship between HV numbers and the mean diagonal values for different loads. The average mean diagonals from Table 3-3 are represented by vertical lines and their junctions to respective load are shown by a star. For smaller loads, the junction point is at the high slope section of the curve. In this case, by a small mismeasurement of the diagonal length, the calculated hardness changes a lot. Therefore, it is better to use the loads that resultant diagonal lengths position at a low slope of the curves. As it is apparent from the figure, at higher loads, the measured HV values have less sensitivity from mismeasurements of the diagonal.

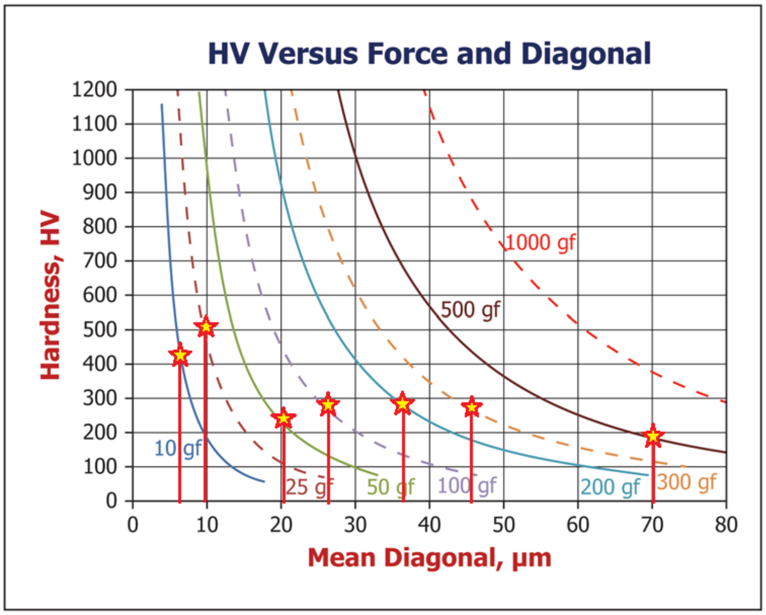

Figure 3-34. Calculated graphs showing relationship between diagonal and load [127]. The test values are also showed by vertical lines

Additionally, another issue makes HV readings from smaller loads more inaccurate. The issue is that indentation sizes of lower loads are very small. This needs a very powerful microscope to capture sharp pictures of indentations. It is crucial in measuring their diagonal lengths because if the pictures are not of good quality the measurements are not accurate. Magnification of 750 works well for larger loads whereas the indentation picture is very small for loads of 10 and 25 gf. As a result, a magnification of 1500 is tested for pictures of small loads. The result was a dim picture that made it even worse to measure the diagonals accurately. So loads less than 100 gf were excluded. Figure 3-35 compares a 25 gf indentation measured at 1500 magnification (Figure 3-35 (a)) and 750 magnification (Figure 3-35 (b)) besides a 500 gf indentation at 750 magnification (Figure 3-35(c)).

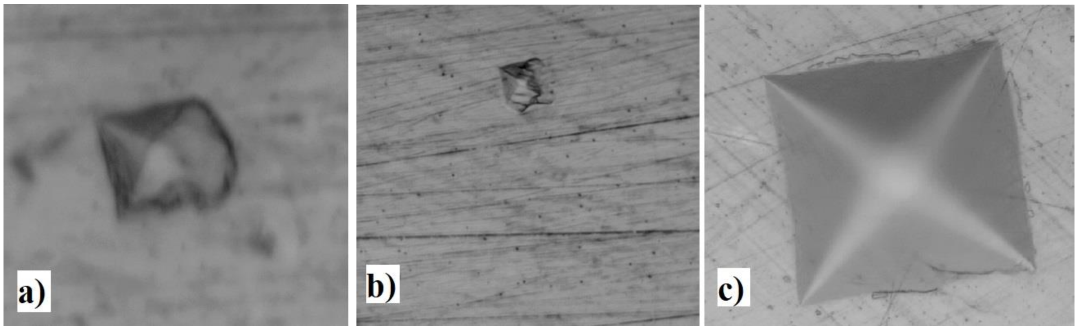

Figure 3-35. Comparison of indentations made by (a) 25 gf at 1500 magnification (b) 25 gf at 750 magnification (c)500 gf at 750 magnification

Based on what is mentioned in reference [127], the residual deformation from mechanical polishing must be removed especially if the indentation load is less than 200 gf. This makes the preparation of samples very critical. This was another important reason to avoid the forces less than 200 gf.

Moreover, small values of load are suitable for hardness measurement cases such as very small workpieces which would be destroyed by application of a large load, measurement of thin samples like foils or wires, the hardness of a surface coating and hardness inside a phase such as pearlite or ferrite phases [128]. However, samples of this research are not categorized in any of these cases; accordingly, they do not need small loads. In this research, microhardness indentation is accomplished by means of Buehler Micromet II machine at 300 and 1000 gf load. The ImageJ-FIJI software was applied to measure indentation diagonals that were prepared by microscope Omax A3580U.

3.5 *Surface Roughness Measurement*

Two characteristics of the fabricated domes questioned the applicability of ordinary roughness measurement techniques first, the geometry of the surface geometry is curved and second, the surface roughness is higher than the measurement limitations for ordinary systems. Although some common techniques were tried for these samples, they were not helpful in providing a reliable roughness value. Therefore, two innovative techniques are developed to extract roughness values of the domes from mount samples and from 3D point cloud.

3.5.1 Standard Measurement Techniques

Two available standard techniques, tactile-based roughness tester and interferometric microscope, were attempted to measure the roughness of the samples. Despite having two common roughness measurement systems available, they were not applicable because of their limitations.The tactile-based system could not measure the dome samples properly because the stylus did not penetrate the deep valleys of the surface. The reason is that target surfaces are rougher than the length of the stylus. Furthermore, the logic of these systems is based on measuring a flat surface.

Measuring the roughness utilizing an interferometric microscope was also attempted. Interferometry works based on interference fringe generation followed by amplitude division and recombination of light from the same light source [129]. The measurement results for the domes are too dim to be able to extract any surface roughness value. The domes are rougher than the maximum detectable roughness of this system.

Finding a specific solution to measure the roughness of curved surfaces fabricated by AM is another motivation for developing new solutions. Since the exposed edges of samples in the mounts shows all the surface texture details under the microscope, the magnified picture of the edges can be used to calculate the roughness. Also, the 3D scanning can provide the surface point cloud that is used in surface roughness measurement.

3.5.2 Roughness Calculation from Points on Mounted Sample

After the sample is mounted, ground and polished, its detailed surface characteristics are clearly exposed (Figure 3-36). Even very tiny details of the edge roughness are visible under a microscope. A magnified picture of the surface edge contains sufficient information to extract all surface textures of the exposed edges. To measure the roughness of the surface in several locations, the mount sample can be prepared accordingly.

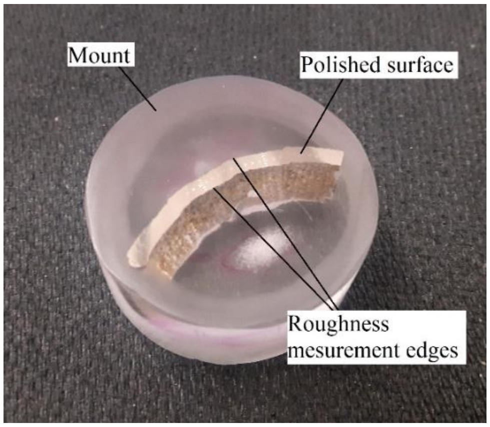
Mount
Polished surface
Roughness
mesurement edges

Figure 3-36. Roughness measurement edges in mount

The measurement process starts with taking pictures of the surface edge using a 750 magnification. As Figure 3-37 shows, since the observation area of the microscope does not cover the whole surface of the sample in one frame, photos of small sections of the sample edge need to be merged to create a single picture to represent the whole edge. The picture is scaled properly within CAD software (Solidworks) to make the dimensions equivalent to the real part. The scaling is based on matching the distance of two specific points in the CAD software with what is measured experimentally on the real surface. As Figure 3-38 shows, the distance between the two corners of the sample is matched.

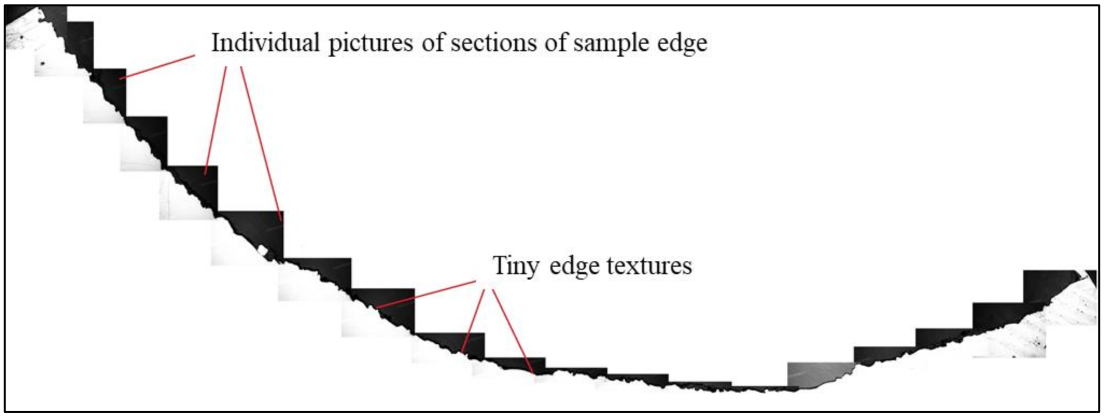
Individual pictures of sections of sample edge
Tiny edge textures

Figure 3-37. Merged pictures of the edge of the sample

The flow chart for the Matlab program is shown in Figure 3-39. The significant technique in this program is that roughness is calculated from projected points onto polar lines. The flow chart is divided into major steps that are explained here.

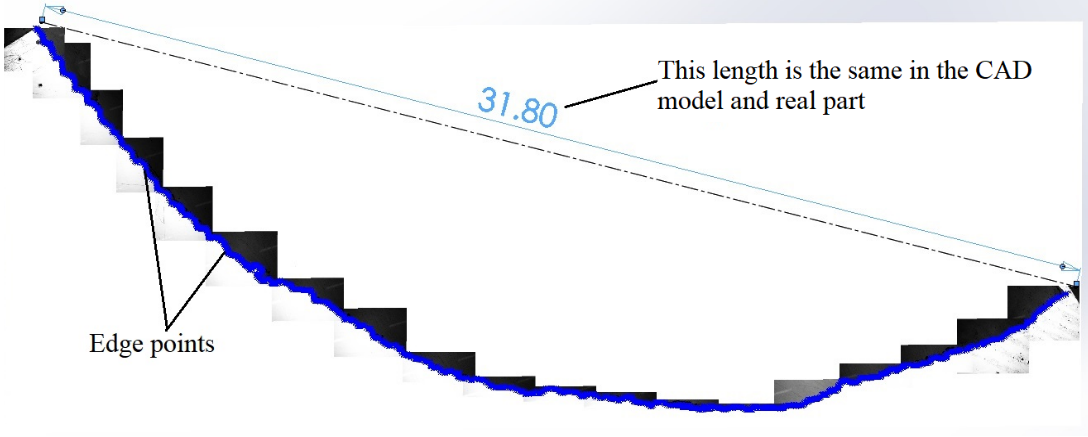
31.80
This length is the same in the CAD model and real part
Edge points

Figure 3-38. Scale of the edge pictures plus the sketch points.

The first step is manually creating sketch points on the surface edge. However, these points in the Solidworks file should be converted to a *.txt file that contains point coordinates. The file is applied in the prepared Matlab program to calculate the Ra. Another txt file is needed that contains 3 points, two at both ends and one in the middle of the mount edge.

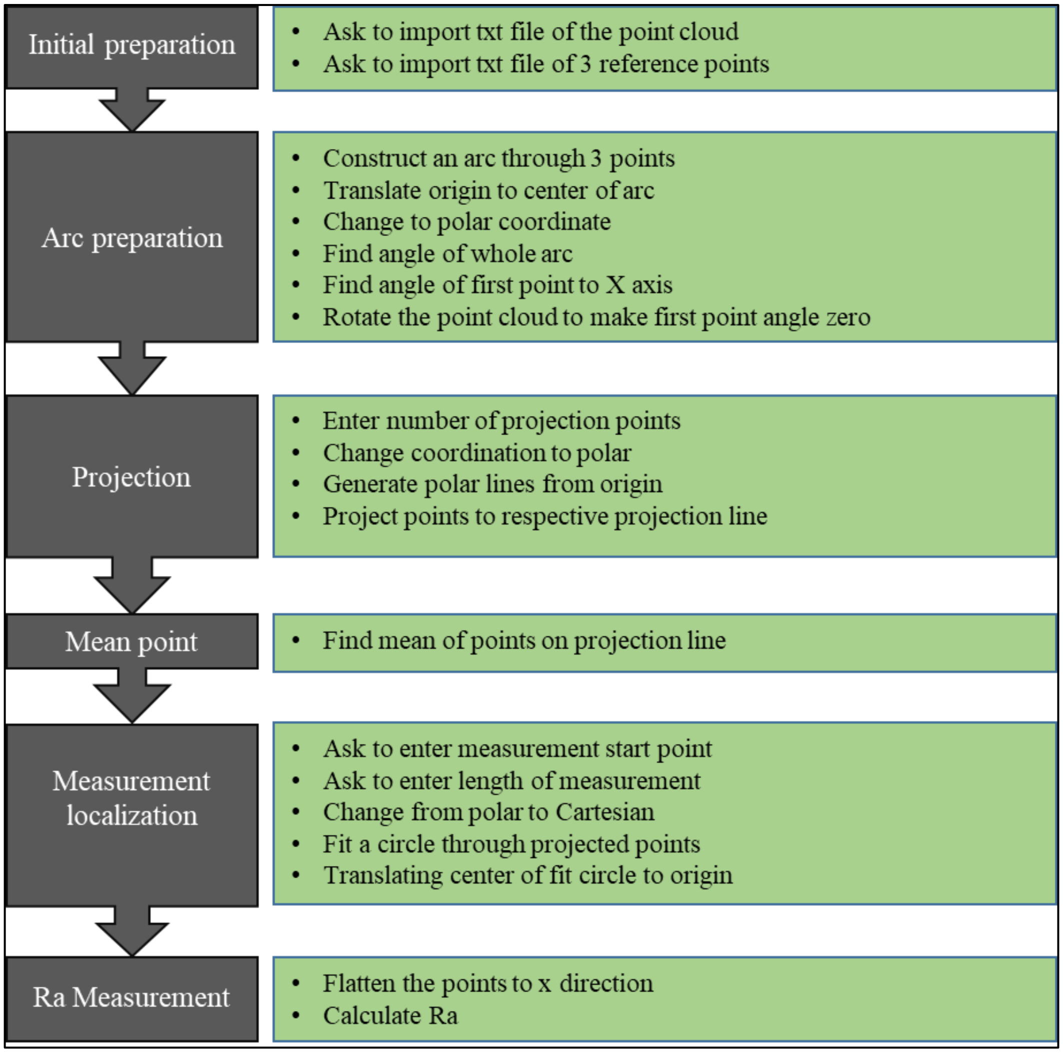
Initial preparation
Ask to import txt file of the point cloud
Ask to import txt file of 3 reference points
Arc preparation
Construct an arc through 3 points
Translate origin to center of arc
Change to polar coordinate
Find angle of whole arc
Find angle of first point to X axis
Rotate the point cloud to make first point angle zero
Projection
Enter number of projection points
Change coordination to polar
Generate polar lines from origin
Project points to respective projection line
Mean point
Find mean of points on projection line
Measurement localization
Ask to enter measurement start point
Ask to enter length of measurement
Change from polar to Cartesian
Fit a circle through projected points
Translating center of fit circle to origin
Ra Measurement
Flatten the points to x direction
Calculate Ra

Figure 3-39. Flow chart used in Matlab program which measures surface roughness from a set of points at the edge of mount sample

The program starts by asking to upload these two txt files. After the txt files are loaded, an arc is best-fit on the points. Then the center of the arc translates and rotates to the origin to make further calculations easier (Figure 3-40).

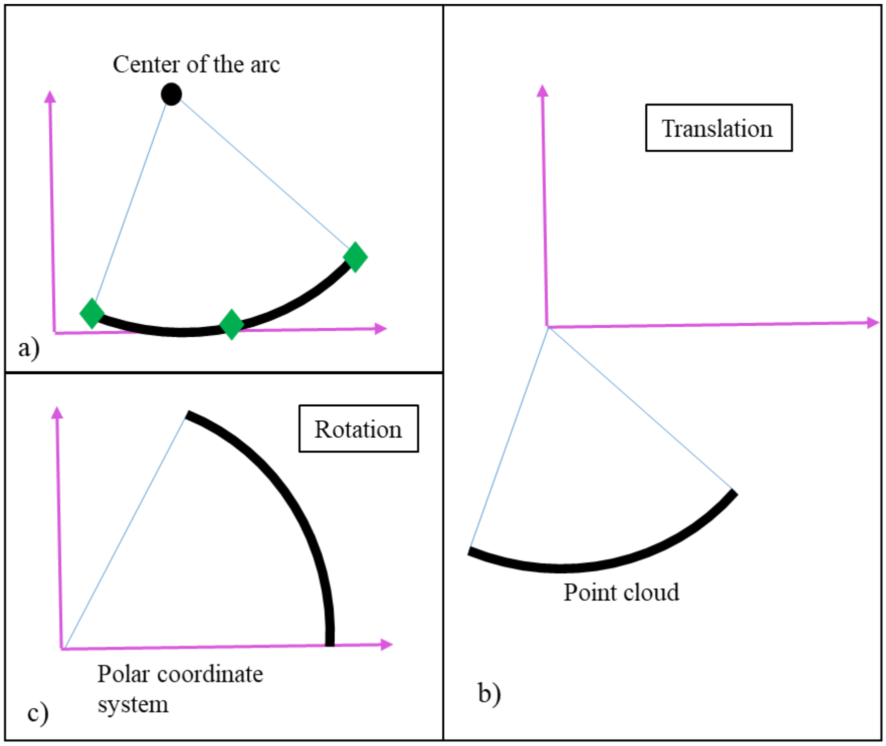

Figure 3-40. (a) Initial points and the center of constructed arc. (b) Translated points. (c) Rotation

The point coordinates convert to the polar system in which the center of the polar coordinate system is the origin. In the next step, the number of projection lines is entered as an input. Then, all points project on projection lines. The logic is projecting each point to the respective nearest line.

Several points are projected on each projection line that needs to be substituted with just one point. The location of the mean point is calculated from Equation (6). Therefore, the program finds the mean of projected points on each line (Figure 3-41). After this step, there is maximum one point on each projection line.

$$R = \frac{1}{n_p} \sum_{1}^{n_p} R_p \tag{6}$$

The distances from the origin to the mean point and projected points are R and R_p, respectively. The n_p represents the number of points on a projection line.

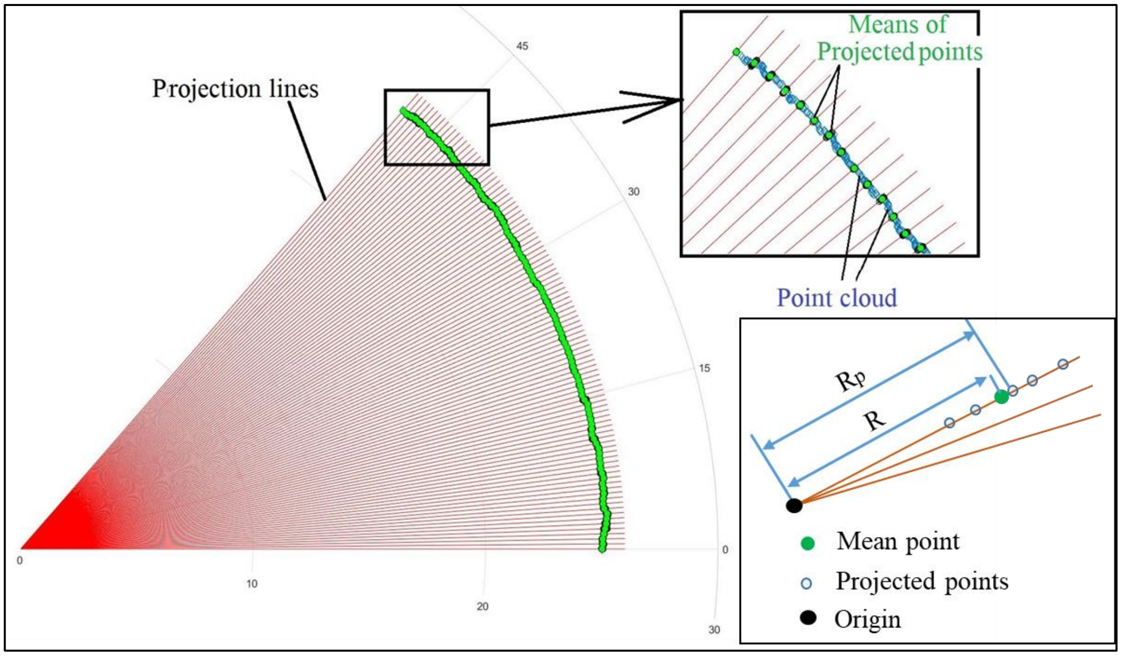
Projection lines
Means of Projected points
Point cloud
45
30
15
0
0
10
20
30
Rp
R
Mean point
Projected points
Origin

Figure 3-41. Polar projection lines and mean points

In this research, it is needed to measure the roughness for a small section of the sample in order to study how it changes in different locations. To reach this goal, the starting point and length of the region that needs to be measured needs to be entered (Figure 3-42).

After the mean points for the measurement region are isolated, a new arc is best-fit through them. The reason for this operation is eliminating macro noise such as waviness. Figure 3-42 illustrates why this stage is needed. As the figure shows, the general fitted arc is not appropriate for the measurement region which has a lifted texture. If the same center of the general fitted arc is used for regional roughness measurement, the result would be incorrect.

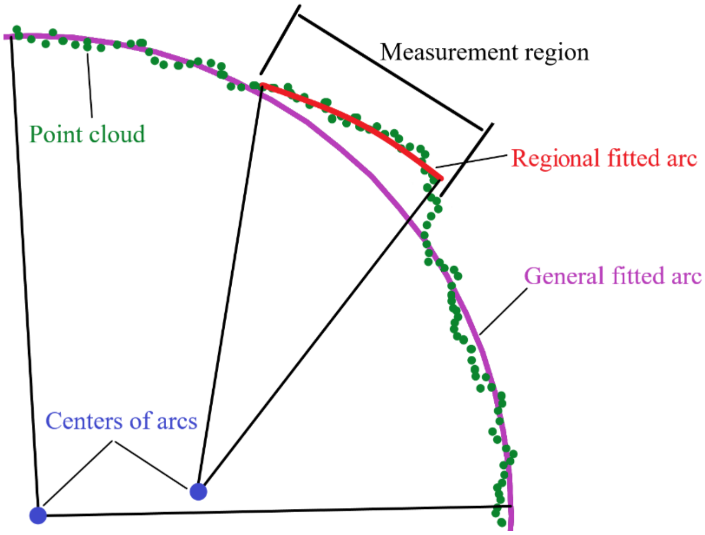
Measurement region
Point cloud
Regional fitted arc
General fitted arc
Centers of arcs

Figure 3-42. Best-fitting a new arc through points of measurement region

Now, everything is ready to flatten the points and to perform the roughness calculation. Figure 3-43 shows the flattening method.

‘α' (radian) is the angle between projection lines, ‘R_m’ is the radius of the arc that is fitted through measurement region points, ‘R’ represents the distances of mean points to origin, ‘L_1’ is the length of best-fitted arc between two adjacent projection lines, ‘L’ is the length of the measurement region, and ‘n_n’ is the number of projection lines in the measurement region.

$$L_1 = R_m \times \alpha \tag{7}$$

$$L = L_1 \times n_n \tag{8}$$

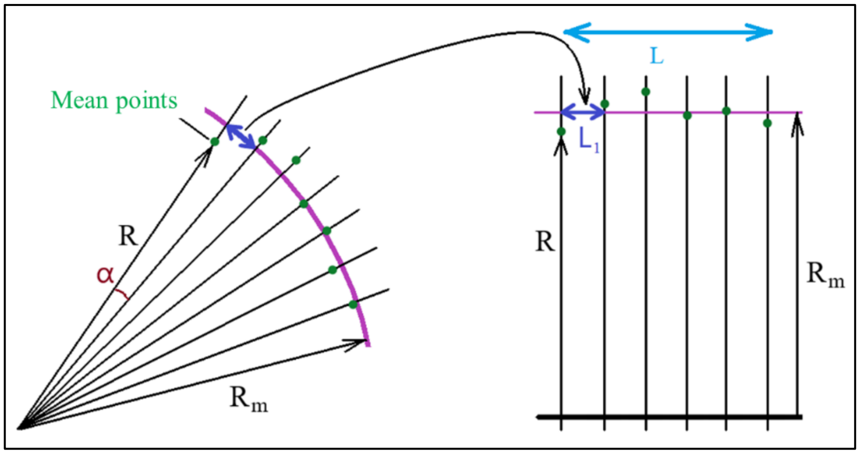
Mean points
R
α
Rm
L
L1
R
Rm

Figure 3-43. Flattening of points for further roughness calculations

The flattened points can be applied to the Ra calculation formula for the flat surfaces. The surface roughness equation (Ra) is:

$$m = \frac{1}{L}\int_0^L R\,dx \tag{9}$$

$$Ra = \frac{1}{L}\int_0^L |R - m| dx \tag{10}$$

'R' is the variable in Equation (9) because it is the height of points from the reference line. In this case, the reference line is the X-axis. In Equation (10), the 'm' value determines the height of the mean line from the reference line. The area between the surface profile and the mean line above the line is equal to that below it [130]. The mean line besides the area between the surface profile and the mean line are shown in Figure 3-44.

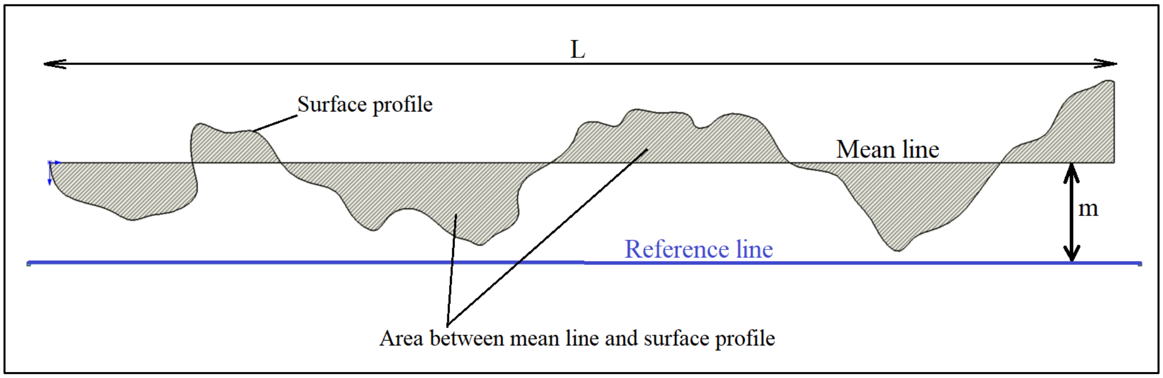

Figure 3-44. Illustration of area between mean line and surface profile

The initial experiments that were performed by the contact measurement technique (explained in Section 3.5.1) provided an Excel graph of the surface texture besides the Ra value. This data set is applied to validate the program in the results chapter.

3.5.3 Surface Roughness Measurement from 3D Point Cloud

Because the surface is curved, a technique is needed to generate initial data from the surface textures. The 3D scanning technology provides a huge number of points from the surface of the part. The main issue is converting the point cloud to a roughness value for any arbitrary region of the surface. In this section, the proposed solution of roughness evaluation from the provided 3D point cloud is explained.

Here, a Matlab program is developed to extract directional Ra from the 3D point cloud. Two txt files are needed as input data, point-cloud txt file, and the txt file of reference points. In the point cloud txt file, each line contains 3 components of 3D point coordinates separated by a Tab character. The reference-points file contains coordinates of 3 reference points. Reference points define the location of the reference plane. The Matlab program measures the roughness at the intersection of the reference plane and the measurement surface. As Figure 3-45 shows, after the point cloud file is opened in a CAD software (here Solidworks), based on the location and direction of the measurement region, the reference plane is created. One of the reference points needs to be at one end of the point cloud to be a reference for rotation of the point cloud (rotation reference point) at later stages. The second point is approximately at the middle of the arc and the third point is at the end of the arc (Figure 3-45 (b)).

The point cloud needs to be filtered before being used in the Matlab program. Since this technique measures the surface roughness at an intersection, the farther points from the intersection need to be deleted. Although the current program can extract the roughness value correctly without filtering, removing the points far from the measurement line enhances the run time of the program. Two planes on both sides of the reference plane determine the filtering boundary. The distance between two boundary planes is 'f ' which can be set by the user. So, as Figure 3-45 (b) shows, all points beyond these 2 planes will be deleted manually. The text file contains just the points between boundary planes. The dependency of roughness results with the distance of 2 boundary planes will be inspected in the result chapter.

Figure 3-46 shows the process flow of the prepared Matlab program. The flow chart is divided into seven steps. The starred steps (*) are the same as mount solution steps. The main difference between this solution and the mount one is how projected points on projection lines are substituted by one point.

First, the program asks the user to import the point cloud and reference-points txt files. It calculates the equation of the reference plane. A plane is defined by a point and normal vector, so, the reference plane is defined by a rotation reference point (Figure 3-45 (b)) and the normal vector of the plane.

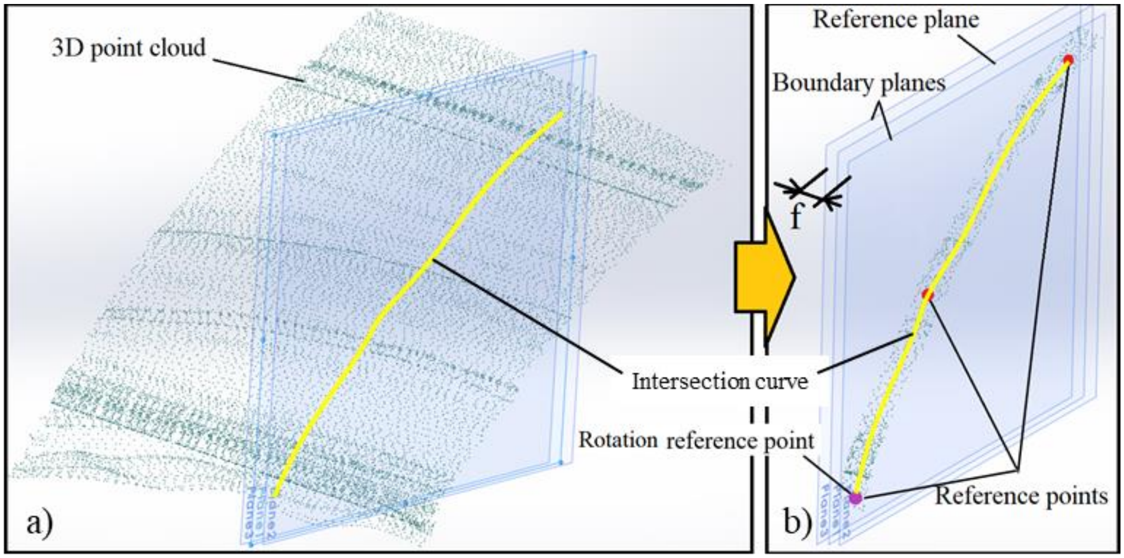
3D point cloud
Intersection curve
Rotation reference point
Reference plane
Boundary planes
f
Reference points
a)
b)

Figure 3-45. Removing points that are far from measurement line. Reference points on reference plane

The reference plane can be positioned anywhere in the 3D space. Hence, as Figure 3-47 shows, the filtered 3D point cloud is located in the 3D space. To make the next calculations easier, it is better to rotate and overlay the point cloud on the XY plane. The vectors from the rotation reference point to second and third reference points are named V1 and V2, respectively. The reference plane is defined by a point on the surface (rotation reference point) and normal vector (N). N is the cross product of V1 and V2 (Equation (11)).

$$N = \overrightarrow{V1} \times \overrightarrow{V2} \tag{11}$$

The normal vector, N, and V1 are used to define the unit coordinate system components on the reference plane (Xr,Yr,Zr). Zr and Yr axes are the unit vectors of N and V1, respectively. Also, Xr is the cross product of Yr and Zr.

$$\overrightarrow{Zr} = \frac{\vec{N}}{|\vec{N}|} \tag{12}$$

$$\overrightarrow{Yr} = \frac{\overrightarrow{V1}}{|\overrightarrow{V1}|} \tag{13}$$

$$\overrightarrow{Xr} = \overrightarrow{Yr} \times \overrightarrow{Zr} \tag{14}$$

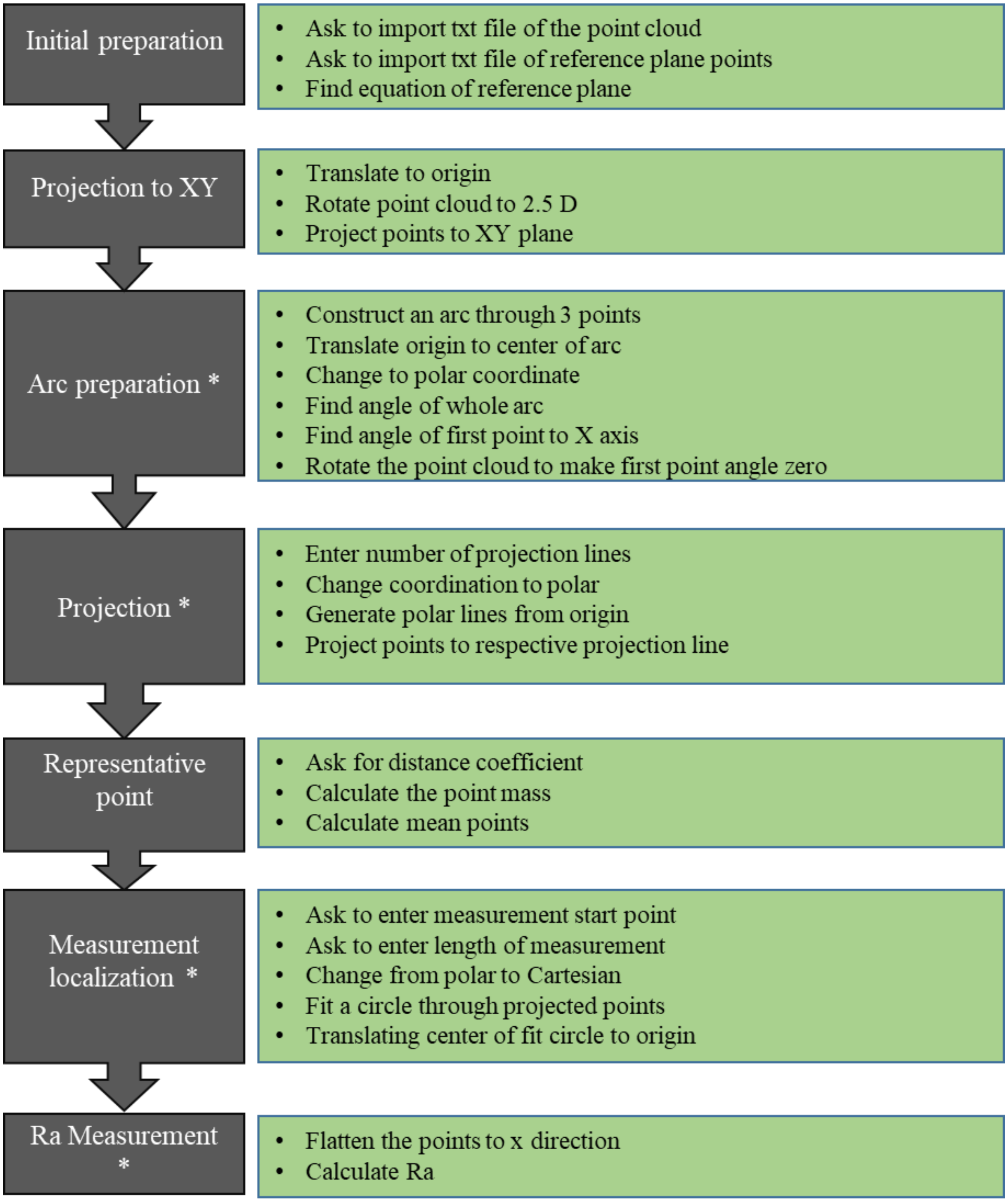
Initial preparation
Ask to import txt file of the point cloud
Ask to import txt file of reference plane points
Find equation of reference plane
Projection to XY
Translate to origin
Rotate point cloud to 2.5 D
Project points to XY plane
Arc preparation *
Construct an arc through 3 points
Translate origin to center of arc
Change to polar coordinate
Find angle of whole arc
Find angle of first point to X axis
Rotate the point cloud to make first point angle zero
Projection *
Enter number of projection lines
Change coordination to polar
Generate polar lines from origin
Project points to respective projection line
Representative point
Ask for distance coefficient
Calculate the point mass
Calculate mean points
Measurement localization *
Ask to enter measurement start point
Ask to enter length of measurement
Change from polar to Cartesian
Fit a circle through projected points
Translating center of fit circle to origin
Ra Measurement *
Flatten the points to x direction
Calculate Ra

Figure 3-46. Flow chart used in Matlab program which measures surface roughness from 3D point cloud. (*) same operations with mount solution

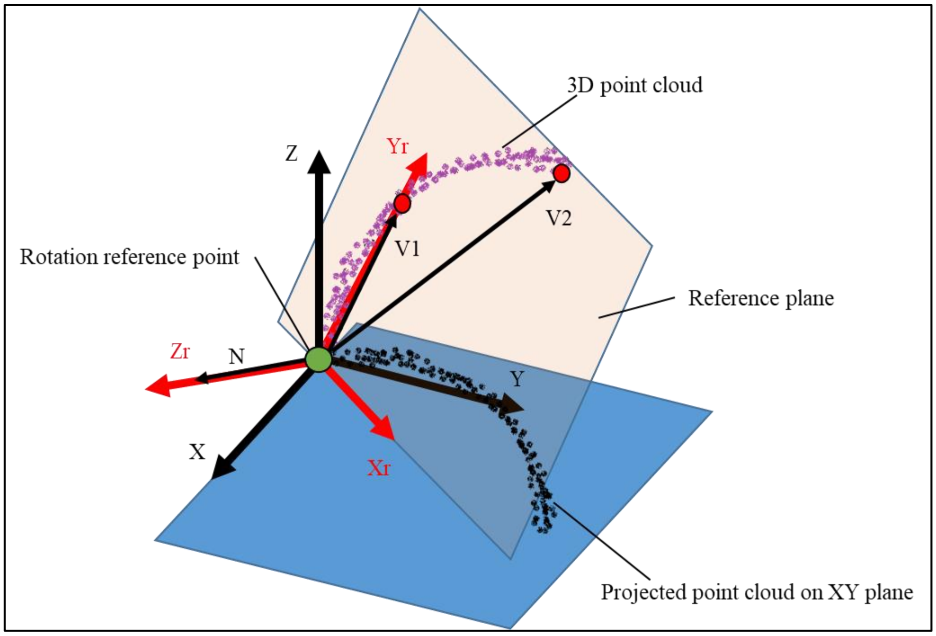
3D point cloud
Z
Yr
V2
V1
Rotation reference point
Reference plane
Zr
N
Y
X
Xr
Projected point cloud on XY plane

Figure 3-47. Rotation of point cloud to XY plane

The rotation of the point cloud to the XY plane is done using Equation (15). P_x, P_y, and P_z are the components of point coordinates before they are rotated, and i , j, and k are unit vectors of X, Y, Z axes, respectively. Rotated point coordinates are P_x', P_y', and P_z'.

$$\begin{bmatrix} P_x' \\ P_y' \\ P_z' \end{bmatrix} = \begin{bmatrix} i.Xr & j.Xr & k.Xr \\ i.Yr & j.Yr & k.Yr \\ i.Zr & j.Zr & k.Zr \end{bmatrix} \begin{bmatrix} P_x \\ P_y \\ P_z \end{bmatrix} \tag{15}$$

As Figure 3-48 shows the rotated points have a distance “d” from the XY plane. This value is very important for later steps so, points will be projected on the XY plane after this value is saved.

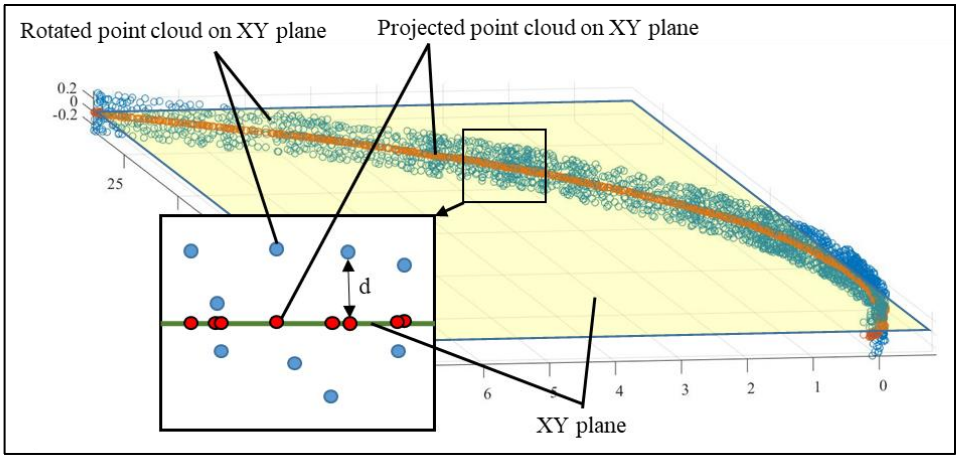

Figure 3-48. Rotated point cloud and its projection on XY plane

The arc preparation and projection processes that are marked with (*) in Figure 4-8 are similar to the same steps in the mount solution. Therefore, it is referred to as the same steps in mount method (Section 3.5.2).

After the point cloud is projected onto projection lines, they need to be replaced with one representative point on each line. In the mount solution, the mean point represented the projected points. However, in the 3D point cloud solution, it is not practical because each data point does not have an equal impact on the representative point's positioning.

As the input points are scattered in 3D space, they are not located exactly on the reference plane. Projecting close points can resolve the sparse data issue. Points near the reference plane can be used to increase the input data. If the points are very close to the reference plane, there is more probability they have the same height as the intersection curve (Figure 3-49).

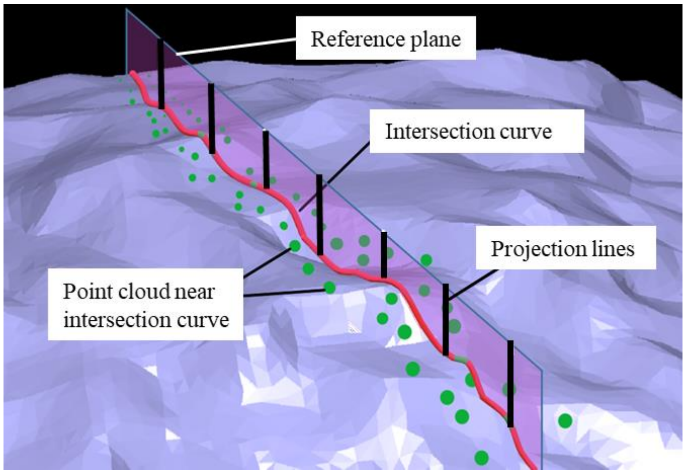

Figure 3-49. The intersection curve and nearby 3D points

A parameter is defined for each point called point weight "M" for measuring the arithmetic mean of the points on the projection line. The point weight is larger for the points that are nearer to the reference plane. Equation (16) calculates the weights of the points. The weight is the reciprocal of the distance of the point to the reference plane "d" to the power of "n". This "d" is the same as what is shown in Figure 3-48. Therefore, as Figure 3-50 illustrates, when there are some points on a projection line, the mean point approaches to the point that has the least distance to the reference plane.

$$M_i = \left(\frac{1}{d_i}\right)^n \tag{16}$$

$$H \times \sum M_i = \sum M_i h_i \tag{17}$$

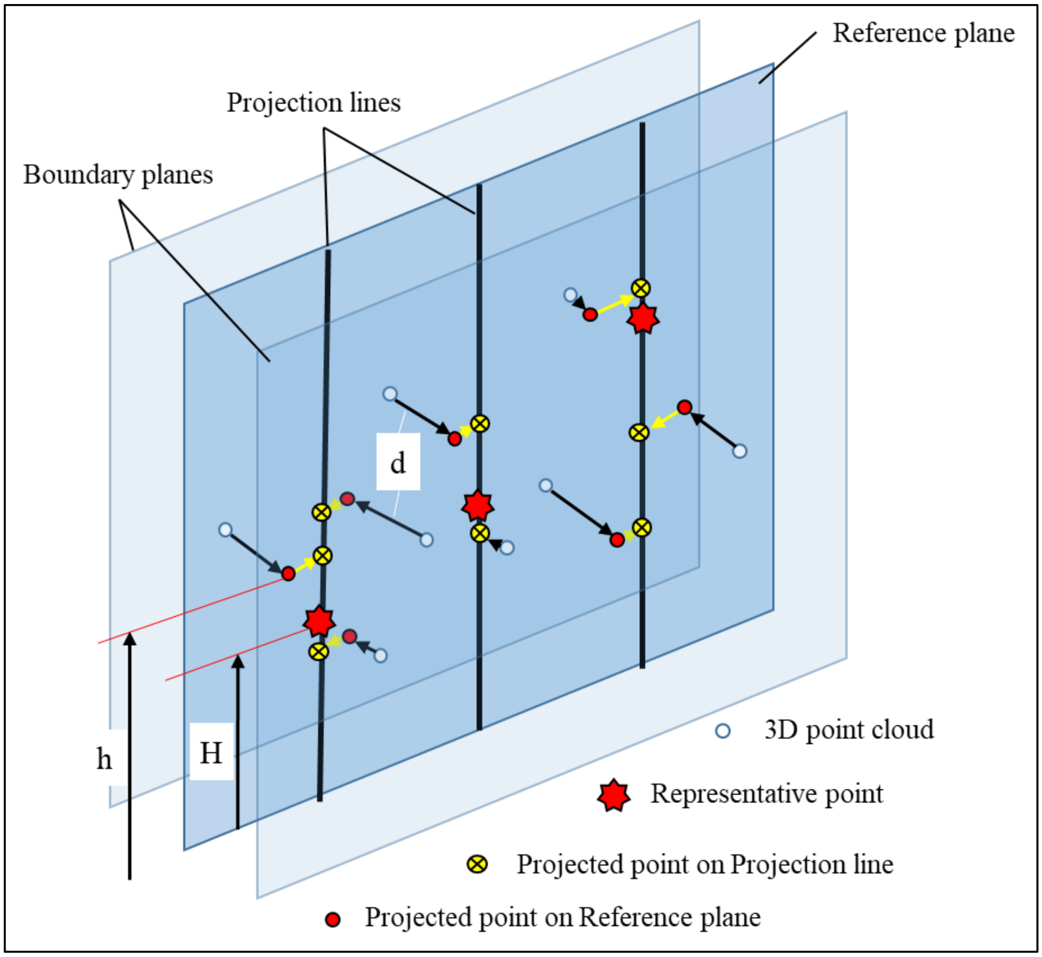
Reference plane
Projection lines
Boundary planes
d
h
H
○ 3D point cloud
Representative point
⊗ Projected point on Projection line
● Projected point on Reference plane

Figure 3-50. Illustration of finding the mean point based on the weight of the points

‘M_i’ is the point weight, ‘n’ is the distance coefficient, ‘d_i’ represents the distance of 3D points to the reference plane, ‘h_i’ is the distance of projected points on lines from the origin, and ‘H’ is the distance from the mean point to the origin.

The role of the distance coefficient “n” is to give the user control over the intensity of the point weight. As the value of ‘n’ increases the effect of farther points diminishes. The effect of changing ‘n’ in roughness result is studied in the results chapter. Figure 3-51 shows the process of projecting point cloud on projection lines and finding the representative point on each line for a test sample. After the representative points are found, the measurement localization and Ra measurement processes (marked with (*) in Figure 3-46) are the same as the last two operations for the mount based evaluation (Figure 3-39).

It is explained more in detail that these results are verified using the results for the mount solution for the same samples.

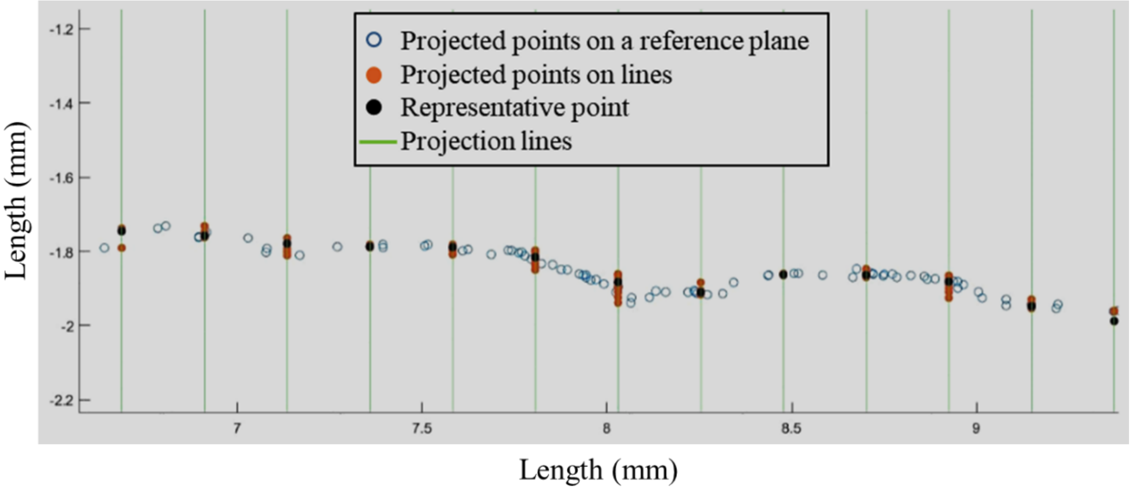

Figure 3-51. Projection of points to projection lines and finding the mean point on each line.

3.6 *FEA Simulation for the Hardness for 2+1+1-Axis Sample*

In order to simulate the hardness and other mechanical properties of the DED-built components, a finite element based numerical analysis is conducted. This simulation investigates the temperature history, hardness and residual stresses. Some physical principles play a role in the mechanical properties of the part, such as the heat absorption from the laser beam to deposited powder and substrate, the heat conduction in the substrate and the deposited bead, the molten pool dynamics, the solidification of the molten pool and heat convection/radiation from the surface of the part. Moreover, the geometry of the part, substrate, and deposited beads, as well as machine parameters during deposition, affect the mechanical properties of the part [131].

The assumptions of this analysis are:

(I) The powder deposition aspects are not considered. The powder particles traveling from the nozzle to the melt pool are not considered. It is assumed that the material is provided directly at the melt pool continuously [111].

(II) Although in this method all beads are preplaced and meshed initially, elements of the melt pool and deposited beads activate as the laser travels along the toolpath. This means all elements are present from the beginning, but the bead elements are deactivated initially. As the laser trajectory passes along the bead, it activates them.

So the heat delivery from the laser to the bead, as well as the heat transfer from the melt pool to the bead, happens just to the elements that already deposited. This makes the simulation and the results closer to what really happens experimentally. This method is called a transient analysis with a moving heat source (MHS) approach.

(III) The bead geometry is important in the modeling of the thin wall bead deposition. In this case, the bead geometry is ascertained from experience and experimental results [48], i.e., the effect of machine parameters on the bead geometry is known. To ensure that the bead geometry assumption is correct, it is verified by the experimental data from built samples.

(IV) The cross section of the beads are assumed to be rectangular. Thus, the geometry of the bead is defined by bead width and bead height.

(V) The laser parameters such as the laser reflection and the laser attenuation are simplified to the laser efficiency parameter, which is represenative of the amount of laser power loss.

3.6.1 Calculation Theories

In this research, a thermal-metallurgical analysis of thin wall bead depositions is accomplished using ESI Sysweld software (version 2019.0). The thermal and metallurgical history of a part can be predicted at all points that are affected by heat. The hardness of a part depends on chemical composition, structure after quench or temper operation, cooling rate and grain size [132].

The equation used for thermo-metallurgical analysis is a modified heat conduction (Equation (18)).

$$\left(\sum_{u} P_u (\rho C)_u\right)\frac{\partial T}{\partial t} - \nabla\left(\left(\sum_{u} P_u \lambda_u\right)\nabla T\right) + \sum_{u<v} L_{uv}(T).A_{uv} = Q \qquad (18)$$

Here, ‘P’ is phase proportion, ‘u, v’ are phase indices, ‘Q’ represents the heat source, ‘L_{uv}(T)’ is the latent heat of u to v transformation, and ‘A_{uv}’ is the proportion of transformed phase from u to v in a time unit.

The temperature gradient is calculated based on Equation (19).

$$\frac{\partial T}{\partial t} = \frac{\lambda}{C \times \rho}\left(\frac{\partial^2 T}{\partial x^2} + \frac{\partial^2 T}{\partial y^2} + \frac{\partial^2 T}{\partial z^2}\right) = a\nabla^2 T \qquad (19)$$

‘T’ is the temperature in Kelvin, ‘t’ time in second, ‘x, y, z’ are the point coordinates, ‘α’ represents the thermal diffusivity coefficient, ‘λ’ is conductivity coefficient, ‘C’ is specific heat, and ‘ρ’ is the mass density.

Another important input of this simulation is the heat source definition. There are several mathematical models to represent welding heat sources for the analysis calculations. The two-dimensional Gaussian surface, Goldak double-elliptical, and the three-dimensional Gaussian conical heat source models are the three main mathematical models. The first one is best suited for surface treatment processes, while the second one performs well for melt-in welding, and the third one models processes with high power density such as laser and electron beam welding [132]. As direct energy deposition additive manufacturing utilizes a laser beam to melt the material, the three-dimensional Gaussian conical heat source is used in this analysis.

The shape of the 3D Gaussian conical heat source model is shown in Figure 3-52. The power intensity increases exponentially as the distance from the center of the laser beam decreases and the radius of the laser beam shrinks as it goes deeper. The shape of the intensity curve stays the same, but the maximum power decreases as the laser penetrates into the part. The maximum depth that laser can melt the part is called the penetration depth.

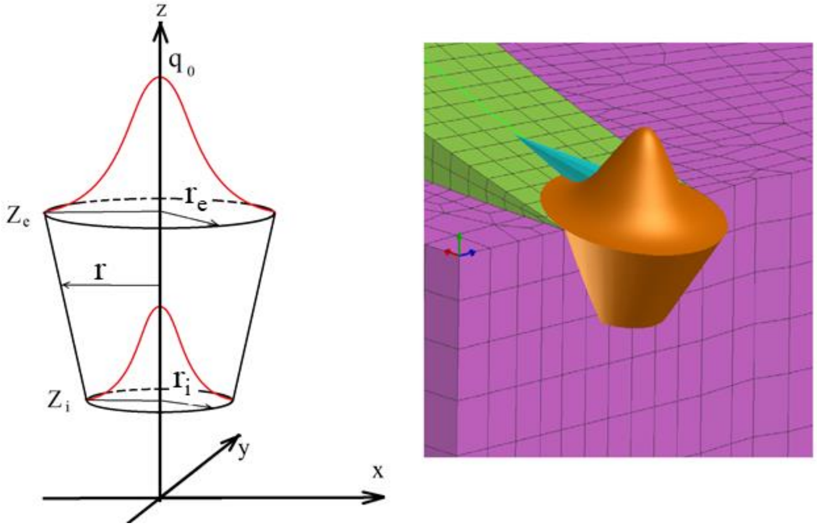

Figure 3-52. 3D Gaussian conical heat source model

$$q(x,y,z) = q_0 exp\left(-\frac{x^2+y^2}{r_0^2(z)}\right) \qquad [20]$$

$$r_0^2(z) = r_e + \frac{r_i - r_e}{z_i - z_e}(z - z_e) \qquad [21]$$

'q_0' is the heat flux density, 'r_e' is beam radius at exposure surface, 'r_i' is the beam radius at penetration depth 'z_e' is the height of exposure surface, and 'z_i' represents the height of the penetration depth.

The initial boundary conditions for the simulation are shown in Figure 3-53. More quantitative boundary conditions are presented in Chapter 7.

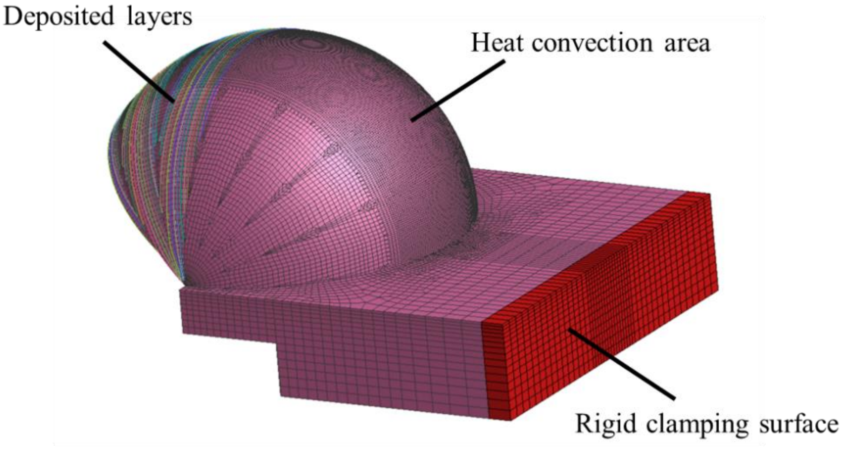

Figure 3-53. Initial boundary conditions for the FEA simulation

3.6.2 Applied FEA Algorithm

Two methods are applied in this research; constant laser efficiency and constant melt pool size. In the constant laser efficiency method, laser efficiency is assumed to be constant for all beads. This causes the melt pool size variation in different layers. The sensitivity analyses are applied for simulation parameters such as laser efficiency, laser penetration, and laser diameter at the bottom of laser penetration. The results are compared to the experimental data to find the appropriate parameters.

The constant melt pool method [133] is the modified one. The applied algorithm for this method is shown in Figure 3-54. This algorithm starts with preparing the CAD models of both the substrate and the product. Slicing the part model into separate beads helps to mesh beads easier at later preparation stages. The models of the substrate and the beads are meshed with Altair-Hypermesh. Using hexagonal meshes and variable element sizes for different regions reduces the overall number of elements and consequently the run time. Figure 3-55 shows the applied method for the model of the dome to reduce the run time of the bead deposition analysis. The measurement area is shown in red ellipses. This is the area that the mechanical properties need to be measured. The mesh size in these regions and regions near them is constant and fine, but for farther regions in the bead, the mesh gradually becomes coarser. The dependency of the results on the mesh size and mesh variation in the beads is presented in the results chapter.

After the mesh file is imported from Hypermesh into Sysweld Visual-Mesh, it needs to be checked for any coincident nodes, and 'elements besides element' quality check needs to be implemented. If there is any coincidence in nodes or elements, they should be fused together. The Jacobian, skewness, and maximum aspect ratios need to be examined and improved if these values violate the limitations. After the elements are enhanced, mesh file exports into Sysweld Visual-Weld for the next steps of analysis.

The melt pool travel path, in addition to the laser beam orientation, needs to be defined in Visual-mesh. The travel paths of 3 beads are created in this step. The process parameters such as nozzle travel speed, laser top diameter (r_e), bottom diameter (r_i), penetration depth (based on dimensions in Figure 3-52), energy per unit length, and laser efficiency are defined. These parameters specify the amount and shape of the input heat source into the system. The laser top diameter and energy per unit are machine parameters that are set on the machine prior to building the sample. However, the laser bottom diameter and penetration depth as well as laser efficiency and surrounding temperature need to be measured experimentally or estimated from the available literature. The penetration depth is defined as the depth that heat flux penetrates in the solid substrate.

A shell element mesh needs to be created to encase the overall model as a skin for heat transfer calculations. The method for defining the clamps affects the resultant distortion of the workpiece and substrate. However, this research is not investigating the distortions. Thermo-metallurgical analysis plus mechanical calculations are available to analyze the temperature gradient history, phase proportions, displacements, residual stresses, and yielding point. Moreover, the software can analyze the hardness separately. Hardness depends on the material chemical composition, structure after a quench and temper operation, the cooling rate, and the grain size [132]. As hardness and yield strength have linear correlation [134], the analysis is performed for yield strength. Then, by a linear ratio, it is converted into the hardness results. The results are verified by experimental hardness measurements. More detailed explanations of the simulation process, as well as the results, are covered in Chapter 7.

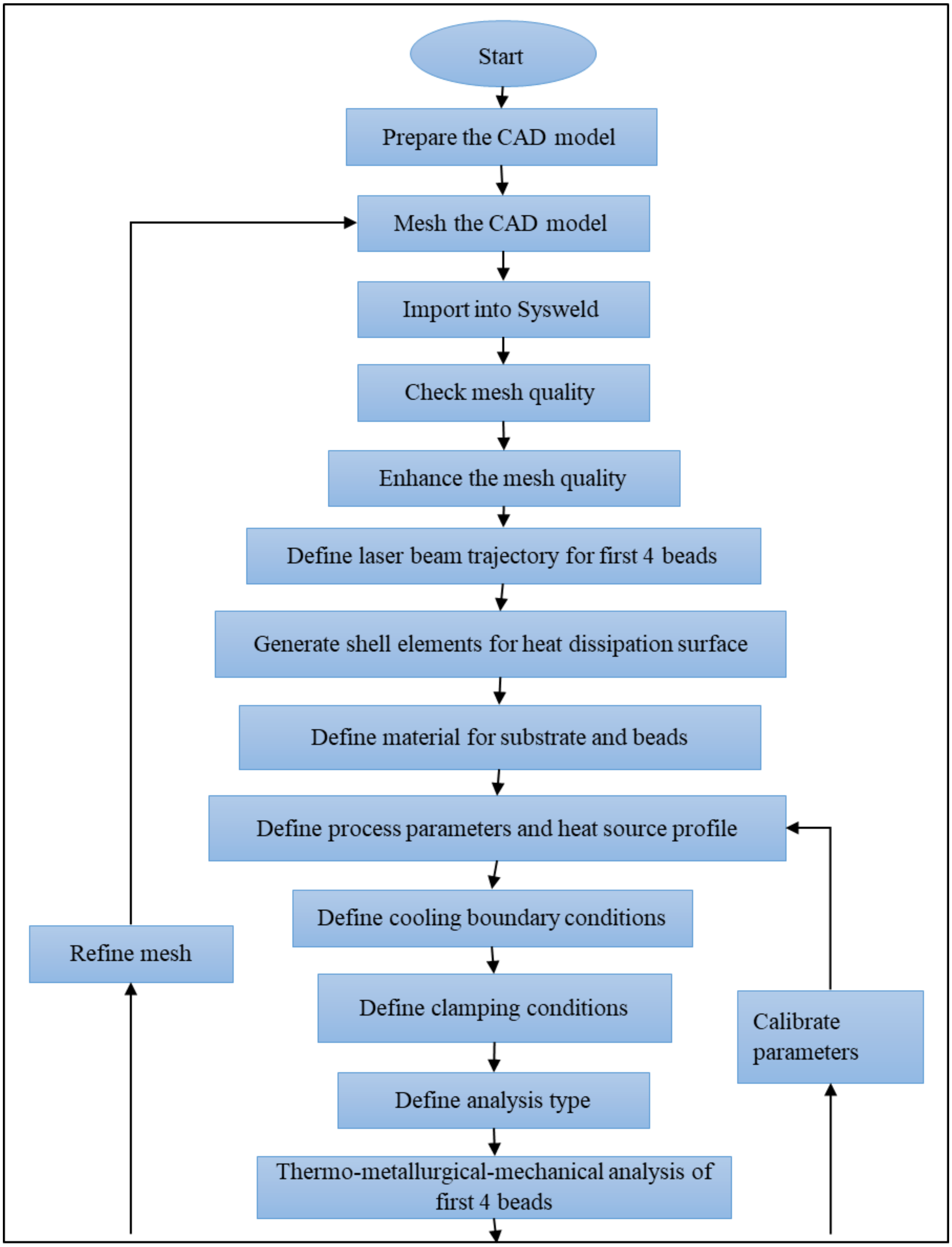
Start
Prepare the CAD model
Mesh the CAD model
Import into Sysweld
Check mesh quality
Enhance the mesh quality
Define laser beam trajectory for first 4 beads
Generate shell elements for heat dissipation surface
Define material for substrate and beads
Define process parameters and heat source profile
Refine mesh
Define cooling boundary conditions
Define clamping conditions
Calibrate parameters
Define analysis type
Thermo-metallurgical-mechanical analysis of first 4 beads

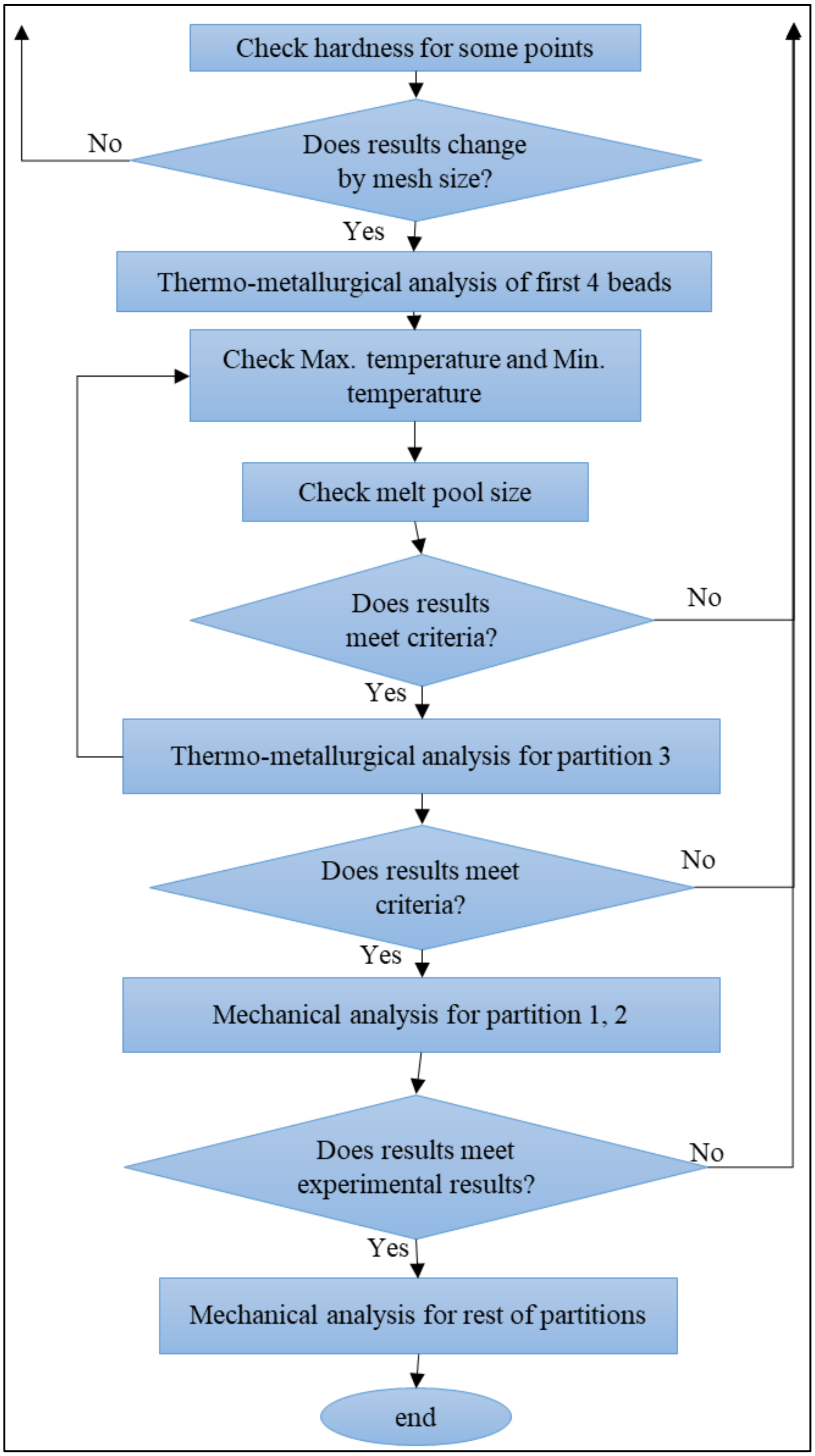
Check hardness for some points
Does results change by mesh size?
No
Yes
Thermo-metallurgical analysis of first 4 beads
Check Max. temperature and Min. temperature
Check melt pool size
Does results meet criteria?
No
Yes
Thermo-metallurgical analysis for partition 3
Does results meet criteria?
No
Yes
Mechanical analysis for partition 1, 2
Does results meet experimental results?
No
Yes
Mechanical analysis for rest of partitions
end

Figure 3-54. Flow chart of numerical analysis applied in this research

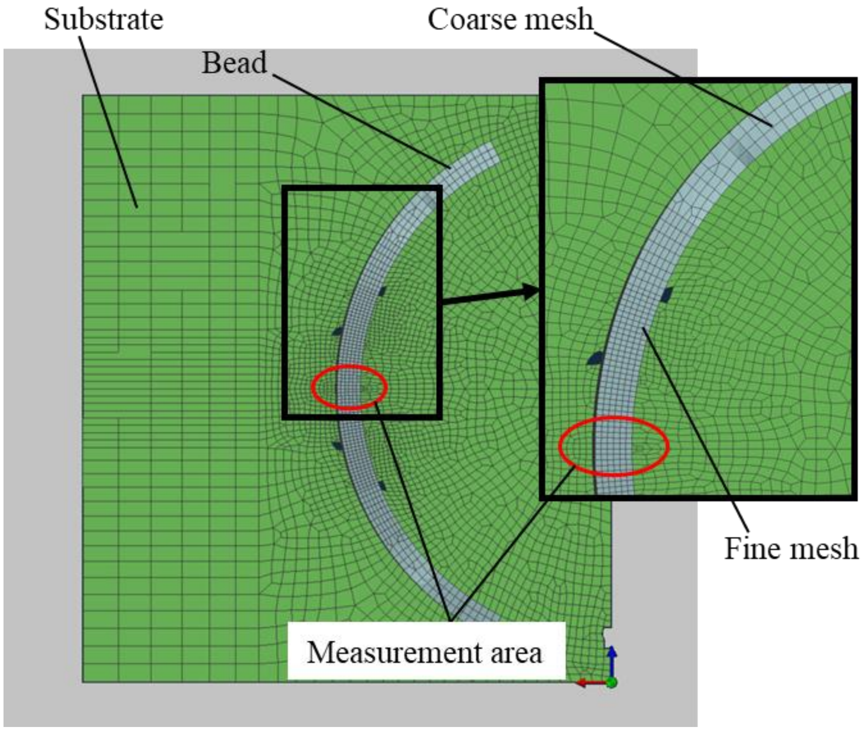

Figure 3-55. Variable mesh size for beads

A mesh dependency (mesh sensitivity) check is performed to ensure the validity of the results. For this, the analysis should be performed for the same geometry and process parameters using finer mesh elements. The whole model is meshed using finer elements (eight-time finer mesh). As mentioned before, the analysis of 4 beads is performed. The hardness variation diagram for the predetermined region in these different analyses are compared. If the mesh is too coarse, the hardness results vary significantly when changing the mesh size. But gradually by refining the elements, the dependency of the hardness results to mesh size will become insignificant. Although the finer mesh provides more accurate results, it increases the analysis runtime. Therefore, a decision needs to be made for practical element size that brings accurate results and reasonable runtime.

The case study sample in this research has unique challenges, as it is split into partitions and this introduces time discontinuities. Therefore, a structured analysis approach is used. To prevent a long analysis of all 144 beads, the analysis is performed for each 2 partitions and 7 beads of the next partition.

To identify the simulation parameters, initially the thermo-metallurgical analysis is executed for the first 4 beads of partition 1 to find the appropriate parameters to meet the melt pool temperature between 1500 °C and 2000 °C as well as the size of melt pool to include the last 2 beads. The initial sensitivity analyses showed that constant laser efficiency for all layers of a partition causes the melt pool size to increase for higher layers of each partition and the melt pool temperature increases very much. Hence, the laser parameter is set to decrease for higher layers of each partition. This maintains the melt pool size and temperature for beads of the partitions. When the parameters are identified the mechanical analysis is executed for all partitions. Sysweld Visual-view provides the yield strength, temperature history, and the residual stresses. The yield strength variation plot is used to extract the hardness data, and compared to the experimental hardness data.

To summarize, in this chapter the techniques, and theories that are applied to the process set up and fabrication, geometry partitioning, surface roughness measurements, micro-hardness measurements, and FEA analysis is presented. In the following chapter, the fabrication processes, geometry, and dimensions of the built domes are compared to nominal values.

CHAPTER 4

PROCESS PLANNING FOR COLLISION AVOIDANCE RESULTS

In this chapter, the fabrication challenges, product geometry, and visual investigation of the domes is presented. The diameter and thickness of the fabricated domes is measured and a visual estimation of the surface finish is covered. One sample per each partitioning strategy is fabricated and tested. Prior research has shown that the process is repeatable [48], [135].

4.1 *Dome Fabricated by Wedge Shape Partitioning*

Two domes are fabricated leveraging the wedge-shaped partitioning algorithm for the 5-axis and 2+1+1-axis scenarios. The partitions for both parts are fabricated with an interval of approximately 10 minutes between operations for visual inspection. Therefore, the previous partition cools down before the next one starts.

4.1.1 Dome Fabricated by 5-Axis Toolpath

Keeping the nozzle tangent to the surface of the dome requires all 5-axes to be continuously involved. Figure 4-1 demonstrates the fabrication procedure of the partitions.

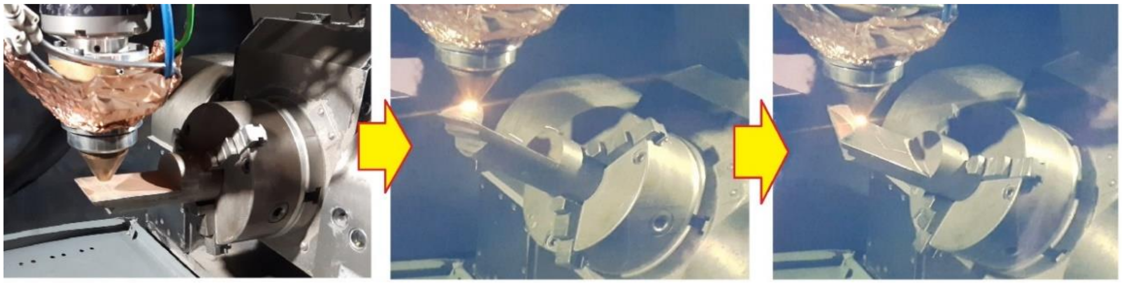

Figure 4-1. All 5 axes involvement in making the hemisphere dome

Controller based fabrication issues occurred. A travel speed variation was observed while producing partitions 1, 2, and 4 in 5-axis mode. The fluctuation of material deposition and heat input rate affected the surface roughness and hardness of the mentioned partitions. However, the travel speed for the 3rd partition was constant. Therefore, the hardness and surface roughness tests are applied just for the 3rd partition as no additional process related noise is introduced. Machine tool companies are developing specialty AM controllers. This research revealed an issue for a 5-axis deposition process that is used successfully for fabricating other less complex geometries.

Fabrication of a hemisphere by this method needs a B-axis rotation of 180°. A machine constraint that appeared during the fabrication process was that the trunnion table of the B-axis can tilt just 0-90°. Therefore the 3rd and 4th partitions could not be made as planned. The solution is to build half of the hemisphere in the first setup then rotate the A-axis 180°, zero the A-axis, and then build the second half. The toolpath is modified for this strategy as Figure 4-2 shows.

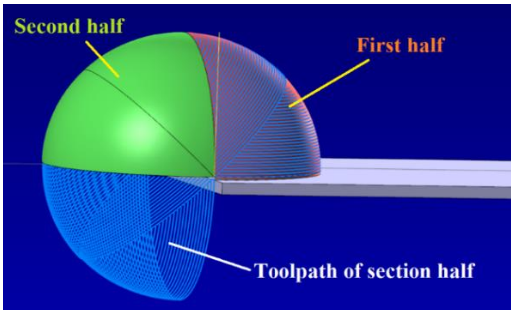

Figure 4-2. Building the dome in two sections by 180 degree rotation

As shown in Figure 4-3 (a), the B-axis is zeroed at the beginning of the build. This means the substrate platform is at a horizontal position. The deposition of the first two partitions continues until the first half of the dome is built. At this point, the B-axis is at 90° (Figure 4-3 (b)). If it continues to build the second half, it exceeds the B-axis limitation (Figure 4-3 (c)). The solution is to rotate the A-axis 180° after partition 2 is built. Then, the new position of the A-axis is set to zero. Afterward, it starts to build the second half from the new orientation (Figure 4-3 (d), (e)). Figure 4-5 shows the fabricated partition.

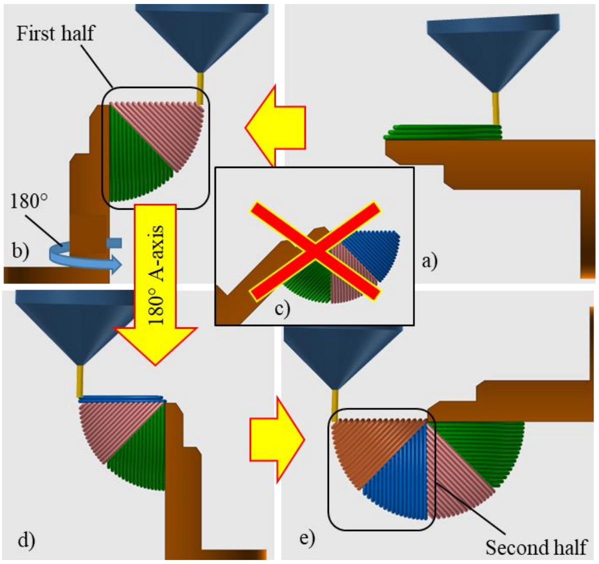

Figure 4-3. (a) Substrate at its horizontal position. (b) Building the first half of the dome (c) Rotation of A-axis 180° (d) Building the second half

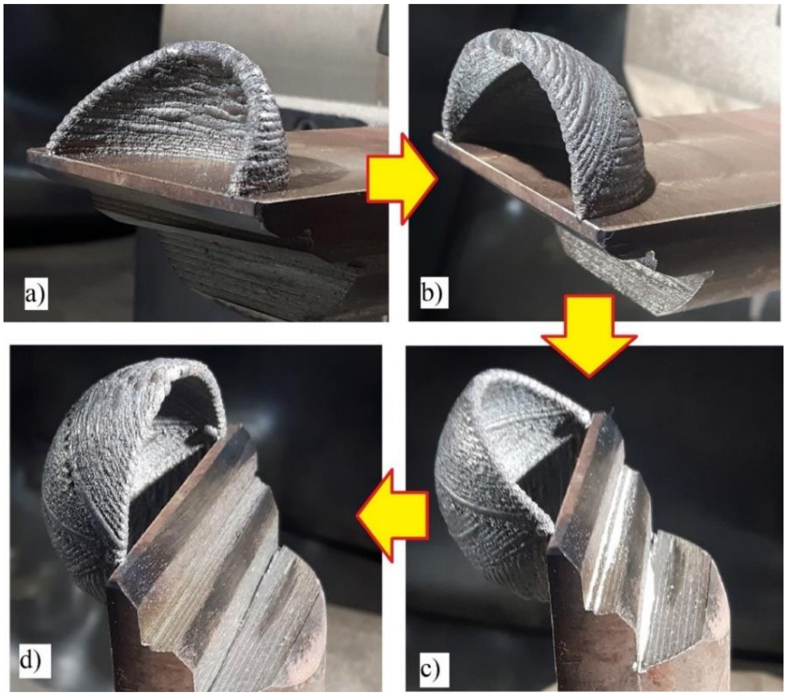

Figure 4-4. Production stages of the dome in 5-axis. (a) to (d) Produced partitions 1 to 4 respectively

Figure 4-5 shows the completed dome made by a 5-axis planar-slicing toolpath. It is apparent that the surface roughness of the 3rd partition is better than other ones.

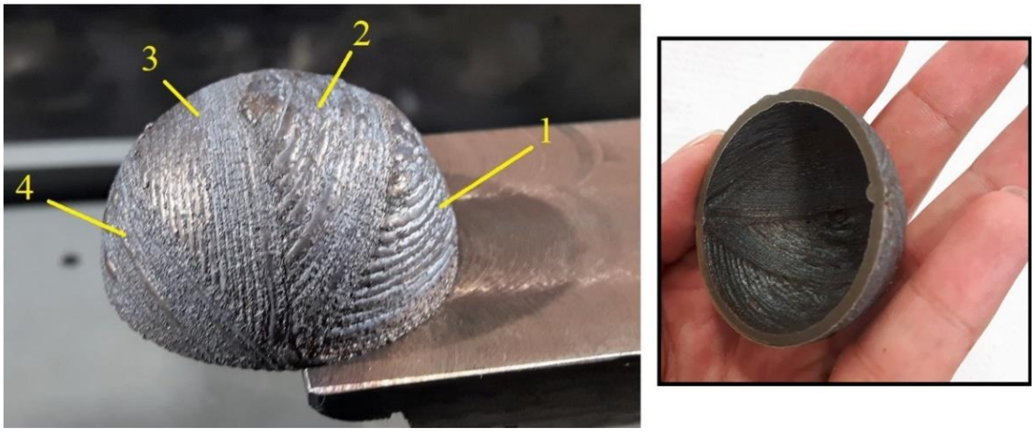

Figure 4-5. Completed 4 sections of 5-axis dome

A sphere is best-fitted to the point cloud data of the dome using Solidworks-ScanTo3D module and Powerinspect software. The inner and outer diameters are calculated as 42.4 mm and 47.8, respectively.

4.1.2 Dome Fabricated by 2+1+1-Axis Toolpath

The same machine and process parameters for the 5-axis process are applied to produce 2+1+1-axis dome. Since this process requires just 2 axes for the bead trajectory, it does not experience the inconsistent movement that the 5-axis process had. Therefore, all partitions are valid for further investigations of the surface roughness and hardness tests. But the fabrication process suffers from constraints on the B-axis, similar to the 5-axis process. As a result, the first four partitions are made as the B-axis goes from 0° to 90°, then the A-axis rotates 180°, and the B-axis travels back to 0° to build the last 4 partitions. This is the reason why the part is built in 8 partitions instead of 9 (Section 3.2.1). If it was built in 9 sections, the angle of the 5th partition would be 80°-100°, which could not be built continuously.

Figure 4-7 shows the process of manufacturing the first 4 partitions of 2+1+1-axis dome. Figure 4-8 shows the process of fabricating the partitions. Figure 4-8 shows the fabricated part including the partition numbers.

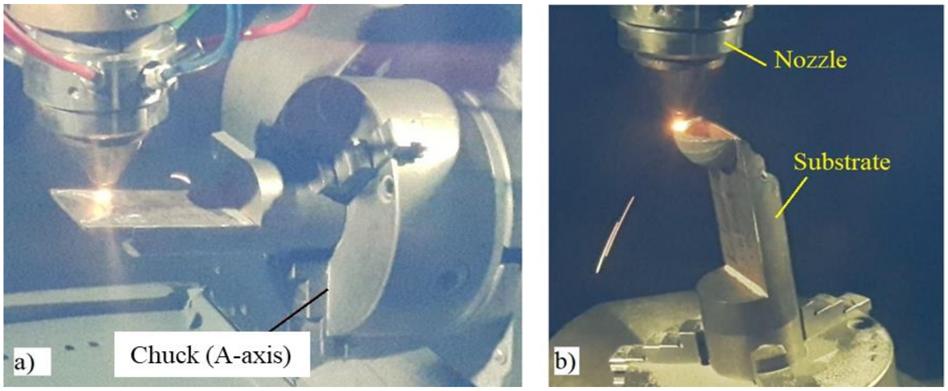

Figure 4-6. 2+1+1-Axis deposition of dome (a) First partition (b) 5th-partition

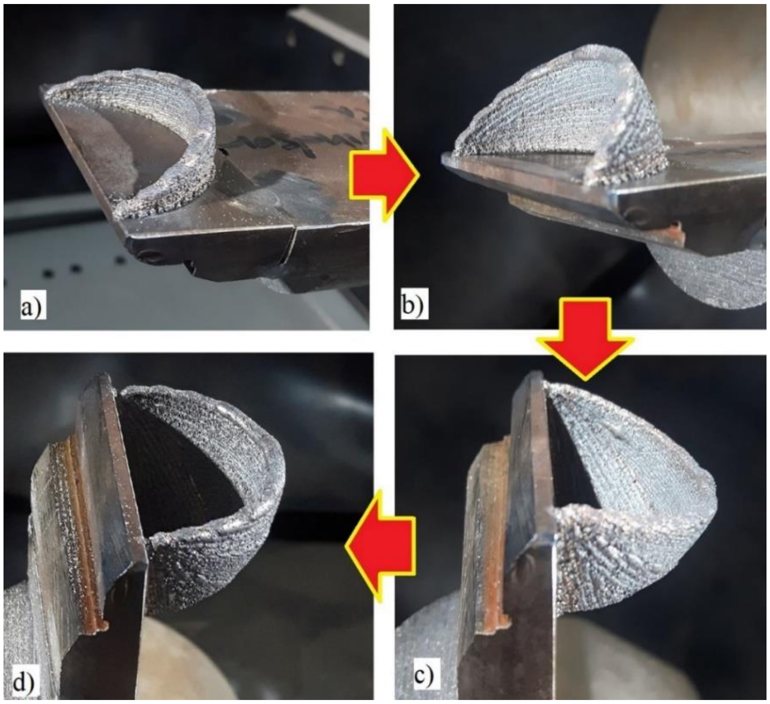

Figure 4-7. 2+1+1-Axis manufacturing of dome (a) to (d) Partitions 1 to 4

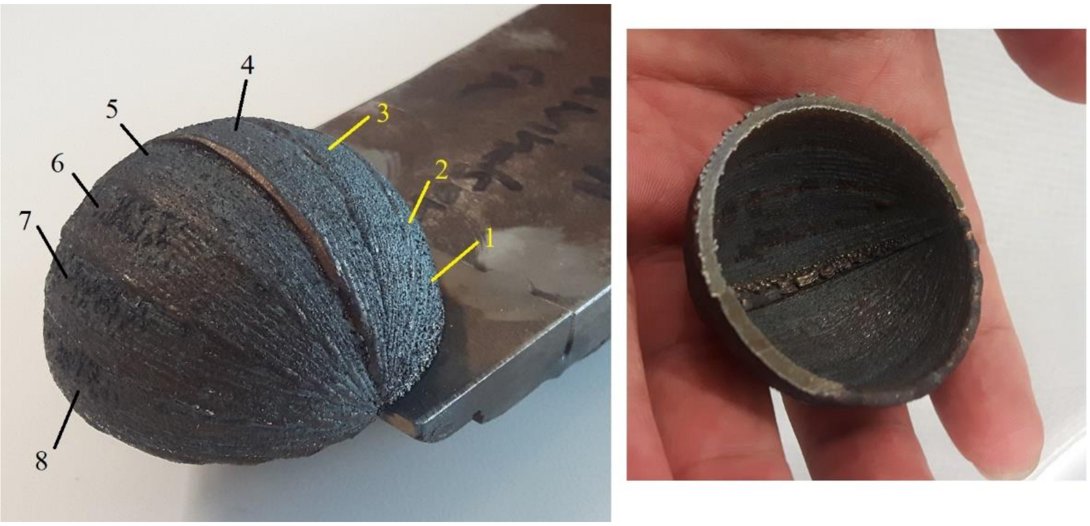

Figure 4-8. Completed 2+1+1 axis dome. Partitions 1-8

The same process as for the 5-axis sample is followed to measure the diameters of 2+1+1 sample (Figure 4-9). The results show the inner and outer diameters of 42.6 mm and 48.1 mm, respectively.

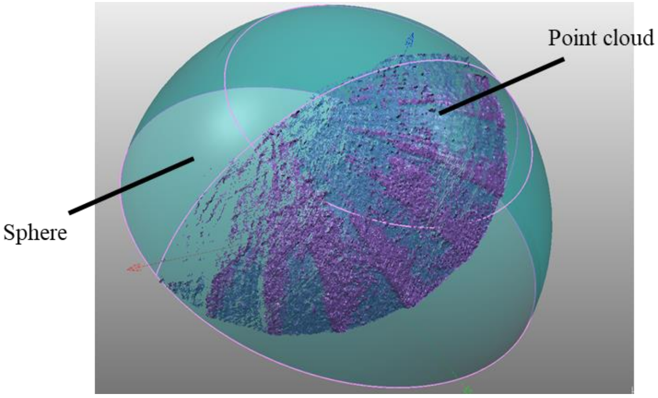

Figure 4-9. Diameter measurement from point cloud

4.2 *Dome Fabricated by Rotary 1+3-Axis Toolpath*

In this case, the deposition toolpath requires just the rotation of the A-axis. When a layer is deposited, three simultaneous movements relocate the nozzle to the next layer. The mentioned 3 movements are rotations about the Z-axis, B-axis, and Y-axis. Figure 4-10 (a) shows the rotary bead deposition. Figure 4-10 (b), (c) show the procedure of fabricating the dome.

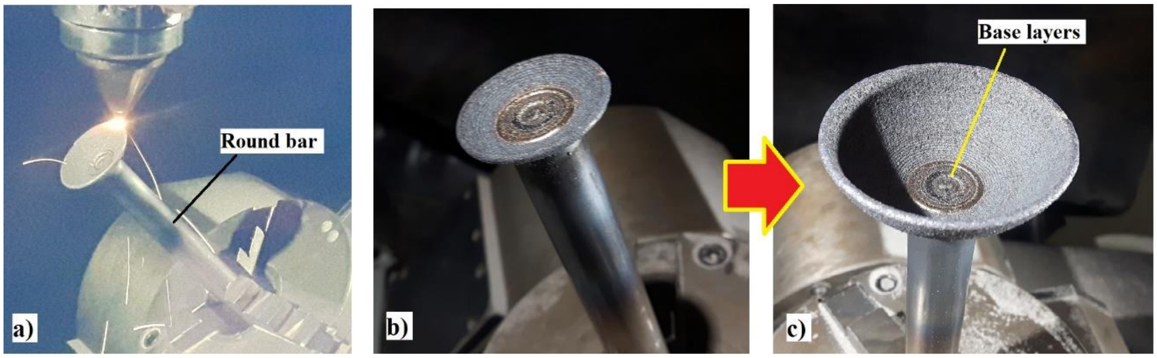

Figure 4-10. (a) Rotary deposition toolpath (b) Initial layers (c) Half fabricated dome

Figure 4-11 shows the produced sample by rotary toolpath strategy. The base 3-axis beads are shown as well.

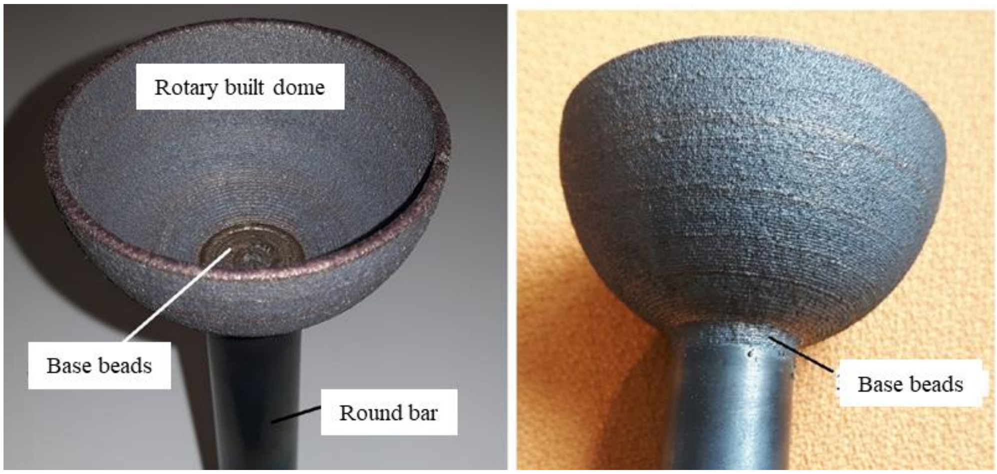

Figure 4-11. Sample made by rotary toolpath strategy

Figure 4-12 compares the inner and outer diameters of three different partitioned domes. For both inner and outer diameters, the 2+1+1-axis dome shows the highest variations whereas the rotary sample has the lowest variations.

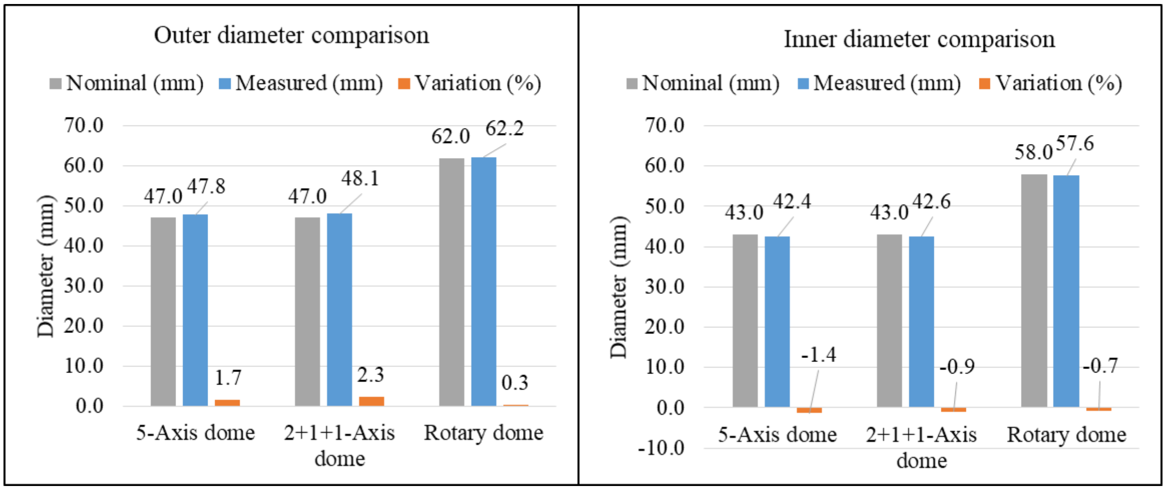

Figure 4-12. Comparison of inner and outer diameters

The thicknesses of the samples are measured in 10 random locations. The measured values, as well as the standard deviation (Std. Dev.) of 10 measurements, are displayed in Figure 4-13. The average diameter of the 2+1+1-axis sample is closest to nominal but has a high standard deviation. On the other hand, the 5-axis sample has the lowest standard deviation.

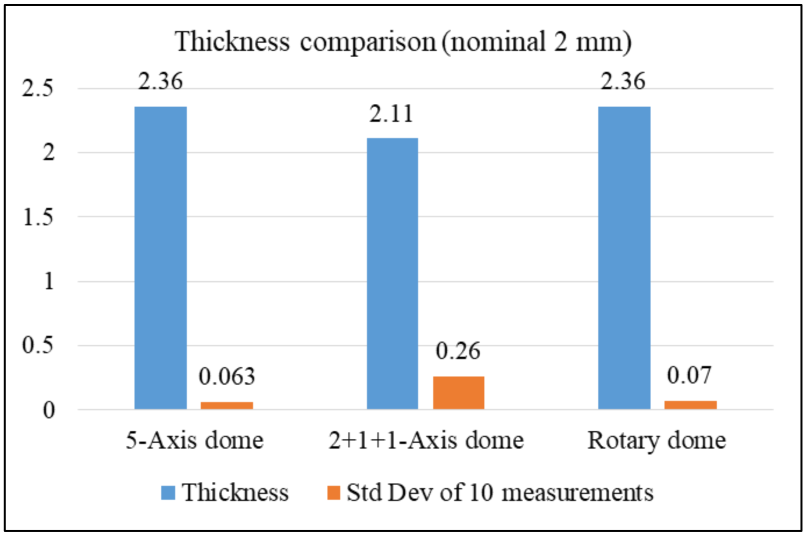

Figure 4-13. Thickness comparison

The process planning results, geometry measurement of fabricated domes and visual investigation of the domes are presented in this chapter. The average diameters and their variations indicate that the 2+1+1-axis is the worst case as the outer diameter is expanded 2.3 % and the inner diameter is shrunk 0.9 %. The reason is the surface inflations at the transition points between partitions that increase the outer diameter. Figure 4-13 supports this as the standard deviation of the thickness has the highest value whereas it has the lowest thickness. It means the thickness within partitions is the lowest but the existence of the bumps increases the standard deviation and the total outer diameter. On the contrary, the rotary dome has the best condition as its diameters are near the nominal value.

A 3D scanner with an accuracy of ±0.044 mm is used to collect the point cloud data. Hence the diameter values have a tolerance of ±0.044 mm. Although the CMM has better accuracy, it is not adequate to collect the point cloud data because the number of provided points are much less. In addition to this, the probe diameter prevents the measurement of the surface texture valleys. The Vernier caliper cannot provide sufficient diameter data as it provides a dimensional measurement, not a geometrical one.

Further experiments are implemented to compare the properties of the domes from different aspects. The exploration of surface roughness and hardness variations are presented in Chapters 5 and 6.

CHAPTER 5

SURFACE ROUGHNESS TESTS RESULTS

The surface roughness results are presented in this chapter for the dome samples to study the Ra variations perpendicular to the slice direction. Based on the surface roughness measurement algorithms, two Matlab programs are developed. The first measurement program is based on the 2D edge points of mount samples, and the second program extracts surface roughness values from a 3D point cloud.

5.1 *Surface Roughness Measurement from Mount Samples*

Before the program is applied to inspect the domes, an assessment is performed to verify the validity of the results. A sensitivity study of the two parameters affecting the results when using the 3D point as input (the number of projection lines and length of measurement) is also realized.

5.1.1 Verification Test of the Mount Program

As mentioned in the methodology chapter, a trial experiment was performed to measure the surface roughness utilizing a skidded contact-based device. Although the results were not reliable to be used to measure the real roughness of the parts, the collected data are employed to verify the results of the Matlab program.

The collected data is provided in two forms: the surface texture profile and their associated point coordinates. When the stylus is traveling along the surface, it records numerous point coordinates of the surface texture. Then, it draws the surface profile as shown in Figure 5-1. The traveling length is set by the user. A sensitivity analysis is performed to find the optimum measurement length. In this case, 3333 and 6000 point coordinates were created for the measurement lengths of 5 mm, 3 mm respectively.

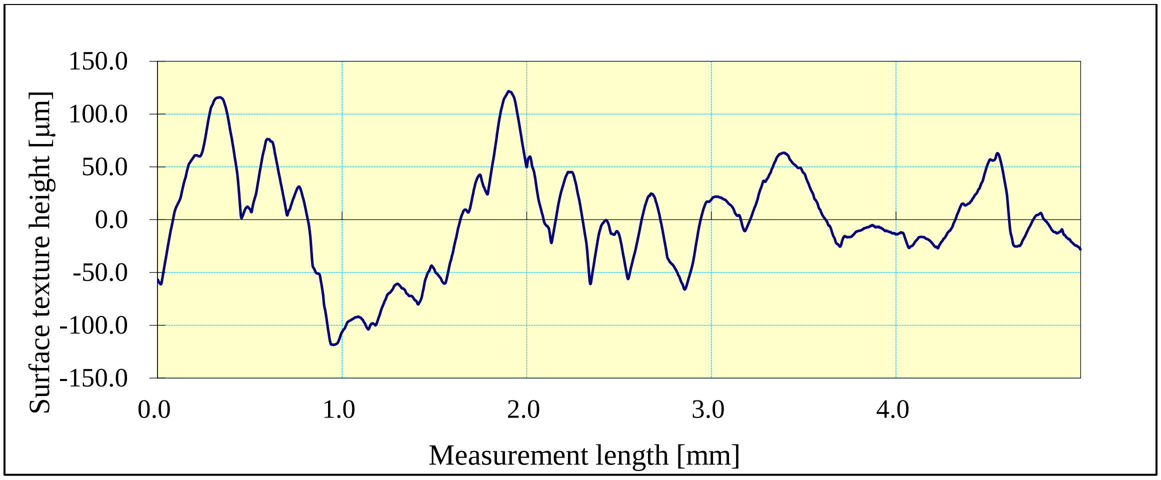

Figure 5-1. A sample surface texture profile is used to verify the Matlab program

Table 5-1 shows some example points of the surface profile related to Figure 5-1. A sample surface texture profile is used to verify the Matlab program. Five point-coordinate files (txt file) of different surface profile samples are utilized.

Table 5-1. Point coordinate sample made by a contact-based surface roughness facility

Point number	X position (mm)	Texture height (μm)
1	0.00150	-56.65
2	0.00300	-57.14
3	0.00450	-57.73
…	…	…
3331	4.99650	-27.55
3332	4.99800	-27.92
3333	4.99950	-28.04

As Table 5-2 indicates, the calculated Ra values from the Matlab program match the contact-based measurement with an average standard deviation of 0.07 (μm). This experiment proves that results evaluations performed by the Matlab program are valid and accurate enough to perform further analyses for the dome samples.

It is expected that as the number of projection lines increases, the Ra value will become more accurate. Also, the measurement length depends on the roughness of the surface. If the surface is very rough, the measurement length should be longer to include more surface textures. Since the slice height is 0.5 mm for partitioned domes, an effective measurement length is needed to be established.

Table 5-2. Verification of results made by prepared Matlab program with results of contact-based measurement

Experiment number	Measured by contact-based facility (µm)	Calculated by prepared Matlab program (µm)	Variation (%)
1	14.61	14.7	0.64
2	38.15	38.3	0.39
3	25.9	25.9	0.02
4	25.16	25	0.6
5	33.07	33	0.05

5.1.2 Sensitivity Study of the Mount Program

The number of projection lines- Two types of sample tests are used for this test: high point density samples and low point density samples. High-density samples are the point coordinate files that were used in section 5.1.1. These files contain 3333 and 6000 points for 5 mm and 3 mm measurement length, respectively, which means average distances between points are 1.5 µm and 0.5 µm, respectively. Low-density samples are associated with the point coordinate files of the mount samples. Five samples are used here that have between 127 to 204 points in 4 mm measurement lengths. The average distance between points for these samples is approximately 25 µm.

For the high-density samples, the Matlab program was run by different numbers of projection lines; 6000, 3000, …, 100, 50, 25, 10. As Figure 5-2 (a) indicates, the calculated roughness (Ra) is independent of the number of projection lines if the number of projection lines is more than 100. If the projection lines are less than 100, the observed Ra value drops severely. The test for low-density samples supports this as well. For projection lines more than 100, the curves are horizontal. Therefore, for later applications of the program, the projection lines should be at least 100 for each measurement length of 4 mm.

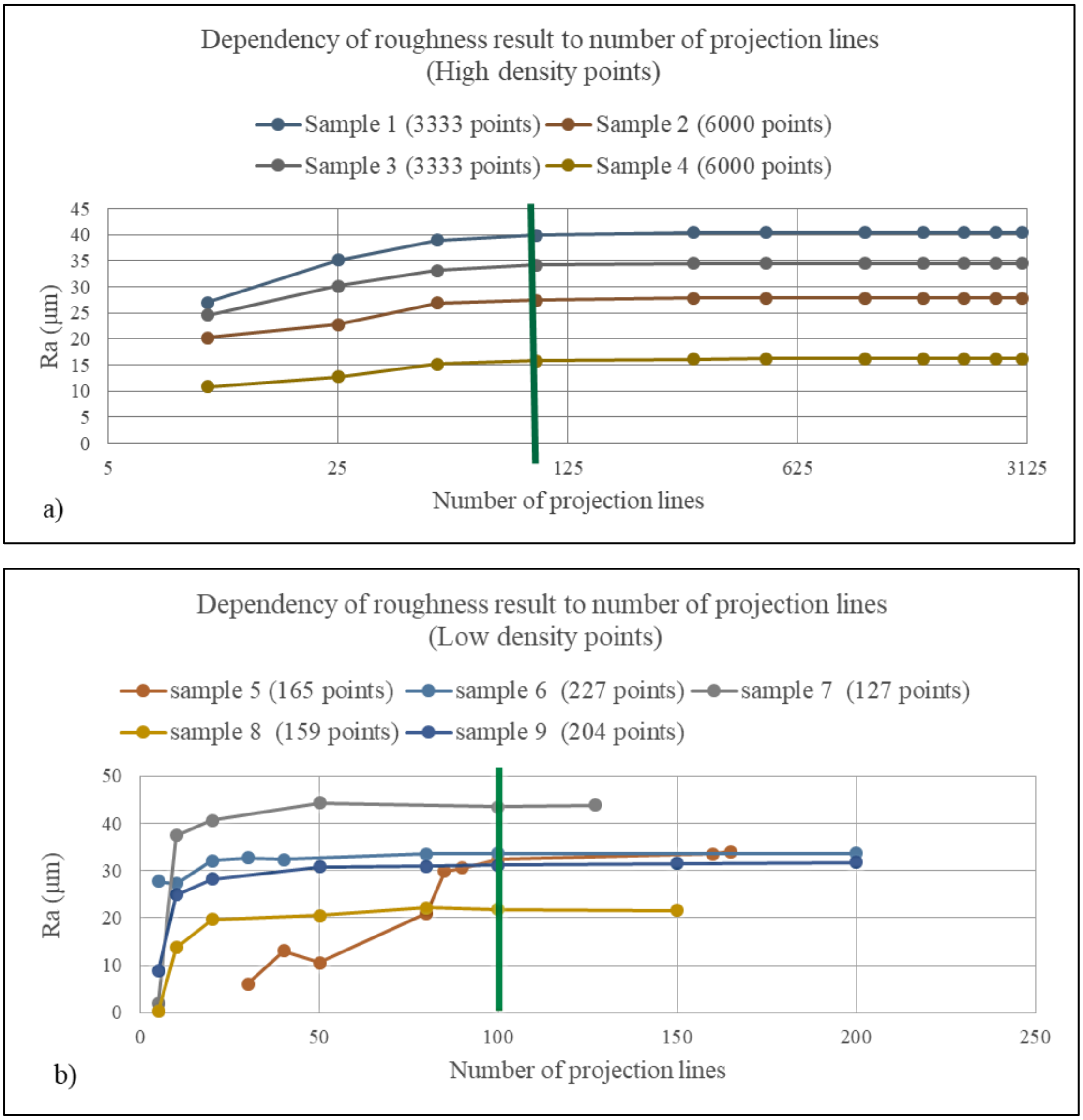

Figure 5-2. Dependency of surface roughness result made by Matlab program to number of projection lines

The measurement length- The txt file related to the inner edge of 2+1+1-axis partitions 1-4 sample is used in this experiment to determine the proper measurement length. Figure 5-3 shows different regions on the inner edge based on their surface quality. The layers within partitions are finer than the joints between partitions. There is a surface inconsistency at the joints that causes an Ra value escalation.

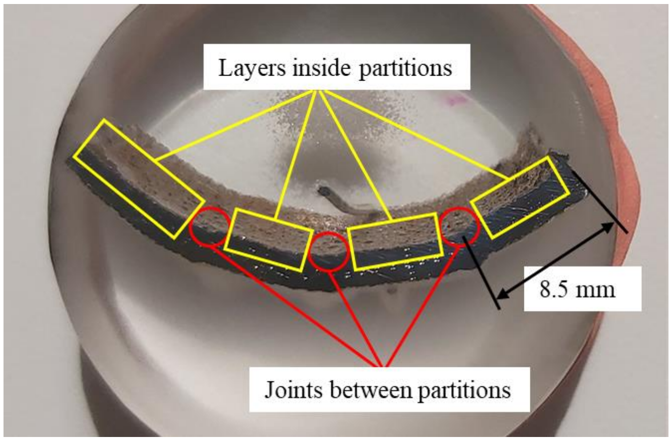

Figure 5-3. Regions of mount samples with different surface quality

The program is applied for a set of measurement lengths of 1, 2, 3, 4, 5, and 8 mm. As Figure 5-4 (a) shows measurement lengths of 1 and 2 mm are very noisy and display no pattern. The reason is the measurement length is just too small compared to the slice height. Also, the transition points between partitions are not detectable.

On the other hand, a pattern is noticeable for the measurement lengths of 3, 4 (Figure 5-4 (b)). Moreover, it shows the Ra variation of the layers inside each partition. This figure shows an Ra convergence within partitions for measurement lengths of 3, 4 mm but they differ for the transition points between layers. Figure 5-5 indicates the reason. For regions within partitions, both methods measure a smooth surface whereas, on transition points, it depends on the length of the region that is covered by the bulge.

Considering measurement lengths of 5, and 8 mm, the sections related to layers inside partitions are too small or even it is not detectable for 8 mm (Figure 5-4 (c)). Although it is advised to perform surface roughness of the samples having Ra = 50 μm (which is the same order as the Ra of the domes) by measurement length of 8 mm [54], it is not applicable here to study the variation of Ra. Also, as Figure 5-3 shows the arc lengths of partitions are around 8 mm in the mount samples. Thus, all measurements are affected by bulges of transition points whereas measurements within the partitions should be free of such noises. It means it does not show the variation of surface roughness within partitions. This conclusion is true for the 5 mm measurement length too. Therefore, lengths of 1, 2, 5, and 8 mm are excluded. On the other hand, the measurement lengths of 3, 4 are applicable. Since a 4 mm measurement includes more layers (theoretically 8 layers), it is chosen for the assessment for the dome experiments.

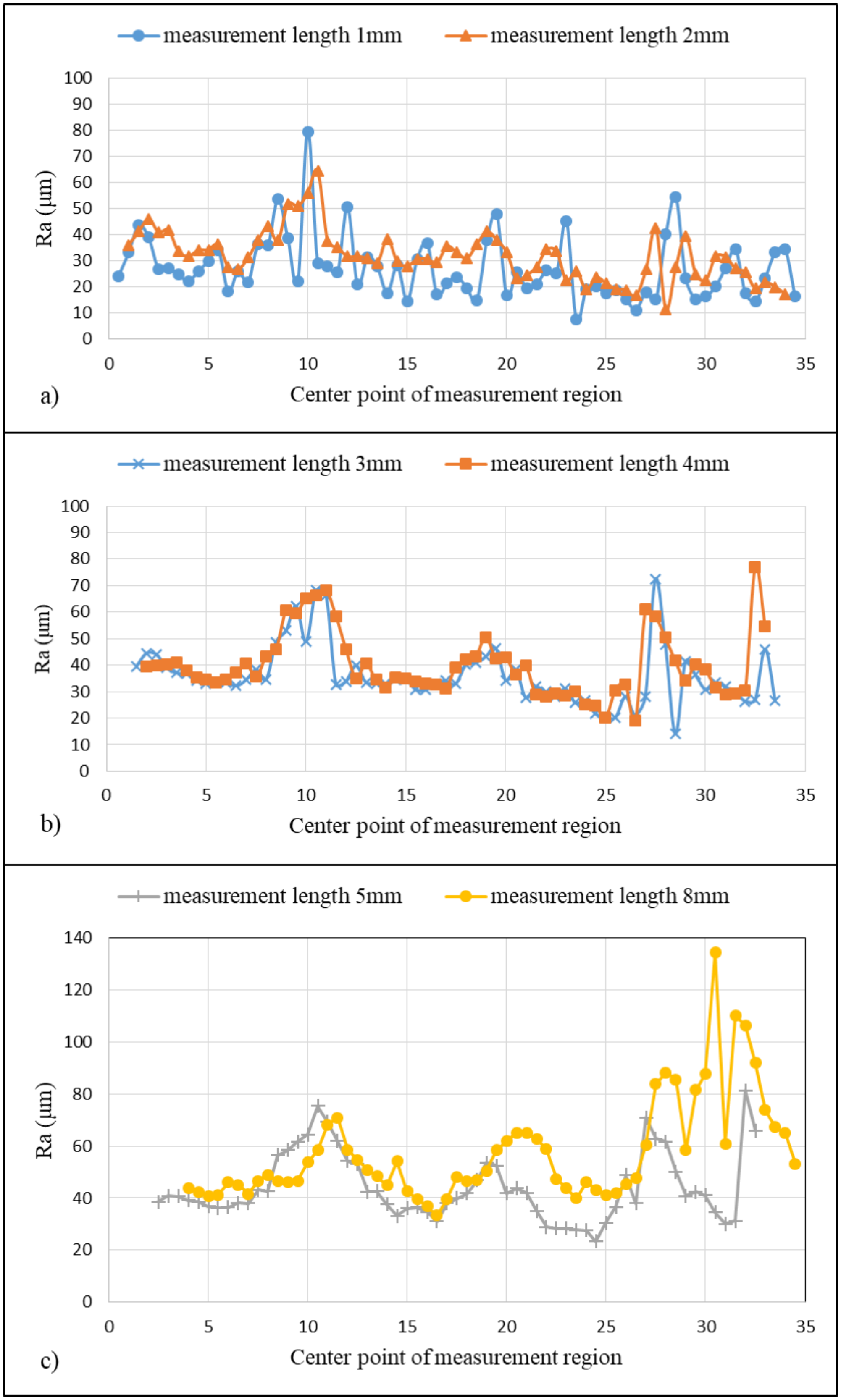

Figure 5-4. Sensitivity analysis for determination of measurement length

In the next sections of this chapter, the variation of the surface roughness along the edges of mount samples is investigated. The purpose of this study is to understand how the partitioning strategies (5-axis, 2+1+1-axis, rotary toolpath), overhang angle, and layer height variations affect the surface roughness. Furthermore, the roughness of the transition points between partitions are considered.

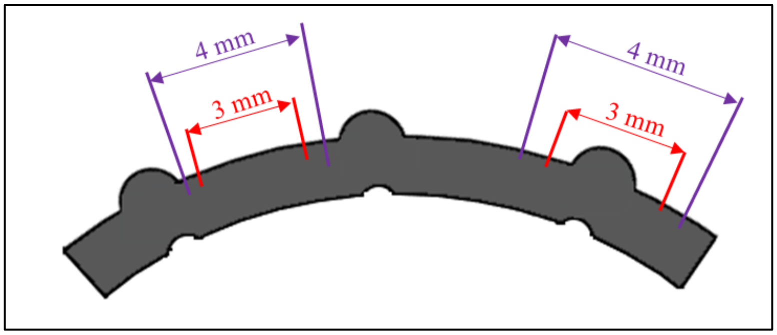

Figure 5-5. Comparison of measurements of transition points with layers inside partitions

To do this, Ra variations along the surface edges of the mount specimens are studied. However, the edge lengths of the case study specimens vary between 14 mm for the 5-axis sample to 35 mm for 2+1+1-axis samples. Therefore, if the specimen edges are divided into sequential 4 mm-length sections, 5 to 9 measurement regions will be available for the 5-axis and 2+1+1-axis samples (Figure 5-6) respectively. Consequently, based on what is shown in Figure 5-8, an increment of 0.5 mm is considered between start points of measurement regions. Although this causes a 3.5 mm overlap between measurement fields, it increases the number of resultant Ra data, which makes later interpretations more accurate.

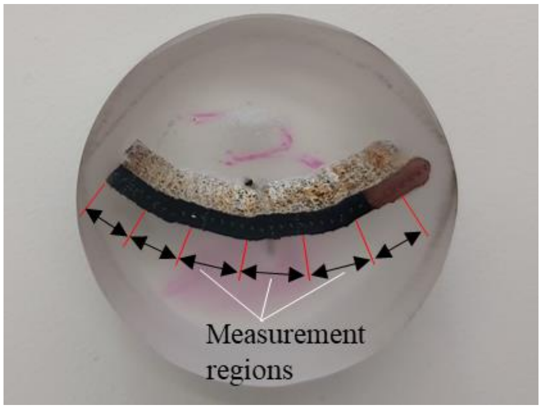

Figure 5-6. Measurement regions for sequential regions

5.1.3 *Roughness Variations for the 5-Axis Sample*

As mentioned before, the effect of two parameters: layer height variations and the tilted overhang angle on Ra are investigated. The layer height variation is associated with the build geometry, as illustrated in Figure 5-7. As the planar slice strategy is used for the dome fabrication, the real layer height increases when the overhang angle increases. The relation between the real layer height and the length of the mount edge arc is calculated by Equation (22).

$$Real\ layer\ height = \frac{Slice\ height}{\cos\left(\frac{L_p}{R}\right)} \tag{22}$$

R is the dome radius (21.5 mm for inner arc and 23.5 mm for outer arc) and L_p is the arc length of the partitions from the bottom layer (Shown in Figure 5-7 and the X-axis in Figure 5-9). The real layer height equals the slice height at the bottom layer of each partition but it increases gradually up to 25 percent larger than slice height at the top layer of the partitions for the 5-axis dome. It means the layer height is 0.5 mm in bottom layers and 0.7 mm in the top layer of the partition.

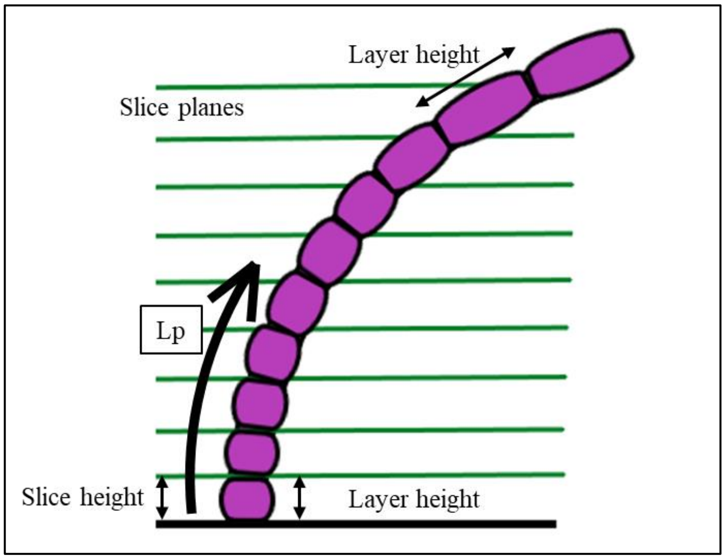

Figure 5-7. Layer height increase

To investigate the effect of the layer height increase on the Ra more accurately, another experiment can be done. In this future work study, the virtual model of the dome, which includes the ideal bead geometries can be modeled in a CAD software. It should be noticed that the shape of the beads change for each layer as they elongate in higher layers

(Figure 5-7). After a cross-section picture (from the same section that mounts are cut) is prepared, its Ra variation can be measured by the developed Matlab program. The achieved ideal Ra variation diagrams can then be compared with experimental ones. Modeling the part with variable bead height should be considered in a future study, as feedback systems related to controlling the layer heights are being developed.

Figure 5-8 depicts the 3rd partition of the 5-axis sample. The measurement direction starts from the bottom layers to the top layers of the partition.

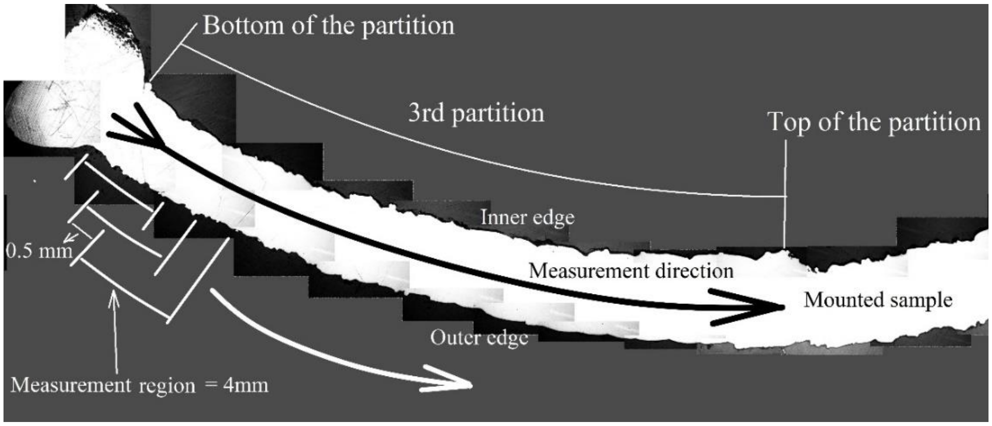

Figure 5-8. Direction of surface roughness measurement in 5-axis sample.

The measured Ra variations are shown in Figure 5-9. The horizontal axis is the center point location of the measurement region. For example, the Ra value of the first measurement region that starts from zero to 4 mm is represented by its center point which is 2 mm. This figure shows that the Ra of the inner surface of the 3rd partition varies between 25-47 μm whereas the outer ranges from 15-35 μm.

Apparently, the pattern for the Ra variation is similar in both surfaces. The Ra increases from the bottom of the partition and reaches its maximum at around L_p= 5 mm for the inner surface and L_p= 6 mm for the outer surface then decreases. For the inner surface, it keeps its initial value without any significant change after L_p= 7 mm. But, the Ra continuously falls to 15 μm in the outer surface.

However, Ra is lower for the outer surface. A closer look at Figure 5-8 and the surface pictures of Figure 5-9 visually supports these patterns, as the inner edge has more severe textures than the outer edges. Also in the higher layers, the layer surfaces are smoother which leads to lower Ra values. In the lower layers, there are several tiny collapsed material regions, which lead to a higher Ra value. Therefore, it can be inferred that real layer height increase can cause lower Ra, which aligns with the adaptive slicing strategies being proposed.

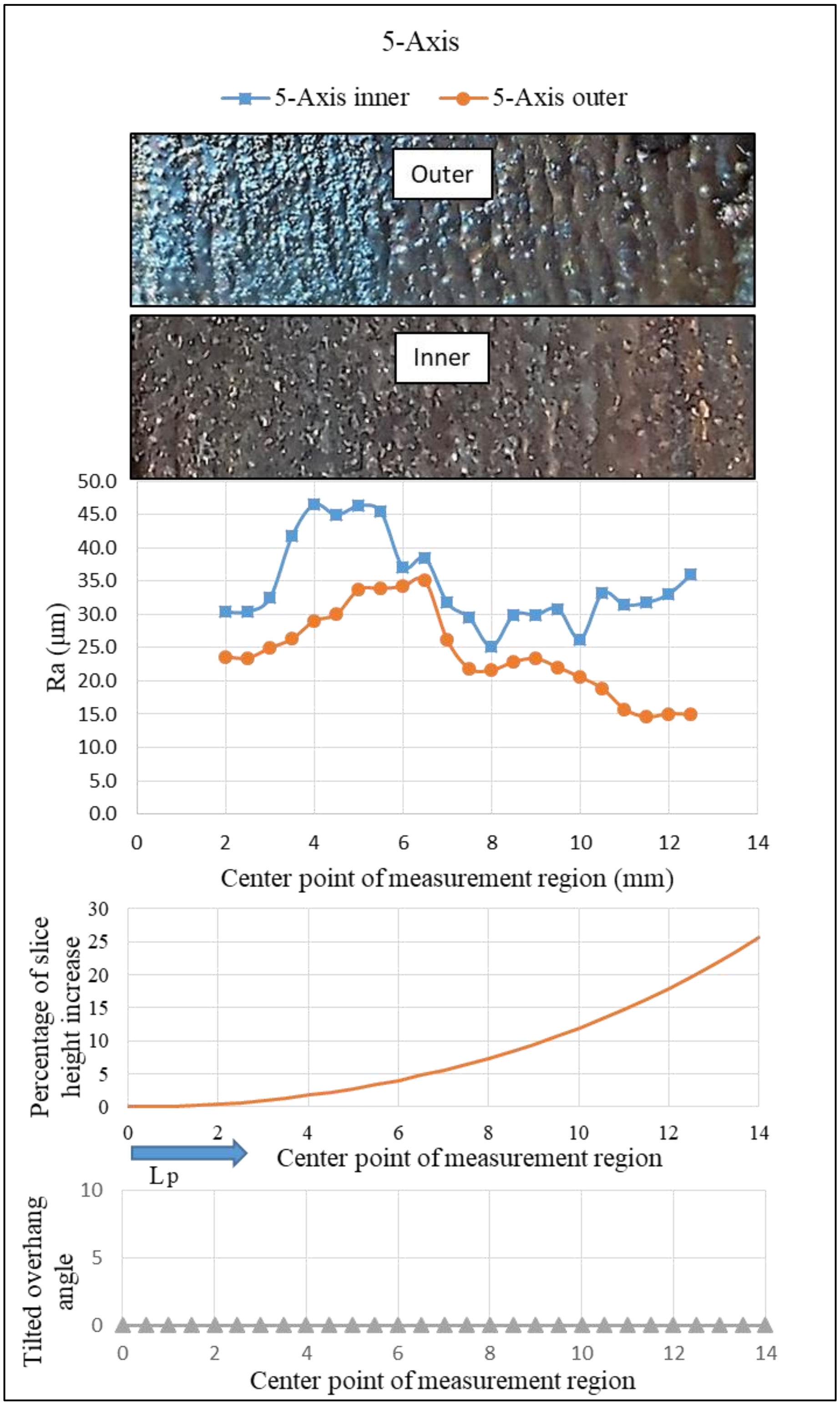

Figure 5-9. Inner edge of 5 axis sample

The tilted overhang angle is indicated in the figure and as the nozzle is always tangent to the surface, the tilted overhang angle is zero for all layers in 5-axis dome. Hence, it does not affect the surface roughness variations.

To assess whether patterns can be extracted, fast Fourier transformations (FFTs) are performed. FFT is a mathematical tool that converts numerical information from time (or here distance) to the frequency domain and vice versa [47]. It is applied here to find the length of repetitive patterns. Figure 5-10 shows the FFT of the 3rd partition for the 5-axis dome. Apparently there is no dominant frequency. The reason is that the analysis is performed for one partition so it does not contain the repetition of the partitions.

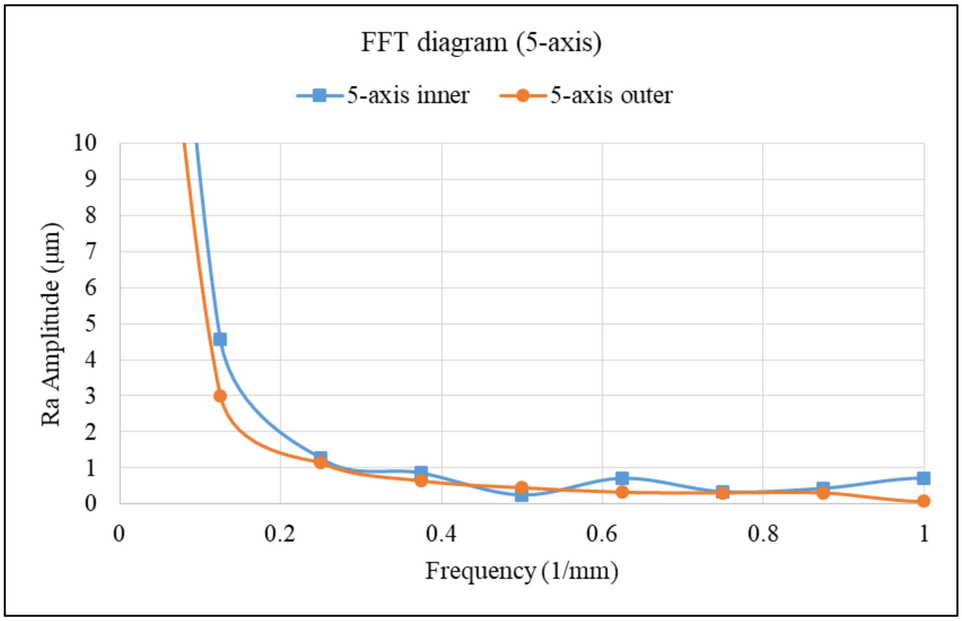

Figure 5-10. FFT diagram and frequency study of the 3rd partition for 5-axis dome

5.1.4 Roughness Variation for 2+1+1-Sample

Partitions 1-4- The 2+1+1-axis dome contains 8 partitions, the first four are in mount 1 and second four are in mount 2. In the first mount, the measurement starts from the bottom layer and measures the surface roughness up to the end of partition 4. The locations of the partition joints are shown in Figure 5-11. It can be detected that within the partitions, roughness variation is smooth whereas there is a small bulge at partition connection points.

Figure 5-12 depicts the Ra results for the partition 1-4 set. Although the Ra is almost constant within partitions, it gradually decreases from 40 µm in partition 1 to approximately

20 µm at the end of partition 3 for both sides. However, it increases in partition 4 to have the same value as the first partition. The Ra rises suddenly at transition points between partitions. This sudden growth is much higher at the connection point of partitions 3-4 in the outer surface. The severe growth is because of the noticeable bump shape texture in Figure 5-11.

A lag for the location of Ra peaks of the outer edge compared to the inner edge is detected in Figure 5-12. It means the peaks of the outer surface are shifted compared to the same peak of the inner surface. Also, this occurs for the diagrams of other samples as well. The X-axis of the diagrams is the length of the arc from the bottom of the partition and the length of the outer arc is larger than the inner. Thus, the textures appear with a lag for the outer edge. Here, the X-axis values are the length of the medium arc of the dome which has a diameter of 45 mm.

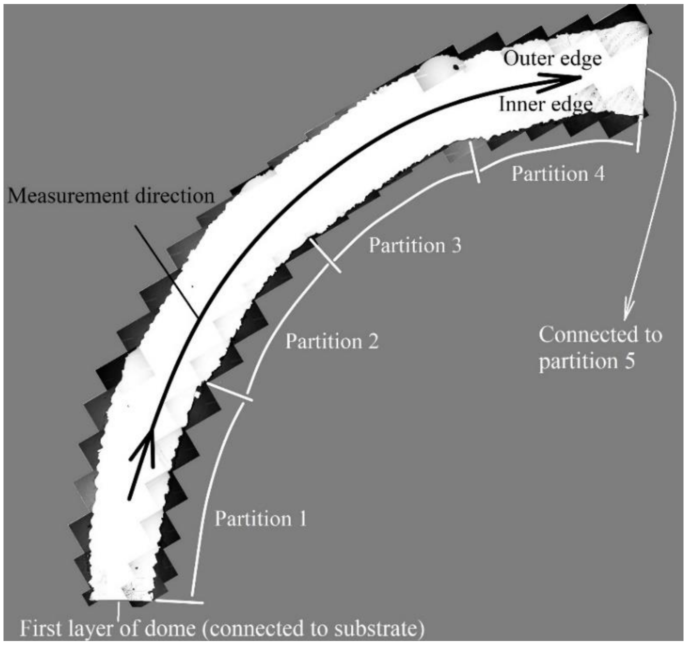

Figure 5-11. 2+1+1 axis specimen that contains partitions 1-4

The reason for the sudden increase in roughness at the connection points is because of the sudden change in nozzle orientation. Figure 5-13 indicates nozzle orientation in the first 3 partitions. During the deposition of a partition, the nozzle orientation keeps constant, but its orientation changes 22.5° (based on Figure 3-18). This severe alteration of deposition angle is more than the maximum recommended overhang angle which caused a little material collapse. Since the orientation of the nozzle at the connection points is in a manner that material collapses toward the outer surface, the outer surfaces have small inflation regions whereas the inner surfaces have small dints.

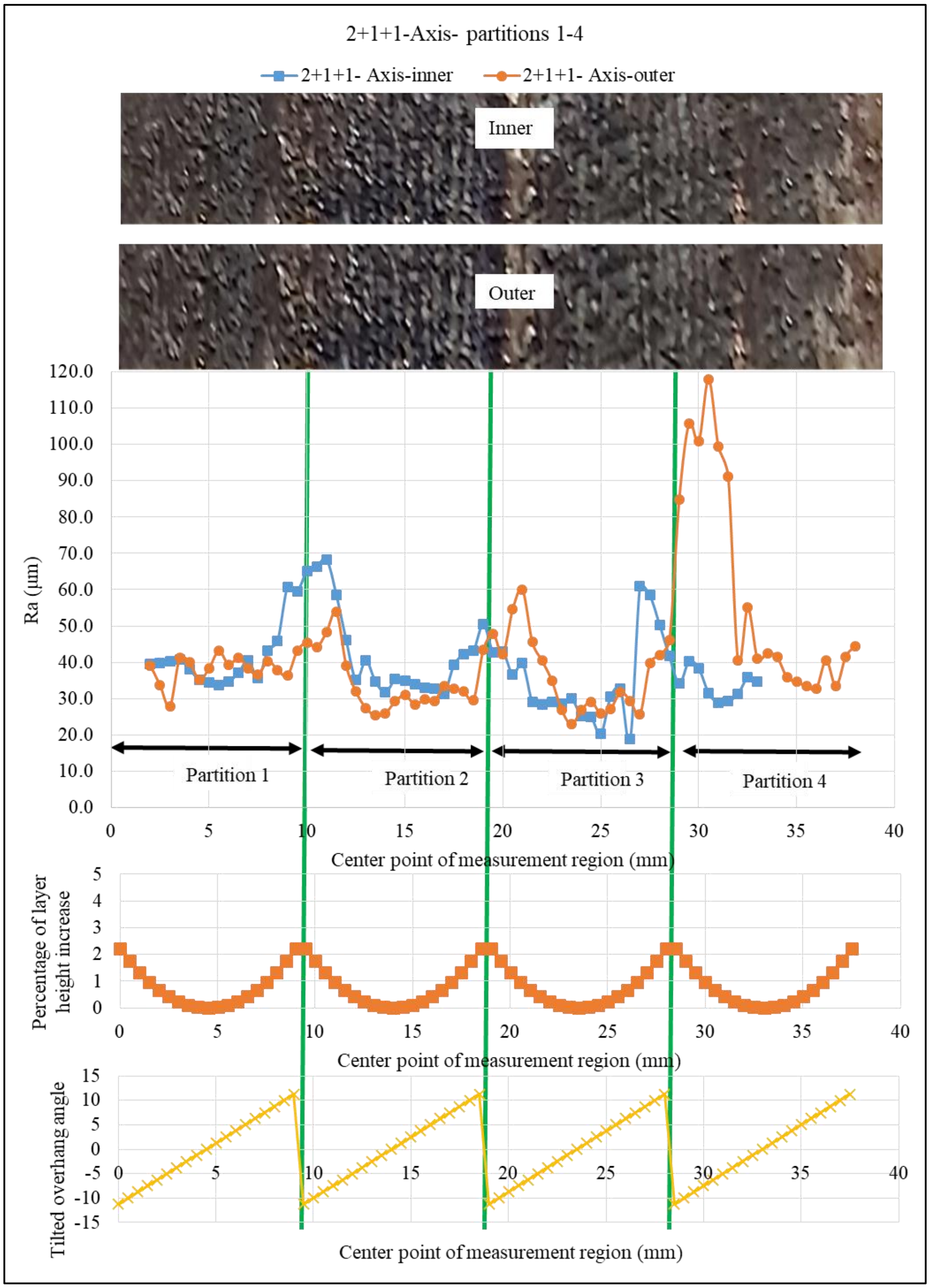

Figure 5-12. Surface roughness variation of 2+1+1-axis sample for partitions 1-4

The percentage of the layer height increase is 2.5 percent in each partition which is negligible. However, the overhang angle is zero for the middle layer within a partition and

11.25° at the bottom and top layers of each partition. The surface roughness variation can be affected by both overhang angle and heating/ cooling of partitions during dome fabrication.

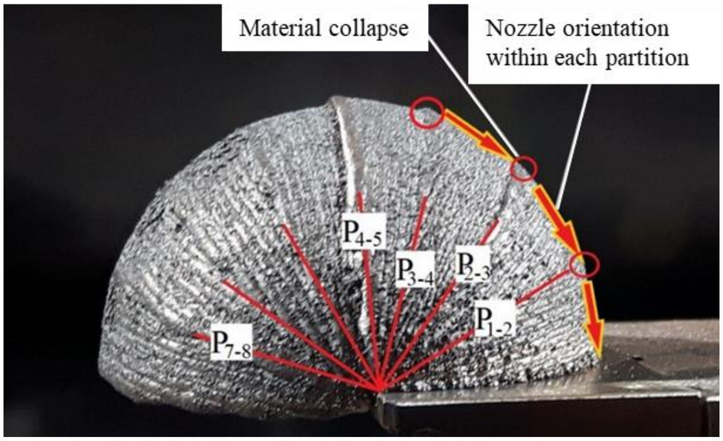
Material collapse
Nozzle orientation within each partition
P4-5
P3-4
P2-3
P1-2
P7-8

Figure 5-13. Material collapse because of sudden nozzle orientation change in 2+1+1 axis sample

Partitions 5-8- As Figure 5-14 shows, there are inconsistencies at the points between partitions 5-8 as well. Visually it can be recognized from the picture that the 6th partition has a better surface finish than other partitions. The Ra diagram shown in Figure 5-15 supports this as the Ra of inner and outer surfaces are 20 µm and 30 µm respectively for partition 6. Except for the Ra value associated with the top of the outer surface of partition 8, which has a sudden rise of Ra = 130 µm, the rest of transient points are less severe than the partitions 1-4. The transient point between partitions 7 to 8 is hardly noticeable.

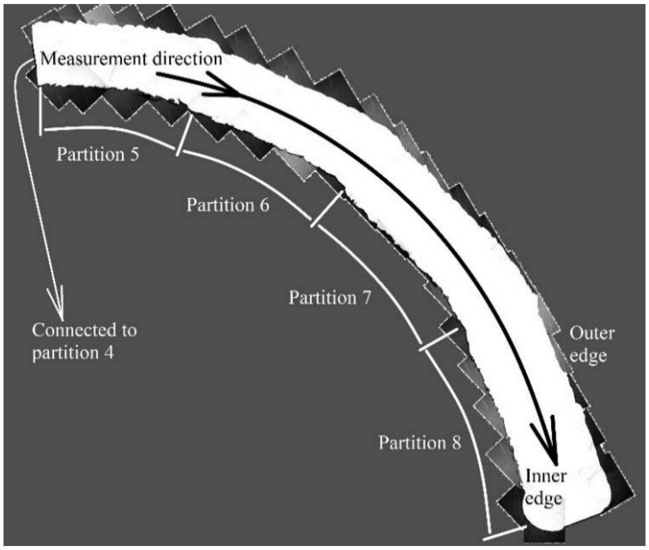
Measurement direction
Partition 5
Partition 6
Partition 7
Partition 8
Connected to partition 4
Outer edge
Inner edge

Figure 5-14. 2+1+1 axis specimen that contains partitions 5-8

There is no obvious dependency between the layer height increase /tilted overhang angle and surface roughness.

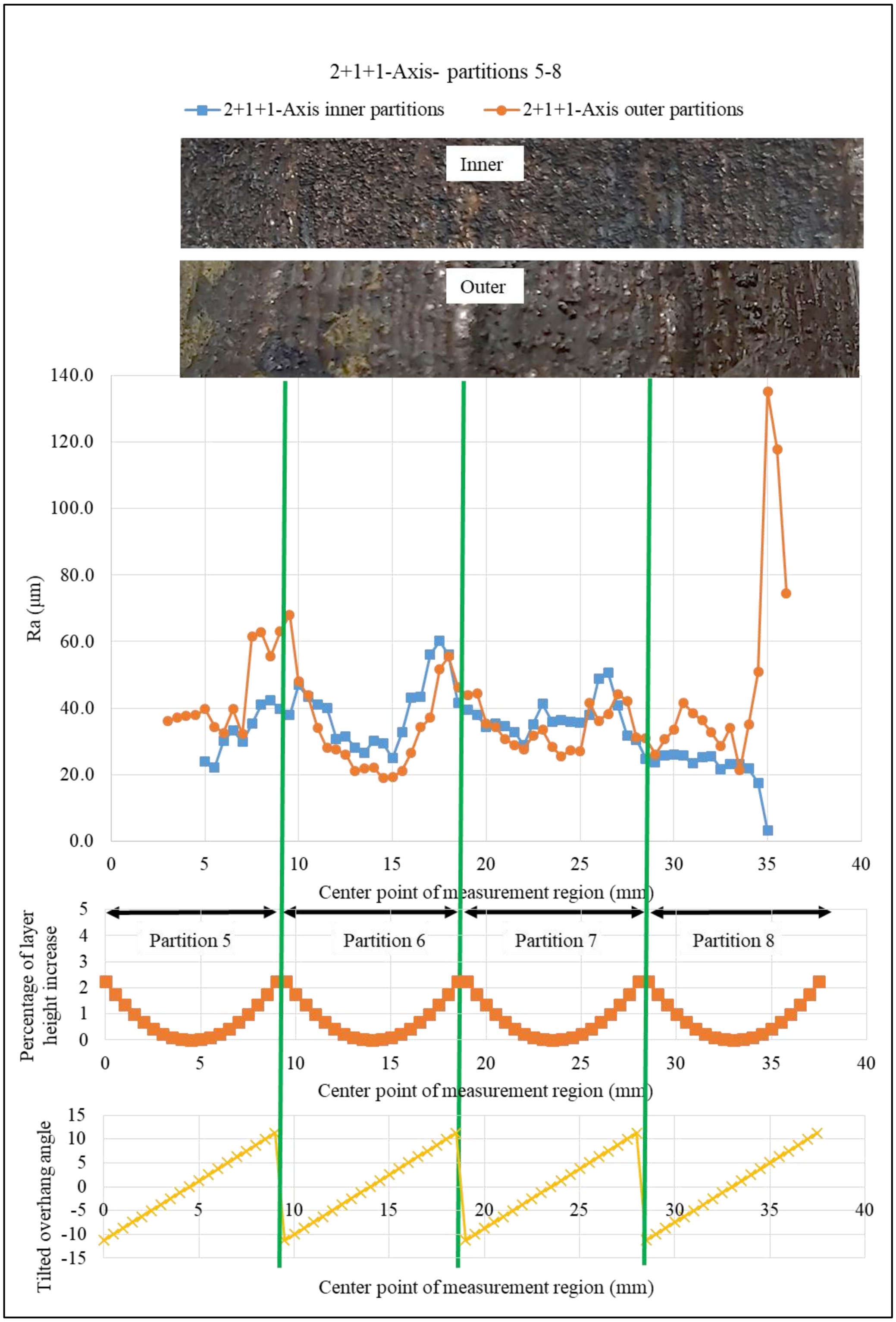

Figure 5-15.Surface roughness variation of 2+1+1 sample for partitions 5-8

The FFT analysis of the 2+1+1-dome (Figure 5-16) shows a dominant frequency of 0.1102 (amplitude of 3 and 5.5 µm). If the frequency is converted to wavelength, it results in a value of 9.07 mm. this value is near the partition lengths (8.83 mm); there is a 9% difference. The length of the partition is one-eighth of the periphery of a half-circle. The main reason for the difference between the FFT result and the real length is the frequency is a discrete value within an FFT analysis.

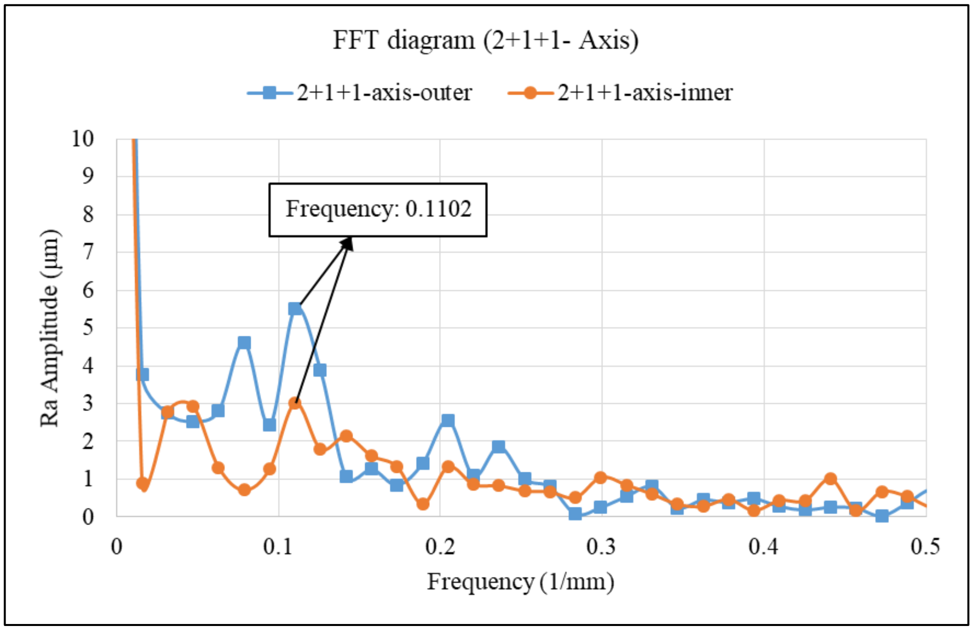

Figure 5-16. FFT diagram and frequency study of the 2+1+1-axis dome

Here the equation between the frequency and wavelength is:

$$wavelenth = \frac{1}{frequency} \tag{23}$$

The frequency is the number of waves in 1 mm length and wavelength is the length of the repetitive wave.

5.1.5 Roughness Variation for Rotary Sample

The slice height of the rotary toolpath is 0.3 mm so it is expected to have a better surface finish than the wedge shape partitioning. However, as Figure 5-17 shows, the bottom layers are rougher and there are two texture defects (shown in red circles) that increase the Ra at the 23 mm point for the outer surface and the 27 mm point for the inner surface. The inner dent is located at the connection point between Sections 2 and 3. An interesting finding is that Ra drops at the connection points between Sections 2 and 3 for the outer surface.

The real layer height for bottom layers is approximately 2.8 times the slice height. This means that the layer height is about 0.85 mm for the lower layers (Section 3.2.2). However, the tilted overhang angle is zero because the nozzle is always tangent to the surface. Excluding the increase in Ra where the surface defects are located, the observed Ra variations for the outer surface tend to follow the curve of layer height increase (Figure 5-18). The FFT study of the rotary sample shows no dominant frequencies (Figure 5-19), as expected.

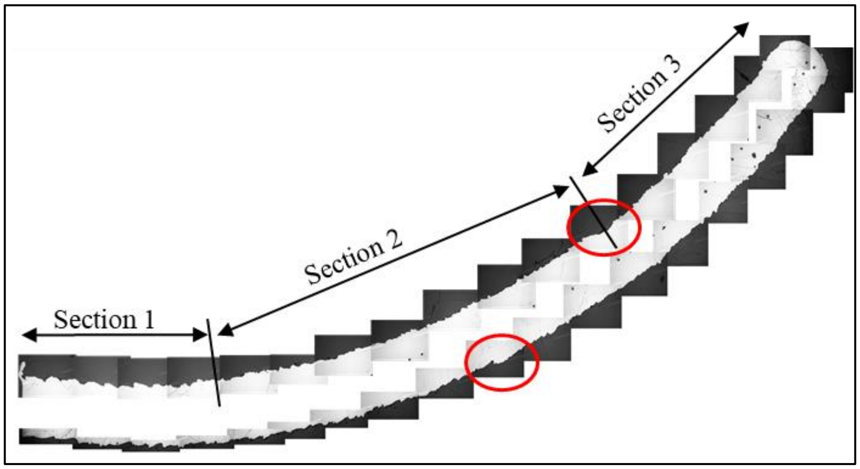

Figure 5-17. Rotary toolpath mount sample

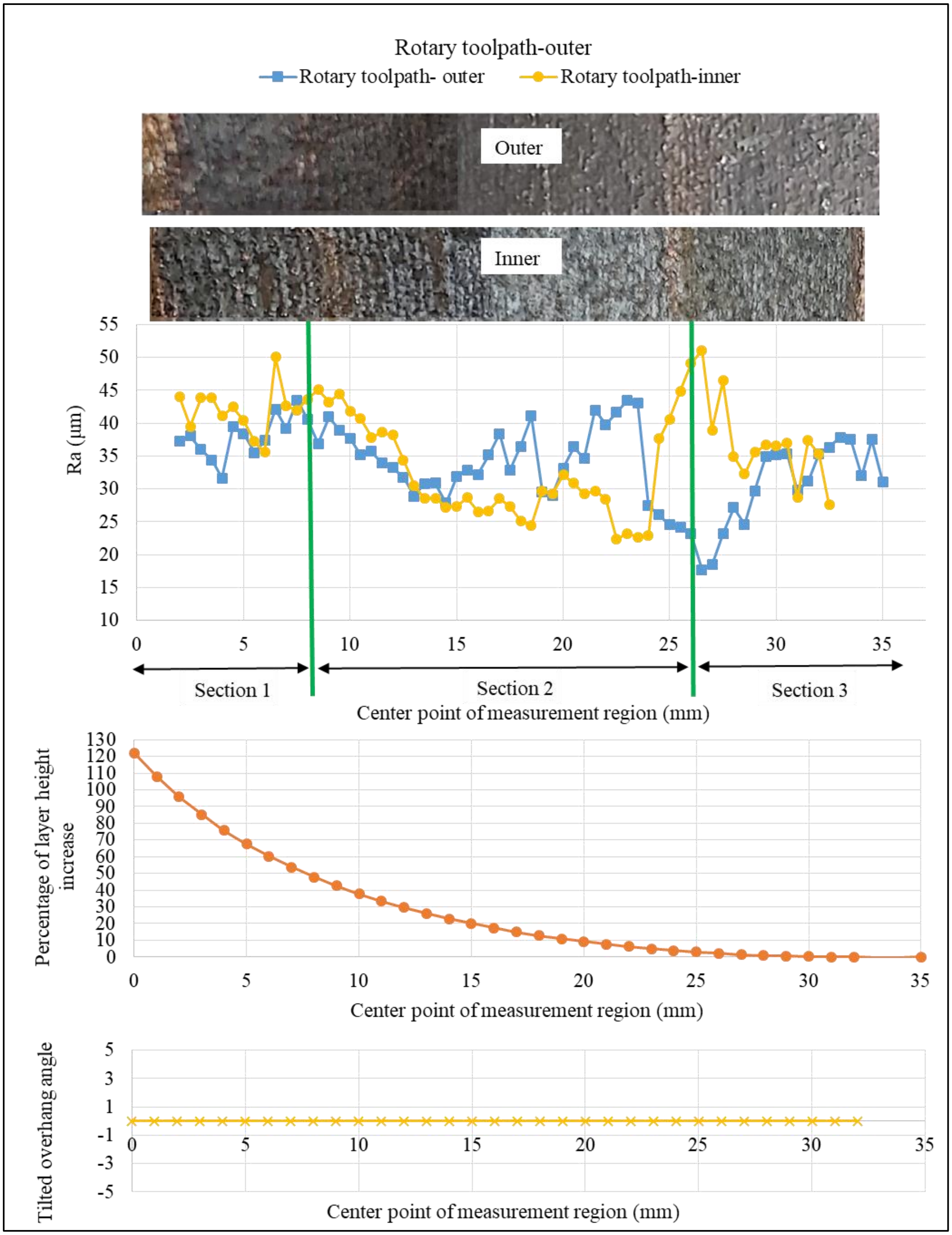

Figure 5-18. Ra variation of rotary toolpath sample- inner surface

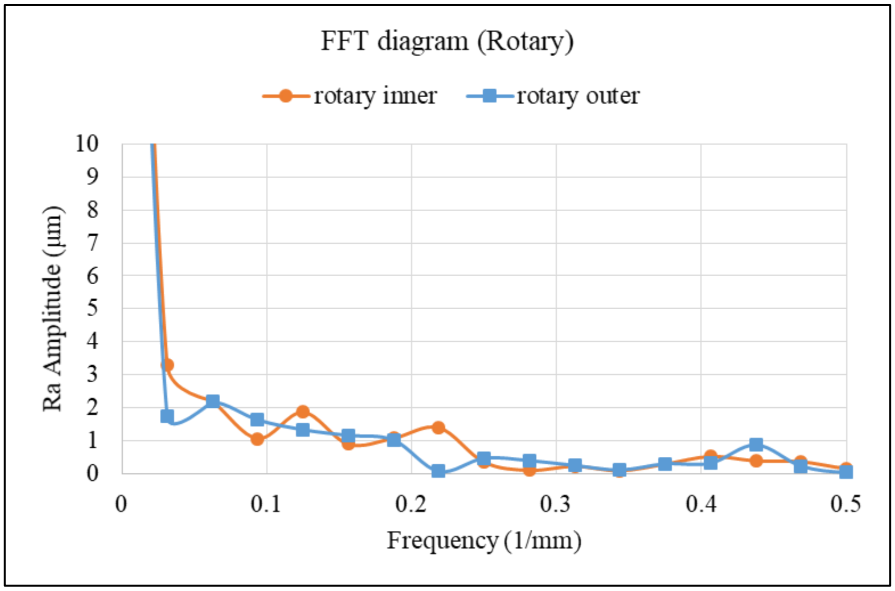

Figure 5-19. FFT diagram and frequency study of the rotary sample

5.1.6 *Statistical Analysis of the Mount Solution*

Table 5-3 shows the outcomes when performing statistical analyses for the mount solution results. Based on the observed average values, the 2+1+1-axis outer surface has the worst values, and the 5-axis outer surface shows the most satisfactory results. In addition to this, the 5-axis outer surface has the least variation of Ra (Max-Min=20.44)

Table 5-3. Table of primary statistical analysis of Ra for the mount solution

Best Worst	5-Axis Inner	5-Axis Outer	2+1+1 Inner	2+1+1 Outer	Rotary Inner	Rotary Outer
Average	34.65	24.18	36.52	41.11	35.31	33.87
Median	32.10	23.40	35.25	36.82	35.55	35.13
Min	25.15	14.60	3.08	18.95	22.30	17.71
Max	46.49	35.04	68.35	135.28	51.05	43.51
Max-Min	21.34	20.44	65.35	116.33	28.75	25.8
Average - Median	2.54	0.78	1.27	4.29	-0.23	-1.26

A distribution analysis based on the probability density of the results is implemented to extract more accurate results. In order to find the proper distribution technique that fits the data better, the p-values of four distributions, Weibull, Gamma, Burr, and Chi-squared, are compared. As Table 5-4 shows, the Burr distribution fits the data with the highest p-values for the Kolmogorov-Smirnov test (confidence interval=0.05).

Table 5-4. P-values of different distributions

rejected	best	Weibull	Gamma	Burr	Chi-squared
5-Axis inner		0.23	0.28	0.88	0.21
5-Axis outer		0.86	0.95	0.76	0.84
2+1+1-Axis inner		0.0035	0.19	0.46	0.57
2+1+1-Axis outer		0.0004	0.0012	0.77	0.0001
Rotary-inner		0.36	0.41	0.32	0.55
Rotary-outer		0.9	0.32	0.96	0.016
Sum		2.3539	2.1512	4.15	2.1861

The histograms and Burr distributions for the Ra samples are shown in Figure 5-20. To interpret the results, the statistical values extracted from Burr distribution are shown in Table 5-5.

Based on the mode values shown in Figure 5-21, the 5-axis outer surface has the finest surface finish and the rotary outer has the roughest surface. Also, 2+1+1-axis outer has the most varied Ra. Altogether, the 5-axis sample has the best surface roughness. The reason is that just one partition is studied and the Ra peaks associated with the transition points do not increase the Ra. This study shows that partitioning introduces unique challenges, and control strategies for a region within a partition, and the transient region, may need to be different.

Kurtosis is the relative peakedness or flatness of the distribution. A positive value means a peaked distribution, whereas a negative value indicates the distribution is flatter. Skewness describes the asymmetricity of a distribution around its mean value. A positive value shows the distribution is asymmetric toward positive values and negative shows it is tilted toward negative values. Zero skew means that the distribution is symmetric. Both the 5-axis inner and 2+1+1-axis outer values are skewed to larger Ra values. It means they contain radical rough textures such as the bumps. Therefore, it can be concluded that visual controls for one surface may provide insufficient knowledge about the build quality.

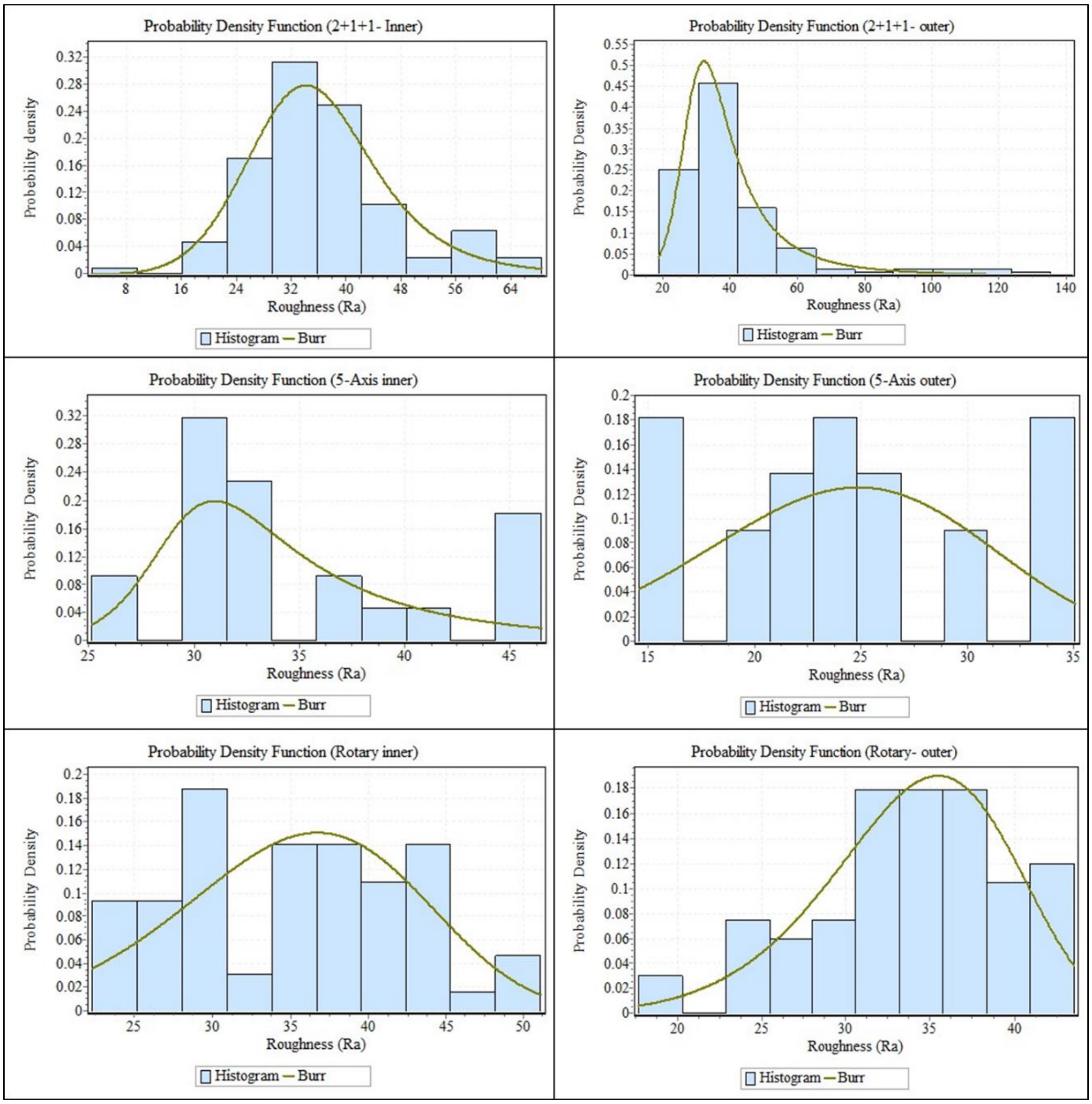

Figure 5-20. Burr distribution of the mount solution results.

Table 5-5. Data extracted from Burr distribution

	Mode Ra	Probability density	Standard deviation	Skewness	Kurtosis
2+1+1-Inner	34	0.28	10.78	0.98	3.49
2+1+1-Outer	32.5	0.5	20.5	11.18	>>100
5-Axis inner	31	0.2	7.8	3.24	28.95
5-Axis outer	25	0.13	6.4	-0.11	-0.19
Rotary inner	37	0.15	7.6	-0.277	-0.06
Rotary outer	35.5	0.19	5.58	-0.47	0.21

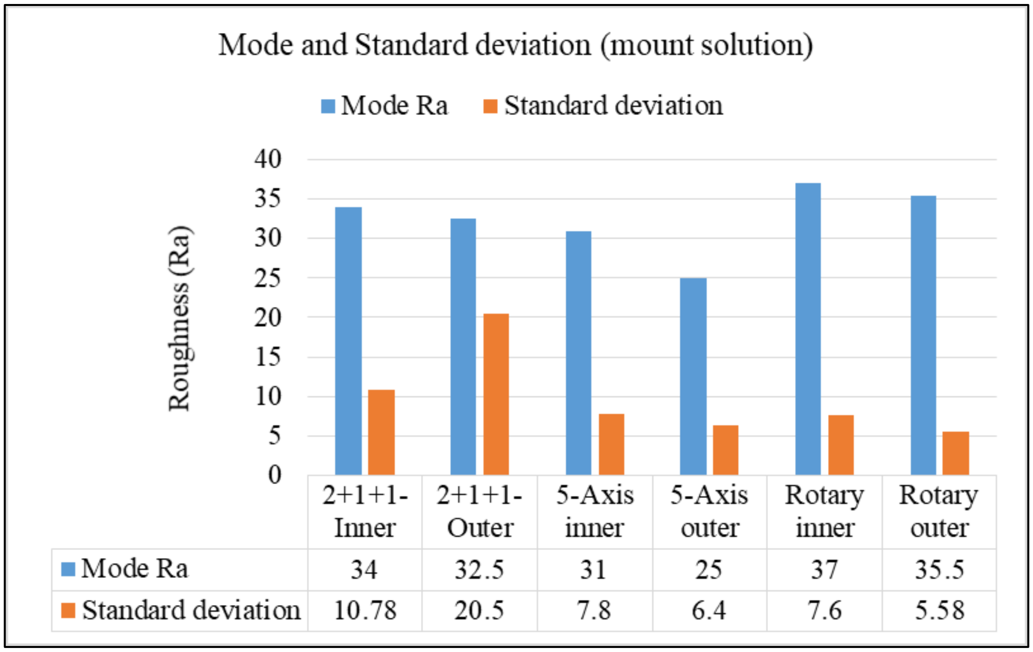

	2+1+1-Inner	2+1+1-Outer	5-Axis inner	5-Axis outer	Rotary inner	Rotary outer
🟦 Mode Ra	34	32.5	31	25	37	35.5
🟧 Standard deviation	10.78	20.5	7.8	6.4	7.6	5.58

Figure 5-21. Mode and standard deviation (mount solution)

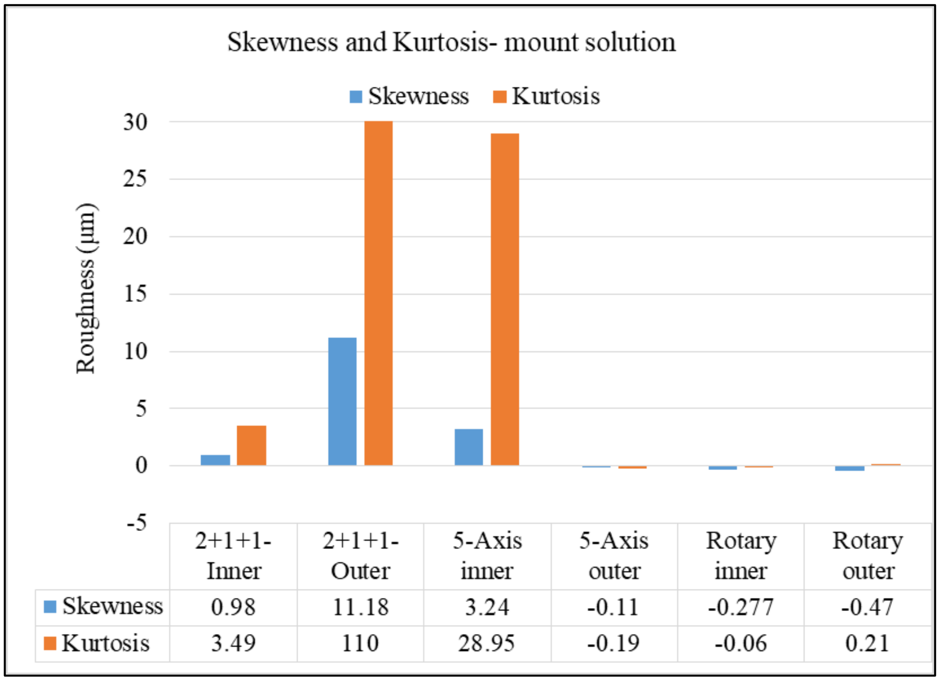

	2+1+1-Inner	2+1+1-Outer	5-Axis inner	5-Axis outer	Rotary inner	Rotary outer
🟦 Skewness	0.98	11.18	3.24	-0.11	-0.277	-0.47
🟧 Kurtosis	3.49	110	28.95	-0.19	-0.06	0.21

Figure 5-22. Skewness and Kurtosis- mount solution

5.2 *Surface Roughness Measurements from the 3D Point Cloud Data*

To measure the roughness from a 3D point cloud, a txt file containing point coordinates is used. This file contains all surface points that are generated by the laser scanning process which needs to be pre-processed. As an example, Figure 5-23 depicts the point cloud pre-processing of the partition 5-8 specimen for the 2+1+1-axis sample.

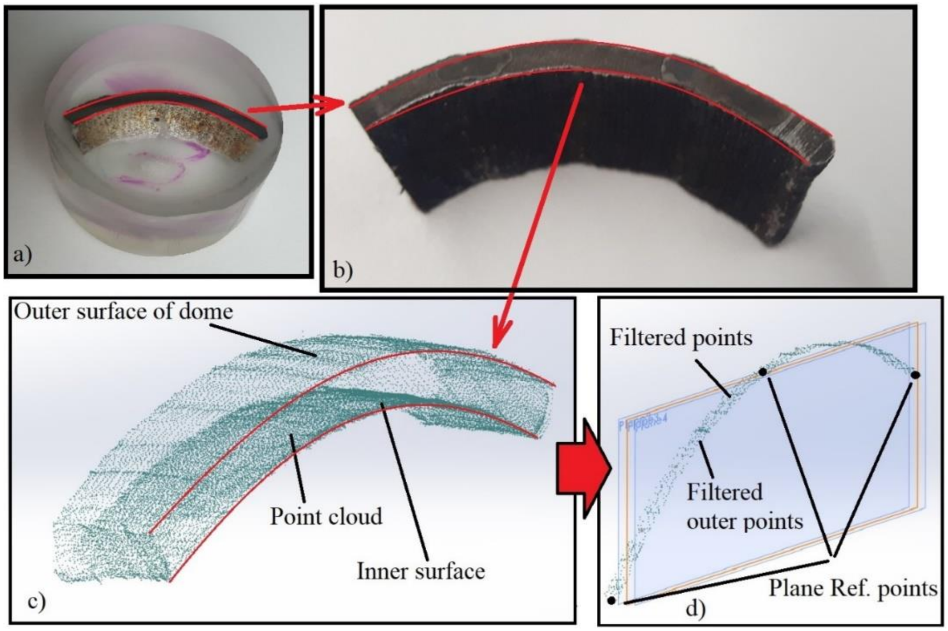

Figure 5-23. Example of point cloud filtration of partitions 5-8 of 2+1+1 sample

The results of this method need to be verified by another accepted method. Since the mount solution has accepted results, it can be used to validate the 3D point cloud solution. As Figure 5-23 (a) shows the Ra is measured for surface edges in mount solution. Therefore, if Ra is measured for the same region by the 3D point cloud method, its results can be verified by comparing them to the mount results. The following Ra result diagrams are measured for the same regions that mount method experiment was performed.

The accuracy of the 3D scanner is a crucial parameter in the validity of the results. The 3D scanner that is utilized to collect the point cloud data has an accuracy of ±0.044 mm. Hence, the Ra values presented in the diagrams have the ±0.044 mm of error. In the Matlab program, the distance between two boundary planes is set to $f = 0.4$ mm, and the distance coefficient set to $n = 5$ for all measurements.

5.2.1 *Roughness Variations for the 5-Axis Sample from the 3D Point Cloud Data*

Figure 5-24 compares the Ra results achieved by 3D point cloud program with the mount solution results. The diagrams show that there are similar trends for the two methods. The Ra values are usually smaller for 3D point cloud method when compared to the mount solution, and the curves have less oscillations. Also it shows that Ra for the inner surface is comparably less than for the outer. As expected, the FFT results for the 3D point cloud results are similar to those for the mount solution. There is no dominant frequency for the 5-axis sample (Figure 5-25).

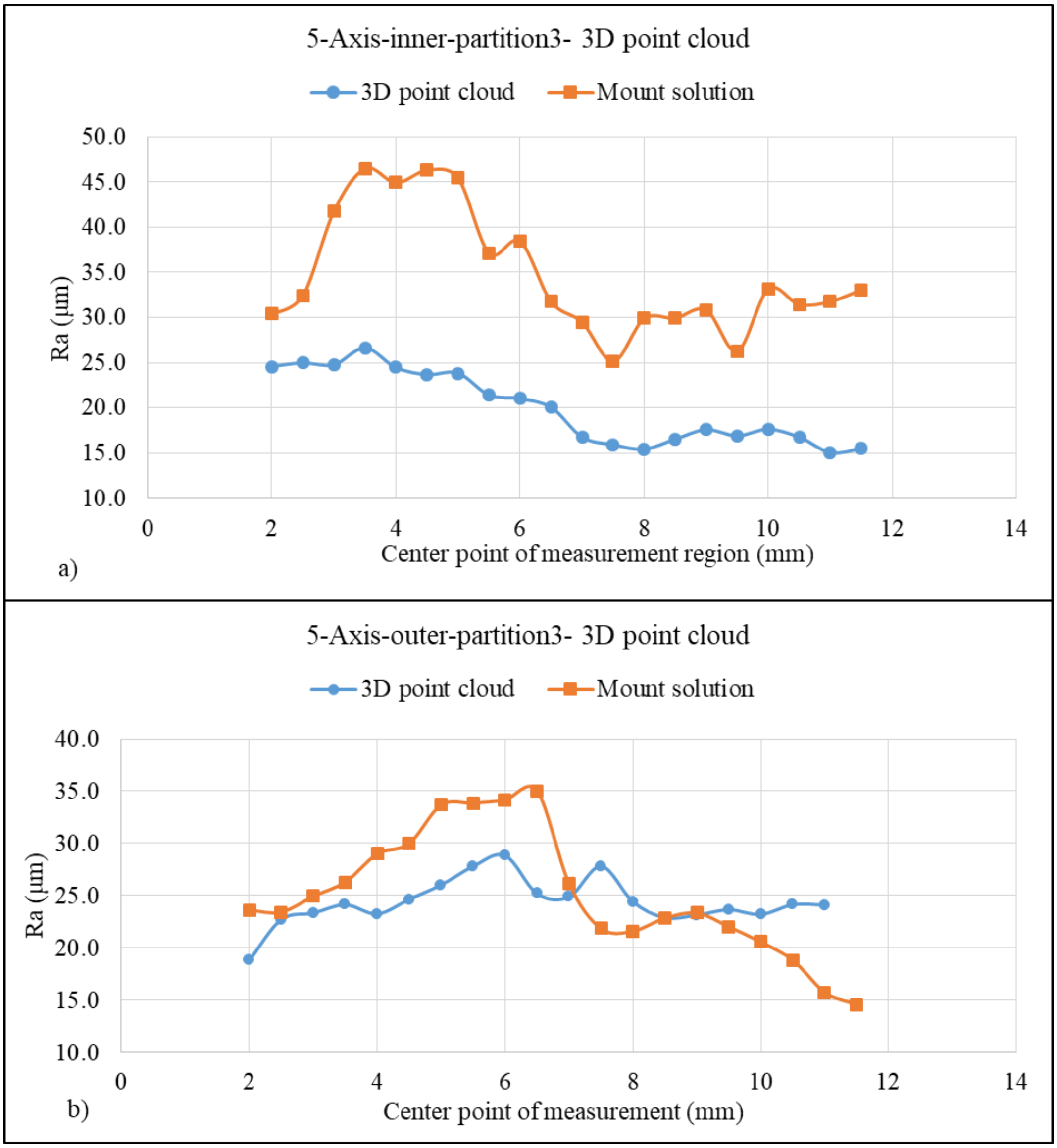

Figure 5-24. Comparison of R_a between 3D point cloud and mount solutions for 5 axis-partition 3 (a) Inner surface (b) Outer surface

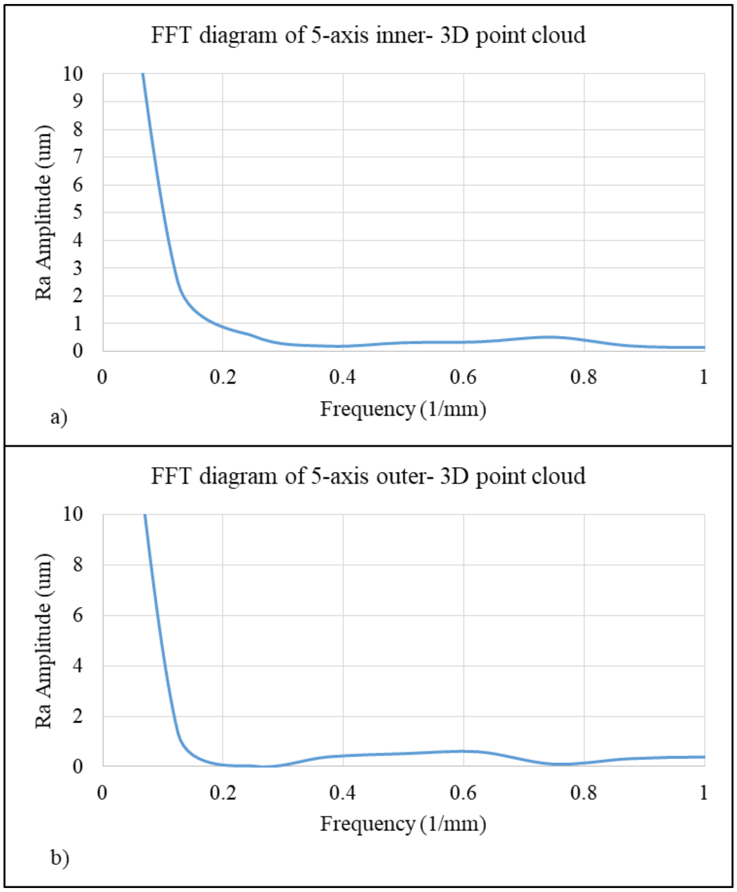
FFT diagram of 5-axis inner- 3D point cloud

FFT diagram of 5-axis outer- 3D point cloud

Figure 5-25. FFT diagram and frequency study of the 5-axis by 3D point cloud (a) Inner surface (b) Outer surface

5.2.2 Roughness Variations for the 2+1+1-Axis Sample from the 3D Point Cloud Data

In Figure 5-26 and Figure 5-27, the point cloud results for partitions 1-4 and partitions 5-8 for the 2+1+1-axis sample are shown. The measurement regions are indicated by the red curves on the point cloud. The measurement edges are the same ones that were measured for the mount program. The average point density is approximately 110, 70 points/mm^2 for specimens for partitions 1-4 and partitions 5-8, respectively.

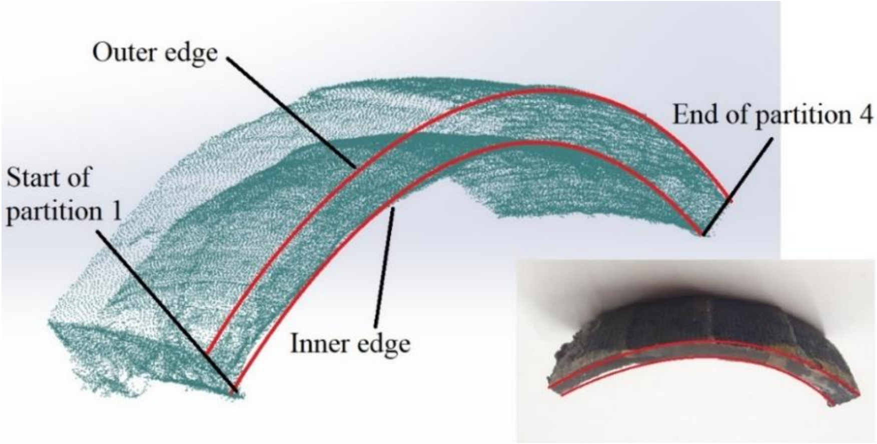
Outer edge
End of partition 4
Start of partition 1
Inner edge

Figure 5-26.Point cloud of partitions 1-4 of 2+1+1 sample

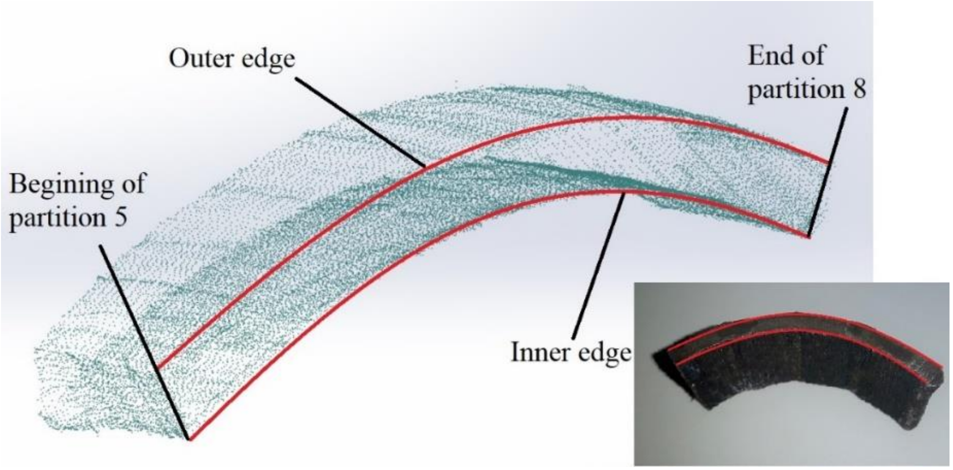
Outer edge
End of partition 8
Begining of partition 5
Inner edge

Figure 5-27. Point cloud of partitions 5-8 of 2+1+1 sample

The surface roughness results for partitions 1-4 are presented in Figure 5-28 for the inner and outer edges. The curve patterns match the result curves for the mount sample. As with the previous example, the curves from the 3D point cloud solution tend to have smaller values. The dimensional inaccuracy of the input data (±0.044) explains the shift between the mount and the 3D point cloud data illustrated in the diagrams.

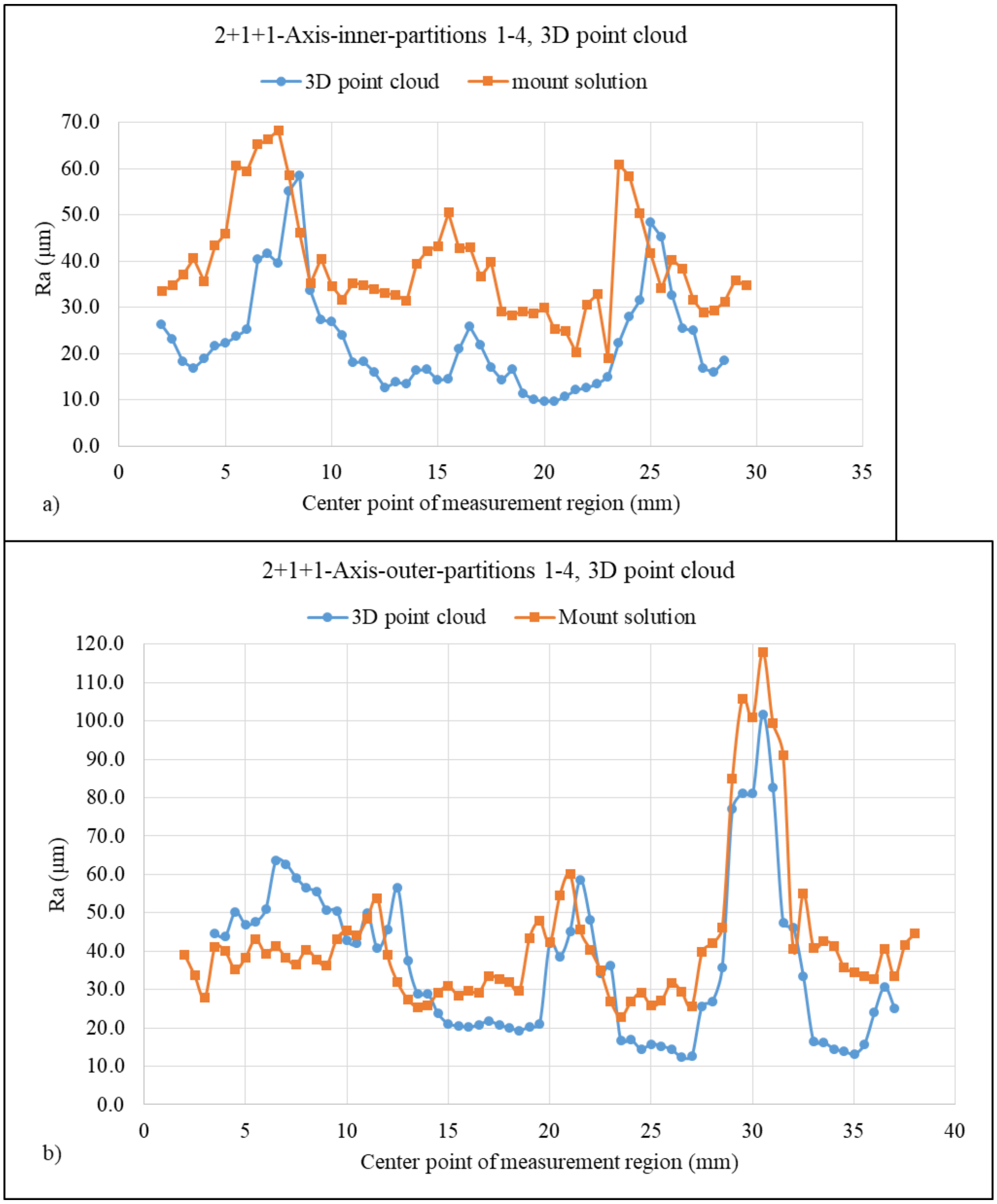

Figure 5-28. Comparison of R_a between 3D point cloud and mount solutions for 2+1+1 axis-partitions 1-4 (a) Inner surface (b) Outer surface

Figure 5-29 compares results of specimen containing partitions 5-8 of 2+1+1-axis sample with results of the same sample measured by mount solution. Unlike the results of partitions 1-4, here, the 3D point cloud does not show any recognizable pattern.

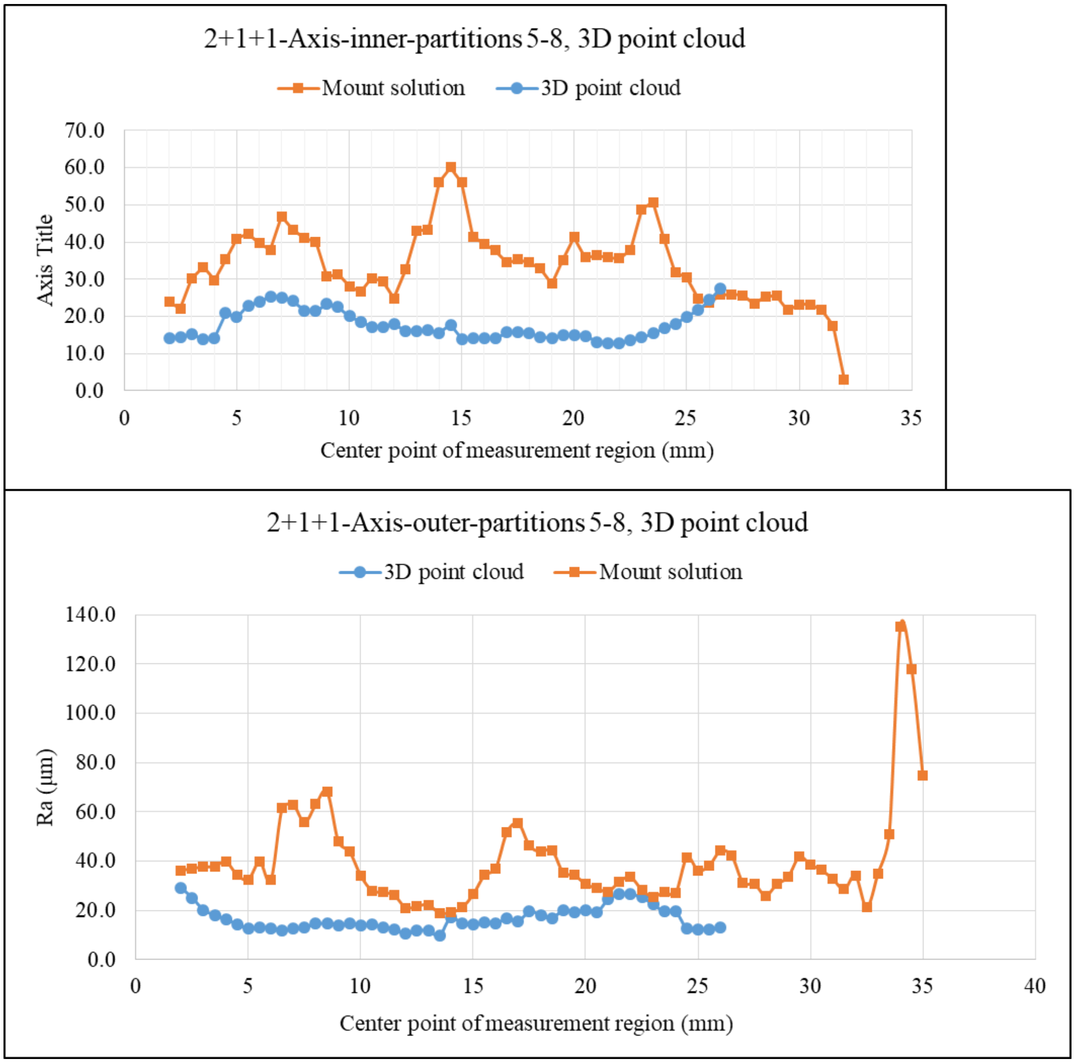

Figure 5-29. Comparison of R_a between 3D point cloud and mount solutions for 2+1+1 axis-partitions 5-8 (a) Inner surface (b) Outer surface

The FFT analysis of the inner surface shows two dominant frequencies of 0.0625 and 0.125 for the inner surface with an amplitude of 2 µm. The associated wavelengths are 16 and 8 mm (Figure 5-30 (a)). The outer surface has a frequency of 0.11 with an amplitude of 4.3 µm. The related wavelength is 9.1 mm which is comparable with the partition length (8.83 mm) and matches the results from the 2D data assessment.

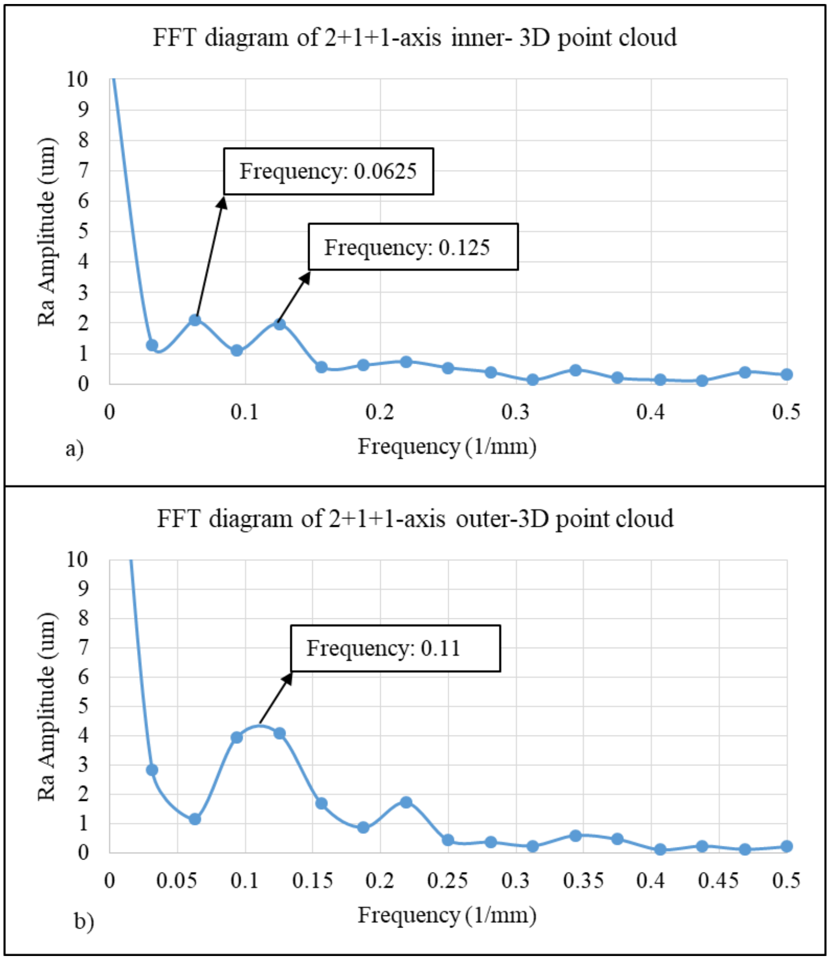

Figure 5-30. FFT diagram and frequency study of the 2+1+1-axis by 3D point cloud (a) Inner surface (b) Outer surface

5.2.3 Roughness Variations for the Rotary Toolpath Sample

Figure 5-31 shows the variation of Ra along the slicing direction for both the mount and 3D point cloud solutions. The values and patterns are similar. The Ra of the 3D point cloud data exceeds the Ra measured by mount solution in some regions.

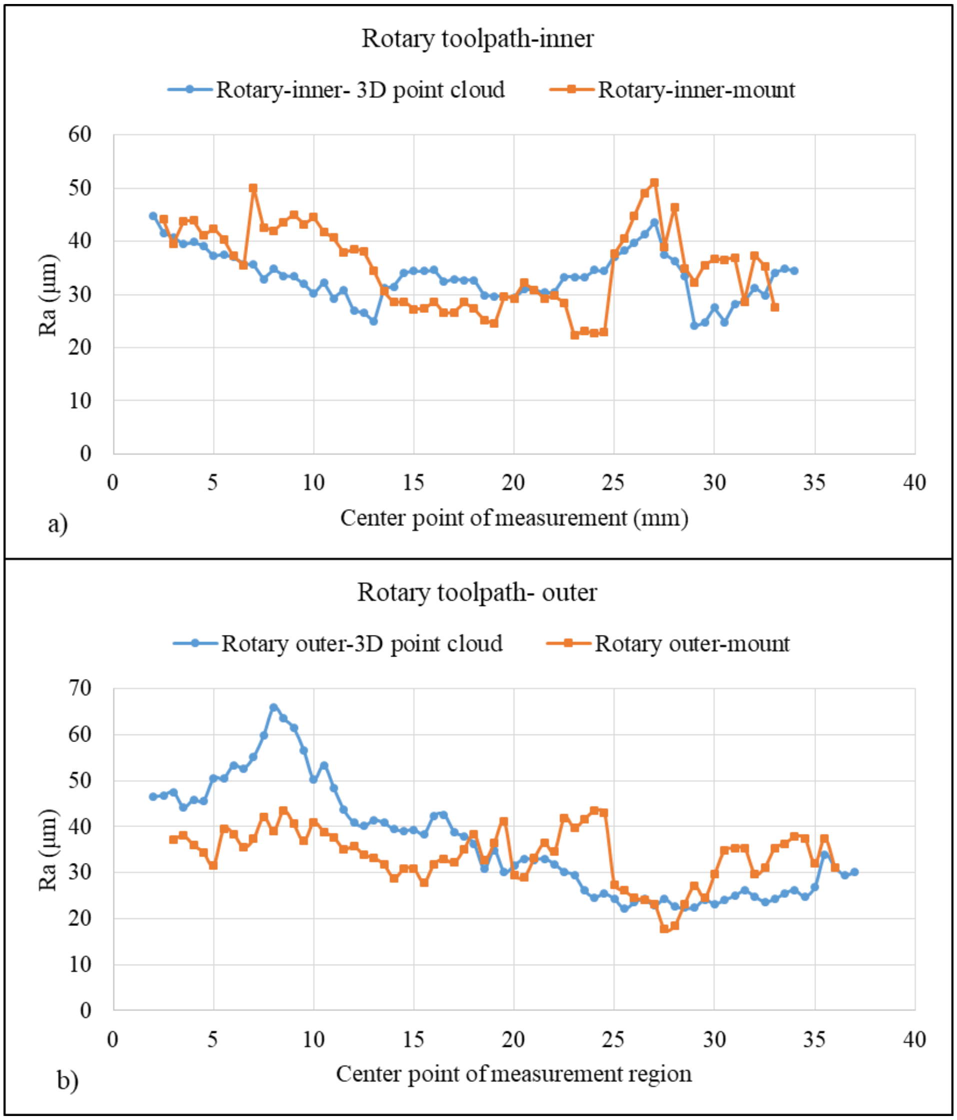

Figure 5-31. Roughness variation of rotary toolpath sample

5.2.4 Sensitivity Study for the 3D Point Cloud Program

Three parameters may affect the validity of the resultant Ra of 3D point cloud program: the point cloud density, the distance between boundary layers, and the distance coefficient. When the Ra diagrams of partitions 1-4 are compared with partitions 5-8, it is concluded that point cloud density affects the validity of results, indicating that a higher point density results in a more accurate Ra. Also, the applied 3D scanner should have a suitable accuracy compared to the roughness of the surface. Further investigations for non-contact surface roughness measurements should be conducted.

Distance coefficient (n) and distance between boundary planes- To explore the sensitivity of the distance between the boundary layers and the distance coefficient, four experiments are conducted using the 3D point cloud data for the 2+1+1-axis inner surface. The input parameters of the sensitivity test are presented in Table 5-6. As the Ra diagrams show in Figure 5-32, these parameters do not significantly affect the Ra results.

Table 5-6. Input parameters of sensitivity experiments

	Distance between boundary layers	Distance coefficient
Experiment 1	0.3	1
Experiment 2	0.3	10
Experiment 3	0.6	1
Experiment 4	0.6	10

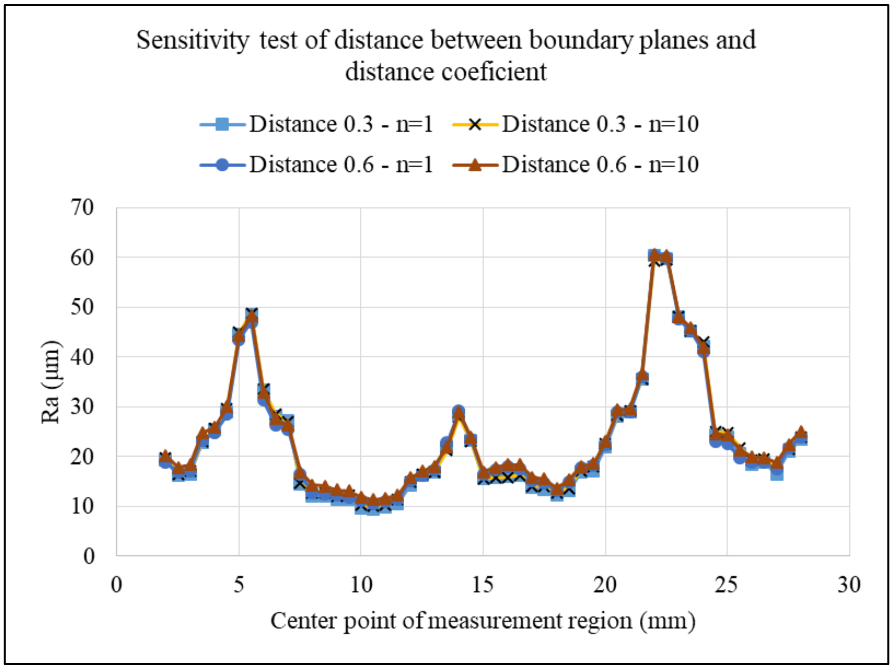

Figure 5-32. Sensitivity test of distance between boundary planes and distance coefficient

A statistical analysis was implemented in the previous section for the mount solution. For the 3D point cloud results, the statistical analysis is applied to the 2+1+1-axis partitions 1-4 sample as it shows similar patterns compared to the mount results.

5.2.5 *Statistical analysis of the 3D point cloud solution*

Table 5-7 shows the p-values of four distributions. The Burr distribution is chosen for statistical analysis.

Table 5-7. P-values of different distributions of 3D-point cloud solution

	Weibull	Gamma	Burr	Chi-squared
2+1+1-Axis inner- Partitions 1-4	0.3	0.7	0.86	0.027
2+1+1-Axis outer- Partitions 1-4	0.27	0.35	0.27	0
Sum	0.57	1.05	1.13	0.027

As Figure 5-33 shows, all the values for the Average, Min, and Max are smaller with the 3D point cloud solution.

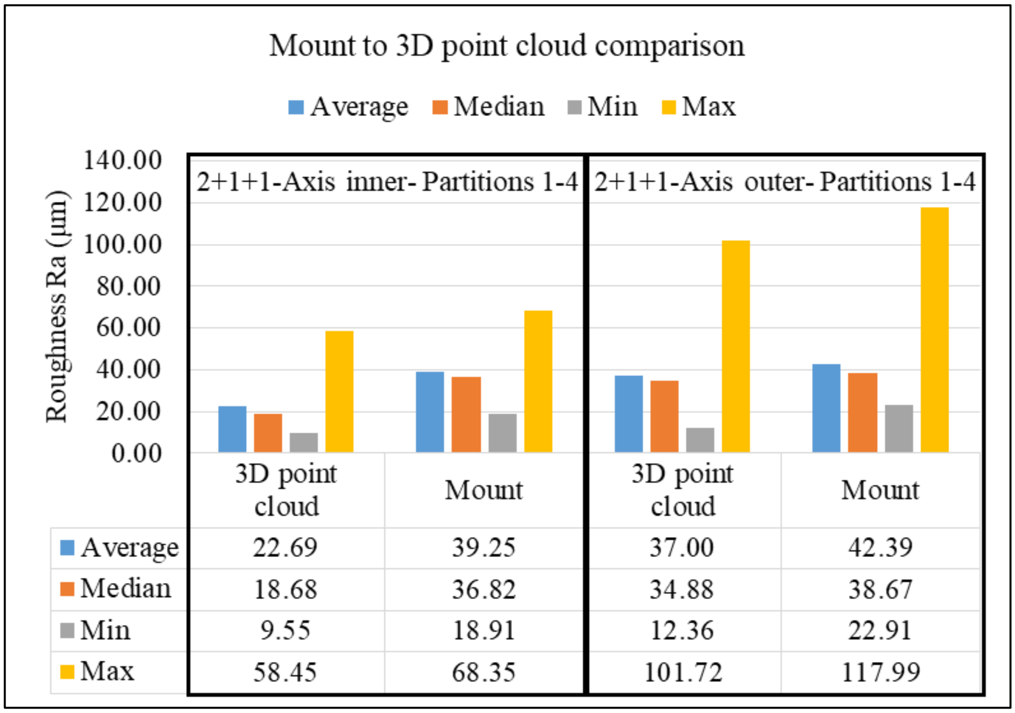

	2+1+1-Axis inner- Partitions 1-4		2+1+1-Axis outer- Partitions 1-4	
	3D point cloud	Mount	3D point cloud	Mount
Average	22.69	39.25	37.00	42.39
Median	18.68	36.82	34.88	38.67
Min	9.55	18.91	12.36	22.91
Max	58.45	68.35	101.72	117.99

Figure 5-33. Initial statistical analysis of 3D point cloud solution

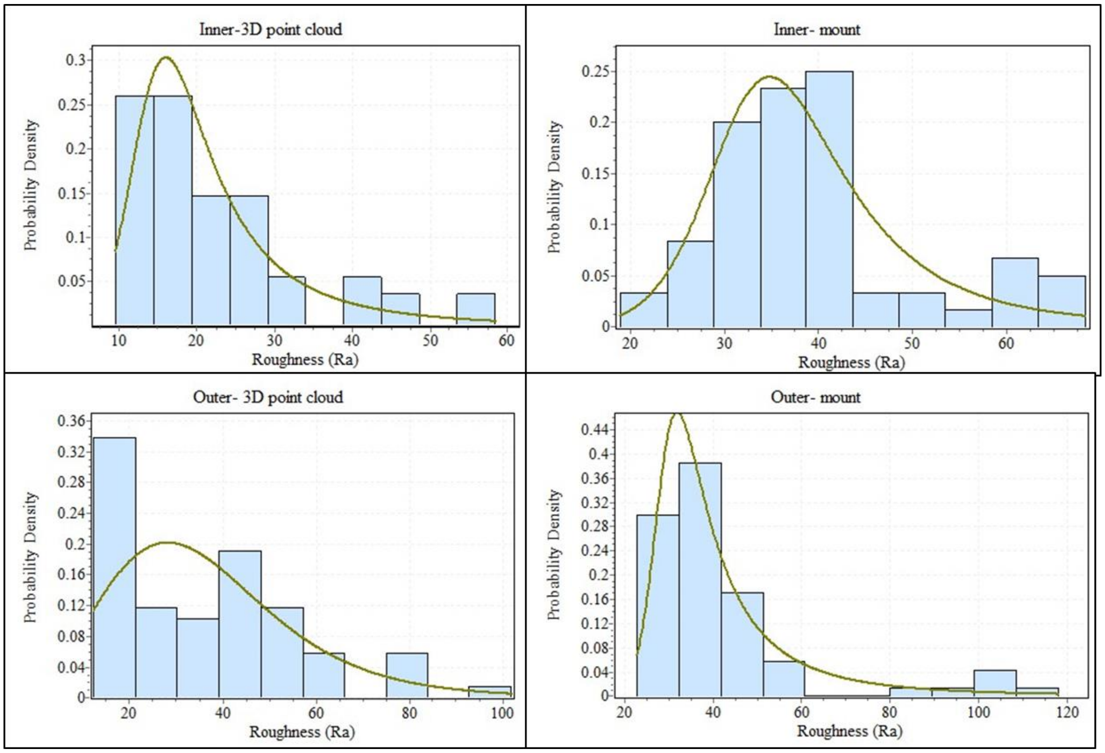

Figure 5-34. Histograms and Burr distributions of 2+1+1-Axis partitions 1-4 by 3D point cloud

The mode values are also larger for mount solution. The skewness value of the outer surface in mount solution shows a very large value whereas this value is much smaller for the 3D point cloud data set. The reason that these values are greater for the mount solution is that the input data to mount solution is more accurate as the data is directly extracted from the 2D boundary curves. The 3D point cloud data set is created by a scanner that cannot detect the deep valleys of the surface. Furthermore, the scanner cannot detect very tiny textures of the surface. Therefore, the Ra results of mount solution are generally larger.

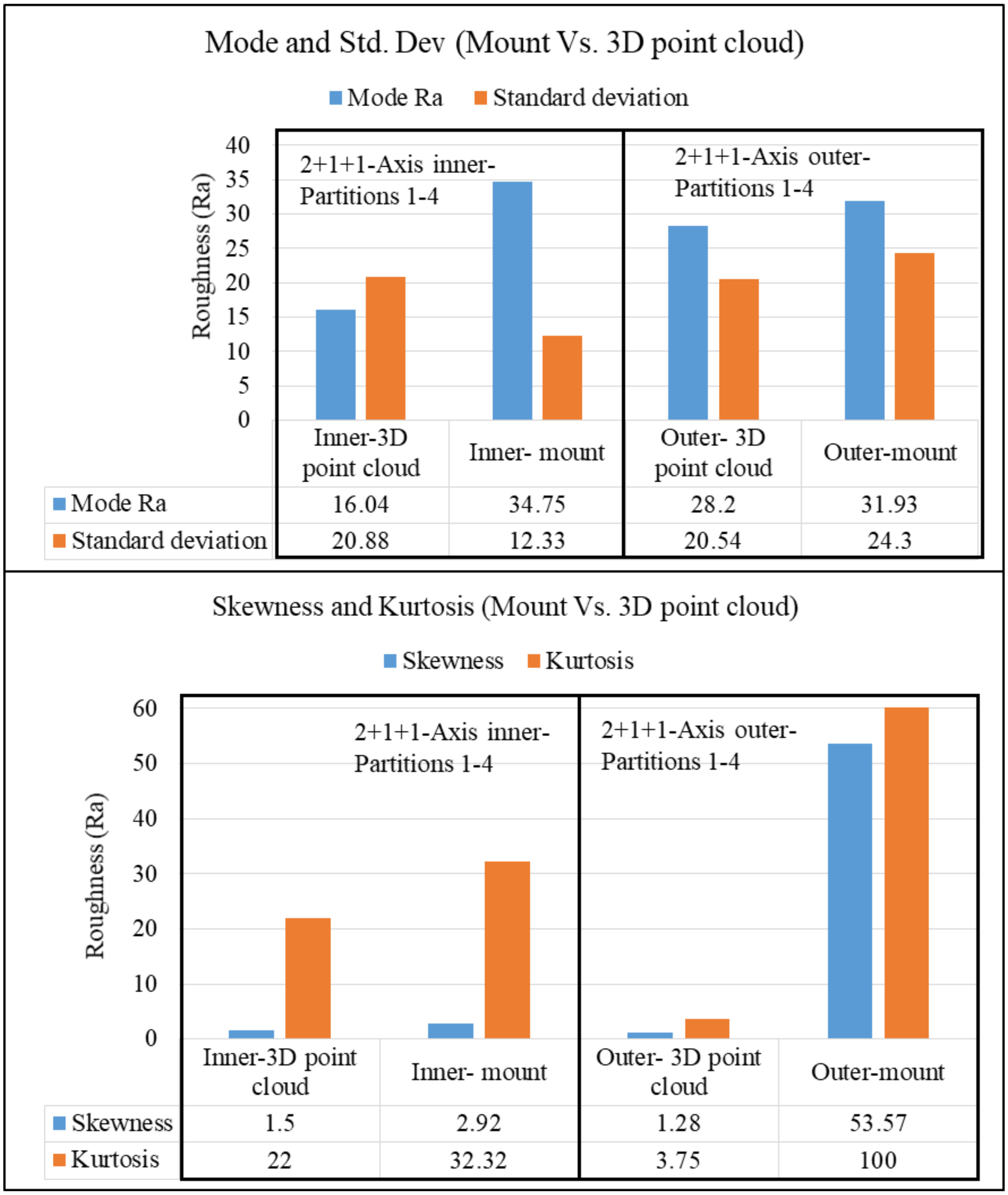

Figure 5-35. Comparison of statistical analysis between mount solution and 3D point cloud

Altogether, the mount solution results in a better measurement than the 3D point cloud as its input data is more accurate. The accuracy of the 3D point cloud results is highly dependent on the point cloud density and the accuracy of the 3D scanner. The shift between the mount solution and 3D solution diagrams that is indicated in Figure 5-28 is because of the low accuracy of the 3D scanner whereas the other point cloud result diagrams that do not show the observed Ra variations are because of the low point cloud density.

Therefore, this 3D point cloud solution is better used for the AM processes that deposit larger beads such as LSAM and BAAM or the accuracy of the applied 3D scanner should be better for smaller bead samples (about 10 times more accurate than the Ra values). The following chapter explores the hardness variations of the 3 fabricated domes.

CHAPTER 6

MICROHARDNESS RESULTS

In this chapter, the exploration of the Vickers microhardness is investigated. First, a noise detection test is implemented for each sample to find the appropriate indentation load that varies the least across the surface. Then the variation of hardness in the middle arc of the surface stripe is explored. Finally, a statistical analysis of the results is presented.

6.1 Microhardness Results for the 5-Axis Toolpath Sample

As shown in Figure 6-1, 18 test points along the surface of partition 3 of the sample are established. The distance between each hardness test point is 1 mm. As the magnified view shows, four indentations are made at each hardness test point. There are two indentation types: two made by a 1000 gf and two others made by a 300 gf.

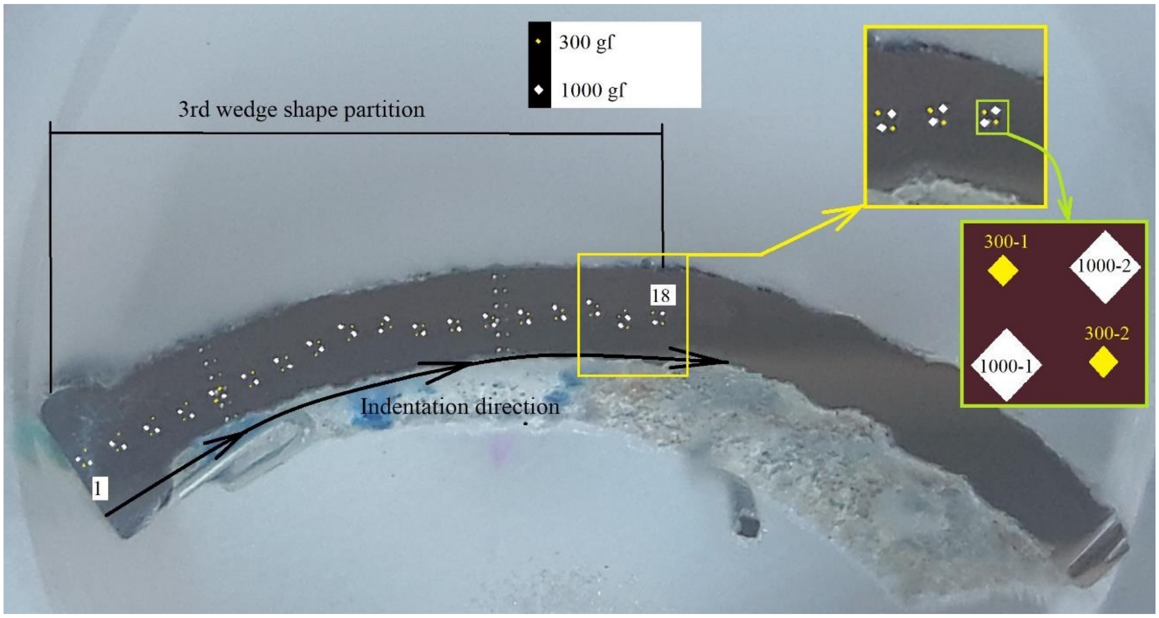

Figure 6-1. Microhardness indentations on partition 3. Four indentations for each test point are made.

Based on the information presented in Section 3.4 the distance between two indentations is more than 2.5 times the diagonal of the larger indentation. Although it is ideal to make indentations exactly at the middle line of the narrow surface, indentations at each test point are separated. This may bring noise into the results if the hardness varies in the surface width direction. Consequently, this was measured and evaluated as well.

6.1.1 Hardness variation test across surface of the 5-axis sample

A hardness variation test across the surface is implemented to investigate the noise. As Figure 6-2 indicates, two sets of indentations in two random locations are measured. Two indentations columns of 1000 gf and 300 gf for each set are created. Each set is made up of 6 rows of indentations across the surface stripe. Two graphical arcs are drawn on the surface to determine the off-centricity of the indentations. Care was taken to include all test indentations between these 2 arcs. Except for the last test point indentations, all others are between these 2 arcs. Furthermore, it can be seen in this picture that the inner arc passes between the 2nd and 3rd indication rows of both sets whereas the outer arc is between the 4th and 5th indication rows.

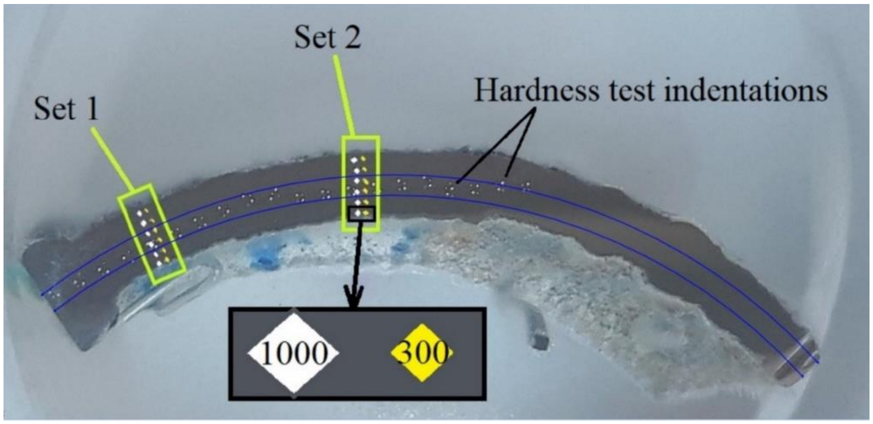

Figure 6-2. Hardness test across the surface

The hardness variations across the 5-axis specimen surface is presented in Figure 6-3. Diagrams are provided both for the average 300 gf (the hardness average associated to the indentations of each 300 gf rows of set 1 and set 2), the average 1000 gf, and the total average (total hardness average of 4 indentations at each row of two sets). The two arcs are presented by vertical lines in Figure 6-3. The hardness variation is 80 HV between inner and outer arcs for 300 gf. It varies between 185 to 215 HV (variation is 30 HV) for the total average. Therefore, hardness measurements by 300 gf are less reliable. On the other hand, the 1000 gf chart shows the variation of 200 to 210 HV (variation is 10 HV) between two arcs. This indicates that 1000 gf measurements are more stable across the surface.

The standard deviation analysis of the hardness results for Set 1 and Set 2 made by loads 300 gf, 1000 gf and average (300, 1000) is shown in Figure 6-4. The average of standard deviations for 1000 gf has the least value. This supports the previous result that 1000 gf has the least noise if the indentation is off from the arc centreline. Therefore all analyses are applied for indentations made by 1000 gf.

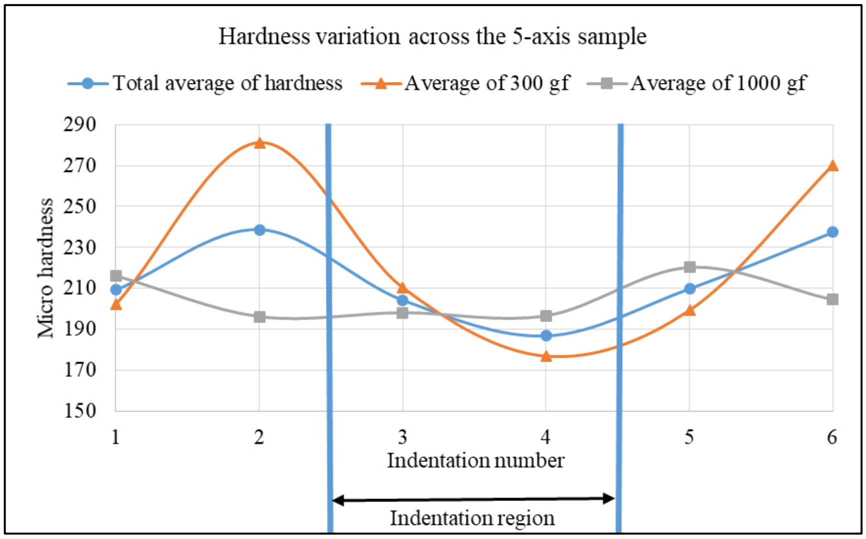

Figure 6-3. Hardness variation across the surface of 5 axis specimen (a) For 300 gf indentation (b) For 1000 gf indentation

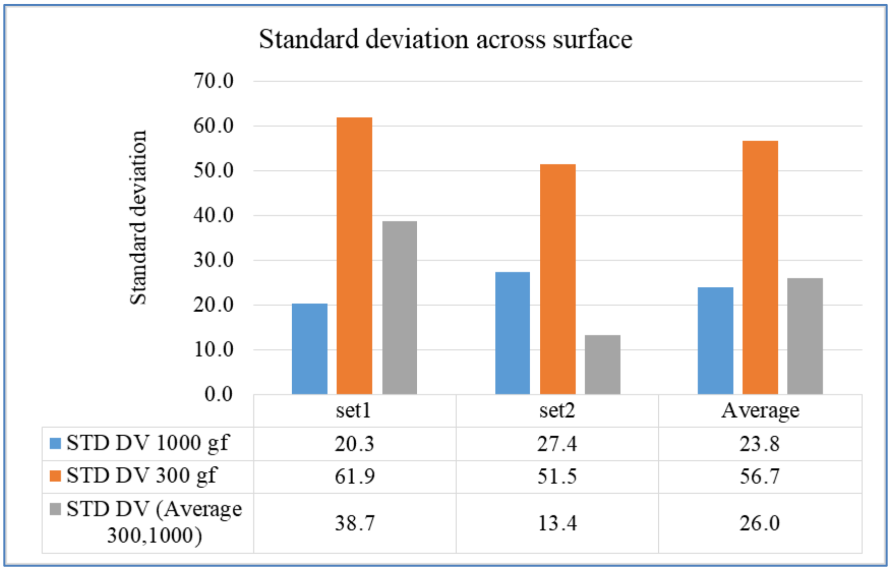

	set1	set2	Average
■ STD DV 1000 gf	20.3	27.4	23.8
■ STD DV 300 gf	61.9	51.5	56.7
■ STD DV (Average 300,1000)	38.7	13.4	26.0

Figure 6-4. Standard deviation of hardness across the surface of 5-axis sample.

6.1.2 Hardness variation for 5-axis sample

Figure 6-5 shows the hardness variation along the middle of the specimen surface for partition 3. Hardness increases initially from 170 HV to 260 HV and then diminishes to 155 HV in higher layers. The FFT analysis shows a dominant frequency of 0.5 (1/mm). The related wavelength is 2 mm that can be noticed in Figure 6-5. This indicates that there may be a low frequency aspect in the system [136]

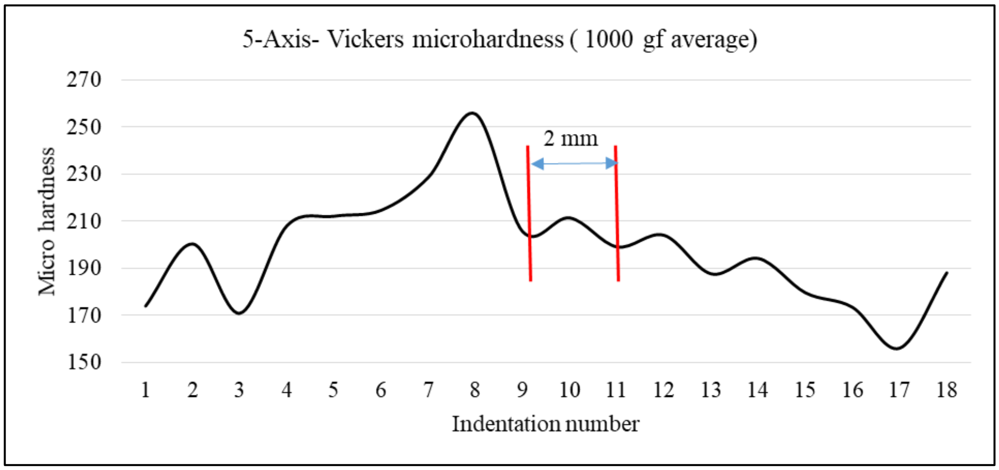

Figure 6-5. Hardness variation along 5-Axis sample by 1000 gf indentation

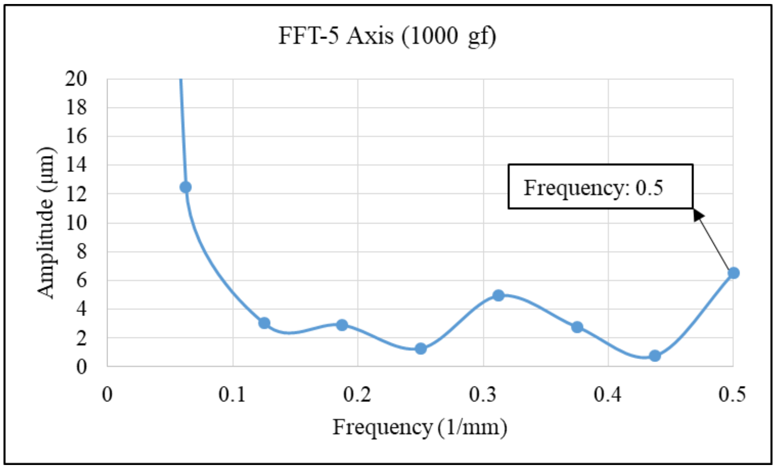

Figure 6-6. FFT analysis for 5-Axis sample

6.2 Microhardness Results for the 2+1+1-Axis Toolpath Sample

A detailed picture of the mounted 2+1+1-axis specimen showing the hardness indentations is presented in Figure 6-7. Table 6-1 distinguishes the test point numbers based on the partition where they are located. Again, each test point consists of four indentations. Two indentations made are by 1000 gf and two others by 300 gf.

The first mount specimen has 1st to 4th partitions and 36 hardness test points whereas the second mount contains 5th to 8th partitions with 37 points. The increment between test points is 1 mm.

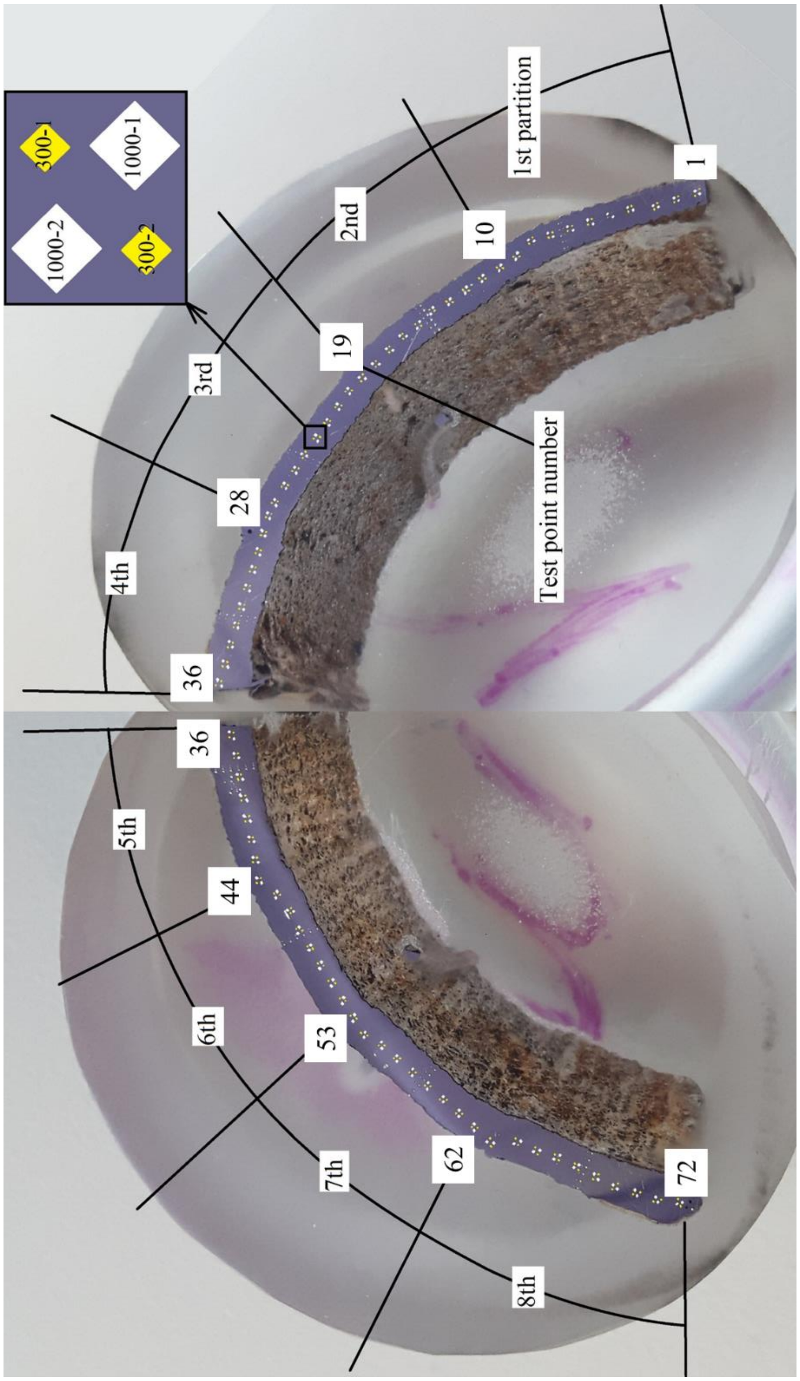
1000-2
300-1
300-2
1000-1
1st partition
2nd
3rd
4th
1
10
19
28
36
Test point number
36
5th
6th
7th
8th
44
53
62
72

Figure 6-7. Hardness indentations on 2 mounts of 2+1+1 axis samples

Table 6-1. Partitions and their indentation test numbers

Partition Number	1	2	3	4	5	6	7	8
Test point Number	1-10	10-19	19-28	28-36	36-44	44-53	53-62	62-72

6.2.1 *Hardness variation test across the surface of the 2+1+1-sample*

As with the 5-axis sample, a test is performed to investigate hardness variations across 2+1+1-axis sample surface. To do so, 8 sets of indentations across the surface are made, 4 on each mount sample. Each set of indentations includes two rows of 1000 gf and 300 gf. The locations of these sets along the surface are randomly chosen. Also, two arcs are drawn to show the indentations are in the middle of the surface. The inner arc passes through the 2nd and 3rd test points of the sets whereas the outer arc passes between the 4th and 5th indentation rows in the sets. (Figure 6-8).

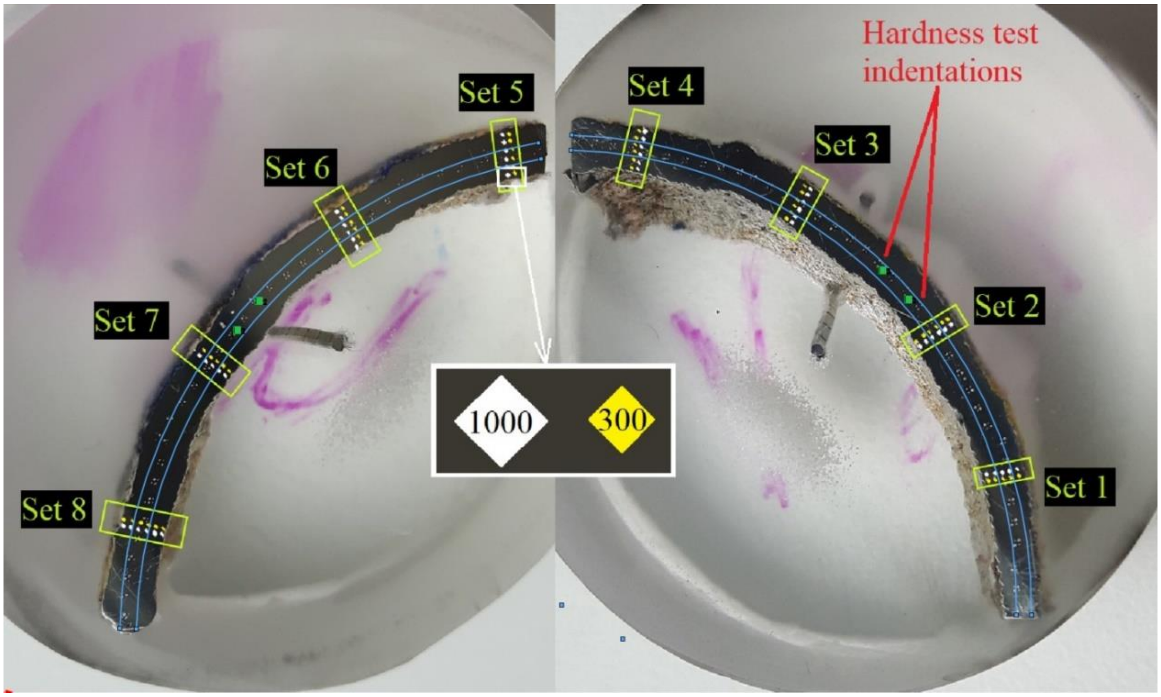

Figure 6-8. Hardness test across the surface and test rows

Hardness variations across the surface are shown separately for the two mounts in Figure 6-9. Each figure depicts the average for the 300 gf and the average of 1000 gf measurements as well as the total average. These diagrams indicate that the hardness variations of 1000 gf measurements are more stable across the surface compared to the 300 gf measurement set. It shows a very minor pattern of increasing the hardness from the 1st row to the 6th. The curves of 1000 gf show the variations of 15 HV and 20 HV for the 1st mount and 2nd mount, respectively. It is observed that the 300 gf based variation chart shows much more variation of 12 HV and 22 HV for the 1st mount and 2nd mount, respectively.

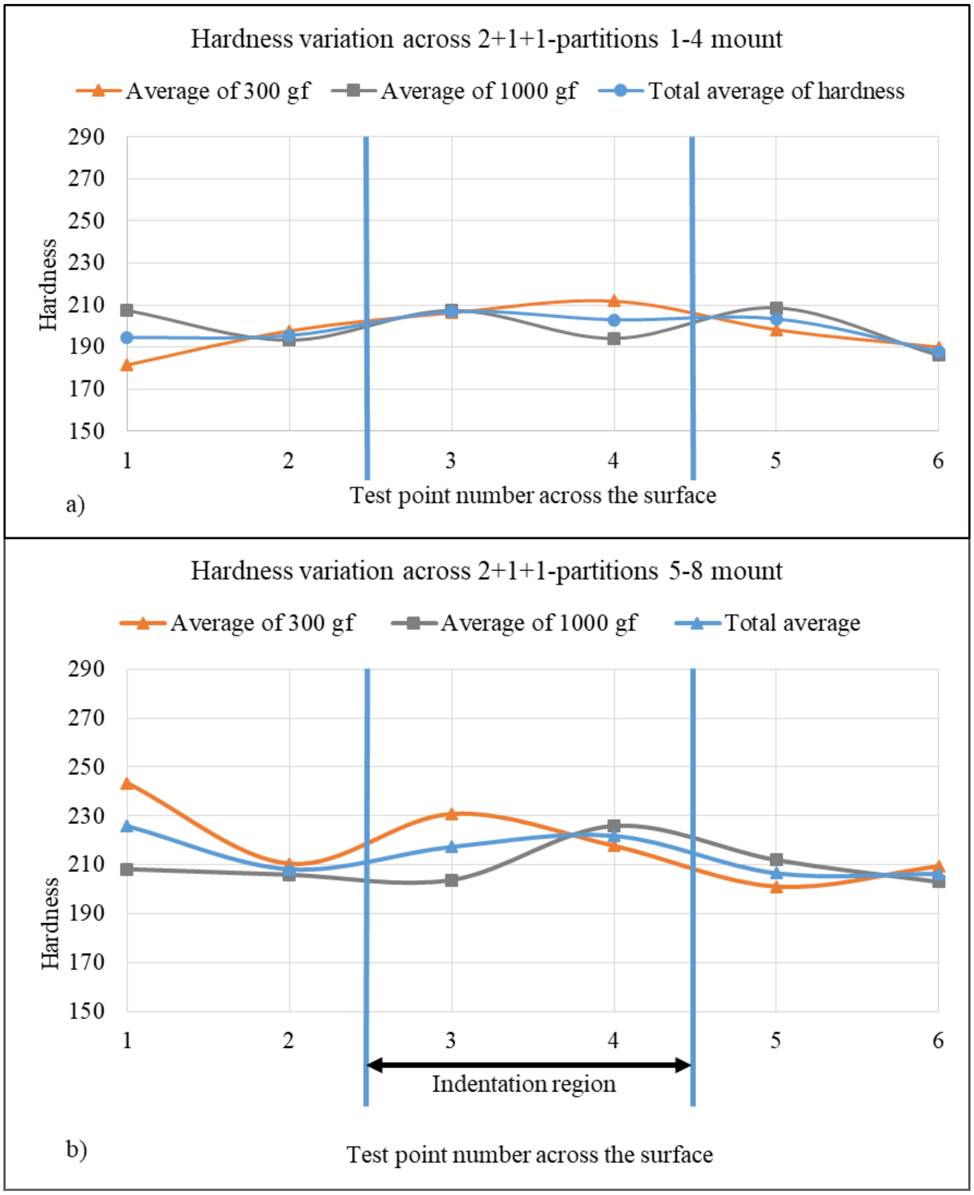

Figure 6-9. Hardness variation across the surface of 2+1+1 axis sample- mount 1

Additionally, a standard deviation test is performed to check the hardness variation across the surface (Figure 6-10). The average standard deviation of hardness measured by 300 gf is 29.5 HV, which is much larger than 1000 gf values (20.6 HV) and the average value (19.5 HV). Since the standard deviation of 1000 gf and 300 gf are close, the 1000 gf is chosen to be consistent with the 5-axis sample.

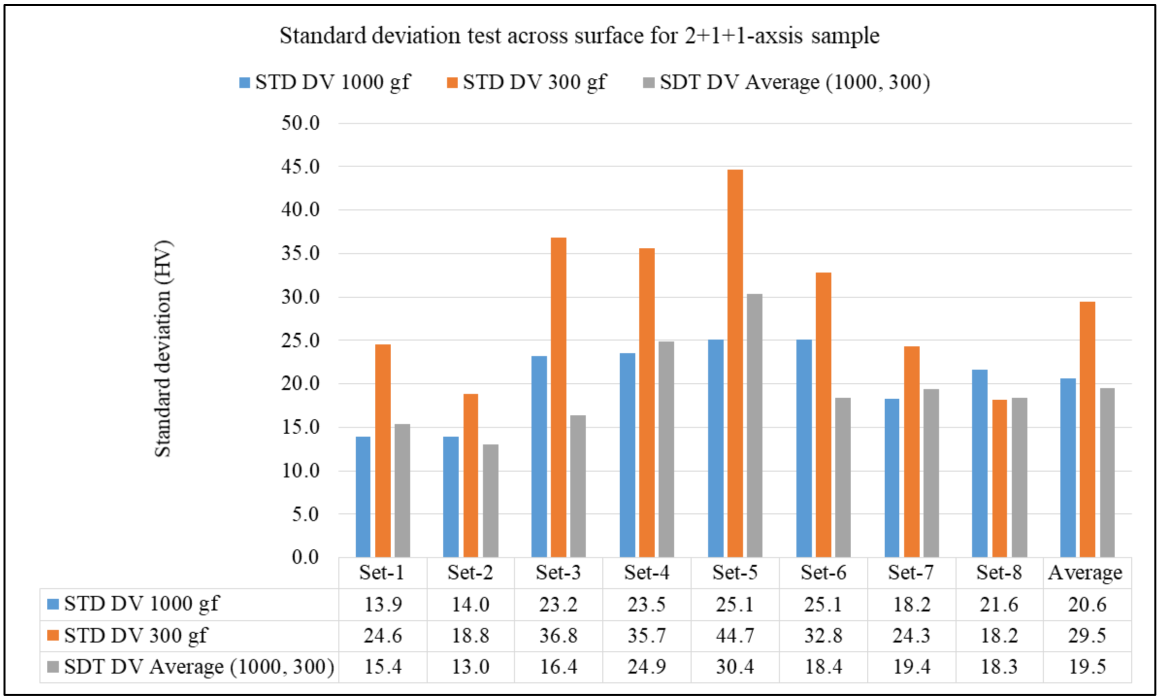

	Set-1	Set-2	Set-3	Set-4	Set-5	Set-6	Set-7	Set-8	Average
STD DV 1000 gf	13.9	14.0	23.2	23.5	25.1	25.1	18.2	21.6	20.6
STD DV 300 gf	24.6	18.8	36.8	35.7	44.7	32.8	24.3	18.2	29.5
SDT DV Average (1000, 300)	15.4	13.0	16.4	24.9	30.4	18.4	19.4	18.3	19.5

Figure 6-10. Standard deviation of hardness across the surface of 2+1+1-sample

6.2.2 Hardness Variations for the 2+1+1-Axis Sample

There are 2 indentations for each of the 72 test points. The averaged hardness values for these 2 indentations is the representative of hardness for each test point. The hardness diagram for all partitions 1-8 is presented in Figure 6-11. The first 4 partitions have a similar pattern as the hardness drops to about 150 HV at the connection points. The bottom of the first partition is different as the hardness is at its highest value at the bottom of the 1st partition. The reason is that the large volume of the substrate absorbs the deposition heat very quickly (this is also why the first layer has a 1000 W power level). Fast cooling generates smaller grains which leads to larger hardness values. For partitions 5-8, there is no noticeable pattern as the hardness variation alters several times within each partition.

The hardness has generally a low value in the first layers of each partition. The reason is that the deposition heat of the first several beads of each partition keeps the first layers of the current partition and the last layers of previous partition warm. So, the cooling rate is low for these layers. As the heat penetration is limited, it can just heat the nearest layers, so the middle layers of partition stay unchanged. A more detailed explanation will be covered in the next chapter. Further exploration to explain hardness variation from microstructure is considered as future work.

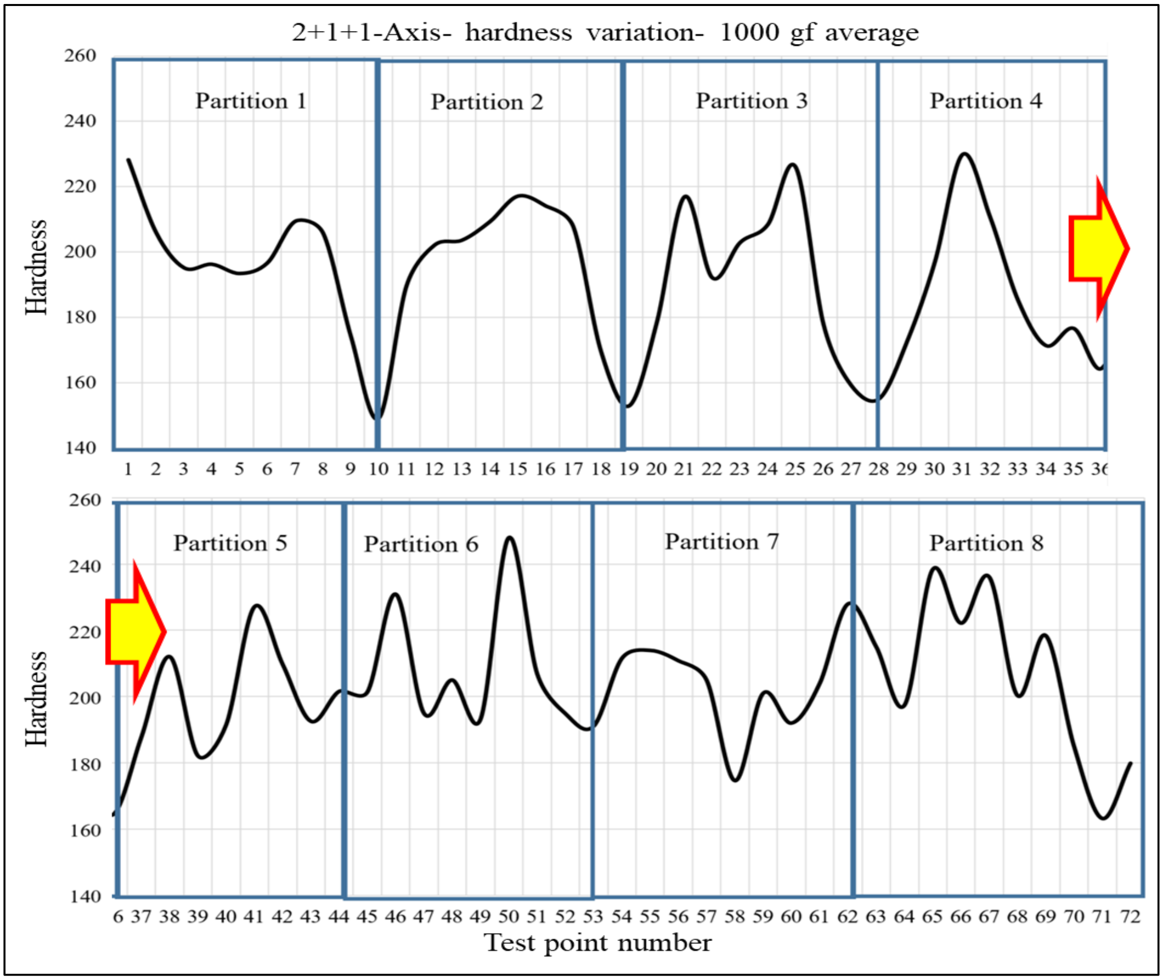

Figure 6-11. Micro hardness chart for 2+1+1 axis sample divided based on the partitions

The FFT analysis shows a dominant frequency of 0.124. This frequency leads to a wavelength of 8.06 mm which is near the partition length (8.8 mm). This also correlates with the hardness pattern shown in Figure 6-11.

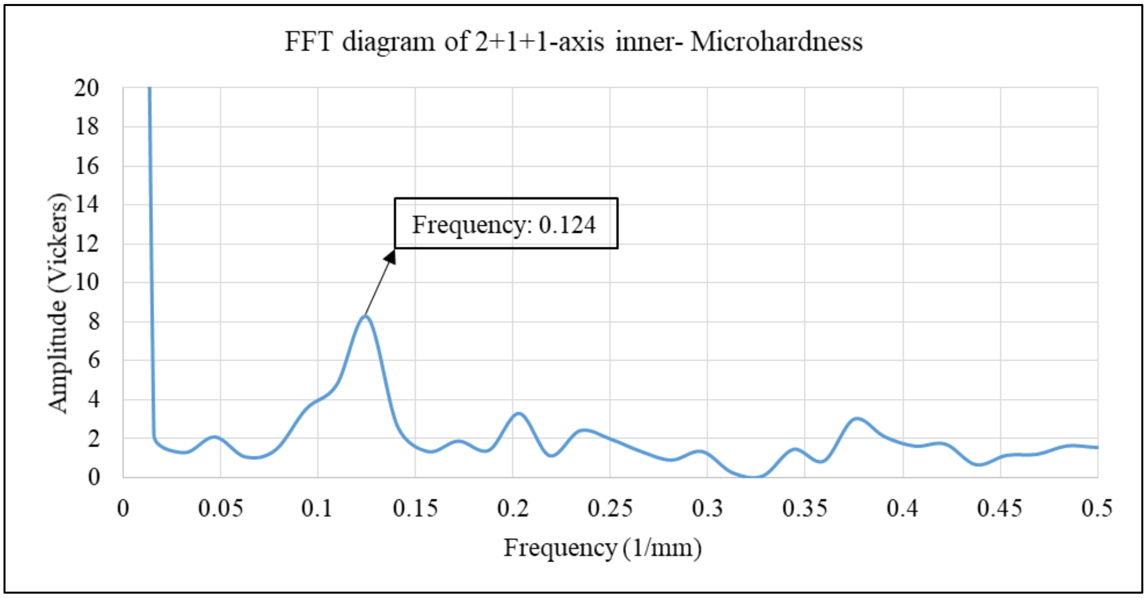

Figure 6-12. FFT diagram of microhardness for 2+1+1-axis sample

6.3 *Microhardness Results for the Rotary Toolpath Sample*

Since the 300 gf load resulted with cross surface noise for the previous samples, indentations are created with 1000 gf only for the rotary sample. Since it is found that hardness does not change noticeably across the thin wall surface for the 1000 gf indentations, a hardness investigation across the surface is not performed for this case. Also, the distance between indentations in a test point is negligible compared to the width of the surface stripe. As a result, since the hardness variation is negligible across the surface, it can be assumed that it does not vary within the test points. Therefore, instead of making 4 indentations at each test point, one indentation is made at each test point (Figure 6-13). However, the distance between test points is reduced to 0.5 mm.

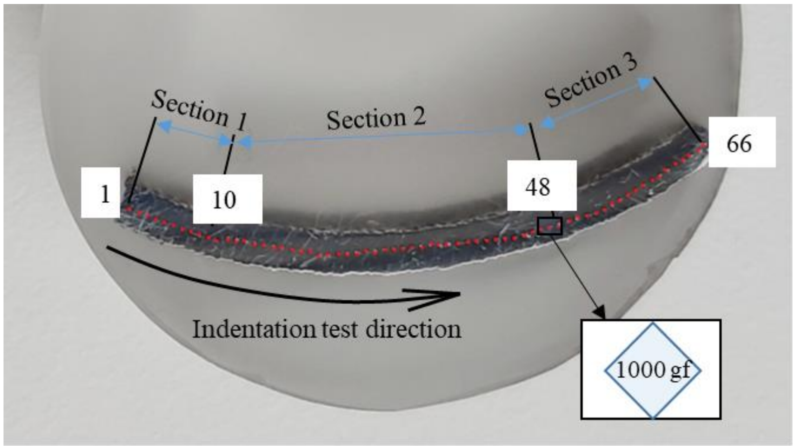

Figure 6-13. Micro indentations on rotary specimen

The hardness variations for the rotary toolpath specimen is represented in Figure 6-14. Three fabrication sections are shown. The diagram shows no special pattern by a visual investigation. However, the hardness decreases at transition points, similar to the 2+1+1-axis sample.

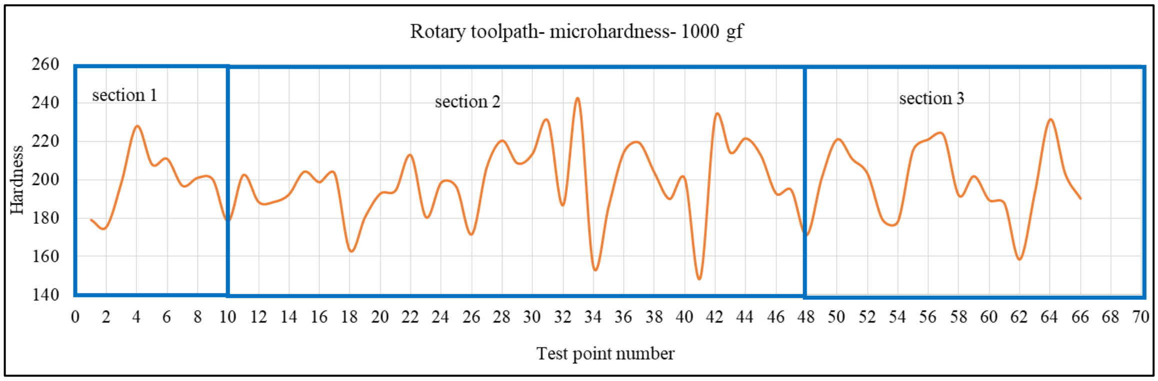

Figure 6-14. Hardness variation for rotary sample

Further exploration by FFT analysis shows a dominant frequency of 0.281 (1/mm). It results in a wavelength of 3.56 mm. This means a repetitive pattern is concealed in the diagram that has a wavelength of 3.56 mm.

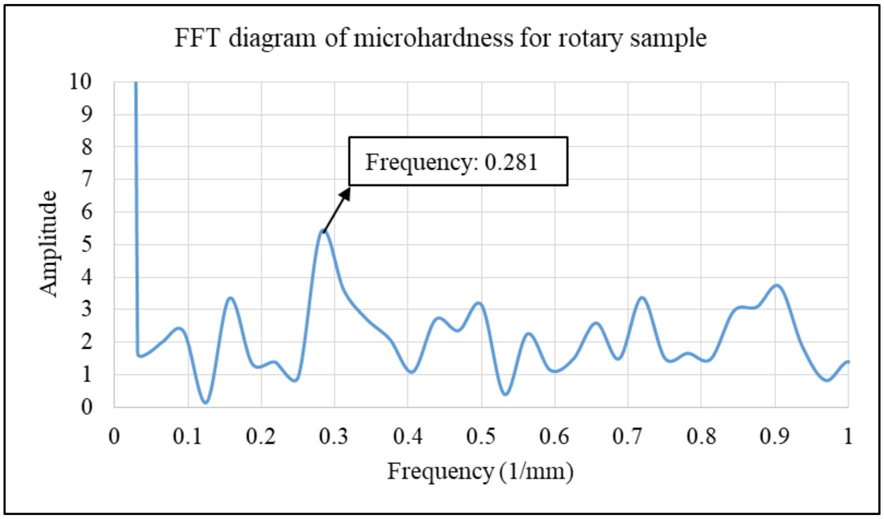

Figure 6-15. FFT diagram of micro-hardness for rotary sample

6.4 Statistical Analysis for the Microhardness Results

A Kolmogorov-Smirnov (K-S test) test is performed to find an appropriate distribution technique for the hardness results. The P-values of the four distributions are compared. The results summarized in Table 6-2 show that the Burr distribution has the highest P-values, which means the results fit better for this distribution.

Table 6-2. Comparison of P-values of four distributions

	Weibull	Gamma	Burr	Chi-squared
5-Axis	0.98	0.94	0.99	0.96
2+1+1-Axis	0.96	0.58	0.98	0.49
Rotary	0.78	0.93	0.92	0.72

As Figure 6-16 shows, the average hardness values of three samples are the same (198 HV). The rotary sample has the lowest hardness variations (Max-Min=93.7 HV).

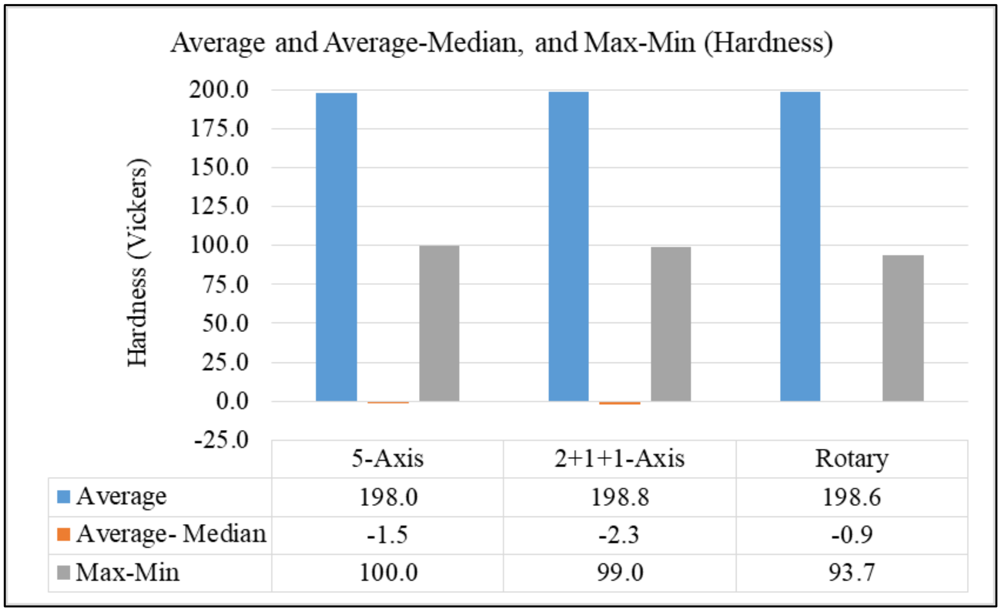

	5-Axis	2+1+1-Axis	Rotary
🟦 Average	198.0	198.8	198.6
🟧 Average- Median	-1.5	-2.3	-0.9
■ Max-Min	100.0	99.0	93.7

Figure 6-16. Average, Average-Median, and Max-Min for hardness results

Figure 6-17 shows the histograms and Burr distributions of the hardness results. The extracted values of mode and standard deviation are shown in Figure 6-18. The 2+1+1-axis sample has a mode hardness value of 202.1 HV whereas the 5-axis sample has the lowest of mode value (195.6 HV). The standard deviations are almost the same.

Based on Figure 6-19, the hardness results of the 5-axis sample are more skewed to the higher hardness values. The measured data shows some points have drastically high hardness values, which skews the distribution curve to the positive direction.

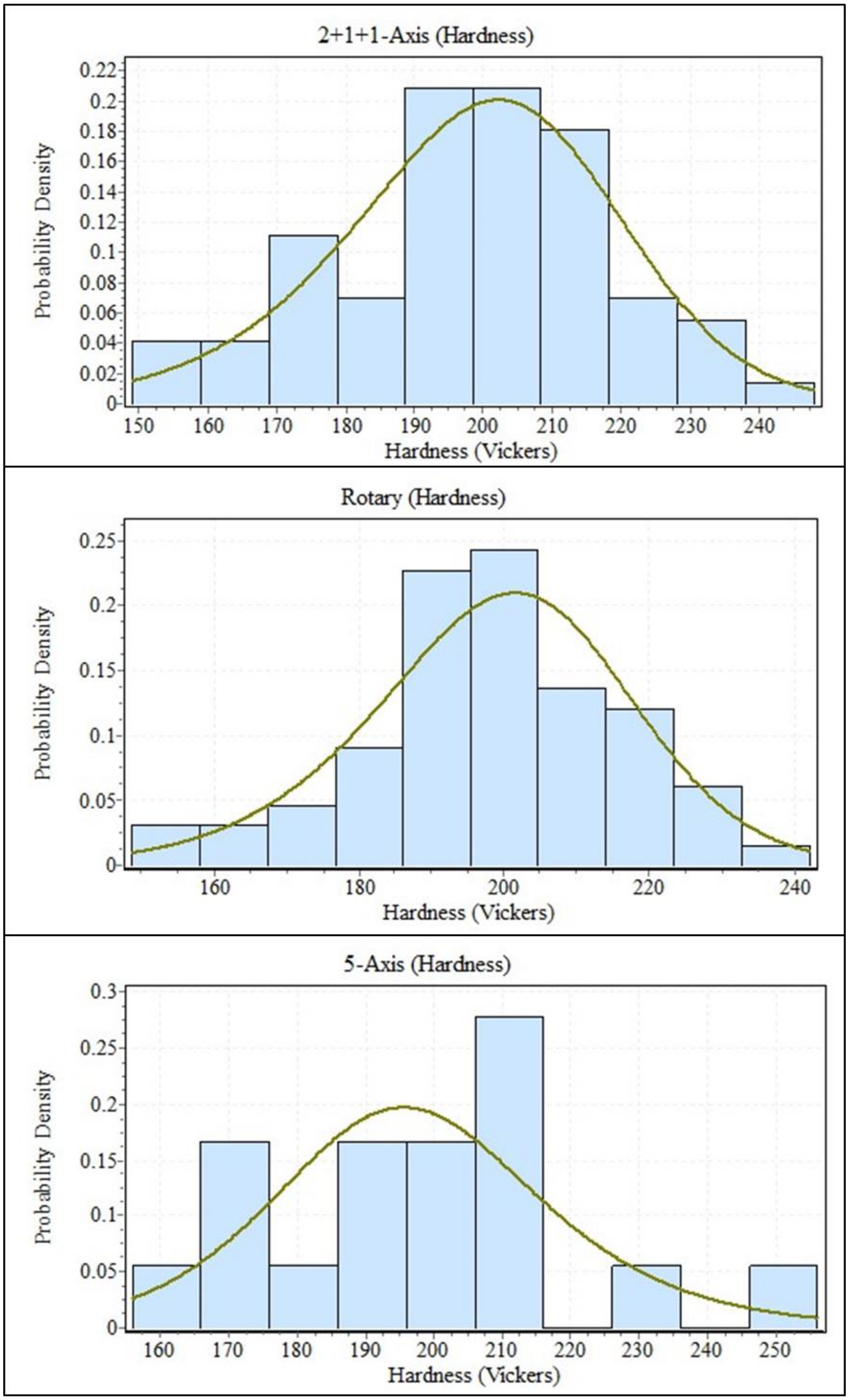

Figure 6-17. Histograms and Burr distributions of hardness results

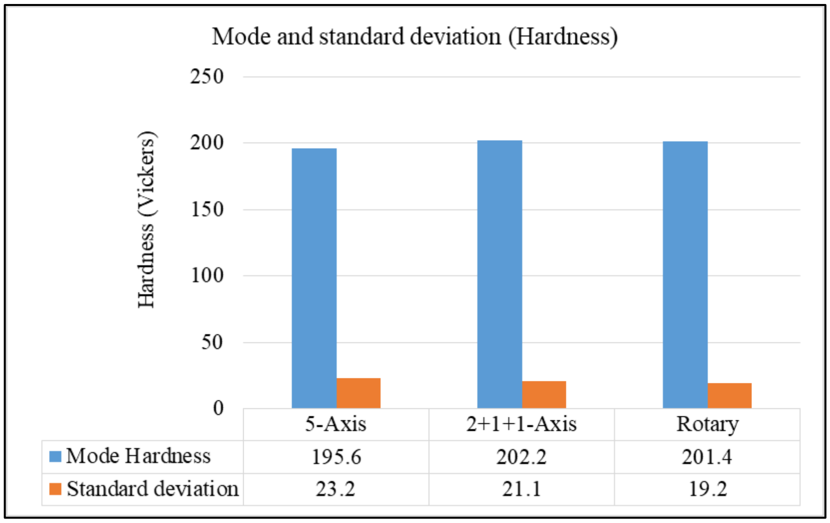

Figure 6-18. Modes and standard deviations of hardness results

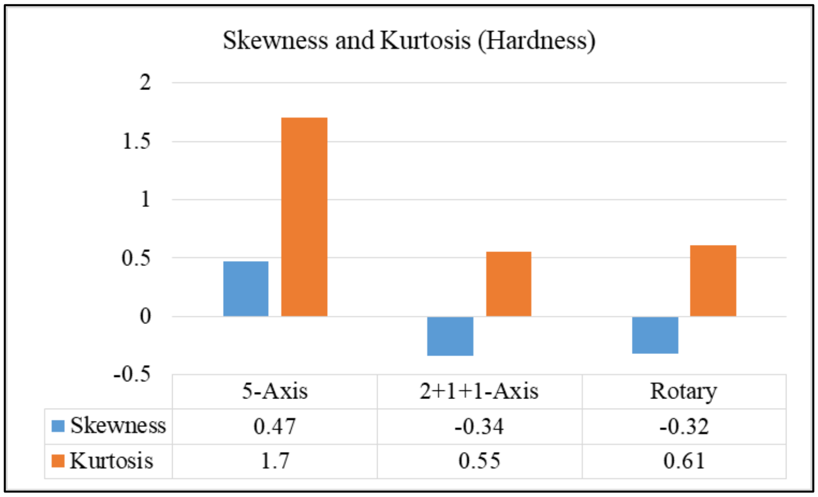

Figure 6-19. Skewness and Kurtosis of hardness results

The hardness of three fabricated domes were measured in this chapter. The measurements are implemented along the slice direction in the middle of the domes. To minimize the noise of the hardness value across the surface stripe, the 1000 gf load was selected to create indentations. For the wedge-shaped partition samples, the hardness is at the lowest value at the bottom and top of each partition. A simple variation pattern is noticeable for the partitions 2-4 whereas it is more complex for the rest of partitions. In the next chapter, the FEA analysis of hardness will be explored. The FEA results will be verified by the experimental ones that were presented in this chapter.

CHAPTER 7

SIMULATION OF MECHANICAL PROPERTIES

Hardness, temperature history, and residual stress simulations of the 2+1+1-axis sample by FEA analysis are presented in this chapter. Hardness simulation will be verified by experimental results. The residual stresses of partitions 1-4 will be presented as well.

7.1 *Hardness Simulation*

In order to implement a hardness simulation, the geometries of all beads need to be meshed. Here, the geometry of the dome is divided into the substrate and 8 partitions. Figure 7-1 (b) shows the bead models within the first partition. There are 18 beads inside each partition. Also, it is indicated in Figure 7-1 (c) that beads are parallel to the bisector plane of each partition; as mentioned in Section 3.2.1.

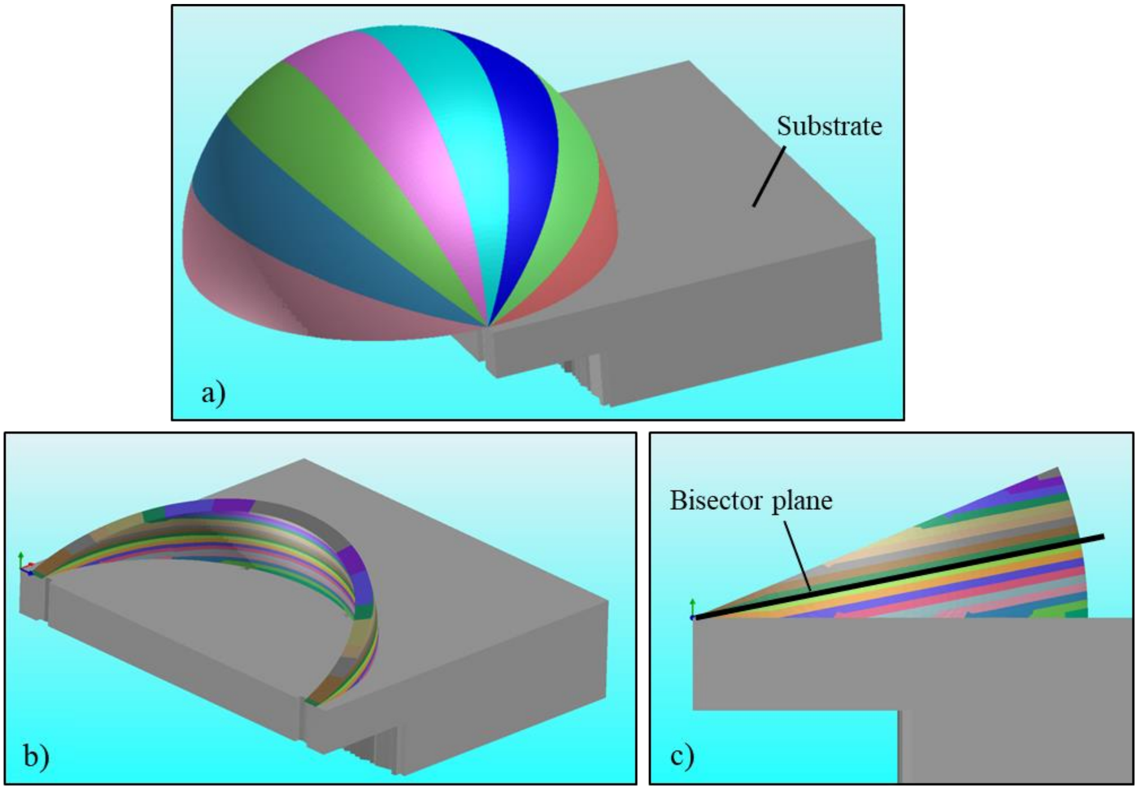

Figure 7-1. Modeling the partitions and beads for FEA analysis

The meshes of both the beads and substrate consist of hexagonal elements and have variable element sizes. As Figure 7-2 shows, the bead near the measurement region has a fine mesh but the mesh size becomes coarser for more distant places. The beads are 6-element wide/2-element thick in the measurement region whereas it is 3-element wide/one-element thick at the end of beads. This kind of variable bead meshing assumes that the impact of laser heat delivery at distant locations on temperature rise in the measurement region is negligible in comparison to the heat that is delivered at the measurement region. Also, it is assumed that the heat conduction from distant points of the bead to the measurement region is not changing by coarsening the mesh. It means, regardless of the mesh size in distant locations, it is assumed that the same heat is deliverd to the measurement area. This will be tested indirectly by the mesh dependency test. This can be true for residual stresses as well. But the distortion analysis cannot be implemented by this kind of variable meshing because the distortion of distant locations affects the distortion of the measurement region. This means that if the coarse mesh results in wrong distortion values, it changes the overall shape of the product regardless of where the coarse mesh is. These are hypotheses that can be explored more in future work.

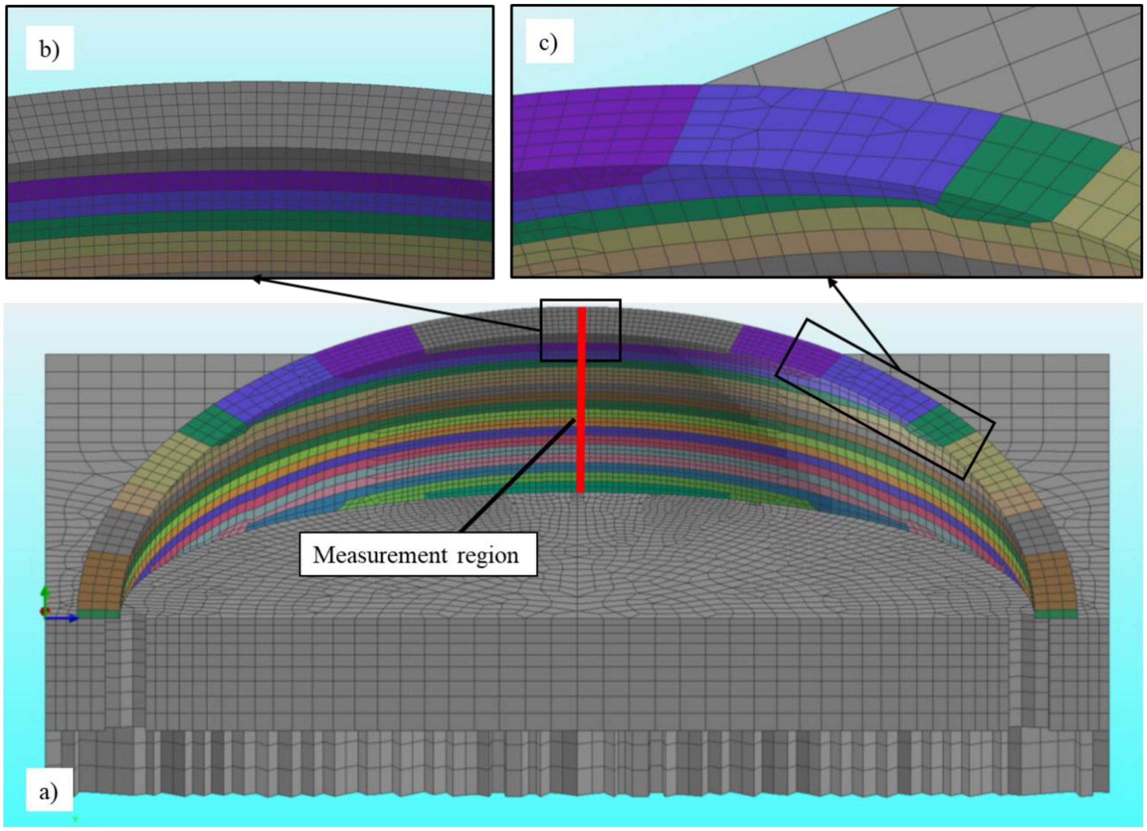

Figure 7-2. Variable mesh structure of beads and substrate

7.1.1 Mesh Dependency Test (Convergence Test)

In this test, the beads and the substrate are meshed with finer meshes to see whether the mesh size affects the hardness results. To decrease the calculation time, three beads are simulated. As the part geometry is symmetric, Figure 7-3 shows half of the part. The measurement location is in the middle of the beads.

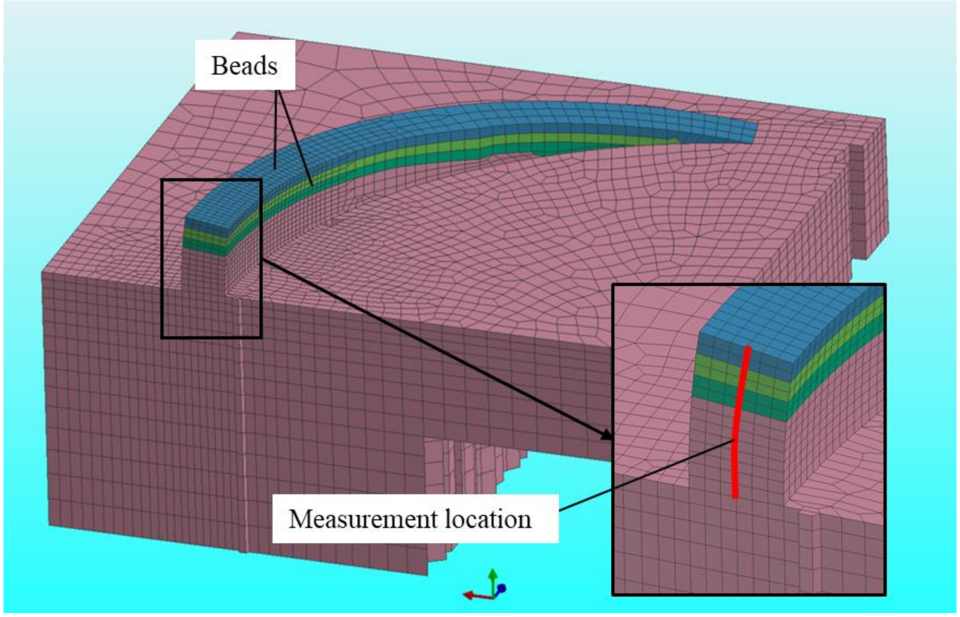

Figure 7-3. Three beads are simulated for mesh dependency check

Three mesh sizes are tested here (Figure 7-4). The ‘mesh 1’ that is shown in Figure 7-4 (a) is used in the simulations. Mesh 2 is the 8 time-finer mesh within mesh 1. Here each hexagonal element of mesh 1 is divided into 8 hexagonal elements. These 2 mesh types have a variable mesh size in the beads. This means that the mesh size of the bead grows for the regions away from the measurement region. Mesh 3 contains a constant mesh size within the beads, and have the mesh size of 6 element-wide/2 element thick. Table 7-1 compares some of the mesh size parameters.

The yielding strength variations of the mentioned mesh sizes are shown in Figure 7-5. The curves of the different meshes match satisfactorily. It can be seen that the results of the coarse mesh (Mesh 1) have the same values as those predicted by the finer meshes (Mesh 2, 3). Therefore the analysis of the whole dome is carried out with Mesh 1. Also, Mesh 1 shows a drastic decrease in calculation time (approximately 15 times) compared to the two other meshes.

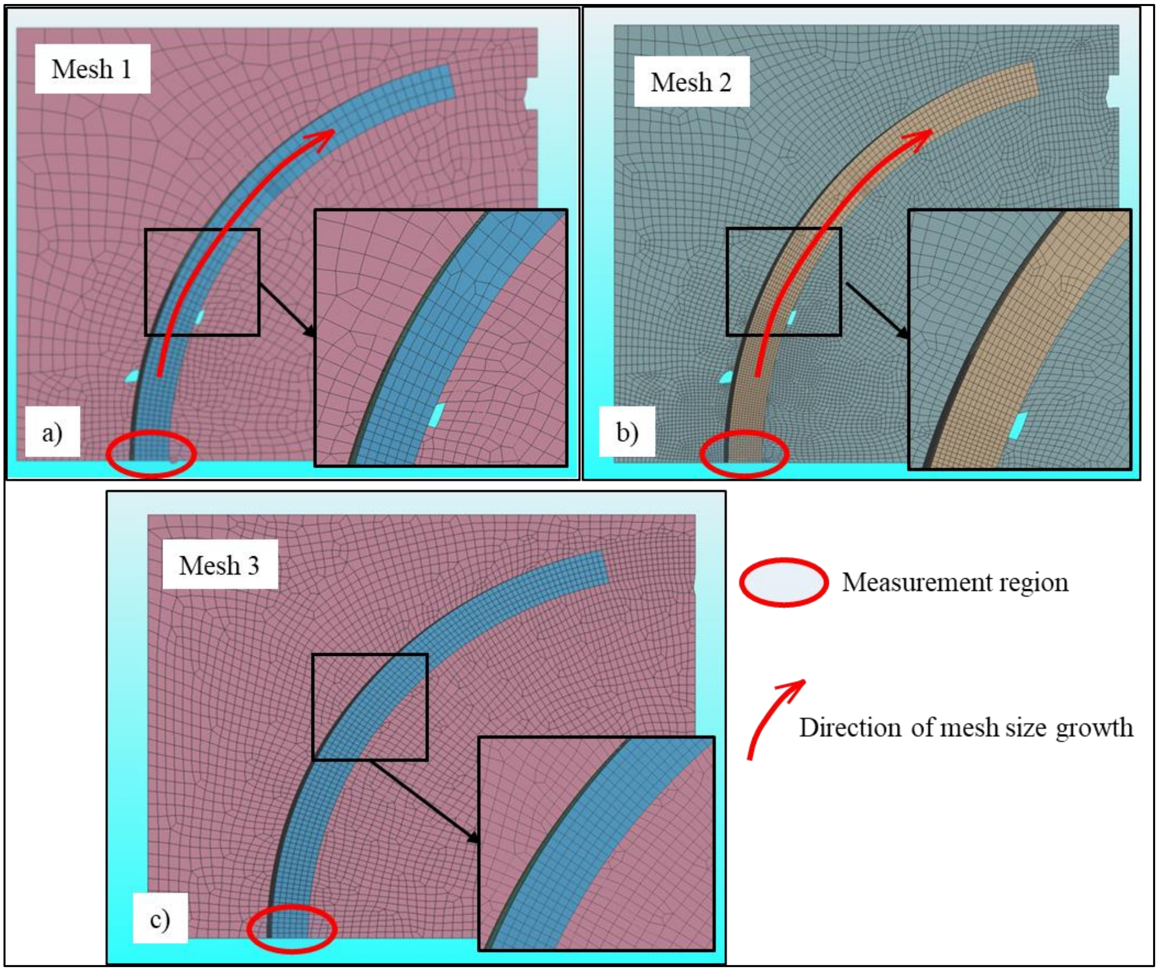
Mesh 1
a)
Mesh 2
b)
Mesh 3
c)
Measurement region
Direction of mesh size growth

Figure 7-4. Models with finer mesh to do the dependency check.

Table 7-1. Mesh dependency check (convergence test)

	Width-thickness of bead at measurement region (elements-elements)	Width-thickness of bead at distant region (elements-elements)	Total number of 3D elements	Run time (hour)
Mesh 1	6-2	3-1	50376	1
Mesh 2	12-4	6-2	402636	17
Mesh 3	6-2	6-2	122404	15

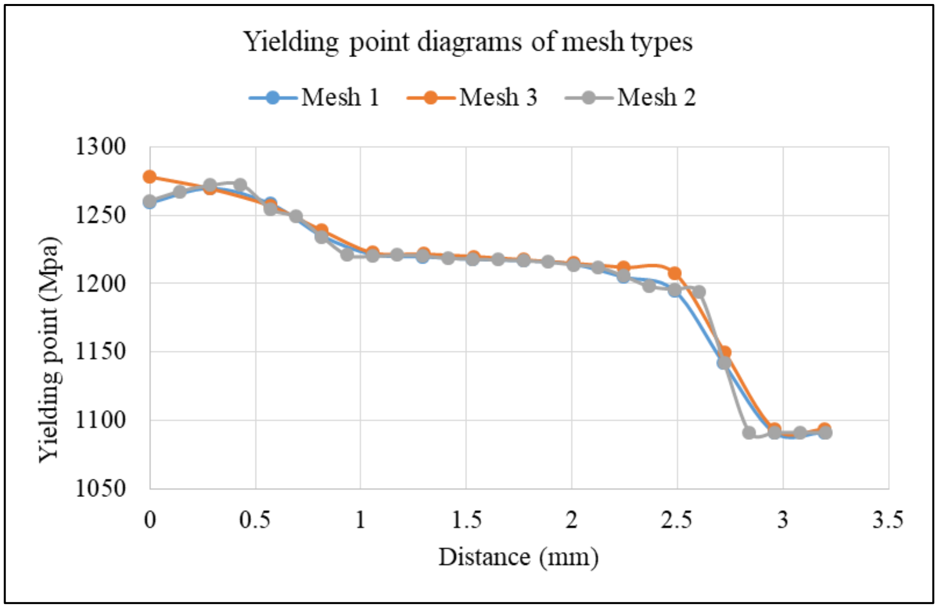

Figure 7-5. Yield strength variation of mesh types

There are two types of input parameters for this analysis; process setup parameters and parameters that need to be determined by simulation tests. The setup parameters are set to the machine before the fabrication. The laser energy, heat source velocity, laser diameter, and surrounding air temperature are the setup parameters (Table 7-2).

Table 7-2. Setup parameters

Energy/unit length (Joule/mm)	Heat source velocity (mm/s)	Laser diameter (mm)	Air temperature (°C)	Substrate temperature (°C)
105- 95- 85	8.4	2	20	20

The laser efficiency, penetration depth, and the laser diameter at the penetration depth are the parameters that need to be identified. Some sensitivity analyses are performed to find the appropriate values. Two approaches are considered in hardness analysis: analysis based on a constant laser efficiency and analysis based on a constant melt pool size.

When partition 5 is being fabricated, its heat conducts into partition 4. This changes the mechanical properties within partition 4. Therefore, as Figure 7-6 shows, 7 beads of partition 5 are added to the simulation. Since the following partition is fabricated on the previous cooled-down one, the first layer of each partition is fabricated by a greater laser power to create a better bond between partitions. Hence, the energy per unit length for the first two layers of each partition are 105, 95 J/mm. The following layers are fabricated by 90 J/mm.

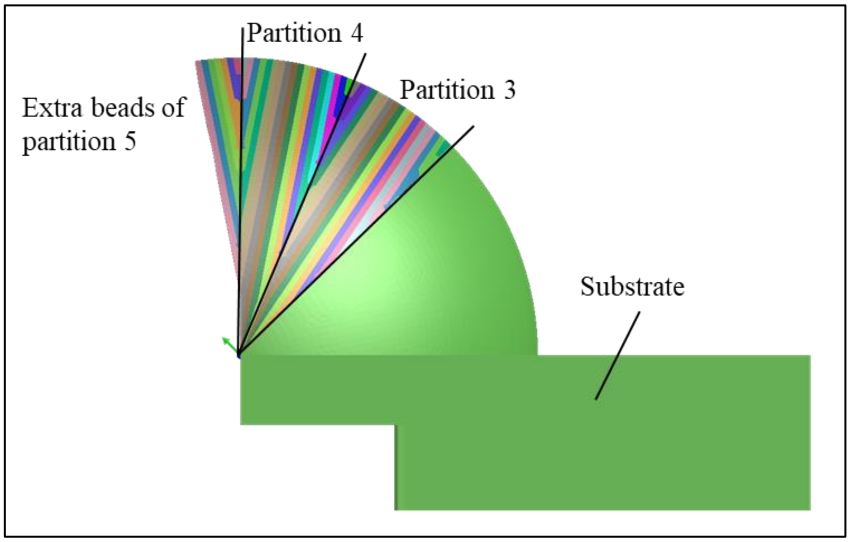

Figure 7-6. Partitions used for parameters-finding simulations

After the parameters are identified, the simulation is executed for all partitions. In order to decrease the analysis preparation time and to use several computers at the same time to calculate, each 2 partitions are simulated separately (Figure 7-7). Each simulation consists of 2 partitions and 7 beads of the next partition. Since there are no other partitions after partition 8, simulation 4 (Figure 7-7 (d)) has just the beads of the last two partitions.

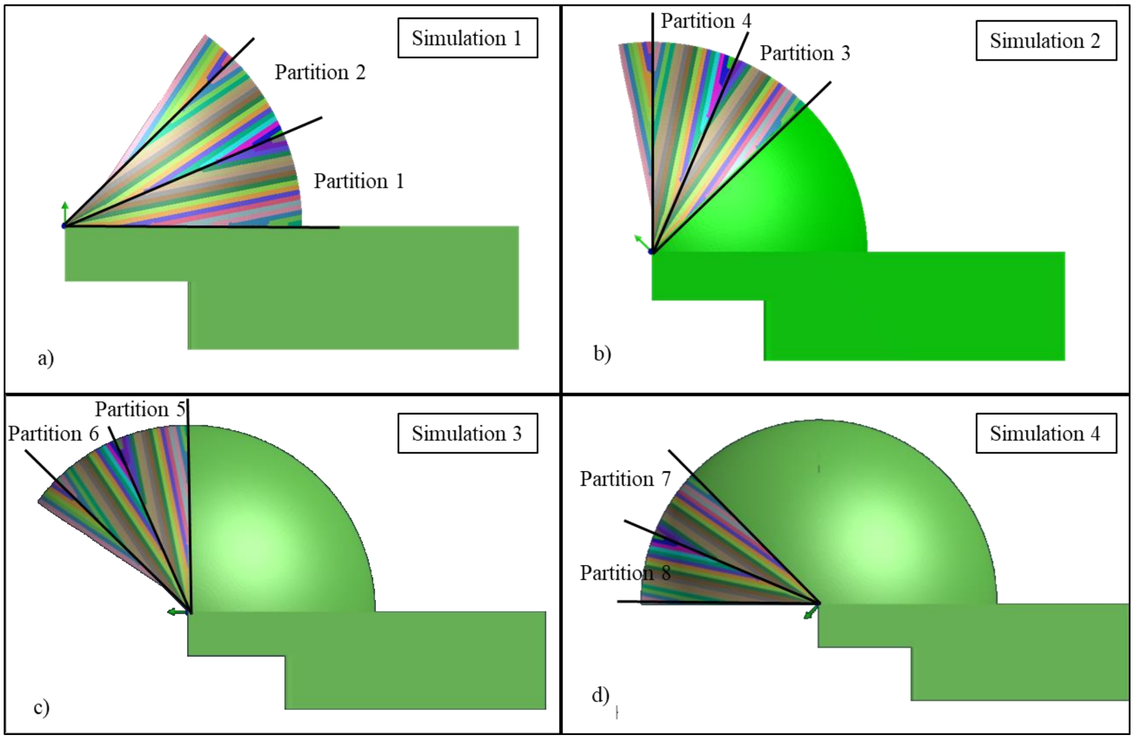
Simulation 1
Partition 2
Partition 1
a)
Partition 4
Partition 3
Simulation 2
b)
Partition 5
Partition 6
Simulation 3
c)
Simulation 4
Partition 7
Partition 8
d)

Figure 7-7. The simulation of the dome is divided into 4 sections

7.1.2 Analysis Based on Constant Laser Efficiency

The focus here is changing the parameters as much as the hardness simulation results matches better to experimental ones. The maximum temperature in the melt pool is checked as well to dismiss the parameter sets that result in very high temperature. The laser efficiency is set to 0.5 to get appropriate results. The other parameters are presented in Table 7-3.

The temperature histories of 3 points indicated in Figure 7-8 (a) are investigated. The temperature history of point 1 is shown in Figure 7-8 (b). Point 1 is located in the first bead of the partition 1. The initial temperature of the substrate is 20°. Therefore, when the first bead is deposited most of the heat is absorbed by the substrate. But there is enough heat to melt the depositing bead. The peak temperature of this bead is about 1800°.

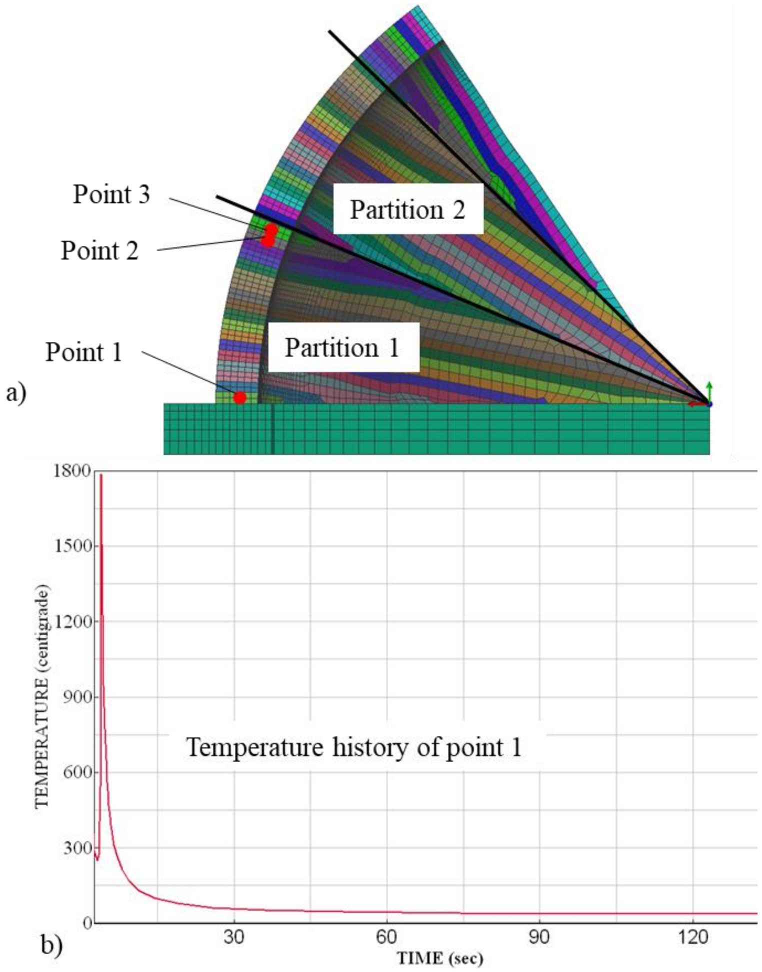

Figure 7-8. (a) Temperature history points are investigated. (b) Temperature history of point 1

Figure 7-9 (a) shows the temperature history of points 2 and 3. Point 3 is located in the last bead (bead 18) of the first partition and point 2 is located in the bead 17. Before the bead 18 is deposited, the heat of 17 previous beads are accumulated in partition 1. Therefore, the temperature of point 3 reaches to about 2800°. This temperature is maintained for a very short time and reduces very quickly.

As Figure 7-9 (b) shows, when bead 17 (where point 2 is located) is depositing temperature reaches to 2500°. Since the time between deposition of bead 17 and bead 18 is enough for bead 17 to cool down to about 1000°, the temperature of bead 18 reaches to 2800°. The last bead of each partition experiences the highest deposition temperature.

Table 7-3. Achieved simulation parameters

Laser efficiency (J/mm)	Penetration depth (mm)	Laser diameter at the bottom (mm)
0.5	1	1.5

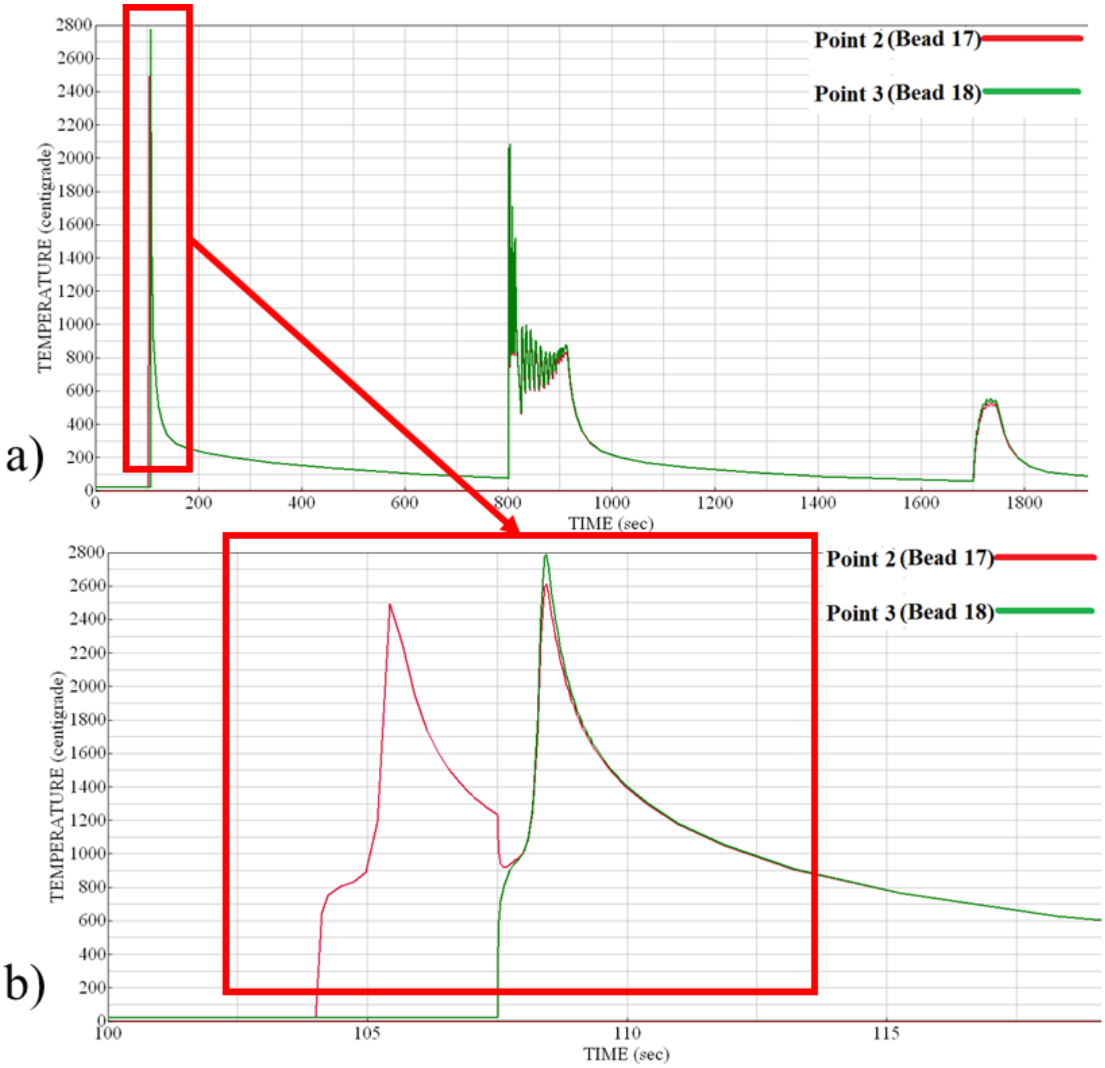

Figure 7-9. (a) Temperature history of points 2, 3 (b) A closer look at temperature histories of points 2, 3 at deposition time

As mentioned in the methodology chapter, the hardness and yield stress have a linear relationship [134]. The linear equation that matches simulation results (yield stress (MPa)) to the experimental ones (Hardness (Vickers)) is presented in Equation (24).

$$Hardness = 0.5 \times (yield\ stress) - 410 \tag{25}$$

The hardness results for all partitions are shown in Figure 7-10. It shows a reasonable match between the experimental data and simulation results for partitions 1-4. The hardness pattern of these regions is simple as they have one peak value. The results for partitions 5-7 predict some of the peak values correctly but it misses some others. The experimental hardness variation of these partitions does not show a recognizable pattern. Some sensitivity analyses are performed to study the dependency of the hardness results in the simulation parameters. Some of the parameter setups for simulation 1, 2 are presented in Table 7-4 and Table 7-5. The resultant hardness variation diagrams show that parameter changes do not change the pattern significantly but it mostly causes shifts in the locations of the peak points. However, the simulation results do not show any variation for partition 8. The main simulation-based difference between partition 8 and other ones is that the simulation 4 (partitions 7, 8) does not have the 7 beads of the following partition. Sensitivity analysis is done to investigate whether different FEA parameters cause a hardness variation for partition 8 (Table 7-6). The results show the variations are insignificant with all parameter configurations (Figure 7-14 and Figure 7-15)

Figure 7-11 presents the contour plot of the simulation results for hardness. Except for a few points where the hardness is higher at the outer edges, the results support the assumption that the hardness is constant across the surface stripe. However, the hardness variation diagram of Figure 6-9 showed a little variation across the surface the same as the contour plot in Figure 7-11 illustrates. The simulation curve of the first partition shows a similar pattern to the experimental data with exaggerated intensity. The hardness is at its peak value for the first layers because of the rapid cooling. Since the last partition does not show any hardness variation, it shows that most of the hardness variations are made by the heat that is conducted after the next partition deposited on the previous one. The boundary conditions of the last partition can be the reason that the hardness variation is zero for partition 8.

The bead geometry of this analysis is supposed to be constant for all layers but as discussed before, the real layer height varies because of the applied planar slicing. This can be a reason for the difference between simulation and experimental results.

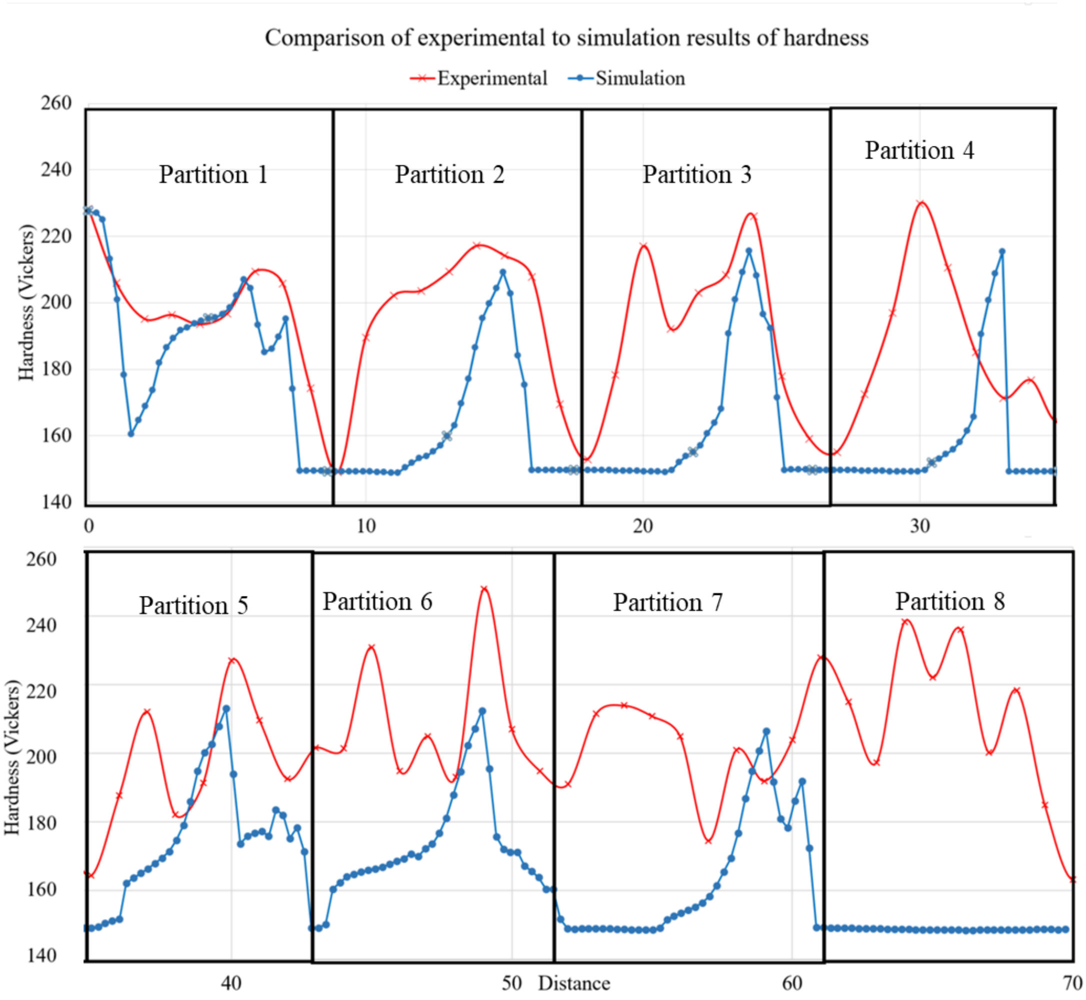

Figure 7-10. Comparison of experimental to simulation results of the hardness

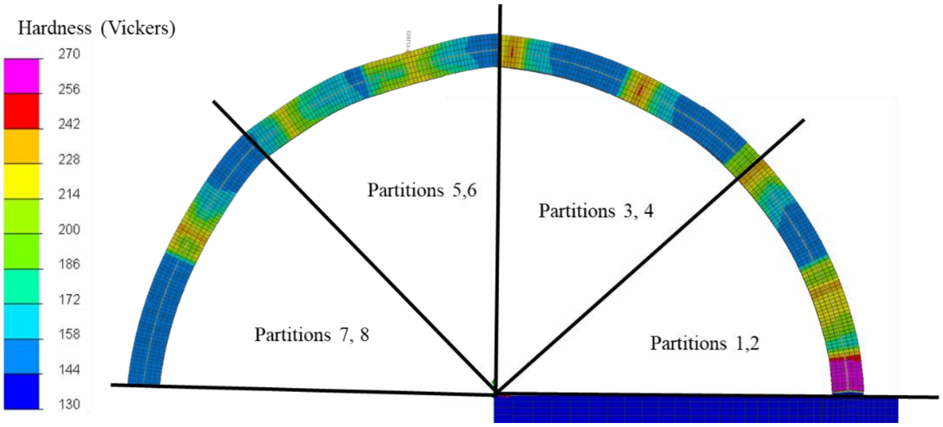
Hardness (Vickers)
270
256
242
228
214
200
186
172
158
144
130
Partitions 5,6
Partitions 3, 4
Partitions 7, 8
Partitions 1,2

Figure 7-11. Hardness variation results of the simulation

Table 7-4. Some of the studied parameters for sensitivity analysis for simulation 1 (partitions 1, 2). The value in parentheses is applied for the rest of the beads of each partition

	Energy/unit (j/mm)	Efficiency	Penetration (mm)	Bottom diameter (mm)
S1,2-1	50, 50, 45, 45, (35)	1	1	1.8
S1,2-2	105, 100, (90)	0.45	1.25	1.8
S1,2-3	105, 95, (90)	0.5	1.2	1.8
S1,2-4	65, (60)	0.7	1.2	1.5

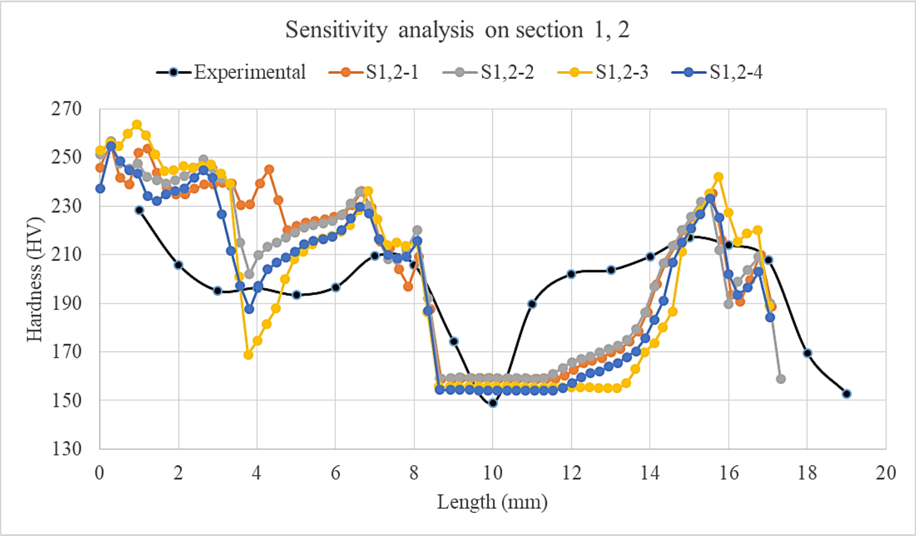

Figure 7-12. Effect of FEA parameters on hardness variation in simulation 1 (partitions 1, 2)

Table 7-5. Some of the studied parameters for sensitivity analysis simulation 2 (partitions 3, 4). The value in parentheses is applied for the rest of the beads of each partition

	Energy/unit (j/mm)	Efficiency	Penetration (mm)	Bottom diameter (mm)
S3,4-1	105, 95, (90)	0.75	1	1.8
S3,4-2	105, 95, (90)	0.75	1.5	1.5
S3,4-3	105, 95, (90)	0.55	1.5	1.5
S3,4-4	105, 95, (90)	0.7	1.2	1.5

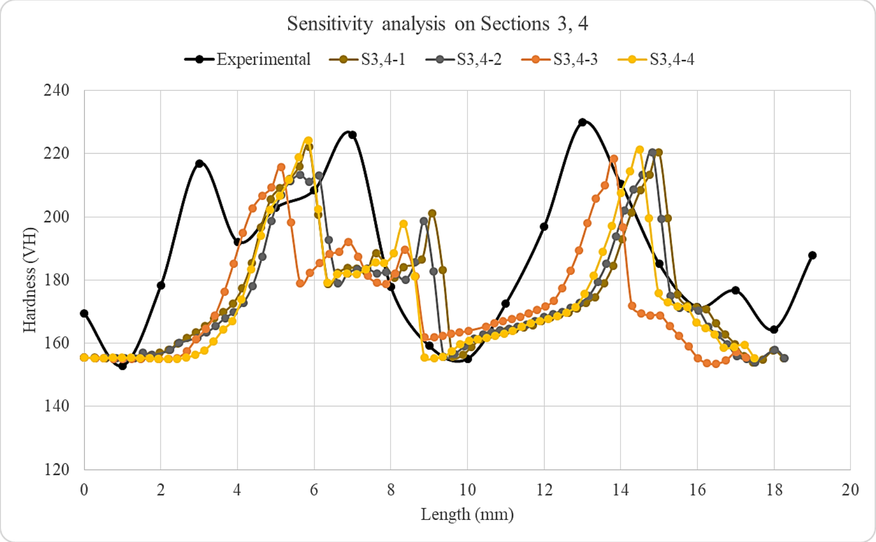

Figure 7-13. Effect of FEA parameters on hardness variation simulation 2 (partitions 3, 4)

Table 7-6. Studied parameters for sensitivity analysis in partition 8. (*) substrate temperature 100 °C. The value in parentheses is applied for the rest of the beads of each partition

	Energy/unit (j/mm)	Efficiency	Penetration (mm)	Bottom diameter (mm)
S8-1	105, 95, (90)	0.4	0.15	1.8
S8-2	105, 95, (90) *	0.45	1.2	1.5
S8-3	105, 95, (90)	0.5	0.2	1.5
S8-4	100, 95, (90) *	0.5	1.5	1.5
S8-5	105, 95, (90)	0.7	1.2	1.8
S8-6	105, 95, (90)	0.44	1	1.5
S8-7	105, 95, (90)	0.46	1.2	1.5

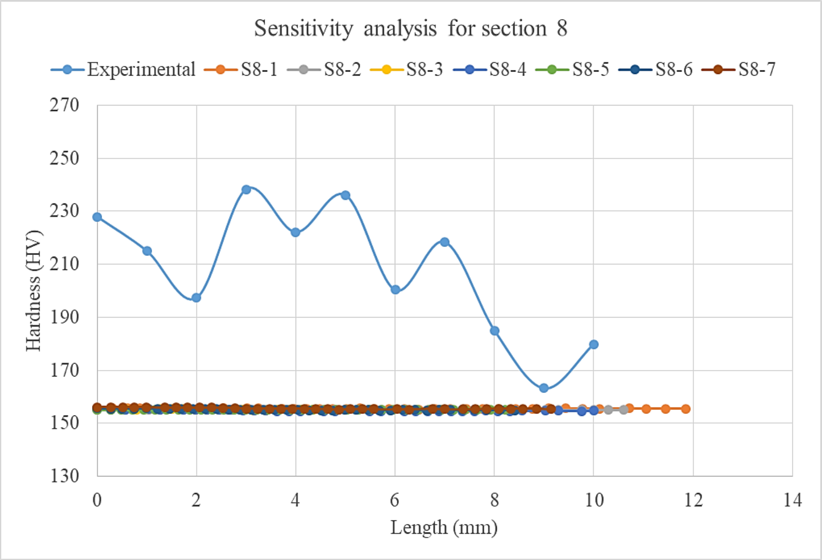

Figure 7-14. Effect of FEA parameters on hardness variation in partition 8

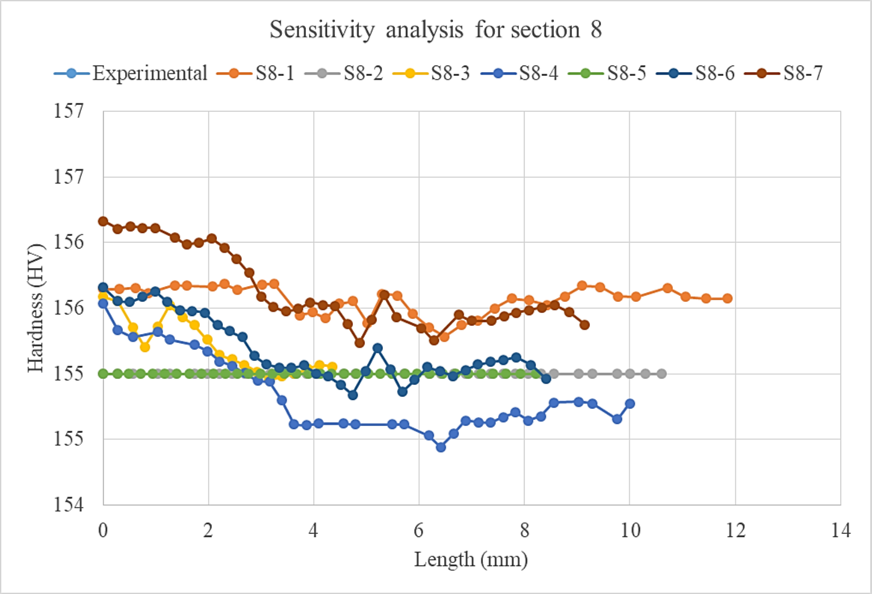

Figure 7-15. Magnified charts of Figure 7-14

7.1.3 Analysis Based on Constant Melt Pool Size

In this approach, the depth of the melt pool is maintained to include maximum 2 beads (the depositing bead and the previous one) [133] and the temperature of the melt pool is to be between 1500 °C- 2000 °C (melting temperature 1510 °C [124]). The laser powers for the first two beads of each partition are deliberately set to a higher value to make a better bond to the substrate, therefore the maximum 2 bead depth of the melt pool is not considered for them. The values of the penetration depth and the laser diameter at the penetration depth are the same as Table 7-3. The laser penetration varies in a way that it decreases in the higher layers of a partition. The variations of the laser efficiency are shown in Figure 7-16. Also, Figure 7-17 shows the melt pool size of some of the beads of partitions 7, 8, and their temperature gradient.

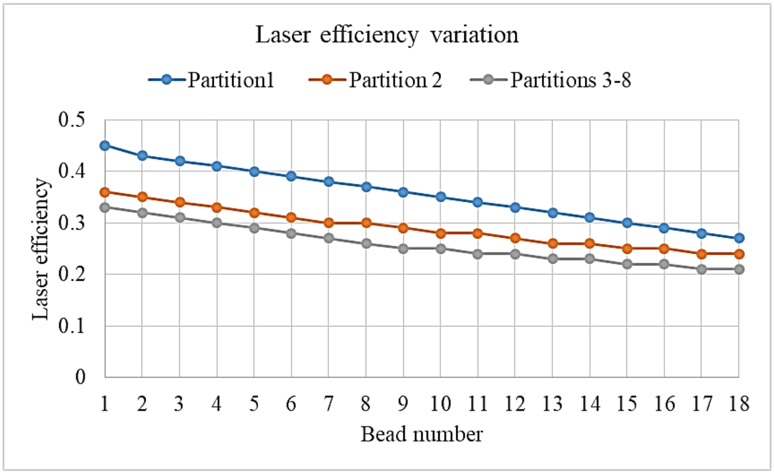

Figure 7-16. Laser efficiency of the beads within partitions

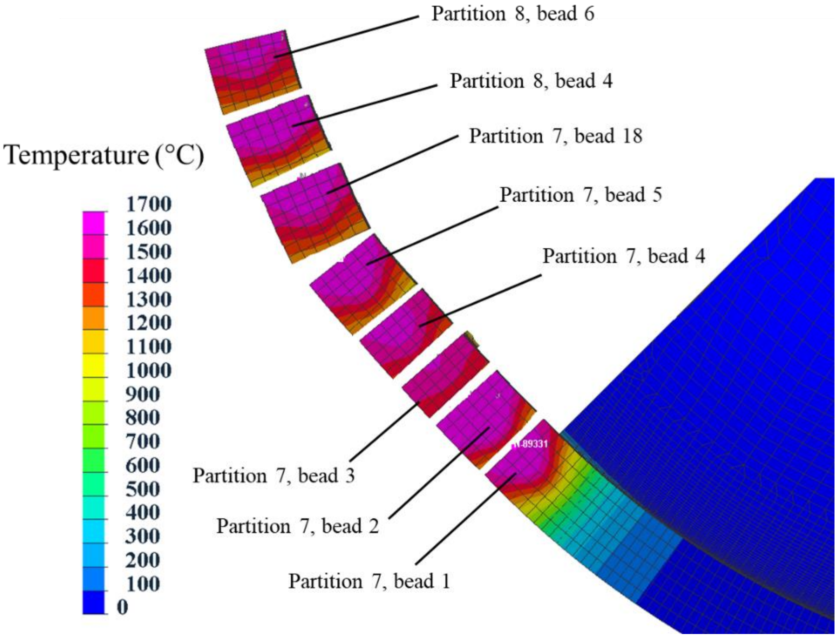
Partition 8, bead 6
Partition 8, bead 4
Partition 7, bead 18
Partition 7, bead 5
Partition 7, bead 4
Partition 7, bead 3
Partition 7, bead 2
Partition 7, bead 1
Temperature (°C)
1700
1600
1500
1400
1300
1200
1100
1000
900
800
700
600
500
400
300
200
100
0

Figure 7-17. Melt pool sizes of some beads

The hardness variation of the constant melt pool size is shown in Figure 7-18. The patterns are almost the same for partitions 1- 7. The hardness increases drastically at the higher layers of each partition. The partition 8 does not show significant hardness variation the same as the constant laser efficiency method (Figure 7-10).

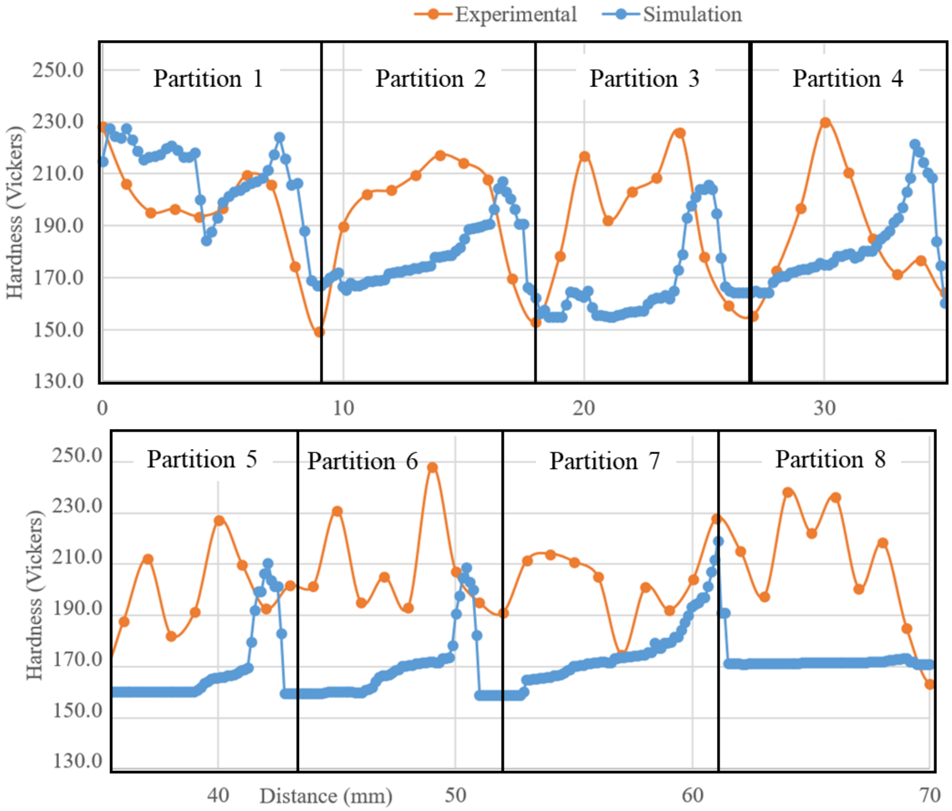

Figure 7-18. Hardness variation of the constant melt pool approach

7.1.4 Discussion

Figure 7-19 explains the reason that hardness does not change in the simulation results of partition 8. Figure 7-19 (a) shows some points within partition 8. The temperature histories of these points are shown in Figure 7-19 (b). The temperature of these points after deposition is kept between the tempering temperatures (605 °C) and austenitizing temperature (1010 °C) [137]. Therefore, during the deposition, the microstructure of the partition 8 is austenite. When the deposition of partition 8 is finished all of the beads cool down at the same rate.

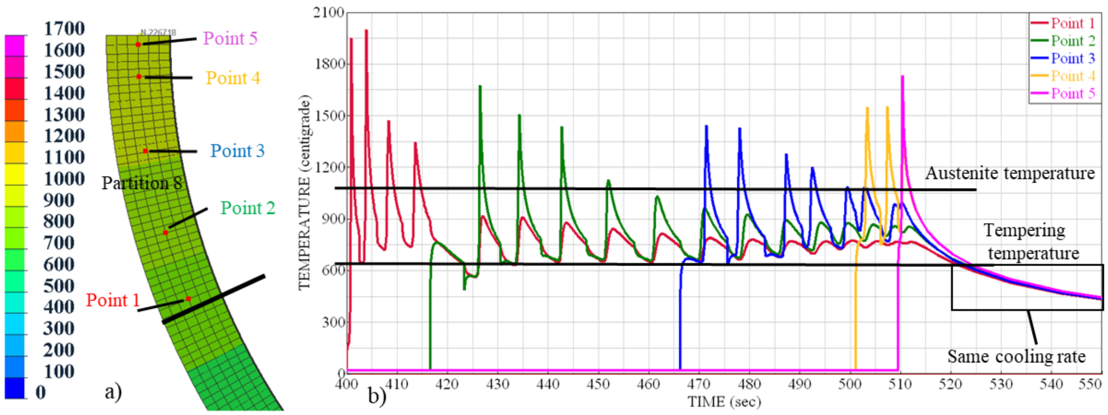

Figure 7-19. (a) Constant temperature along the partition 8 during cooling (b) The temperature history of some points along partition 8

As Figure 7-20 (a) illustrates, the heat conduction along the dome is faster than the amount of heat that dissipates from the dome by radiation and convection along the partition 8. As a result the deposition energy keeps the partition above the tempering temperature until the partition is fabricated. After the deposition is done the heat dissipates by radiation and convection at the same rate along the dome. This causes the phase distribution in partition 8 to become uniform (Figure 7-20 (b)). Also, another thermos-metallurgical analysis is done for partition 3 without including partition 4 in the simulation (Figure 7-20 (c)). The same uniform phase distribution happens. This shows the hardness variation of the simulation is mostly created from the heat effect of the succeeding partition to the previous one. Mechanical analysis is done for partition 2 which its hardness diagram is shown in Figure 7-21. This diagram also supports that the hardness variation is not significant if just one partition is simulated. It is possible to make a hardness variation for partition 8 by virtually adding partition 9 after that.

This shows that the heat dissipation rate caused by bead deposition of a thin wall on another thin wall substrate is not happening the same as what is happening during the experimental procedure. As it is clear for both simulation methods the results for partition 1, 2 is satisfactory. The reason can be that it is being built on a solid substrate and the shape of the deposited part is similar to a vertical wall. Also, the surrounding temperature is room temperature during fabrication. For higher partitions, the simulation assumptions such as melt pool size, surrounding temperature, laser penetration needs to be checked experimentally. This can be because the assumption of the melt pool size or the boundary conditions need to be revised by increasing process information during fabrication. This can be done by adding some facilities during the process to measure the surrounding temperature during fabrication. The complex geometry of the dome may cause the hot air being trapped at its inner surface that causes the surrounding temperature variation during fabrication. Also, some experiments need to be developed to measure the melt pool size during the process by an infrared camera or by depositing a single layer at various locations of a dome and measure the melt pool indirectly by measuring the heat-affected zone. Also, the calculation techniques of Sysweld software needs to be explored more to find any parameter that is missing in calculations (this may cause the missing hardness variation of the partition 8) and develop this if needed.

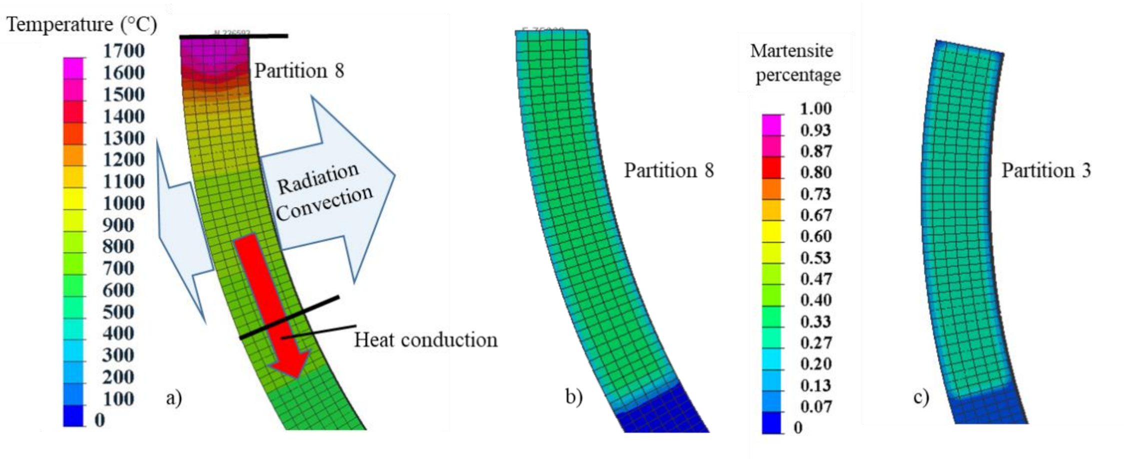
Temperature (°C)
1700
1600
1500
1400
1300
1200
1100
1000
900
800
700
600
500
400
300
200
100
0
Partition 8
Radiation
Convection
Heat conduction
a)
Partition 8
b)
Martensite percentage
1.00
0.93
0.87
0.80
0.73
0.67
0.60
0.53
0.47
0.40
0.33
0.27
0.20
0.13
0.07
0
Partition 3
c)

Figure 7-20. (a) Heat dissipation from the thin wall (b) Austenite percentage of the partition 8 (c) Martensite percentage of the partition 8

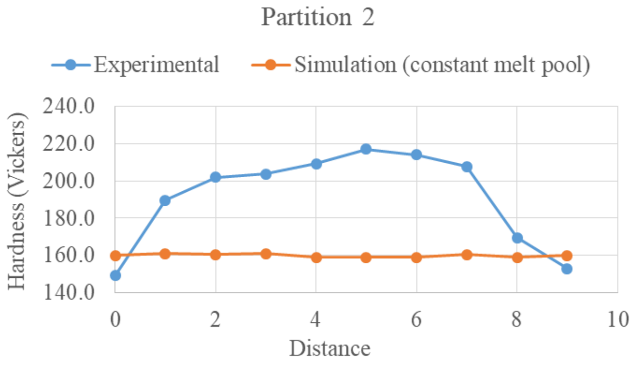

Figure 7-21. Hardness variation of partition 2

Figure 7-22 compares the results of two applied simulation methods with the experimental results. It shows that the results of the constant melt pool method are shifted about 2 mm toward the higher distance values. The simulation parameters of the constant melt pool method are more reasonable by physical phenomena but the results of the first simulation method seem to better match the experimental data. Higher efficiency that is applied to the successive partitions in constant laser efficiency method shifts the hardness peak point more the center of the partitions. Here, by unrealistically increasing the laser energy (this causes melt pool temperatures higher than boiling temperature), the hardness variation becomes more similar to experimental results. As a future, work the boundary and initial conditions of the model can be improved with experimental measurement. Also, another simulation with tetra mesh may improve the results as the number of calculation nodes increases.

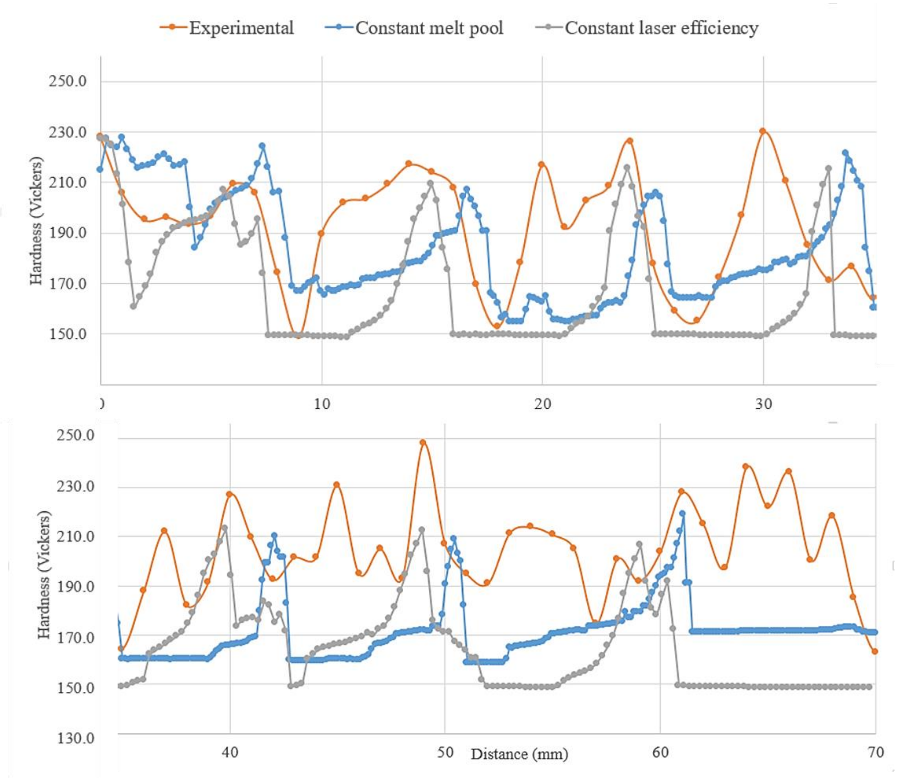

Figure 7-22. Comparison between the results of two applied simulation methods with the experimental result

Figure 7-23 and Table 7-7 compare the FFT analysis of the experimental results to the simulation results. The simulation pattern matches the partition length with a variation of 1.1 % whereas the length of the repetitive pattern of the experimental results has 9.6 %.

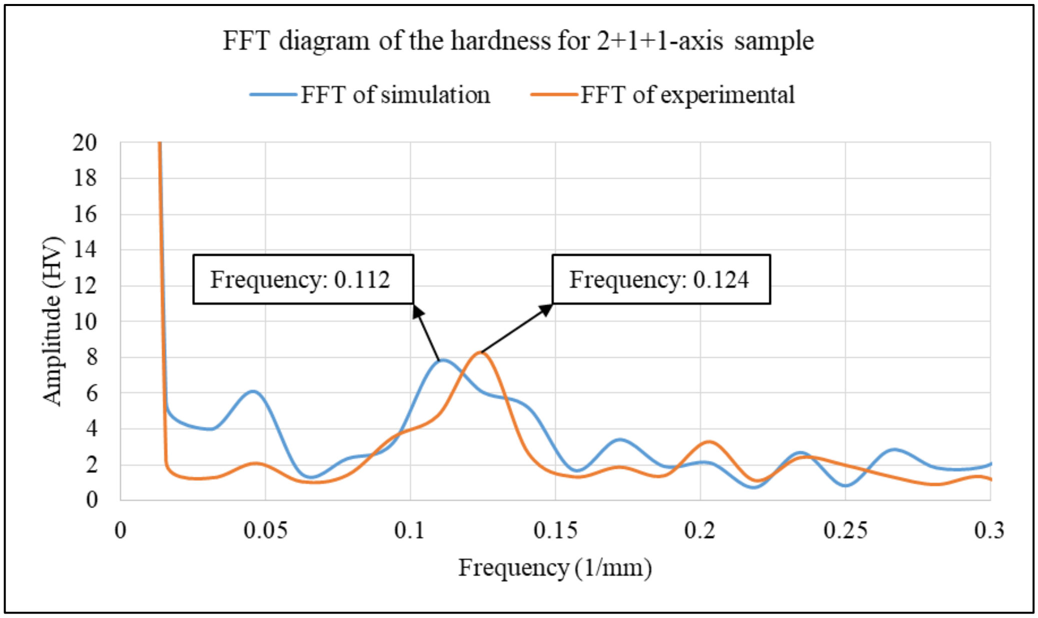

Figure 7-23. FFT diagram of simulation data of the hardness for 2+1+1-axis sample

Table 7-7. Comparison of the simulation and experimental FFT results

	Frequency (1/mm)	Wavelength mm	Partition length mm	Variation (%)
Simulation	0.112	8.93	8.84	1.1
Experimental	0.124	8.06		9.6

7.2 *Residual Stress Variation*

Since the hardness variation diagram of partitions 1-4 matches the experimental results better than the results of partitions 5-8, the residual stress contour is presented for partitions 1-4 in Figure 7-24. Verification of the simulation results with experimental data is considered as future work.

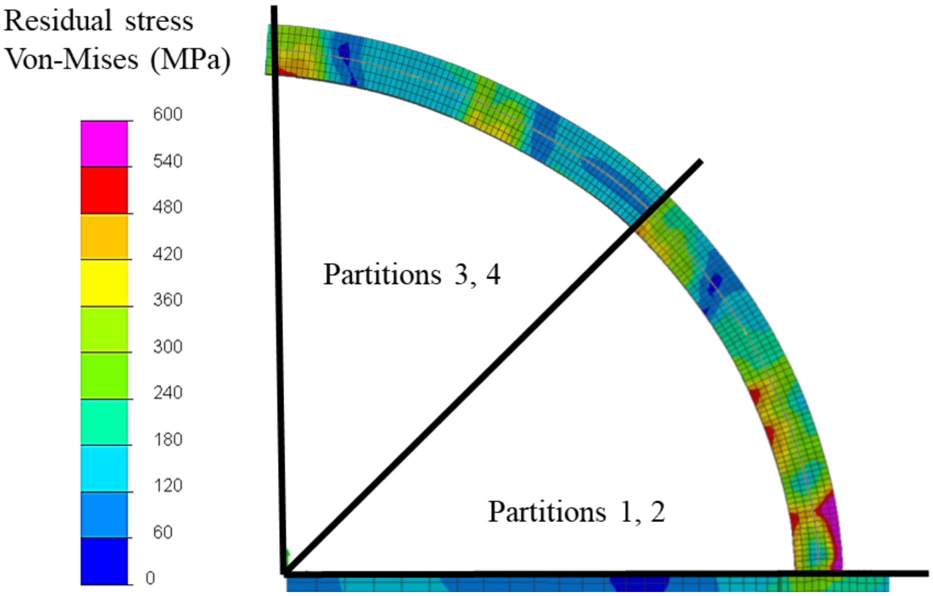

Figure 7-24. Residual stresses of partitions 1-4

The residual stress is at the highest value for the bottom of the partition 1. The substrate has a large volume and absorbs the heat of the first layers. This leads to rapid cooling of the first beads after they are deposited. Therefore, the residual stress is high in the bottom layers of partition 1.

The first partition works as the substrate for the deposition of the second partition. As the first partition is a thin wall, its temperature elevates quickly when the second partition material is being deposited. After the deposition of the second partition is finished, both partitions cool down at the same rate which leads to less residual stress trapped in the second partition. This occurs for the next partitions as well. As a result, the residual stress is lower for partitions 2-4.

In this chapter, the results of the numerical analyses for hardness, temperature history, and residual stress of the 2+1+1-axis sample was covered. The simulation was implemented for 144 beads with a drastically reduced run time. The simulation results of the hardness were verified by experimental data, and overall the results correlate well. There are challenges with addressing the variable observed bead sizes, differing heat inputs and dwell times (as discussed in the methodology section), and the scope of the simulation. The summary, conclusion, and future work are presented in the next chapter.

CHAPTER 8

SUMMARY, CONCLUSION AND FUTURE WORK

8.1 *Summary*

Appropriate process planning solutions need to be developed for fabricating complex geometries by multi-axis DED systems in a supportless manner. This introduces several collision issues; however, it is essential to detect and avoid collisions. The developed algorithm in this research uses tool orientations and geometry segmentation to avoid collisions. Based on this algorithm, two strategies are developed to fabricate a hemisphere dome: they are wedge-shaped partitioning, and an offset rotary toolpath. A 5-axis toolpath and a 2+1+1-axis toolpath are used to implement the wedge-shaped partitioning approach. The wedge-shaped partition domes are built at the end of a flat substrate to eliminate collisions, whereas the rotary sample is fabricated at the end of a round bar.

As metal AM built products have a rough surface in addition to usually having a curved surface, standard methods for surface roughness measurement have limitations to measure these parts. Process planning, data collection, and experimental/numerical procedures are implemented to investigate the surface roughness variations of three fabricated domes along the slice direction. The developed Matlab program associated with the mount solution uses the exposed edges of the specimen in the mount. Since the exposed surface is polished, it reveals detailed surface textures under the microscope. The results are verified by comparing the Ra from a set of edge points where the associated Ra is known.

A Matlab program for the Ra measurement for round surfaces from 3D point cloud data was developed as well. A distance factor was introduced into the calculations that signifies the points that are nearer to the measurement region. The results of this solution are compared to the mount solution. For assessing the surface roughness, the mount solution needs much pre-processing and is labour intensive, but this process is more accurate. The 3D-point cloud can be used to measure the surface roughness of bead-deposition based AM technologies using 3D scanner with a 10 times more accurate resolution than a predicted Ra value. Tools need to be used to predict the Ra [53]. It can be used for online monitoring as it is a quick and non-contact method, but the measured roughness of the inner surface of the dome is different from the outer surface. The reason can be the orientation of the nozzle which is not tangent to the surface in 2+1+1-axis sample.

The Ra variation diagrams show lower Ra values for the 5-axis sample and the highest values for the rotary sample. The reason that the 5-axis shows the best results is likely because the layers within one partition are explored and it does not reveal the surface irregularities at the points between the partitions. The 2+1+1-axis sample shows bumps at the transition points between partitions. The reason is a sudden alteration of nozzle orientation which exceeds the maximum allowed overhang angle.

Additionally, a procedure for data collection, experimental, and numerical measurements for the hardness of the fabricated products is developed. The hardness is measured along the slicing direction. A data collection strategy is developed to eliminate the noise from the inconsistency of the hardness across the surface stripe of the mount sample. This led to utilizing an indentation load of 1000 gf to minimize this noise. The experimental hardness diagram of the 2+1+1-axis sample shows a recognizable pattern for partitions 2-4. However, there is no simple recognizable pattern for the next partitions.

The hardness for partition 3 of the 5-axis sample shows the same pattern. Although the rotary sample is fabricated in 3 intermittent sections, it does not show any significant pattern related to the sectioning. The statistical analysis of the hardness shows the highest standard deviation for the 5-axis sample and the least for the rotary one. Also, the hardness modes of the 3 samples are almost equal.

The results of this research showed the pros and cons of fabricating a part in partition-based mode that need to be addressed when a functional part is being produced. On one hand, the complex geometries become manufacturable, on the other hand, it results instability in mechanical properties. The hardness drops significantly at transition regions between partitions.

An FEA analysis for the hardness is performed using ESI Sysweld software for 144 beads for the 2+1+1-axis dome. Two methods are applied; constant laser efficiency and constant melt pool size. The hardness variation in partition 8 is not significant which is because of the resultant uniform phase. The heat dissipation from the surface results in a uniform phase along partition 8. The FFT analyses of experimental and numerical data show the whole 2+1+1-axis dome show that the length of the repetitive pattern is the same as partition length.

8.2 *Conclusion*

Similar to the machining process that decades of exploration solved most of its obstacles to control the process parameters and collision problem, much research needs to be conducted for multi-axis AM deposition processes as well.

For the case study sample that was investigated in this research, the fabrication sequence of the partitions cannot be changed as each one is the base for the next one. But for other geometries, the sequence of the fabrication may be needed to be determined. In this case, more experimental research needs to be accomplished to control the effect of the heating and cooling cycles (introduced from partitioned fabrication) on the mechanical properties of the product.

Advanced automation methods like machine learning and artificial intelligence can be applied in the partitioning algorithm. It makes the decision making of how to partition the very complex geometries faster and with less interaction with the user. Also, by teaching it with simpler geometries it can gradually learn to partition other geometries.

The availability of the manufacturing DED machine should be considered in the algorithm (i.e. 3-axis machine, 5- axis machine, or a robotized DED). If the geometry can be partitioned in a way that is buildable by less axes, it reduces the complexity of the fabrication.

The transition regions between partitions cause drastic alteration of mechanical properties and surface roughness changes that may cause failure. Therefore a post-heat treatment and machining may be needed to blend it.

The reason that the rotary sample has the highest Ra value can be the tiny splashes of molten powder attached to the surface. The nozzle travels the periphery of the dome to deposit each layer. It takes time to pass the same point of the previous layer which is cooled down. Therefore, some powder particles that are not molten splash out of the melt pool and attach to the side of the dome wall. This increases the roughness value. This is a hypothesis and needs more investigation as future work.

Before FEA analysis of the mechanical properties of a product, the decision needs to be made to choose between experimental fabrication of a dedicated sample or doing an

FEA analysis. In some cases it is more efficient based on the time, labor cost, and the precision of the results to fabricate an initial sample and measure the mechanical properties rather than going through the long process of mesh creation, parameter determination, and finally less accurate results. If the FEA analysis is needed for complex geometries, measurement of some of the simulation parameters such as the melt pool size as well as measuring the surrounding temperature can narrow down the number of iterations to achieve these parameters and create a more precise FEA analysis.

Microstructure analysis of the product can help to find how much the hardness variation is caused by the phase variation along the partitions. Other possible fabrication inconsistencies (that need to be explored and determined) may cause minor changes in the hardness that are not included in the simulation.

The preprocessing time of the FEA model including mesh preparation and parameter identification reveals that a better and faster numerical analysis technique should be developed to lead to faster and more accurate results. Artificial intelligent techniques such as a neural network can be applied for this purpose. Also, new developing additive manufacturing modules of some commercial software can be explored.

8.3 *Future Work*

This research can be developed to explore many different aspects of DED-AM in much more detail. Besides the outcomes, this research brought many new questions that can be answered by more experiments, analyses, and programming. Some possible future work expanding this research is listed:

- The collision detection and prevention algorithm can be explored in more detail for surface tool paths, components with complex junctions, and then automated.
- The constant stepover toolpath that was introduced to build the domes should be fabricated. Their hardness and roughness variations should be compared to the domes that were fabricated by planar slicing.
- A CAD model of the dome that includes the detailed geometry of the beads with variable layer height should be prepared. This CAD model can be used to extract the required txt file of the surface edge points. These points are the input data for surface roughness measurement program. The outcome is the ideal Ra variation. Then, the results can be compared with hardness variation of fabricated domes.

- The surface roughness methodology should be modified to measure all curved surfaces.
- Microstructure analyses should be performed to understand and interpret the hardness variations.
- The FEA analysis is implemented by using a moving heat source (MHS) method. The same simulations can be executed by using an imposed thermal cycle (ITC) method to decrease the calculation time. The results can be compared with the results of this research.
- The residual stresses can be measured experimentally to compare with the simulation results.
- More investigation is needed to realize why the FEA results do not match satisfactorily to the experimental results for partitionss 5-8 and especially for partition 8. For example the sample geometry can be analyzed again by another mesh type like tetra mesh to double check the results.

REFERENCES/BIBLIOGRAPHY

[1] H. Kalami and J. Urbanic, “Process Planning of Creating a Surface Dome with Bead Deposition Additive Manufacturing,” *IFAC-PapersOnLine*, vol. 52, no. 10, pp. 230–235, 2019.

[2] S. A. McMains, “Rapid prototyping of solid Three-Dimensional Parts,” University of California, Berkley, 1996.

[3] X. Yan and P. Gu, “A review of rapid prototyping technologies and systems,” *Computer Aided Design*, vol. 28, no. 4, pp. 307–318, 1996.

[4] W. E. Frazier, “Metal Additive Manufacturing: A Review,” *Journal of Materials Engineering and Performance*, vol. 23, no. 6, pp. 1917–1928, 2014.

[5] P. J. Bártolo, *Stereolithography: Materials, Processes and Applications*. Springer US, 2011.

[6] Q. Mu *et al.*, “Digital light processing 3D printing of conductive complex structures,” *Additive Manufacturing*, vol. 18, pp. 74–83, 2017.

[7] M. Mele, G. Campana, and G. L. Monti, “Modelling of the capillarity effect in Multi Jet Fusion technology,” *Additive Manufacturing*, vol. 30, p. 100879, 2019.

[8] D. X. Luong *et al.*, “Laminated Object Manufacturing of 3D-Printed Laser-Induced Graphene Foams,” *Advanced Materials*, vol. 30, no. 28, pp. 1–6, 2018.

[9] R. Rexavier, “Optimal placement of metal foils in ultrasonic consolidation process,” Clemson University, 2007.

[10] A. Sung-Hoon *et al.*, “Anisotropic material properties of fused deposition modeling ABS,” *Rapid Prototyping Journal*, vol. 8, no. 4, pp. 248–257, Jan. 2002.

[11] C. Körner, “Additive manufacturing of metallic components by selective electron beam melting — a review,” *International Materials Reviews*, vol. 61, no. 5, pp. 361–377, 2016.

[12] S. Singh, V. S. Sharma, and A. Sachdeva, “Progress in selective laser sintering using metallic powders: a review,” *Materials Science and Technology*, vol. 32, no. 8, pp. 760–772, 2016.

[13] J. Nandy, H. Sarangi, and S. Sahoo, “A Review on Direct Metal Laser Sintering: Process Features and Microstructure Modeling,” *Lasers in Manufacturing and*

Materials Processing, vol. 6, no. 3, pp. 280–316, 2019.

[14] G. Yang *et al.*, "Inkjet and inkjet-based 3D printing: connecting fluid properties and printing performance," *Rapid Prototyping Journal*, vol. 23, no. 3, pp. 562–576, 2017.

[15] M. Manoharan and S. Kumaraguru, "Path Planning for Direct Energy Deposition with Collaborative Robots: A Review," in *2018 Conference on Information and Communication Technology (CICT)*, 2018, pp. 1–6.

[16] I. Gibson, D. W. Rosen, and B. Stucker, *Additive Manufacturing Technologies 3D Printing, Rapid Prototyping, and Direct Digital Manufacturing,* 2nd ed. 20. New York, NY: Springer New York, 2015.

[17] "Support Materials for FDM and Polyjet 3D Printing _ Stratasys," *Stratasys Ltd.* ©, 2020. [Online]. Available: https://www.stratasys.com/materials/search/support-materials.

[18] J. Wu, "The Chemistry Behind Soluble Support Removal in Fused Deposition Modeling," 2016. [Online]. Available: https://www.padtinc.com/blog/chemistry_soluble_support_removal_fdm_3d_printing/. [Accessed: 12-Jan-2020].

[19] I. Maskery *et al.*, "Insights into the mechanical properties of several triply periodic minimal surface lattice structures made by polymer additive manufacturing," *Polymer,* vol. 152, pp. 62–71, 2018.

[20] R. Vaidya and S. Anand, "Optimum Support Structure Generation for Additive Manufacturing Using Unit Cell Structures and Support Removal Constraint," *Procedia Manufacturing,* vol. 5, pp. 1043–1059, 2016.

[21] G. Strano, L. Hao, R. M. Everson, and K. E. Evans, "A new approach to the design and optimisation of support structures in additive manufacturing," *The International Journal of Advanced Manufacturing Technology,* vol. 66, no. 9, pp. 1247–1254, 2013.

[22] J. Vanek, J. A. G. Galicia, and B. Benes, "Clever Support: Efficient Support Structure Generation for Digital Fabrication," *Computer Graphics Forum,* vol. 33, no. 5, pp. 117–125, 2014.

[23] R. Schmidt and N. Umetani, "Branching Support Structures for 3D Printing," *ACM SIGGRAPH 2014 Studio*, vol. 9, p. 1, 2014.

[24] M. X. Gan and C. H. Wong, "Practical support structures for selective laser melting," *Journal of Materials Processing Technology*, vol. 238, pp. 474–484, 2016.

[25] M. A. Habib and B. Khoda, "Support grain architecture design for additive manufacturing," *Journal of Manufacturing Processes*, vol. 29, pp. 332–342, 2017.

[26] W. Du *et al.*, "Binder jetting additive manufacturing of ceramics: A literature review," in *ASME International Mechanical Engineering Congress and Exposition, Proceedings (IMECE)*, 2017, vol. 14, pp. 1–12.

[27] Matt Sand, "How to Compare the Various Metal 3D Printing Processes," *3D PRINTING NEWS,* 2017. [Online]. Available: https://www.fabbaloo.com/blog/2017/11/10/how-to-compare-the-various-metal-3d-printing-processes. [Accessed: 20-Dec-2019].

[28] "3D Printing Support Structures: A Complete Guide," *AMFG/Autonomus Manufacturing*, 2018. .

[29] T. W. Simpson, "Will My AM Part Explode," *Modern Machine shop*. [Online]. Available: https://www.mmsonline.com/columns/will-my-am-part-explode. [Accessed: 20-Feb-2020].

[30] ASTM F2792-12a, "StandardTerminology for Additive Manufacturing Technologies."

[31] K. Zhang, W. Liu, and X. Shang, "Research on the processing experiments of laser metal deposition shaping," vol. 39, no. 0030, pp. 549–557, 2007.

[32] P. Ghosal, M. C. Majumder, and A. Chattopadhyay, "Study on direct laser metal deposition," *Materials Today: Proceedings*, vol. 5, no. 5, pp. 12509–12518, 2018.

[33] G. Lewis, "Direct Laser Metal Deposition Process Fabricates Near-Net-Shape Components Rapidly," *Materials Technology*, vol. 10, no. 3–4, pp. 51–54, 1995.

[34] A. W. Gebisa and H. G. Lemu, "Additive manufacturing for the manufacture of gas turbine engine components: Literature review and future perspectives," in *Proceedings of the ASME Turbo Expo*, 2018, vol. 6.

[35] S. M. Thompson, L. Bian, N. Shamsaei, and A. Yadollahi, "An overview of Direct Laser Deposition for additive manufacturing; Part I: Transport phenomena, modeling and diagnostics," *Additive Manufacturing*, vol. 8, pp. 36–62, 2015.

[36] A. Saboori, D. Gallo, S. Biamino, P. Fino, and M. Lombardi, "An overview of

additive manufacturing of titanium components by directed energy deposition: Microstructure and mechanical properties," *Applied Sciences (Switzerland),* vol. 7, no. 9, p. 883, 2017.

[37] S. Kaierle *et al.*, "Single-crystal turbine blade tip repair by laser cladding and remelting," *CIRP Journal of Manufacturing Science and Technology,* vol. 19, pp. 196–199, 2017.

[38] L. Shepeleva, B. Medres, W. D. Kaplan, M. Bamberger, and A. Weisheit, "Laser cladding of turbine blades," *Surface and Coatings Technology,* vol. 125, no. 1, pp. 45–48, 2000.

[39] I. Shishkovsky and I. Smurov, "Titanium base functional graded coating via 3D laser cladding," *Materials Letters,* vol. 73, pp. 32–35, 2012.

[40] Inovar Communications Ltd, "Open Architecture Additive Manufacturing project investigates DED for aerospace," *Metal Am,* 2018. [Online]. Available: https://www.metal-am.com/open-architecture-additive-manufacturing-project-investigates-ded-for-aerospace/. [Accessed: 20-Apr-2019].

[41] W. Shen, L. Wang, and Q. Hao, "Agent-based distributed manufacturing process planning and scheduling: a state-of-the-art survey," *IEEE Transactions on Systems, Man, and Cybernetics, Part C (Applications and Reviews),* vol. 36, no. 4, pp. 563–577, 2006.

[42] C. Chiang and K. Jamil, *Design for manufacturability and yield for nano-scale CMOS*. Springer Science & Business Media, 2007.

[43] R. J. Urbanic, R. W. Hedrick, and C. G. Burford, "A process planning framework and virtual representation for bead-based additive manufacturing processes," *The International Journal of Advanced Manufacturing Technology,* vol. 90, no. 1, pp. 361–376, 2017.

[44] S. Kapil *et al.*, "5-Axis Slicing Methods for Additive Manufacturing Process," *Annual International Solid Freeform Fabrication Symposium,* pp. 1186–1896, 2017.

[45] R. J. Urbanic and B. Hedrick, "Additive manufacturing bead deposition based rotary tool path applications," in *ASME International Mechanical Engineering Congress and Exposition, Proceedings (IMECE),* 2018, vol. 2, no. 10, pp. 230–235.

[46] I. Lazoglu, S. Ehsan, Layegh, Khavidaki, and A. Mamedov, "Mechanics of Titanium

Machining," in *Machining of Titanium Alloys*, 2014, pp. 57–78.

[47] L. Arnaud, O. Gonzalo, S. Seguy, H. Jauregi, and G. Peigné, "Simulation of low rigidity part machining applied to thin-walled structures," *The International Journal of Advanced Manufacturing Technology*, vol. 54, no. 5, pp. 479–488, 2011.

[48] S. Saquib, "Experimental Investigation of Laser Cladding Bead Morphology and Process Parameter Relationship for Additive Manufacturing Process Characterization," University of Windsor, 2016.

[49] A. Kush, R. J. Urbanic, and S. M. Saqib, "Development of predictive models for effective process parameter selection for single and overlapping laser clad bead geometry," *Rapid Prototyping Journal*, vol. 24, no. 1, pp. 214–228, 2018.

[50] S. M. Saqib and R. J. Urbanic, "Investigation of the Transient Characteristics for Laser Cladding Beads Using 420 Stainless Steel Powder," *Journal of Manufacturing Science and Engineering*, vol. 139, no. 8, May 2017.

[51] M. K. Alam, J. Urbanic, S. M. Saqib, and A. Edrisy, "Effect of process parameters on the microstructural evolutions of laser cladded 420 martensitic stainless steel," *Materials Science and Technology Conference and Exhibition 2015, MS and T 2015*, vol. 1, no. September 2017, pp. 35–54, 2015.

[52] V. Raghavendra, N and L. Krishnamurthy, "Metrology of Surface Finish," in *Engineering Metrology and Measurements*, Oxford University Press, 2013, pp. 217–230.

[53] R. J. Urbanic and L. DiCecco, "Virtual bead representation and surface roughness evaluation challenges for additive manufacturing material extrusion processes," *The International Journal of Advanced Manufacturing Technology*, vol. 102, no. 9, pp. 2993–3009, Jun. 2019.

[54] A. Huckstepp, "Surface Roughness," *Digital Alloys' Guide to Metal Additive Manufacturing – Part 11*, 2019. [Online]. Available: https://www.digitalalloys.com/blog/surface-roughness/.

[55] H. Gohari *et al.*, "Intelligent Process Planning for Additive Manufacturing," *IFAC-PapersOnLine*, vol. 52, no. 10, pp. 218–223, 2019.

[56] R. J. Urbanic, R. W. Hedrick, S. Saquib, and N. Nazemi, "Material bead deposition with 2 + 2 ½ multi-axis machining process planning strategies with virtual

verification for extruded geometry," *International Journal of Advanced Manufacturing Technology*, vol. 95, pp. 3167–3184, 2018.

[57] Y. Jin, J. Du, and Y. He, "Optimization of process planning for reducing material consumption in additive manufacturing," *Journal of Manufacturing Systems*, vol. 44, pp. 65–78, 2017.

[58] H. Eiliat and J. Urbanic, "Visualizing, analyzing, and managing voids in the material extrusion process," *The International Journal of Advanced Manufacturing Technology*, vol. 96, no. 9, pp. 4095–4109, 2018.

[59] Y. Zhang *et al.*, "Evaluating the Design for Additive Manufacturing: A Process Planning Perspective," *Procedia CIRP*, vol. 21, pp. 144–150, 2014.

[60] B. Vayre, F. Vignat, and F. Villeneuve, "Designing for Additive Manufacturing," *Procedia CIRP*, vol. 3, pp. 632–637, 2012.

[61] M. Liang *et al.*, "From Topology Optimization Design to Additive Manufacturing: Today's Success and Tomorrow's Roadmap," *Archives of Computational Methods in Engineering*, pp. 1–26, 2019.

[62] M. Schumann, M. Witt, and P. Klimant, "A real-time collision prevention system for machine tools," *Procedia CIRP*, vol. 7, pp. 329–334, 2013.

[63] H. T. Yau *et al.*, "NC simulation for adaptive look-ahead interpolator with on-line collision detection," *Computer-Aided Design and Applications*, vol. 13, no. 6, pp. 863–871, 2016.

[64] L. Zhiwei *et al.*, "Approximate tool posture collision-free area generation for five-axis CNC finishing process using admissible area interpolation," *International Journal of Advanced Manufacturing Technology*, vol. 62, no. 9–12, pp. 1191–1203, 2012.

[65] T. D. Tang and E. L. J. Bohez, "A new collision avoidance strategy and its integration with collision detection for five-axis NC machining," *International Journal of Advanced Manufacturing Technology*, vol. 81, no. 5–8, pp. 1247–1258, 2015.

[66] J. Wang, M. Luo, and D. Zhang, "A GPU-Accelerated approach for collision detection and tool posture modification in multi-axis machining," *IEEE Access*, vol. 6, pp. 35132–35142, 2018.

[67] T. Chen, P. Ye, and J. Wang, "Local interference detection and avoidance in five-

axis NC machining of sculptured surfaces," *International Journal of Advanced Manufacturing Technology*, vol. 25, no. 3–4, pp. 343–349, 2005.

[68] J. Xu, Z. Geng, Y. Sun, and L. Li, "Generating gouge-free tool paths for ball-end cutter CNC milling of cloud of point by projecting guide curves," *International Journal of Advanced Manufacturing Technology*, vol. 102, no. 5–8, pp. 1193–1204, 2019.

[69] D. Plakhotnik *et al.*, "CAM planning for multi-axis laser additive manufacturing considering collisions," *CIRP Annals*, vol. 68, no. 1, pp. 447–450, 2019.

[70] B. Lauwers, P. Dejonghe, and J. P. Kruth, "Optimal and collision free tool posture in five-axis machining through the tight integration of tool path generation and machine simulation," *CAD Computer Aided Design*, vol. 35, no. 5, pp. 421–432, 2003.

[71] L. Chen, K. Xu, and K. Tang, "Collision-free tool orientation optimization in five-axis machining of bladed disk," *Journal of Computational Design and Engineering*, vol. 2, no. 4, pp. 197–205, 2015.

[72] D. Boisselier, S. Sankaré, and T. Engel, "Improvement of the laser direct metal deposition process in 5-axis configuration," *Physics Procedia*, vol. 56, no. C, pp. 239–249, 2014.

[73] J. S. Panchagnula and S. Simhambhatla, "Manufacture of complex thin-walled metallic objects using weld-deposition based additive manufacturing," *Robotics and Computer-Integrated Manufacturing*, vol. 49, no. July 2017, pp. 194–203, 2018.

[74] T. Shi, B. Lu, S. Shi, W. Meng, and G. Fu, "Laser metal deposition with spatial variable orientation based on hollow-laser beam with internal powder feeding technology," *Optics and Laser Technology*, vol. 88, no. April 2016, pp. 234–241, 2017.

[75] Y. Ding, R. Dwivedi, and R. Kovacevic, "Process planning for 8-axis robotized laser-based direct metal deposition system: A case on building revolved part," *Robotics and Computer-Integrated Manufacturing*, vol. 44, pp. 67–76, 2017.

[76] R. Dwivedi, S. Zekovic, and R. Kovacevic, "A novel approach to fabricate uni-directional and branching slender structures using laser-based direct metal deposition," *International Journal of Machine Tools and Manufacture*, vol. 47, no.

7–8, pp. 1246–1256, 2007.

[77] R. Sundaram and J. Choi, “A slicing procedure for 5-axis laseraided DMD process,” *Journal of Manufacturing Science and Engineering, Transactions of the ASME*, vol. 126, no. 3, pp. 632–636, 2004.

[78] Y. Murtezaoglu, D. Plakhotnik, M. Stautner, T. Vaneker, and F. J. A. M. van Houten, “Geometry-Based Process Planning for Multi-Axis Support-Free Additive Manufacturing,” *Procedia CIRP*, vol. 78, pp. 73–78, 2018.

[79] L. Ren *et al.*, “Process planning strategies for solid freeform fabrication of metal parts,” *Journal of Manufacturing Systems*, vol. 27, no. 4, pp. 158–165, 2008.

[80] S. T. Newman *et al.*, “Process planning for additive and subtractive manufacturing technologies,” *CIRP Annals*, vol. 64, no. 1, pp. 467–470, 2015.

[81] K. Lee and H. Jee, “Slicing algorithms for multi-axis 3-D metal printing of overhangs,” *Journal of Mechanical Science and Technology*, vol. 29, no. 12, pp. 5139–5144, Dec. 2015.

[82] J. Ruan *et al.*, “Automated Slicing for a Multiaxis Metal Deposition System,” *Journal of Manufacturing Science and Engineering*, vol. 129, no. 2, pp. 303–310, Sep. 2006.

[83] M. H. Ahmad Fadzil *et al.*, “3D surface roughness measurement for scaliness scoring of psoriasis lesions,” *Computers in Biology and Medicine*, vol. 43, no. 11, pp. 1987–2000, 2013.

[84] M. Drbúl *et al.*, “Analysis of roughness profile on curved surfaces,” *MATEC Web of Conferences*, vol. 244, p. 1024, 2018.

[85] M. Launhardt *et al.*, “Detecting surface roughness on SLS parts with various measuring techniques,” *Polymer Testing*, vol. 53, pp. 217–226, 2016.

[86] L. Fan and P. M. Atkinson, “A new multi-resolution based method for estimating local surface roughness from point clouds,” *ISPRS Journal of Photogrammetry and Remote Sensing*, vol. 144, pp. 369–378, 2018.

[87] D. Wu, Y. Wei, and J. Terpenny, “Predictive modelling of surface roughness in fused deposition modelling using data fusion,” *International Journal of Production Research*, vol. 57, no. 12, pp. 3992–4006, 2019.

[88] P. A. S. Guru, M. V. Matham, and K. H. K. Chan, “Fiber Optic probe for surface

roughness measurement of ALM samples based on laser speckle intensity," in *2016 IEEE International Conference on Recent Trends in Electronics, Information and Communication Technology, RTEICT 2016 - Proceedings*, 2016, pp. 908–912.

[89] A. Lalehpour and A. Barari, "A more accurate analytical formulation of surface roughness in layer-based additive manufacturing to enhance the product's precision," *International Journal of Advanced Manufacturing Technology*, vol. 96, no. 9–12, pp. 3793–3804, 2018.

[90] G. Mills and G. Fotopoulos, "On the estimation of geological surface roughness from terrestrial laser scanner point clouds," *Geosphere*, vol. 9, no. 5, pp. 1410–1416, 2013.

[91] L. Tonietto *et al.*, "New Method for Evaluating Surface Roughness Parameters Acquired by Laser Scanning," *Scientific Reports*, vol. 9, no. 1, pp. 1–17, 2019.

[92] J. Vijayarangan, "Non-contact method to assess the surface roughness of metal castings by 3D laser scanning," Iowa State University, 2017.

[93] D. Przestacki, R. Majchrowski, and L. Marciniak-podsadna, "Applied Surface Science Experimental research of surface roughness and surface texture after laser cladding," *Applied Surface Science*, vol. 388, pp. 420–423, 2016.

[94] A. Bliss *et al.*, "Qualitative assessment of surface roughness of limestone specimens from the orientation of unwrapped triangulated point clouds," in *Conference Proceedings - IEEE SOUTHEASTCON*, 2017, pp. 1–5.

[95] A. Sachdeva, S. Singh, and V. S. Sharma, "Investigating surface roughness of parts produced by SLS process," *International Journal of Advanced Manufacturing Technology*, vol. 64, no. 9–12, pp. 1505–1516, 2013.

[96] I. Smurov, M. Doubenskaia, and A. Zaitsev, "Comprehensive analysis of laser cladding by means of optical diagnostics and numerical simulation," *Surface and Coatings Technology*, vol. 220, pp. 112–121, 2013.

[97] K. Zhang *et al.*, "Effects of substrate preheating on the thin-wall part built by laser metal deposition shaping," *Applied Surface Science*, vol. 317, pp. 839–855, 2014.

[98] G. Y. Baek *et al.*, "Effects of substrate preheating during direct energy deposition on microstructure, hardness, tensile strength, and notch toughness," *Metals and Materials International*, vol. 23, no. 6, pp. 1204–1215, 2017.

[99] Y. Chew *et al.*, "Thermo-mechanical model for simulating laser cladding induced

residual stresses with single and multiple clad beads," *Journal of Materials Processing Technology*, vol. 224, pp. 89–101, 2015.

[100] F. Caiazzo and V. Alfieri, "Simulation of Laser-assisted Directed Energy Deposition of Aluminum Powder: Prediction of Geometry and Temperature Evolution," *Materials* , vol. 12, no. 13. 2019.

[101] W. Gao *et al.*, "Numerical simulation of thermal field and Fe-based coating doped Ti," *International Journal of Heat and Mass Transfer*, vol. 92, pp. 83–90, 2016.

[102] R.-S. Long, S.-N. Sun, and Z.-S. Lian, "Crack restriction mechanism of thin wall metal parts fabricated by laser direct deposition shaping," *Materials Science and Technology*, vol. 32, no. 6, pp. 523–539, 2016.

[103] J. Li, Q. Wang, and P. (Pan) Michaleris, "An Analytical Computation of Temperature Field Evolved in Directed Energy Deposition," *Journal of Manufacturing Science and Engineering*, vol. 140, no. 10, Jul. 2018.

[104] J. C. Heigel, P. Michaleris, and E. W. Reutzel, "Thermo-mechanical model development and validation of directed energy deposition additive manufacturing of Ti–6Al–4V," *Additive Manufacturing*, vol. 5, pp. 9–19, 2015.

[105] M. Javidani *et al.*, "Additive Manufacturing of AlSi10Mg Alloy Using Direct Energy Deposition: Microstructure and Hardness Characterization," *Journal of Thermal Spray Technology*, vol. 26, no. 4, pp. 587–597, 2017.

[106] Q. Wang *et al.*, "Functionally graded stainless steel fabricated by direct laser deposition: Anisotropy of mechanical properties and hardness," *Acta Metallurgica Sinica (English Letters)*, vol. 31, no. 1, pp. 19–26, 2018.

[107] D. S. Shim *et al.*, "Effect of layer thickness setting on deposition characteristics in direct energy deposition (DED) process," *Optics and Laser Technology*, vol. 86, pp. 69–78, 2016.

[108] Y. Huang, M. B. Khamesee, and E. Toyserkani, "A new physics-based model for laser directed energy deposition (powder-fed additive manufacturing): From single-track to multi-track and multi-layer," *Optics and Laser Technology*, vol. 109, no. June 2018, pp. 584–599, 2019.

[109] Y. Huang *et al.*, "Rapid prediction of real-time thermal characteristics, solidification parameters and microstructure in laser directed energy deposition (powder-fed

additive manufacturing),” *Journal of Materials Processing Technology*, vol. 274, p. 116286, 2019.

[110] M. Ansari *et al.*, “Laser directed energy deposition of water-atomized iron powder: Process optimization and microstructure of single-tracks,” *Optics & Laser Technology*, vol. 112, pp. 485–493, 2019.

[111] N. Nazemi, J. Urbanic, and M. Alam, “Hardness and residual stress modeling of powder injection laser cladding of P420 coating on AISI 1018 substrate,” *International Journal of Advanced Manufacturing Technology*, vol. 93, no. 9–12, pp. 3485–3503, 2017.

[112] M. K. Alam, A. Edrisy, J. Urbanic, and J. Pineault, “Microhardness and Stress Analysis of Laser-Cladded AISI 420 Martensitic Stainless Steel,” *Journal of Materials Engineering and Performance*, vol. 26, no. 3, pp. 1076–1084, Mar. 2017.

[113] Y. Zhang *et al.*, “Numerical and experimental investigation of multilayer SS410 thin wall built by laser direct metal deposition,” *Journal of Materials Processing Technology*, vol. 212, no. 1, pp. 106–112, 2012.

[114] A. Kumar *et al.*, “Numerical Simulation of Laser Rapid Manufacturing of Multi-Layer Thin Wall Using an Improved Mass Addition Approach,” *Numerical Heat Transfer, Part A: Applications*, vol. 65, no. 9, pp. 885–910, 2014.

[115] S. Bontha *et al.*, “Thermal process maps for predicting solidification microstructure in laser fabrication of thin-wall structures,” *Journal of Materials Processing Technology*, vol. 178, no. 1, pp. 135–142, 2006.

[116] X. Wang *et al.*, “Overhang structure and accuracy in laser engineered net shaping of Fe-Cr steel,” *Optics & Laser Technology*, vol. 106, pp. 357–365, 2018.

[117] X. Wu and J. Mei, “Near net shape manufacturing of components using direct laser fabrication technology,” *Journal of Materials Processing Technology*, vol. 135, no. 2-3 SPEC., pp. 266–270, 2003.

[118] B. He *et al.*, “Influence of scanning pattern on the edge collapse of solid parts in laser metal direct forming,” *Optics & Laser Technology*, vol. 48, pp. 171–177, 2013.

[119] Z. L. Lu *et al.*, “Fabricating the Steam Turbine Blade by Direct Laser Forming,” *Materials and Manufacturing Processes*, vol. 26, no. 7, pp. 879–885, 2011.

[120] N. Nazemi and R. J. Urbanic, “A numerical investigation for alternative toolpath

deposition solutions for surface cladding of stainless steel P420 powder on AISI 1018 steel substrate," *The International Journal of Advanced Manufacturing Technology,* vol. 96, no. 9, pp. 4123–4143, 2018.

[121] L. Peng *et al.*, "Direct laser fabrication of thin-walled metal parts under open-loop control," *International Journal of Machine Tools and Manufacture*, vol. 47, no. 6, pp. 996–1002, 2007.

[122] M. Akbari and R. Kovacevic, "Closed loop control of melt pool width in robotized laser powder–directed energy deposition process," *The International Journal of Advanced Manufacturing Technology*, pp. 2887–2898, 2019.

[123] A. Kumar, A. G. Banerjee, S. Paul, and A. Roy Choudhury, "Maximization of slice height with uniformity in surface roughness in the direct slicing of freeform surfaces," *Proceedings of the Institution of Mechanical Engineers, Part B: Journal of Engineering Manufacture,* vol. 217, no. 6, pp. 765–777, 2003.

[124] F. Cardarelli, *Materials handbook*. Springer, 2000.

[125] S. G. Sandomirskii, "Estimation of the Ultimate Tensile Strength of Steel from Its HB and HV Hardness Numbers and Coercive Force," *Russian Metallurgy (Metally)*, vol. 2017, no. 11. pp. 989–993, 2017.

[126] H. Konrad, "The Fundamentals of Hardness Testing," in *Hardness Testing Principles and Applications*, ASM International, 2011.

[127] "Standard Test Method for Microindentation Hardness of Materials," in *ASTM Handbook Designation: E384-17*, 2017, pp. 1–40.

[128] G. Sundararajan, "Hardness Testing," in *Encyclopedia of Materials: Science and Technology 2st Edition*, 2001, pp. 3728–3736.

[129] P. Hariharan, *Optical Interferometry (2nd Edition)*. Elsevier, 2003.

[130] B. Bhushan, "Surface roughness analysis and measurement techniques," in *Modern Tribology Handbook: Volume One: Principles of Tribology*, 2000.

[131] N. Nazemi and J. Urbanic, "An Experimental and Simulation Study for Powder Injection Multitrack Laser Cladding of P420 Stainless Steel on AISI 1018 Steel for Selected Mechanical Properties," *Journal of Manufacturing Science and Engineering, Transactions of the ASME*, vol. 140, no. 1, pp. 1–12, 2018.

[132] ESI Group, "Sysweld 2016," 2016.

[133] L. Wang, S. D. Felicelli, and P. Pratt, “Residual stresses in LENS-deposited AISI 410 stainless steel plates,” *Materials Science and Engineering: A*, vol. 496, no. 1, pp. 234–241, 2008.

[134] E. J. Pavlina and C. J. Van Tyne, “Correlation of Yield Strength and Tensile Strength with Hardness for Steels,” *Journal of Materials Engineering and Performance*, vol. 17, no. 6, pp. 888–893, Dec. 2008.

[135] S. Simhambhatla, K. K.P., C. U, and S. M Adinarayanappa, “A Study of the Mechanical Properties of Objects Built through Weld-Deposition,” *Proceedings of the Institution of Mechanical Engineers Part B Journal of Engineering Manufacture*, vol. 227, 2013.

[136] S. Saqib, R. J. Urbanic, and K. Aggarwal, “Analysis of Laser Cladding Bead Morphology for Developing Additive Manufacturing Travel Paths,” *Procedia CIRP*, vol. 17, no. Complete, pp. 824–829, 2014.

[137] R. T. ; L. Kiepura H.F ; Thomas, P ; Wheaton, N.D;, *ASM Handbook. Vol. 4. Heat Treating*. 1991.

APPENDICES

Appendix A

Surface Roughness Data

Table A-1. Surface roughness values

L (partition length)	5-axis		2+1+1-axis		Rotary	
	Inner	Outer	Inner	Outer	Inner	Outer
2	30.4	23.6	39.5	39.1	44.1	37.2
2.5	30.4	23.4	39.8	33.6	39.5	38.1
3	32.4	24.9	40.2	27.8	43.8	36.0
3.5	41.7	26.3	40.9	41.2	43.9	34.4
4	46.5	29.0	38.0	40.0	41.1	31.6
4.5	44.9	30.0	35.2	35.2	42.4	39.4
5	46.3	33.7	34.5	38.3	40.4	38.4
5.5	45.4	33.9	33.6	43.2	37.2	35.5
6	37.1	34.2	34.7	39.3	35.5	37.4
6.5	38.4	35.0	37.0	41.3	50.1	42.1
7	31.8	26.2	40.6	38.2	42.6	39.1
7.5	29.5	21.9	35.6	36.6	42.0	43.5
8	25.1	21.6	43.3	40.4	43.6	40.6
8.5	29.9	22.9	46.0	37.9	45.1	36.9
9	29.9	23.4	60.8	36.3	43.2	40.9
9.5	30.8	22.0	59.5	43.2	44.5	38.9
10	26.3	20.6	65.2	45.4	41.8	37.7
10.5	33.2	18.9	66.3	44.1	40.6	35.1
11	31.5	15.8	68.4	48.4	37.9	35.7
11.5	31.8	14.6	58.5	53.8	38.6	33.9
12	33.1	15.1	46.1	39.0	38.2	33.2
12.5	35.9	15.0	35.1	31.9	34.4	31.8
13			40.5	27.4	30.5	28.9
13.5			34.6	25.3	28.5	30.8
14			31.6	26.0	28.6	30.8
14.5			35.3	29.2	27.2	27.9
15			34.8	30.9	27.3	31.9
15.5			34.0	28.4	28.7	32.9
16			33.1	29.7	26.6	32.2
16.5			32.7	29.2	26.6	35.1
17			31.3	33.6	28.5	38.4
17.5			39.3	32.7	27.3	32.8
18			42.1	31.9	25.2	36.4
18.5			43.3	29.7	24.5	41.1
19			50.5	43.4	29.7	29.6

19.5	42.7	47.9	29.2	29.0
20	43.0	42.2	32.1	33.2
20.5	36.6	54.6	30.9	36.4
21	39.7	60.0	29.2	34.6
21.5	29.1	45.6	29.7	42.0
22	28.3	40.4	28.5	39.8
22.5	29.1	34.9	22.3	41.6
23	28.6	26.9	23.2	43.4
23.5	30.0	22.9	22.7	43.1
24	25.3	26.8	22.8	27.5
24.5	24.9	29.1	37.6	26.1
25	20.2	25.8	40.6	24.5
25.5	30.6	27.0	44.8	24.1
26	32.8	31.8	49.1	23.2
26.5	18.9	29.4	51.0	17.7
27	61.0	25.7	38.9	18.5
27.5	58.4	39.7	46.4	23.2
28	50.3	42.0	35.0	27.1
28.5	41.6	46.1	32.3	24.6
29	34.1	84.8	35.6	29.7
29.5	40.2	105.7	36.6	34.9
30	38.2	100.8	36.5	35.2
30.5	31.5	118.0	36.9	35.3
31	28.8	99.3	28.7	29.8
31.5	29.3	91.0	37.3	31.2
32	31.2	40.5	35.3	35.4
32.5	35.8	55.0	27.6	36.3
33	34.7	40.9		37.8
33.5	23.9	42.6		37.5
34	22.1	41.4		32.0
34.5	30.1	35.8		37.5
35	33.3	34.6		31.1
35.5	29.8	33.4		
36	35.3	32.8		
36.5	40.9	40.6		
37	42.3	33.4		
37.5	39.7	41.6		
38	37.8	44.5		
38.5	47.0	36.2		
39	43.3	37.0		
39.5	41.0	37.7		
40	40.1	37.9		
40.5	30.7	39.8		
41	31.4	34.4		
41.5	28.1	32.6		

42	26.6	39.7
42.5	30.3	32.2
43	29.4	61.6
43.5	24.8	62.8
44	32.7	55.7
44.5	43.2	63.0
45	43.3	68.1
45.5	56.1	48.0
46	60.1	43.9
46.5	56.0	34.1
47	41.5	28.0
47.5	39.6	27.5
48	37.8	26.0
48.5	34.4	21.1
49	35.4	21.8
49.5	34.6	22.2
50	32.8	18.9
50.5	28.7	19.3
51	35.1	21.2
51.5	41.3	26.6
52	35.9	34.3
52.5	36.5	37.1
53	35.9	51.8
53.5	35.6	55.5
54	37.9	46.3
54.5	48.8	43.8
55	50.7	44.5
55.5	40.8	35.3
56	31.8	34.3
56.5	30.5	30.7
57	24.7	29.0
57.5	23.7	27.7
58	25.8	31.7
58.5	25.9	33.5
59	25.7	28.3
59.5	23.4	25.5
60	25.3	27.4
60.5	25.5	26.9
61	21.7	41.5
61.5	23.1	36.2
62	23.2	38.2
62.5	21.8	44.2
63	17.5	42.1
63.5	3.1	31.1

🟨 Partitions 1-4

🟩 Partitions 5-8

64	30.9
64.5	26.0
65	30.6
65.5	33.5
66	41.7
66.5	38.5
67	36.3
67.5	32.7
68	28.5
68.5	34.1
69	21.2
69.5	35.0
70	50.9
70.5	135.3
71	117.8
71.5	74.5

Appendix B

Hardness data

Table B-1. All Hardness data

	Test point No.	300 gf-1	300 gf-2	1000 gf-1	1000 gf-2	1000 gf Ave.	300 gf Ave.	Total average
2+1+1-axis sample	1	229	217	219	238	228	223	226
	2	211	196	205	207	206	204	205
	3	198	223	193	197	195	211	203
	4	191	185	189	203	196	188	192
	5	163	163	199	187	193	163	178
	6	217	181	183	211	197	199	198
	7	186	190	181	238	209	188	199
	8	264	179	216	195	206	222	214
	9	201	189	170	178	174	195	185
	10	215	222	151	147	149	219	184
	11	206	152	167	212	190	179	184
	12	150	195	235	169	202	172	187
	13	238	149	226	182	204	193	199
	14	255	186	212	207	209	221	215
	15	281	144	230	204	217	212	215
	16	217	272	212	216	214	244	229
	17	177	197	199	216	208	187	197
	18	182	172	169	170	170	177	173
	19	151	163	151	155	153	157	155
	20	173	188	163	193	178	180	179
	21	190	213	190	244	217	202	209
	22	273	222	208	177	192	248	220
	23	237	275	217	189	203	256	229
	24	260	203	208	209	208	231	220
	25	285	217	243	209	226	251	239
	26	185	203	185	170	178	194	186
	27	147	192	150	168	159	169	164
	28	173	168	167	143	155	171	163
	29	137	187	163	182	173	162	167
	30	216	281	155	238	197	248	223

	31	239	225	220	239	230	232	231
	32	188	268	195	226	210	228	219
	33	248	225	177	193	185	236	211
	34	187	165	176	167	171	176	174
	35	171	219	175	179	177	195	186
	36	185	189	156	173	164	187	176
	37	195	196	189	186	188	195	192
	38	182	202	198	226	212	192	202
	39	207	202	157	207	182	205	193
	40	266	193	192	191	191	229	210
	41	222	226	221	233	227	224	226
	42	204	219	233	186	210	212	211
	43	245	197	185	200	193	221	207
	44	154	196	202	202	202	175	188
	45	194	208	185	217	201	201	201
	46	202	251	207	255	231	227	229
	47	191	167	214	176	195	179	187
	48	239	185	212	198	205	212	208
	49	216	199	236	150	193	208	200
	50	200	169	243	253	248	185	216
	51	270	199	214	200	207	234	221
	52	165	164	179	210	195	165	180
	53	163	189	196	187	191	176	184
	54	303	212	227	196	212	257	234
	55	188	183	209	219	214	185	200
	56	289	167	229	193	211	228	219
	57	174	221	215	195	205	197	201
	58	173	301	166	183	175	237	206
	59	182	159	187	215	201	171	186
	60	196	197	180	204	192	196	194
	61	239	188	209	199	204	214	209
	62	275	189	199	257	228	232	230
	63	165	257	218	212	215	211	213
	64	203	237	207	188	197	220	209
	65	161	178	238	239	238	170	204
	66	189	238	198	246	222	214	218
	67	208	153	241	231	236	181	208
	68	200	230	215	186	200	215	207
	69	255	222	235	202	218	239	229

	70	207	165	201	169	185	186	186
	71	256	154	165	161	163	205	184
	72	216	156	153	206	180	186	183
5-axis sample	1	178	148	191	157	174	163	168
	2	197	149	212	188	200	173	187
	3	232	151	140	202	171	192	181
	4	260	237	198	218	208	249	228
	5	220	258	227	198	212	239	226
	6	274	162	239	190	215	218	216
	7	224	246	222	236	229	235	232
	8	182	230	254	258	256	206	231
	9	254	232	225	186	206	243	224
	10	176	279	205	218	211	227	219
	11	227	251	208	190	199	239	219
	12	192	263	200	208	204	227	216
	13	235	168	173	203	188	201	195
	14	224	165	200	188	194	194	194
	15	174	182	170	189	180	178	179
	16	196	184	174	173	173	190	182
	17	172	171	159	154	156	172	164
	18	164	163	181	195	188	163	176
Rotary sample	1	179						
	2	175						
	3	199						
	4	228						
	5	208						
	6	211						
	7	197						
	8	201						
	9	200						
	10	178						
	11	202						
	12	188						
	13	188						
	14	192						
	15	204						
	16	199						
	17	203						
	18	163						

	19	181
	20	193
	21	194
	22	213
	23	180
	24	198
	25	196
	26	171
	27	207
	28	220
	29	209
	30	213
	31	231
	32	187
	33	242
	34	155
	35	186
	36	214
	37	219
	38	204
	39	190
	40	200
	41	149
	42	232
	43	214
	44	221
	45	213
	46	193
	47	194
	48	171
	49	201
	50	221
	51	211
	52	203
	53	179
	54	178
	55	215
	56	221
	57	223

	58	192
	59	202
	60	189
	61	188
	62	158
	63	193
	64	231
	65	203
	66	190

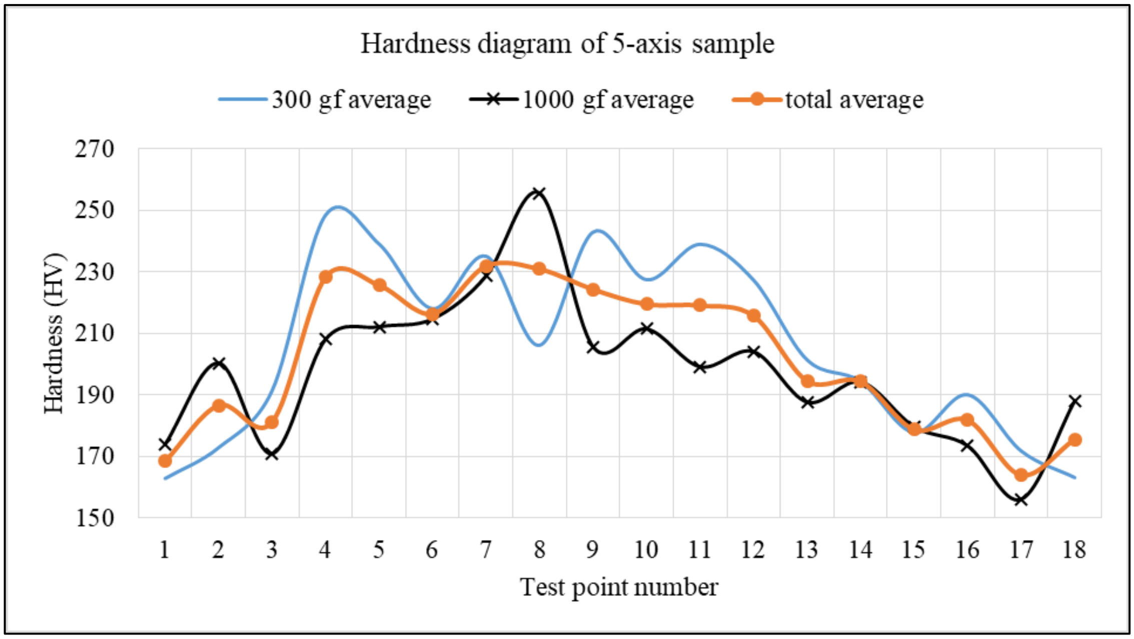

Figure B-1. Hardness Diagrams of 5-axis sample

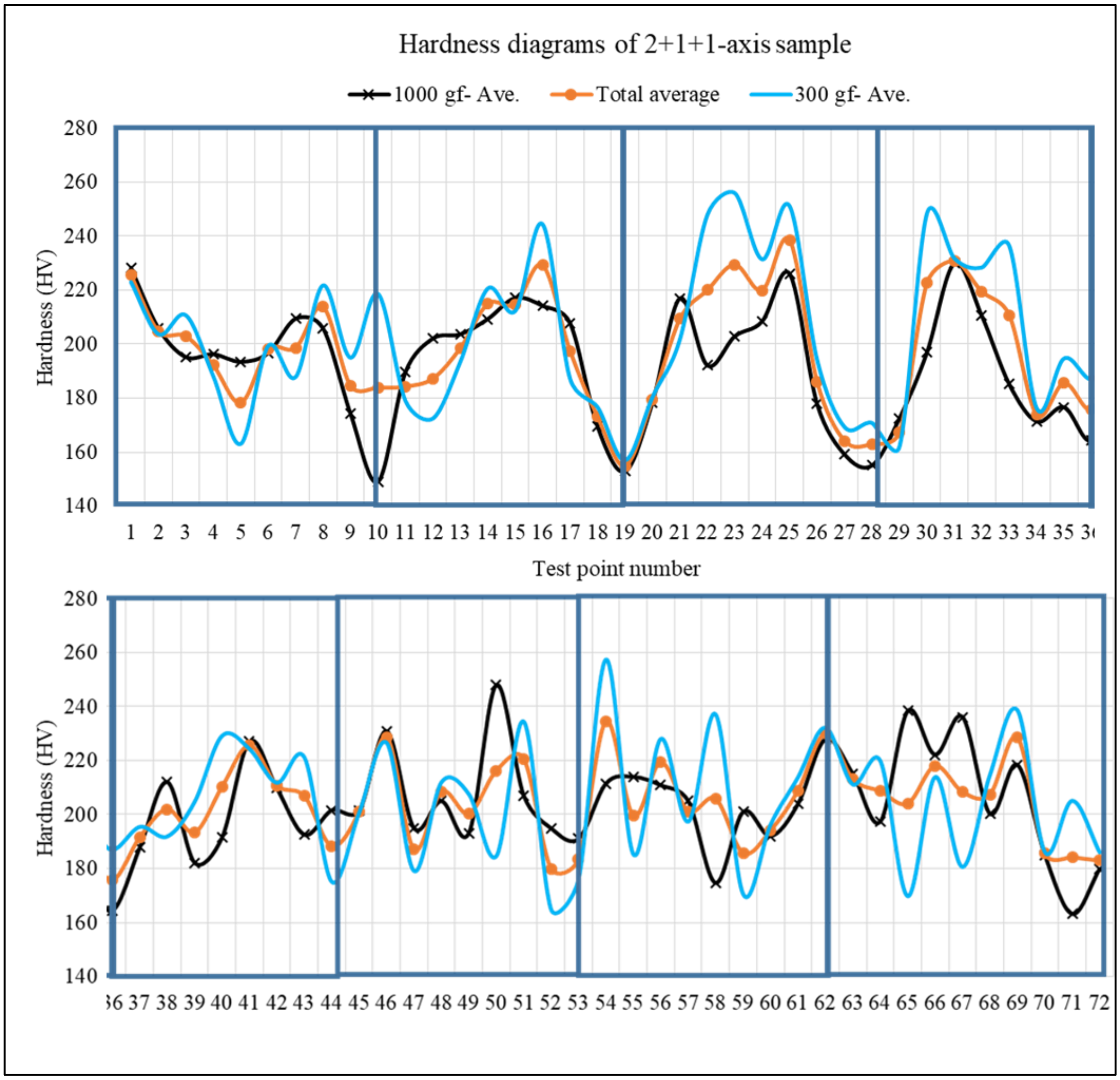

Figure B-2. Hardness Diagrams of 2+1+1-axis sample

VITA AUCTORIS

NAME: Hamed Kalami

PLACE OF BIRTH: Tehran, Iran

YEAR OF BIRTH: 1982

EDUCATION: University of Windsor, Windsor, Ontario,
2020 PhD, Mechanical Engineering

K.N .Toosi University of Technology, Thran, Iran
2009 M.A.Sc., Mechanical Engineering

University of Mazandaran, Babol, Iran
2005 B.Sc., Mechanical Engineering